



McNamara, Paul William (1998) *Development of optical techniques for space-borne laser interferometric gravitational wave detectors*. PhD thesis.

<http://theses.gla.ac.uk/8477/>

Copyright and moral rights for this thesis are retained by the author

A copy can be downloaded for personal non-commercial research or study, without prior permission or charge

This thesis cannot be reproduced or quoted extensively from without first obtaining permission in writing from the Author

The content must not be changed in any way or sold commercially in any format or medium without the formal permission of the Author

When referring to this work, full bibliographic details including the author, title, awarding institution and date of the thesis must be given

**Development of Optical Techniques for  
Space-Borne Laser Interferometric  
Gravitational Wave Detectors**

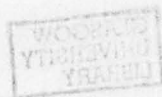
Paul William McNamara

Department of Physics and Astronomy,  
University of Glasgow.

Presented as a thesis for the degree of Ph.D.,  
in the University of Glasgow.

© P.W. McNamara, 1998.

September 28, 1998



1998  
11421

# Contents

*To my parents,  
to whom I owe so much.*

Acknowledgements	xiii
Preface	xv
Summary	xvii
1 Gravitational Waves in General Relativity	1
1.1 Introduction	1
1.2 Review of General Relativity	2
1.3 Existence of Gravitational Waves	5
1.4 Sources of Gravitational Waves	7
1.4.1 Burst Sources	8
1.4.2 Periodic Sources	12
1.4.3 Stochastic Sources	14
1.5 Conclusions	15
2 Gravitational Wave Detectors	18
2.1 Introduction	18
2.2 Resonant Mass Detectors	19
2.2.1 Sensitivity of Resonant Mass Detectors	19
2.2.2 Resonant Spherical Mass Detectors	20
2.3 Laser Interferometric Detectors	21
2.3.1 Noise Sources in Laser Interferometers	26
2.4 Space-borne Laser Interferometers	31

# Contents

2.3 Other Detection Techniques . . . . .	34
2.6 Conclusions . . . . .	38
<b>3 LISA - The Laser Interferometer Space Antenna . . . . .</b>	<b>37</b>
3.1 Introduction . . . . .	37
3.2 LISA Mission . . . . .	38
3.2.1 Point Aiming . . . . .	41
3.3 A LISA Satellite . . . . .	43
3.3.1 The Spacecraft . . . . .	45
<b>Acknowledgements . . . . .</b>	<b>xiii</b>
<b>Preface . . . . .</b>	<b>xv</b>
<b>Summary . . . . .</b>	<b>xvii</b>
<b>1 Gravitational Waves in General Relativity . . . . .</b>	<b>1</b>
1.1 Introduction . . . . .	1
1.2 Review of General Relativity . . . . .	2
1.3 Existence of Gravitational Waves . . . . .	5
1.4 Sources of Gravitational Waves . . . . .	7
1.4.1 Burst Sources . . . . .	8
1.4.2 Periodic Sources . . . . .	12
1.4.3 Stochastic Sources . . . . .	14
1.5 Conclusions . . . . .	15
<b>2 Gravitational Wave Detectors . . . . .</b>	<b>18</b>
2.1 Introduction . . . . .	18
2.2 Resonant Mass Detectors . . . . .	19
2.2.1 Sensitivity of Resonant Mass Detectors . . . . .	19
2.2.2 Resonant Spherical Mass Detectors . . . . .	20
2.3 Laser Interferometric Detectors . . . . .	21
2.3.1 Noise Sources in Laser Interferometers . . . . .	26
2.4 Space-borne Laser Interferometers . . . . .	31

2.5	Other Detection Techniques . . . . .	34
2.6	Conclusions . . . . .	36
<b>3</b>	<b>LISA - The Laser Interferometer Space Antenna</b>	<b>37</b>
3.1	Introduction . . . . .	37
3.2	Overview of LISA Mission . . . . .	38
3.2.1	Point Ahead . . . . .	43
3.3	A LISA Satellite . . . . .	43
3.3.1	The Spacecraft . . . . .	45
3.3.2	The Science Payload . . . . .	46
3.4	Interferometric Techniques . . . . .	49
3.5	Interferometer Readout . . . . .	51
3.5.1	Vertex Interference Signal . . . . .	52
3.5.2	Long Arm Interference Signal . . . . .	56
3.6	Conclusions . . . . .	59
<b>4</b>	<b>Laser Frequency Stabilisation for LISA</b>	<b>60</b>
4.1	Introduction . . . . .	60
4.2	Radio Frequency Reflection Locking . . . . .	61
4.3	<i>rf</i> Reflection Locking Theory . . . . .	63
4.4	Experimental Arrangement . . . . .	67
4.4.1	Introduction . . . . .	67
4.4.2	Optical Layout . . . . .	68
4.4.3	Feedback Control Electronics . . . . .	72
4.5	Results . . . . .	81
4.6	Conclusions . . . . .	86
<b>5</b>	<b>Weak Light Phase Locking</b>	<b>88</b>
5.1	Introduction . . . . .	88
5.2	Calculation of the Shot Noise Limit . . . . .	89
5.3	Capture and Lock of a Phase-Locked-Loop . . . . .	92
5.3.1	MATLAB Simulation of a Phase-Locked-Loop . . . . .	95

5.4	Experimental Arrangement . . . . .	98
5.4.1	Calibration of Mixer . . . . .	98
5.5	Initial Optical Layout . . . . .	99
5.5.1	Results . . . . .	101
5.6	Improvements to Optical Layout and Electronics . . . . .	104
5.6.1	Results . . . . .	109
5.7	Conclusions . . . . .	119
<b>6</b>	<b>Telescope Design for LISA</b> . . . . .	<b>120</b>
6.1	Introduction . . . . .	120
6.2	Two Mirror Reflecting Telescopes . . . . .	121
6.3	Mathematical Model of a Cassegrain Type Telescope . . . . .	124
6.4	Numerical Model of the LISA Telescope . . . . .	127
6.5	ASAP Analysis of the LISA Telescope . . . . .	130
6.6	Wavefront Aberration Analysis in the Far-Field . . . . .	131
6.6.1	Wavefront Errors in LISA . . . . .	132
6.6.2	Wavefront Error Budget . . . . .	133
6.6.3	Calculation of the Wavefront Error . . . . .	138
6.6.4	Results of Telescope Aberration Analysis . . . . .	141
6.7	Conclusions . . . . .	142
<b>7</b>	<b>Conclusions</b> . . . . .	<b>143</b>
<b>A</b>	<b>MATLAB Code To Calculate Voltage Spectral Density</b> . . . . .	<b>145</b>
<b>B</b>	<b>Telescope Model: Source Code</b> . . . . .	<b>153</b>
B.1	CODEV Model of LISA Telescope System . . . . .	153
B.2	ASAP Model of LISA Telescope System . . . . .	159
	<b>Bibliography</b> . . . . .	<b>170</b>

# List of Figures

1.1	<b>Illustration of Parallel Transport.</b> <i>Vector <math>A^\nu</math> is displaced from point <math>P</math> to <math>Q</math> via <math>P_1</math>. The same vector is displaced from <math>P</math> to <math>Q</math> via <math>P_2</math>. The difference in the resulting vectors (<math>D_2D_1A^\nu</math> and <math>D_1D_2A^\nu</math>) gives a measure of the curvature of the manifold. . . . .</i>	4
1.2	<b>Illustration of the polarisations of a gravitational wave.</b> <i>The two polarisations of the wave are shown acting on a ring of free test particles. The motion of each particle can be seen by comparing it to its original position (unfilled circles). . . . .</i>	7
1.3	<b>Spectra of expected gravitational wave sources.</b> <i>The “characteristic amplitude” is the amplitude expected for an optimised detector. To the left of the “Gravity Gradient Wall” (shaded area), background noise restricts the sensitivity of ground based detectors, and so any signals in this region are only accessible via space-borne detectors. (adapted from [10]) . . . . .</i>	16
2.1	<b>Schematic diagram of a simple Michelson interferometer.</b> . . . .	23
2.2	<b>Schematic diagrams of laser interferometers.</b> <i>(a) A Multipass Michelson, (b) A Fabry-Pérot Michelson. . . . .</i>	25
2.3	<b>Diagrams showing test mass suspension systems.</b> <i>The left hand diagram shows a single pendulum suspension, isolated from the ground through a 5-layer seismic isolation stack, the right hand diagram shows the same isolation stack, but with the test mass suspended using a double pendulum. . . . .</i>	27

2.4	<b>Sensitivity limit for GEO 600 from individual noise sources.</b> <i>The thermal noise calculation assumes a <math>Q</math>-factor for internal modes of <math>5 \times 10^6</math>, and a pendulum <math>Q</math>-factor of <math>10^7</math>. The shot-noise curve is calculated for a beamsplttter power of 7 kW (with power recycling).</i>	32
2.5	<b>Layout of proposed space-borne interferometric detectors.</b>	33
3.1	<b>Comparison of the frequency range of sources for space-borne and ground based detectors.</b> <i>The line marked 'LISA' shows the expected noise floor for LISA. All signals above this line should be detectable. The sensitivity for an advanced ground based detector is shown for comparison. (IWDB = Interacting White Dwarf Binary)[12]</i>	39
3.2	<b>Location of LISA with respect to the Earth.</b> <i>Adapted from [12]</i>	40
3.3	<b>Diagram of the LISA orbits, showing the rotation of the s/c around the centroid of the triangle.</b> <i>Diagram used with the permission of R. Schilling</i>	41
3.4	<b>Diagram of a LISA spacecraft.</b> <i>Adapted from [12]</i>	42
3.5	<b>Schematic diagram showing the need for "Point Ahead" in LISA.</b> <i>The point ahead angle in this diagram has been greatly exaggerated to allow the effect to be seen more clearly.</i>	44
3.6	<b>Detailed view of a LISA optics bench.</b> <i>The red line represents local laser light, and green lines represent light from the other optics benches. (P.D. = Photodiode)</i>	47
3.7	<b>Nomenclature of lasers in LISA</b>	49
3.8	<b>Scheme to extract error signal for phase locking and clock stabilisation.</b> <i>Where NPRO = Numerical Programmed Oscillator, and USO = Ultra Stable Oscillator</i>	55
4.1	<b>Schematic layout of rf reflection locking scheme.</b>	61
4.2	<b>Experimental DC and de-modulated fringes.</b> <i>The reflected fringes are obtained by scanning the frequency of the laser through the resonant frequency of the cavity.</i>	62

4.3	<b>Fabry-Pérot cavity used in reflection.</b> . . . . .	63
4.4	<b>DC and de-modulated fringes obtained using Equations 4.18 and 4.21.</b> . . . . .	67
4.5	<b>Photograph of miniature diode-pumped Nd:YAG non-planar ring oscillator.</b> <i>Laser manufactured by the Laser Zentrum Hannover.</i> . . . . .	69
4.6	<b>Diagram of miniature diode-pumped Nd:YAG non-planar ring oscillator.</b> <i>The lasing cavity is formed from internal reflections from faces 1-4. The reflection at face 2 reflects the light up to the top of the crystal, creating the non-planar ring cavity.</i> . . . . .	69
4.7	<b>Experimental arrangement to frequency stabilise and measure the frequency noise of the laser.</b> . . . . .	70
4.8	<b>Photograph of reference cavity.</b> <i>The reference and analyser cavity are both manufactured from monolithic blocks of Zerodur, giving the cavity better structural stability, and low thermal expansion.</i> . . . . .	71
4.9	<b>Photograph of “Actuator Mirror”.</b> <i>This mirror is used as the actuator to control the pathlength of the analyser cavity, thereby allowing the cavity length to be locked to the laser frequency.</i> . . . . .	72
4.10	<b>Schematic diagram of “Actuator Mirror”.</b> . . . . .	72
4.11	<b>Circuit diagram of photodiode and resonant passband amplifier.</b> . . . . .	73
4.12	<b>Digital auto-locking circuit to find resonance condition, and close feedback loop.</b> . . . . .	74
4.13	<b>Feedback circuit to lock laser frequency to reference cavity.</b> . . . . .	77
4.14	<b>Gain and phase response of the laser frequency stabilisation servo - HIGH gain state</b> . . . . .	79
4.15	<b>Transfer function of feedback electronics including laser frequency actuators.</b> . . . . .	80
4.16	<b>Feedback circuit to lock analyser cavity length to laser frequency.</b> . . . . .	82

4.17	<b>Gain and phase response for analyser servo, showing both low and high gain transfer functions.</b> . . . . .	83
4.18	<b>Uncalibrated error point measurement.</b> <i>The middle trace (red) shows the spectrum of the in-loop error signal of the frequency locking servo when the laser is locked to the reference cavity. The top trace shows the level of shot noise corresponding to the detected intensity when the laser frequency is locked. The bottom trace shows the spectrum analyser noise floor.</i> . . . . .	84
4.19	<b>Spectrum of temperature fluctuations measured inside the reference cavity vacuum tank.</b> <i>The right hand axis shows the equivalent limit to laser frequency noise due to these temperature fluctuations, assuming a thermal expansion coefficient for Zerodur of <math>\alpha = 2 \times 10^{-8}/K</math>.</i> . . . . .	85
4.20	<b>Frequency Noise of Master Laser.</b> <i>The top trace shows the noise spectrum of the free running laser, and the bottom trace shows the apparent frequency noise of the stabilised laser measured by the analyser cavity.</i> . . . . .	87
5.1	<b>Block diagram of a second order phase-locked-loop to offset phase lock two independent oscillators.</b> . . . . .	90
5.2	<b>Calibration curve for mixer.</b> <i>This graph shows a typical mixer response for the two input frequencies being equal, with the phase difference between them swept through 180°.</i> . . . . .	93
5.3	<b>Diagram showing the output of the mixer during acquisition.</b> <i>The non-symmetric nature of the output produces a non-zero average level, which pulls the beat note between the lasers towards the offset frequency.</i> . . . . .	94
5.4	<b>Simulink Model of Phase-Locked-Loop.</b> <i>This simulation approximates the two lasers and photodiode as a single voltage controlled oscillator, producing the beat note at the input of the phase detector.</i> . . . . .	95

5.5	<b>Time Evolution of Error and Feedback Signal.</b> <i>The top graph shows the time evolution of the error signal as the system acquires lock. The bottom trace shows the evolution of the feedback signal. Once the signals are at a common frequency, the feedback becomes almost constant, as the phase of the VCO is pulled to 90° away from the reference.</i> . . . . .	97
5.6	<b>Schematic diagram to show the calibration scheme of the locking side mixer</b> . . . . .	99
5.7	<b>Schematic diagram of an initial optical layout to simulate phase locking in a far s/c of LISA.</b> ( <i>BS = Beam Splitter</i> ) . . . . .	100
5.8	<b>RF spectral analysis of measurement photodiode output.</b> <i>Trace (a) shows the case with no phase modulation on the master laser, trace (b) is with phase modulation (13.2 MHz).</i> . . . . .	102
5.9	<b>Relative phase noise of slave laser measured using initial optical layout.</b> <i>Master laser power = 50 nW, Slave laser power = 5 mW. The red line indicates the shot noise limit. The relative phase noise is clearly far from being limited by photon shot noise.</i> . . . . .	103
5.10	<b>New optical layout using polarisation splitting techniques.</b> <i>PFBS - Polarisation Fixing Beam Splitter, MPBS - Main Polarising Beam Splitter, BS45° - Beam Splitter oriented at 45° to the master laser polarisation</i> . . . . .	105
5.11	<b>Detailed view of Main Polarising Beam Splitter (MPBS), showing polarisation of beams.</b> . . . . .	106
5.12	<b>Circuit diagrams of photodiodes and associated pre-amplifiers.</b> <i>(a) Measurement photodiode, and (b) Locking photodiode.</i> . . . . .	108
5.13	<b>Circuit diagram of new feedback circuit to phase lock lasers.</b> . . . . .	110
5.14	<b>Photograph of temperature stabilised copper block, with mixers and 1st stage amplifiers attached.</b> . . . . .	111

5.15	<b>Circuit diagram for temperature stabilisation of mixers and first stage amplifiers.</b> <i>590 kh - IC temperature sensor (current output), 78/9xx - voltage regulators, and LM135 - high current op-amp.</i> . . . . .	111
5.16	<b>Temperature spectrum of stabilised copper block.</b> <i>The top trace (green) shows the temperature spectrum of the lab environment. The bottom trace (blue) shows the temperature spectrum of the stabilised copper block (both passive and active stabilisation used).</i> . . . . .	112
5.17	<b>Uncalibrated error point measurement.</b> . . . . .	114
5.18	<b>High frequency components of phase noise of slave laser.</b> <i>The red curve shows the unstabilised phase noise of the slave laser, and the blue curve shows the stabilised laser performance. The green (straight) line shows the calculated level of the photon shot noise limit.</i> . . . . .	115
5.19	<b>Effect of increasing shot noise on locking photodiode.</b> <i>The blue trace (bottom) shows the relative phase noise of the slave laser under normal locking conditions. The green trace shows the relative phase noise when the shot noise level on the locking photodiode is increased.</i> . . . . .	117
5.20	<b>Low frequency components of relative phase noise of slave laser.</b> <i>The green line shows the shot noise limiting level for this measurement.</i> . . . . .	118
6.1	<b>Diagram of a Cassegrain type telescope.</b> <i>The subscripts 1/2 refer to the primary and secondary mirrors respectively. "d" is the separation of the mirrors, and (d+b) is known as the back focal length.</i> . . . . .	121
6.2	<b>Spot diagrams showing the intensity patterns for an off-axis object imaged through a Cassegrain type telescope[60].</b> . . . . .	123
6.3	<b>CODEV plot of the LISA telescope.</b> <i>The model has been set up to trace an off-axis ray from the fibre output through the telescope, stopping just after the primary mirror.</i> . . . . .	128

6.4	<b>ASAP ray trace of the LISA telescope.</b> <i>The target has been placed a short distance from the primary to reduce the computation time of the raytrace.</i> . . . . .	131
6.5	<b>Schematic diagrams of (a) ideal wavefront, and (b) aberrated wavefront.</b> <i>Figure (a) shows the case of an ideal spherical wave, centred on the transmitting craft. (b) shows a diagram of the real case where the wavefront is likely to deviate from being ideal.</i> . . . . .	133
6.6	<b>ASAP plots of the reference beam in the near field.</b> <i>(a) shows a cross section of the energy of the beam located at the target of Figure 6.4, (b) shows an isometric plot of the wavefront at the target plane. Both (a) and (b) clearly show the clipping of the telescope aperture, and the obscuration caused by the secondary and spider.</i> . . . . .	135
6.7	<b>ASAP plots of the reference beam in the far field.</b> <i>Plot (a) shows the cross section of the energy profile, and (b) an isometric plot of the wavefront at a distance equal to ten times the Rayleigh length.</i> . . . . .	136
6.8	<b>ASAP plots of wavefront aberration due to defocus of the telescope.</b> <i>The wavefront aberrations at the extremities of the beam are due to numerical rounding errors in ASAP.</i> . . . . .	139
6.9	<b>ASAP plots of wavefront aberration due tilt of the primary mirror.</b> <i>The wavefront aberrations at the extremities of the beam are due to numerical rounding errors in ASAP.</i> . . . . .	140

4.1	<i>Properties of Reference and Analyser Cavities. 4.1.1 refer to the cavity mirrors, with 4 being the input coupler.</i> . . . . .	71
-----	--	----

6.1	<i>The first most common two mirror "Cassegrain" telescopes[66]. The constant "K" is known either as the "Coma constant", or more commonly in telescope design as the "Schwarzschild constant". The coma constant characterizes the deformation of a surface from a paraboloid.</i> . . . . .	122
-----	---	-----

# List of Tables

1.1	<b>Gravitational wave amplitude estimates from known rapidly rotating neutron star sources.</b> <i>The gravitational eccentricity is defined as <math>1 - \frac{a}{b}</math>, where <math>a</math> is the length of the semi-major axis of the neutron star, and <math>b</math> the semi-minor axis.</i> . . . . .	13
2.1	<b>Overview of resonant bar detectors around the world.</b> [15][16]	20
2.2	<b>Overview of prototype interferometric detectors</b> [12]. . . . .	22
2.3	<b>Overview of long baseline interferometers.</b> . . . . .	22
2.4	<b>Sources of acceleration noise in LISA</b> [12]. . . . .	35
3.1	<b>Example of offset frequency and modulation scheme for LISA.</b>	50
3.2	<b>Beat signals and strengths at the output of the rear photodiode of optics bench 6.</b> <i>The bold entries are the signals that can be used to phase lock the lasers and clocks.</i> . . . . .	54
4.1	<b>Properties of Reference and Analyser Cavities.</b> <i>1,2,3 refer to the cavity mirrors, with 1 being the input coupler.</i> . . . . .	71
6.1	<b>The four most common two mirror “Cassegrain” telescopes</b> [60]. <i>The constant “<math>k</math>” is known either as the “Conic constant”<sup>2</sup>, or more commonly in telescope design as the “Schwarzschild constant”. The conic constant characterises the deformation of a surface from a perfect sphere.</i> . . . . .	122

6.2	<b>Comparison of a classical Cassegrain and a Ritchey-Chretien telescopes.</b> <i>The two telescopes have been set-up to have the same size of mirrors, and approximately the same beam sizes on the two mirrors. The beam sizes on the lenses are for the beam striking the surface nearer the fibre.</i> . . . . .	129
6.3	<b>The telescope error budget for defocus, tilt, and point ahead.</b> <i>The percentage of total error budget assumes a total error in displacement noise of <math>1\text{ pm}/\sqrt{\text{Hz}}</math>.</i> . . . . .	142
B.1	<b>Results from CODEV Gaussian beam analysis</b> . . . . .	158

I would firstly like to thank my supervisor Harry Ward for his help, and guidance throughout this project. I would also like to thank Jim Hough for his continued encouragement, and for the many helpful suggestions given to me since I joined the Gravitational Waves Group.

I also express my thanks to the other members of the Gravitational Waves Group: Norma Robertson, Gavin Newton, Ken Strain, Mike Plissi, Sheila Rowan, David Robertson, Alastair Gains, Sharon Twyford, Morag Casey, Galan Torrie, David Faber, and Stephen Scholten.

My fellow office mates see due special thanks, Ken Steadon and Stuart Kirkborn for their help and advice at the start of my research career, and David Clabber for having to put up with me on a daily basis.

Technical assistance was provided by Angus McKeelhar, Colin Craig, Allan Latta and Ray Hutchins, who not only encouraged me through the writing of this thesis, but also taught me how to saw in a straight line!

Thanks are also due to the members of the optics group of the Space Science Department of the Rutherford Appleton Laboratory, especially to my supervisor, Martin Cahill, whose patience and expertise in optical raytracing were very much appreciated. Also to Ian, Suz, Kate and Chris who made my visits to RAL all the more enjoyable.

I would also like to express my gratitude to Professors R.P. Ferrier and D.H. Young and the Department of Physics and Astronomy at the University of Glasgow for support over the last four years.

Finally I wish to express my sincere gratitude to my family, first and foremost to

# Acknowledgements

I would firstly like to thank my supervisor Harry Ward for his help, and guidance throughout this period of research, and in the writing of this thesis. I would also like to thank Jim Hough for his continued encouragement, and for the many helpful suggestions given to me since I joined the Gravitational Waves Group.

I also express my thanks to the other members of the Gravitational Waves Group; Norna Robertson, Gavin Newton, Ken Strain, Mike Plissi, Sheila Rowan, David Robertson, Alistair Grant, Sharon Twyford, Morag Casey, Calum Torrie, David Palmer, and Stephen McIntosh.

My fellow office mates are due special thanks; Ken Skeldon and Stuart Killbourn for their help and advice at the start of my research career, and David Clubley for having to put up with me on a daily basis.

Technical assistance was provided by Angus McKellar, Colin Craig, Allan Latta and Ray Hutchins, who not only encouraged me through the writing of this thesis, but also taught me how to saw in a straight line!

Thanks are also due to the members of the optics group of the Space Science Department of the Rutherford Appleton Laboratory, especially to my supervisor, Martin Caldwell, whose patience and expertise in optical raytracing were very much appreciated. Also to Ian, Sue, Kate and Chris who made my visits to RAL all the more enjoyable.

I would also like to express my gratitude to Professors R.P. Ferrier and D.H. Saxon and the Department of Physics and Astronomy at the University of Glasgow for support over the last four years.

Finally I wish to express my sincere gratitude to my family; first and foremost to

my mother and father, without whose continuous encouragement and support, this thesis would not have been possible, also to Andrew, whose own academic success has encouraged me throughout my entire education, and lastly to Uncle Jackie for letting me beat him at golf every week!

During this period of research, funding was provided by the Particle Physics and Astronomy Research Council, and the Rutherford Appleton Laboratory.

During the period of research presented in this thesis, the author was in receipt of a PPARC CASE studentship, in association with the Rutherford Appleton Laboratory. The author was under the joint supervision of Dr H. Ward at the University of Glasgow and Dr M. Caldwell at the Rutherford Appleton Laboratory.

The work presented in this thesis is directed towards the detection of low frequency gravitational radiation, primarily in the region of  $10^{-4}$  Hz to 1 Hz.

Chapter 1 gives a brief description of Einstein's General Theory of Relativity, together with the prediction and nature of gravitational radiation. The latter half of the chapter reviews some of the expected sources of gravitational waves, along with current estimates of signal strengths and event rates. The content is based mainly on standard literature.

Chapter 2 is a brief review of the instruments designed to detect gravitational radiation. The chapter deals with the detectors in chronological order, starting with resonant bars, through to long baseline ground-based and space-borne laser interferometers. Finally, present and possible future detection techniques for measuring ultra-low frequency radiation are described. This review material is based on current literature from the research groups developing the detectors.

The content of Chapter 3 describes, in detail, the space-borne laser interferometric detector, LISA. After an initial description of the mission along with its similarities and differences to ground based interferometers, a scheme is described to allow all relevant error signals to be extracted, as well as the gravitational wave signature. The description is a summary of the mission proposal prepared by the LISA Science Team, with contributions from the author on a possible error signal

# Preface

During the period of research presented in this thesis, the author was in receipt of a PPARC CASE studentship, in association with the Rutherford Appleton Laboratory. The author was under the joint supervision of Dr H. Ward at the University of Glasgow, and Dr M. Caldwell at the Rutherford Appleton Laboratory.

The work presented in this thesis is directed towards the detection of low frequency gravitational radiation, primarily in the region of  $10^{-4}$  Hz to 1 Hz.

Chapter 1 gives a brief description of Einstein's General Theory of Relativity, focusing on the prediction and nature of gravitational radiation. The latter half of the chapter reviews some of the expected sources of gravitational waves, along with current estimates of signal strengths and event rates. The content is based mainly on standard literature.

Chapter 2 is a brief review of the instruments designed to detect gravitational radiation. The chapter deals with the detectors in chronological order, starting with resonant bars, through to long baseline ground-based and space-borne laser interferometers. Finally, present and possible future detection techniques for measuring ultra-low frequency radiation are described. This review material is based on current literature from the research groups developing the detectors.

The content of Chapter 3 describes, in detail, the space-borne laser interferometric detector, LISA. After an initial description of the mission along with its similarities and differences to ground based interferometers, a scheme is described to allow all relevant error signals to be extracted, as well as the gravitational wave signature. The description is a summary of the mission proposal prepared by the LISA Science Team, with contributions from the author on a possible error signal

extraction scheme.

Chapter 4 describes an experiment designed to frequency stabilise a solid state Nd:YAG laser over timescales of several hours. The author was responsible for the planning and execution of this experiment; some electronic assistance was provided by Dr H. Ward. The experimental results presented are taken from a series of measurements made, and analysed by the author.

Chapter 5 deals with the development of a weak light phase locking scheme. The apparatus and electronic servo circuits used to make the measurements were designed and constructed by the author, with some assistance from Dr H. Ward, and Mr A. McKellar. The experimental measurements and subsequent presentation of results was entirely the work of the author.

In association with the Rutherford Appleton Laboratory, a study was made of the telescope system to be used in LISA. Chapter 6 describes this work. A model of the LISA telescope was set up in the optical design package CODEV, and analysed using the optical raytrace program ASAP. This work was largely the responsibility of the author, in conjunction with Dr M. Caldwell. Input to the initial telescope design was made by Dr P. Gray and Dr D. Robertson.

Appendix A lists the MATLAB code used to calculate the voltage spectrum of the acquired time series data, and Appendix B lists the code used for the telescope model used in Chapter 6. These programs are entirely the work of the author.

# Summary

In 1918, Albert Einstein first showed that *gravitational waves* – propagating ripples in the curvature of spacetime – were a consequence of his General Theory of Relativity. However, it was not until the early 1960s that the experimental search for gravitational waves began.

The expected spectrum of gravitational radiation from violent astrophysical events spans a wide frequency range. Ground-based interferometric detectors, optimised for signals from a few tens of Hertz to a few kHz, have been developed for over twenty years, culminating in the multi-kilometre instruments currently being built. Over this time, improvements have been continually made, especially towards increasing the sensitivity of the detectors at ever lower frequencies. However, due to the seismic and gravity gradient noise of the Earth, it is impossible to build a ground based detector with high gravitational wave sensitivity at frequencies below a few Hertz. To observe at these frequencies, the detector must be free from all Earth induced noise, necessitating the need to go into space. LISA, the *Laser Interferometer Space Antenna* is such a detector, aimed at detecting the abundance of astrophysical signals expected in the  $10^{-4}$  Hz to 1 Hz range.

This thesis deals with aspects of gravitational wave detection relating directly to the proposed LISA mission.

The thesis begins with a review of gravitational wave astrophysics, starting with a brief description of the prediction and nature of gravitational radiation as a consequence of General Relativity. A short description of possible astrophysical sources is given along with current estimates of signal sources and strengths.

The history of gravitational wave detectors is then briefly outlined, from the

early 1960s and the first resonant bar, through to the modern long baseline laser interferometers currently under construction.

Discussion then turns to the joint ESA/NASA space-borne interferometer, LISA. LISA involves picometre precision laser interferometry between spacecraft separated by millions of kilometres. Among the considerable technical challenges involved are the need for laser and clock frequency stabilisation schemes, active phase-locked laser transponders and precision telescope design.

After an overview of the mission concept, the thesis deals with the issue of gravitational wave signal extraction from the various interferometric data streams produced in the six LISA spacecraft. A scheme for obtaining the necessary transfer of clock stability around the set of spacecraft is presented.

LISA is planned to use diode-pumped solid state lasers. Experiments carried out to characterise the frequency noise of such a laser over the timescales of interest to the LISA mission are then described. Active frequency stabilisation to a triangular Fabry-Pérot reference cavity is undertaken, with independent measurements of residual frequency noise obtained from a second analyser cavity.

In LISA, the divergence of the laser beams as they propagate along the long arms of the interferometer means that only a very small amount of light is received by any spacecraft. The phase locking system has to function with this low received intensity and should, ideally, produce a transponded beam with relative phase fluctuations determined by the photon shot noise of the weak received light.

A test and demonstration of the phase-locked laser transponder scheme for LISA is then presented. The frequency stabilised laser is used as the master oscillator, and a second identical laser is used as the slave. Results are obtained both from within the stabilisation system and also from out-of-loop measurements using an independent optical path. At relative power levels approaching those in LISA, performance close to the shot noise limit was demonstrated over part of the frequency spectrum of interest. Some excess noise was, however, found at milliHertz frequencies, most probably due to thermal effects.

The thesis then continues with an investigation of far-field wavefront aberrations caused by errors in the transmitting telescopes originally planned for LISA. Any

phase variation across the near field wavefront (defined as the wavefront on the primary mirror), caused, for example, by a mis-alignment of the telescope mirrors, will produce phase variation in the far-field wavefront. Coupled with pointing fluctuations of the incoming light, these wavefront distortions can cause excess displacement noise in the interferometer readout. The starting point of the investigation was to redesign the LISA telescope in order to remove both spherical and coma aberrations. Using Gaussian raytracing techniques, the effect of near field aberrations on the far field phase was explored. A revised Ritchey-Chretien telescope design is described and numerical simulations presented.

Finally the thesis concludes with a summary of the work carried out, setting the results in the context of the development of the LISA mission.

## 1.1 Introduction

In 1916 Albert Einstein showed that Gravitational Waves were a consequence of his General Theory of Relativity (GR). These waves are ripples in the fabric of spacetime, propagating through space at a velocity equal to that of light.

The weak nature of the gravitational interaction with matter necessitates the use of the test coherent motion of large quantities of mass to produce waves of sufficient amplitude to be observed directly. As a result, the only sources of gravitational radiation which might be detected experimentally are from violent astrophysical sources, e.g. black hole formation, supernovae explosions, or compact binary star coalescence. Unlike electromagnetic waves, gravitational waves are quadrupole in nature, as the single sign of mass and the conservation of momentum forbid the existence of monopole or dipole radiation.

In this chapter a brief description of the General Theory of Relativity is given, leading to the Einstein field equations and the prediction of gravitational waves. This is followed by a review of the most likely sources that are expected to emit gravitational radiation with amplitudes that may be detected by proposed ground based and space-borne detectors.

# Chapter 1

# Gravitational Waves in General Relativity

## 1.1 Introduction

In 1918, Albert Einstein showed that *Gravitational Waves* were a consequence of his General Theory of Relativity (GR)[1]. These waves are ripples in the fabric of spacetime, propagating through space at a velocity equal to that of light.

The weak nature of the gravitational interaction with matter necessitates the need for fast coherent motion of large quantities of mass to produce waves of sufficient amplitude to be observed directly. As a result, the only sources of gravitational radiation which might be detected experimentally are from violent astrophysical sources, *e.g.* black hole formation, supernovæ explosions, or compact binary star coalescences. Unlike electromagnetic waves, gravitational waves are quadrupole in nature, as the single sign of mass and the conservation of momentum forbid the existence of monopole or dipole radiation.

In this chapter a brief description of the General Theory of Relativity is given, leading to the Einstein field equations and the prediction of gravitational waves. This is followed by a review of the most likely sources that are expected to emit gravitational radiation with amplitudes that may be detected by proposed ground based and space-borne detectors.

## 1.2 Review of General Relativity

Einstein's General Theory of Relativity (GR) [2] is based on two fundamental corner stones: the equivalence principle and the principle of general covariance. In its weaker form the equivalence principle simply states that the inertial mass,  $M_I$ , and the gravitational mass,  $M_G$ , of a body are equal; in a gravitational field, all test bodies accelerate at the same rate. GR incorporates this result by demanding that test particles have world lines that are geodesics in curved spacetime. Put more strongly, in a local inertial frame, all physical phenomena accord with the Special Theory of Relativity (SR).

The principle of general covariance states that all physical laws should remain valid under all coordinate transformations. Thus in GR all laws must be covariant under all transformations, forcing GR to be tensorial in nature.

In order to deal with curved space, it is essential to introduce the concept of a manifold. A manifold is essentially a continuous space which locally looks like Euclidean space; however on the large scale, the topology of the manifold can be far from Euclidean. At any point, one can define a tensor function known as the *metric tensor* to describe the local curvature of space. Consider two points labelled  $(x_0, x_1, x_2, x_3)$  and  $(x_0 + \delta x_0, x_1 + \delta x_1, x_2 + \delta x_2, x_3 + \delta x_3)$ , the proper distance between these points can be expressed as <sup>1</sup>

$$ds^2 = g^{\alpha\beta} dx_\alpha dx_\beta \quad (1.1)$$

In SR, the proper distance between the two points is given by <sup>2</sup>

$$ds^2 = -dt^2 + dx^2 + dy^2 + dz^2 \quad (1.2)$$

---

<sup>1</sup>In this chapter, the Einstein summation convention will be used. Whenever an expression contains one index as a superscript and the *same* index as a subscript, a summation is implied over all values the index can take. Roman indices take the values 1,2,3; Greek indices take the values 0,1,2,3.

<sup>2</sup>Using *Geometrised Units* where  $G=c=1$ , such that  $1 \equiv \frac{G}{c^2} \equiv 7.425 \times 10^{-28} \text{ mkg}^{-1}$

i.e. the metric having components (in matrix form)

$$g^{\alpha\beta} = \begin{pmatrix} -1 & 0 & 0 & 0 \\ 0 & 1 & 0 & 0 \\ 0 & 0 & 1 & 0 \\ 0 & 0 & 0 & 1 \end{pmatrix} \quad (1.3)$$

This is the metric for flat spacetime. When the manifold is curved, the metric becomes more complicated.

Before dealing with curvature directly, it is useful to firstly introduce the notion of *Parallel Transport*[3]. Consider two neighbouring points on the manifold,  $P$  and  $Q$ , and a vector,  $\vec{A}$  at  $P$ . In order to displace the vector,  $\vec{A}$ , from  $P$  to  $Q$  one needs to construct a vector,  $\vec{D}A$ , which is somehow related to  $\vec{A}$ . This mapping should be linear and unique. In a particular coordinate patch, the vector,  $\vec{A}$ , at  $P$  and the displaced vector,  $\vec{D}A$ , at  $Q$  can be written in component form as  $A^\nu(x)$  and  $DA^\nu(x + dx)$ . Defining

$$DA^\nu(x + dx) = A^\nu(x) + \delta A^\nu(x) \quad (1.4)$$

linearity requires that  $\delta A^\nu(x)$  be linearly dependent on the components of  $A^\nu$ . This leads to the definition of the *affine connections*,  $\Gamma_{\alpha\beta}^\nu$ , by

$$\delta A^\nu(x) = -\Gamma_{\alpha\beta}^\nu(x)A^\alpha(x)dx^\beta \quad (1.5)$$

In Riemannian manifolds, the affine connections are normally referred to as the *Christoffel Symbols*, and will be referred to as this from now on.

Substituting Equation (1.5) into Equation (1.4), and evaluating at point  $P_1$  (Figure 1) gives

$$D_1A^\nu(x + d_1x) = A^\nu(x) - \Gamma_{\alpha\beta}^\nu(x)A^\alpha(x)d_1x^\beta \quad (1.6)$$

This in turn can be transported through  $d_2x$  to the point  $Q$ , using the Christoffel symbols at the point  $P_1$  at  $(x + d_1x)$ . Thus

$$D_2(D_1A^\nu) = D_1A^\nu - \Gamma_{\tau\sigma}^\nu(x + d_1x)(D_1A^\tau)d_2x^\sigma \quad (1.7)$$

A similar expression can be obtained for  $D_1D_2A^\nu$ .

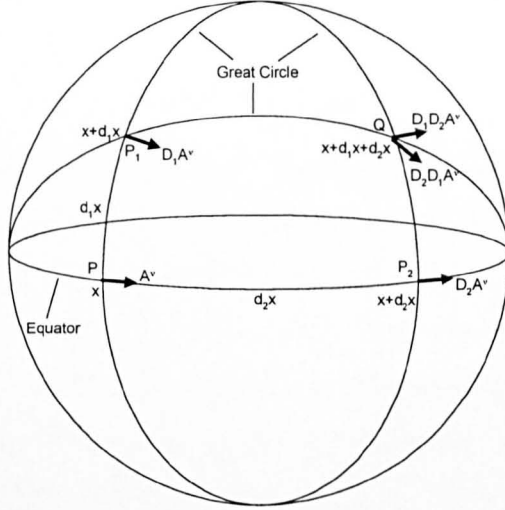


Figure 1.1: **Illustration of Parallel Transport.** Vector  $A^\nu$  is displaced from point  $P$  to  $Q$  via  $P_1$ . The same vector is displaced from  $P$  to  $Q$  via  $P_2$ . The difference in the resulting vectors ( $D_2D_1A^\nu$  and  $D_1D_2A^\nu$ ) gives a measure of the curvature of the manifold.

Expanding  $\Gamma_{\tau\sigma}^\nu(x + d_1x)$  to first order using <sup>3</sup>

$$\Gamma_{\tau\sigma}^\nu = \frac{1}{2}g^{\alpha\nu} (g_{\alpha\tau,\sigma} + g_{\alpha\sigma,\tau} - g_{\tau\sigma,\alpha}) \quad (1.8)$$

and subtracting  $D_1D_2A^\nu$  from  $D_2D_1A^\nu$  one obtains

$$D_1D_2A^\nu - D_2D_1A^\nu = R_{\tau\beta\mu}^\nu A^\tau d_1x^\beta d_2x^\mu \quad (1.9)$$

where  $R_{\tau\beta\mu}^\nu$  is the *Riemann Christoffel Tensor*. In geodesic coordinates, the tensor has components

$$R_{\alpha\beta\delta\gamma} = \frac{1}{2}(g_{\alpha\gamma,\beta\delta} - g_{\alpha\delta,\beta\gamma} + g_{\beta\delta,\alpha\gamma} - g_{\beta\gamma,\alpha\delta}) \quad (1.10)$$

This tensor describes the curvature of the metric space, and is zero in a flat spacetime manifold. As the curvature of the manifold is dependent on second order derivatives of the metric tensor, one would expect the Riemann Christoffel Tensor to depend on the second derivatives of  $g^{\alpha\beta}$ . This is indeed the case.

<sup>3</sup>The notation used is that a ',' (comma) represents differentiation with respect to the coordinate following the comma e.g.  $g_{\alpha,\beta} = \frac{\partial g_{\alpha\beta}}{\partial x^\beta}$

By contracting this tensor on the first and third indices, one arrives at the *Ricci Tensor*.

$$R_{\beta\gamma} = g^{\alpha\delta} R_{\alpha\beta\delta\gamma} \quad (1.11)$$

Other contractions, in principle, are possible: on the first and second, and first and fourth, etc. However, because  $R_{\alpha\beta\delta\gamma}$  is antisymmetric on  $\alpha$  and  $\beta$  and on  $\delta$  and  $\gamma$ , all these contractions either vanish identically or reduce to  $\pm R_{\alpha\beta}$ . Therefore the Ricci tensor is in fact the *only* contraction of the Riemann tensor.

By further contraction of the Ricci tensor, one obtains the *Ricci Scalar*,  $R$ . Using both the Ricci tensor and Ricci scalar, Einstein arrived at a tensor known as the *Einstein Curvature Tensor*, defined as

$$G^{\mu\nu} = R^{\mu\nu} - \frac{1}{2}g^{\mu\nu}R \quad (1.12)$$

This now allows one to write down the *Einstein Field Equations*:

$$G^{\mu\nu} + \Lambda g^{\mu\nu} = kT^{\mu\nu} \quad (1.13)$$

where  $G^{\mu\nu}$  is as defined above,  $\Lambda$  is the Cosmological Constant<sup>4</sup>, and  $k$  is the constant of proportionality, taking the value in SI units of  $k = \frac{8\pi G}{c^4}$ .  $T^{\mu\nu}$  is the energy momentum tensor, and describes the presence and motion of gravitating matter. In particular, it determines the matter/energy density (material particles, electromagnetic fields, particle fields, etc.) in any given coordinate system.

### 1.3 Existence of Gravitational Waves

In a region of spacetime where the gravitational field is weak (i.e. which is *nearly flat*) the metric  $g^{\mu\nu}$  can be written:

$$g^{\mu\nu} = \eta^{\mu\nu} + h^{\mu\nu} \quad (1.14)$$

---

<sup>4</sup>Originally the cosmological constant was not present in the field equations. Einstein added it years later to give a solution of a static universe. However, after observations of an expanding universe were made, he rejected it and added that it was the biggest mistake of his life. Recent observations have shown that  $\Lambda$  does exist, but is a very small number approaching zero. From now on, it will be assumed to take the value of zero.

where  $\eta^{\mu\nu}$  is the metric of SR (flat space), and  $h^{\mu\nu}$  is a small perturbation ( $|h^{\mu\nu}| \ll 1$ ) to this flat space.  $h^{\mu\nu}$  is not a tensor as such, but under certain transformations, transforms as if it were a tensor. From now on  $h^{\mu\nu}$  will be considered as a tensor sitting on a “background” Minkowski spacetime. This is not a valid assumption in all coordinate transformations, but is true for a class of transformations known as *gauge transformations*. One can now define a new “tensor” called the *trace reverse* of  $h$ :

$$\bar{h}^{\mu\nu} = h^{\mu\nu} - \frac{1}{2}\eta^{\mu\nu}h \quad (1.15)$$

where  $h \equiv h^\alpha_\alpha$  and is the trace of  $h^\mu_\nu$ . This allows the weak field Einstein field equations to be written in the simple form (in geometrised units).

$$\left(-\frac{\partial^2}{\partial t^2} + \nabla^2\right)\bar{h}^{\mu\nu} = -16\pi T^{\mu\nu} \quad (1.16)$$

In vacuum,  $T^{\mu\nu} = 0$ , and so the weak field equations reduce to

$$\left(-\frac{\partial^2}{\partial t^2} + \nabla^2\right)\bar{h}^{\mu\nu} = 0 \quad (1.17)$$

which is the 3D wave equation, with periodic solutions of the form

$$\bar{h}_{\mu\nu}^{\text{TT}} = A_{\mu\nu} \exp(ik_\mu x^\mu) \quad (1.18)$$

*i.e.* a wave travelling with velocity  $c$ . The superscript “TT” has been added to  $\mathbf{h}$ , as, according to GR, the wave field is both *transverse* and *traceless*.

Since sources of gravitational waves are at cosmological distances, the waves appear very nearly flat by the time they reach the earth. If one chooses a reference frame in which the waves propagate along the  $z$ -direction, then the transverse nature of the wave field means that all  $z$ -components of the field are zero. Therefore the non-zero components of the tensor  $\mathbf{h}^{\text{TT}}$  are

$$\mathbf{h}^{\text{TT}} = \begin{pmatrix} h_{xx} & h_{xy} \\ h_{yx} & h_{yy} \end{pmatrix} \quad (1.19)$$

The traceless property of  $\mathbf{h}^{\text{TT}}$  means that  $h_{xx}^{\text{TT}} + h_{yy}^{\text{TT}} = 0$ , *i.e.*  $h_{xx}^{\text{TT}} = -h_{yy}^{\text{TT}}$ . Further, by the symmetry of the curvature tensor,  $h_{xy}^{\text{TT}} = h_{yx}^{\text{TT}}$ . Therefore there are only *two* independent components of the wave field, *i.e.* two polarisation states. These states

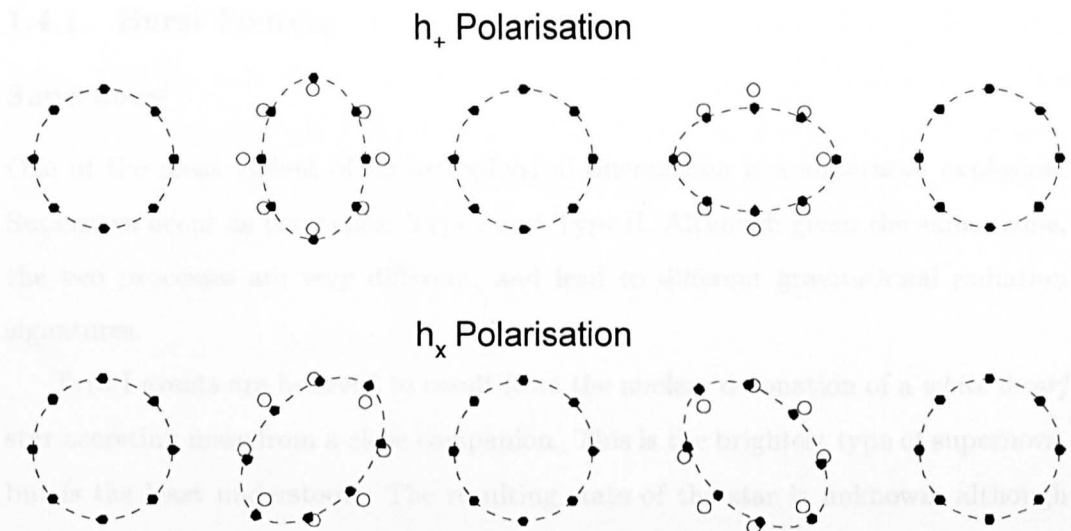


Figure 1.2: **Illustration of the polarisations of a gravitational wave.** *The two polarisations of the wave are shown acting on a ring of free test particles. The motion of each particle can be seen by comparing it to its original position (unfilled circles).*

are denoted by  $h_+ \equiv h_{xx}^{\text{TT}} \equiv h_{yy}^{\text{TT}}$ : the *plus* polarisation, and  $h_\times \equiv h_{xy}^{\text{TT}} \equiv h_{yx}^{\text{TT}}$ : the *cross* polarisation. The former,  $h_+$ , produces a force field with the orientation ‘+’, the latter a force field oriented in a ‘ $\times$ ’ direction (Figure 1.2).

## 1.4 Sources of Gravitational Waves

Any massive system whose quadrupole moment changes with time will emit gravitational radiation. However, it has been shown that only astronomical sources ( $M \geq M_\odot$ )<sup>5</sup> will emit waves with sufficiently large amplitude to be detected by present (and future) detectors. In this section I will briefly describe the cosmological events that can produce detectable wave fields by earth based and space-borne detection techniques. The sources considered fall into three main classes: (i) Burst Sources, (ii) Periodic Sources, and (iii) Stochastic Sources.

<sup>5</sup> $1 M_\odot = 1 \text{ Solar Mass } (2 \times 10^{30} \text{ kg})$

### 1.4.1 Burst Sources

#### Supernovæ

One of the most violent of all astrophysical phenomena is a supernova explosion. Supernova occur as two types: Type I and Type II. Although given the same name, the two processes are very different, and lead to different gravitational radiation signatures.

Type I events are believed to result from the nuclear detonation of a *white dwarf* star accreting mass from a close companion. This is the brightest type of supernova, but is the least understood. The resulting state of the star is unknown, although it is thought that a fraction of the star's core may collapse to form a *neutron star* (NS). If, prior to the explosion, the effects of the accretion disk make the white dwarf rotate rapidly, then the resulting core collapse may be very non-spherical, producing a rotating “bar” shaped NS. This NS would have high quadrupole moment, and would therefore be a strong source of gravitational radiation.

On the other hand, Type II supernovæ are much better understood. This type of event is caused by the core collapse of a massive star. After the nuclear fuel is exhausted through fusion reactions of successively heavier elements, an iron core forms. At this stage the radiation pressure from the core is greatly reduced, and the gravitational pressure of the surrounding matter dominates the interior of the star. The temperature within the core builds up causing the iron to photo-disintegrate, with the now free protons and electrons being forced together under the immense gravitational pressure, forming a hot mass of neutrons at nuclear densities. At this stage the core rapidly collapses to a very dense compact body, and the infalling matter “bounces” off the surface, causing a shock wave which travels outward through the star until it reaches the surface, causing the explosion.

The end state of the star can be one of two things. If the progenitor star has a mass greater than  $6 M_{\odot}$ , then the resulting compact object will be a *neutron star*. If the mass of the progenitor is greater than  $\sim 20 M_{\odot}$ , then even after mass loss, the star will still be massive enough to collapse to form a *black hole*.

The total luminosity of gravitational radiation from a Type II supernova explo-

sion is hard to quantify. The intensity of the radiation emitted depends on two things: (1) the extent to which the core collapses non-axisymmetrically (*i.e.* its quadrupole moment) which is strongly dependent on the rotation of the progenitor star, and (2) the rate of collapse of the core, which may be slowed by the interaction of outgoing neutrinos and electromagnetic radiation with the infalling matter. However an estimate of the frequency and intensity of the waves at the earth has been made by Piran and Stark[4] to be

$$f = 1.3 \times 10^4 \left( \frac{M_\odot}{M} \right) \text{ Hz}, \quad (1.20)$$

$$h \cong 7 \times 10^{-22} \left( \frac{\varepsilon}{0.01} \right)^{\frac{1}{2}} \left( \frac{M}{M_\odot} \right) \left( \frac{10 \text{ Mpc}}{r_o} \right) \quad (1.21)$$

where  $h$  is the gravitational wave amplitude,  $\varepsilon$  is the efficiency of gravitational wave production (defined as  $\varepsilon = \Delta E/Mc^2$ , where  $\Delta E$  is the total energy radiated),  $r_o$  is the distance to the source, and  $M$  is the mass of the source. The event rate for such a supernova is expected to be approximately one every forty years in our own galaxy, or a few per year out to a distance of 10 Mpc (the distance to the centre of the Virgo cluster of galaxies). However, there may be another class of event called *optically silent supernovae*. This type of supernova could be much more frequent, as statistics on high mass stars in our galaxy predict a neutron star production rate of about one every four years - roughly ten times more frequent than presently seen.

### Neutron Star Binary Coalescence

Neutron star binary coalescence could prove to be the most exciting of the short lived sources of gravitational waves. Several neutron star binaries[5] (NS-NS) are now known to exist in our Galaxy *e.g.* PSR B1913+16 (the Hulse-Taylor Binary Pulsar), PSR B2003+46, PSR B1543+12, and PSR B2127+11C. The Hulse-Taylor binary was the first such binary to be discovered (in 1975) and has been studied ever since. The orbit of the two stars is decaying due to the loss of energy to gravitational waves, exactly as predicted by GR[6][7]. This system will continue to lose energy, and will coalesce to a single object in  $3.5 \times 10^8$  years. The event rate due to binary neutron star coalescence out to 100 Mpc could be  $\geq 3/\text{yr}$ .

The frequency of the emitted gravitational radiation is at twice the orbital frequency of the binary system. In the case of the Hulse-Taylor binary, the period of which is  $\sim 7.68$  hours, the gravity wave frequency is in the region of  $\sim 7 \times 10^{-5}$  Hz. This is lower than the frequency bands of all proposed detectors. However, although this system will never be seen to coalesce, there may be other systems with much shorter orbital periods and hence higher gravitational wave frequencies. For ground based detectors, the gravity wave signal only becomes accessible during the last thousand or so seconds before coalescence, as the local gravitational noise of the earth hides the earlier lower frequency signal (Figure. 1.4). However, a combination of space-borne and ground based detectors will allow the coalescence to be observed from the quasi-stable, periodic phase through to the final coalescence.

If the masses of the two stars ( $M_1$  and  $M_2$ ) are approximately the same, as could be the case for a NS-NS binary, and are in a circular orbit<sup>6</sup>, then an approximation of the amplitude of the waves is dependent only on what is called the *chirp mass*:

$$\mathcal{M} = \mu^{\frac{3}{5}} M^{\frac{2}{5}} \quad (1.22)$$

where  $\mu$  is the *reduced mass*,  $\frac{M_1 M_2}{(M_1 + M_2)}$ , and  $M$  is the total mass, ( $M_1 + M_2$ ), of the binary. The formula for the amplitude of the waves is then given by [8]

$$h = 1.5 \times 10^{-19} \left[ \frac{f}{1 \text{ Hz}} \right]^{\frac{2}{3}} \left[ \frac{\mathcal{M}}{M_{\odot}} \right]^{\frac{5}{3}} \left[ \frac{r_o}{1 \text{ kpc}} \right]^{-1} \cos \left( \int_0^t f(t') dt' + \phi_o \right) \quad (1.23)$$

where  $\phi_o$  is an arbitrary initial phase, and where the rate of change of the logarithmic frequency of the signal is given by:

$$\frac{d \ln f}{dt} = 0.126 \left[ \frac{\mathcal{M}}{M_{\odot}} \right]^{\frac{5}{3}} \left[ \frac{f}{100 \text{ Hz}} \right]^{\frac{8}{3}} \text{ s}^{-1} \quad (1.24)$$

From the two above equations, it can be seen that if one can measure the time-dependence of the frequency and amplitude, then the chirp mass,  $\mathcal{M}$ , can be eliminated, and the distance to the source deduced.

---

<sup>6</sup>This is a valid approximation to make, as a system that can be observed by ground based detectors, has already lost eccentricity as the stars spiral in toward each other.

## Black Hole Binary Coalescence

There may exist other forms of compact binaries containing at least one black hole. The black hole - black hole binary (BH-BH) is of great interest, as numerical relativity can predict to a high accuracy the final coalescence and the waveforms produced, including the dependence on the angular momenta and spin of the holes. Comparison of the observed and calculated waveforms will give one of the strongest tests of GR yet.

As well as BH-BH binaries being produced from the collapse of massive stars, it is also hypothesised[9] that shortly before NS-NS coalescence, the neutron stars may become individually unstable and gravitationally collapse to form black holes. The onset of the instability is difficult to predict and is highly dependent on the equation of state used in the calculations. However, in Wilson and Mathews (1995)[9], it has been observed that the collapse can occur while the stars are still in a quasi-stable orbit, *i.e.* many orbits away from the time when the stars actually coalesce.

## Infall into Supermassive Black Holes

At the centre of most major galaxies, supermassive black holes, SMBH ( $M > 10^5 M_\odot$ ) are thought to exist. These holes can grow by either colliding, and hence coalescing, with other SMBH (*i.e.* in a galaxy merger), or from accretion of surrounding matter. When a hole grows to  $\sim 10^9 M_\odot$ , main sequence stars, neutron stars and small black holes can be captured, and pass through the event horizon undisrupted, giving out a pulse of gravitational waves. If the SMBH is less massive ( $10^6 M_\odot < M < 10^9 M_\odot$ ), then an infalling object will be disrupted due to tidal forces. However the strength of the gravitational radiation emitted will not significantly decrease[10]. The waveforms for stars or small black holes falling into SMBH have been calculated to high precision by *e.g.* Kojima and Nakamura [10]. The typical frequency and amplitude for such an event are

$$f = 10^{-4} \left( \frac{10^8 M_\odot}{M_1} \right) \text{ Hz} \quad (1.25)$$

and

$$h = 2 \times 10^{-21} \left( \frac{M_2}{M_\odot} \right) \left( \frac{10 \text{ Mpc}}{r_o} \right) \quad (1.26)$$

where  $M_1$  is the mass of the supermassive black hole,  $M_2$  is the mass of the infalling body, and  $r_o$  is the distance to the source.

The frequency for such a source is too low to be seen by ground based detectors, but is in the frequency band of space-borne laser interferometers (see chapter 3).

## 1.4.2 Periodic Sources

### Rotating Neutron Stars

Rotating neutron stars are known to exist in our galaxy, *e.g.* *pulsars*. If the star rotates non-axisymmetrically, then it will emit gravitational waves, with the strength being dependent on the speed of rotation, and the amount of deviation from the axisymmetric case.

The non-axisymmetry of the star can arise in several ways: (i) the solid crust of the star may become distorted due to “star quakes”, (ii) the internal magnetic field of the star may be strong enough to distort the shape of the star, and (iii) if the star is rotating too rapidly, then it may suffer from an instability driven by gravitational radiation reaction. This produces hydrodynamic waves on the surface of the star, propagating in the opposite direction to the rotation. These waves will strongly emit gravitational radiation.

Rapidly rotating neutron stars are hard to observe with standard astronomical techniques, and so the population of such stars in our vicinity of the galaxy is not well defined. For an unstable neutron star, the energy radiated in gravitational waves and X-rays is directly proportional to the accretion rate onto the star, and so the amplitude of gravitational waves will be proportional to the flux of X-rays observed at the earth giving

$$h = 2 \times 10^{-27} \left( \frac{300 \text{ Hz}}{f} \right)^{\frac{1}{2}} \left( \frac{F_x}{10^{-11} \text{ J m}^{-2} \text{ s}^{-1}} \right)^{\frac{1}{2}} \quad (1.27)$$

where  $F_x$  is the flux of X-rays observed at the earth.

Name	Distance to Source	Gravity Wave Period	Gravitational Eccentricity	Gravity Wave Amplitude, h
Crab	2 kpc	60 Hz	$3 \times 10^{-6}$	$4 \times 10^{-27}$
Vela	500 pc	22 Hz	$3 \times 10^{-5}$	$2 \times 10^{-26}$
PSR1937+21	5 kpc	1.25 kHz	$7 \times 10^{-11}$	$1 \times 10^{-28}$

Table 1.1: **Gravitational wave amplitude estimates from known rapidly rotating neutron star sources.** *The gravitational eccentricity is defined as  $1 - \frac{a}{b}$ , where  $a$  is the length of the semi-major axis of the neutron star, and  $b$  the semi-minor axis.*

Estimates for the amplitude of gravitational waves at the earth have been made for several candidates *e.g.* the Crab, Vela and PSR 1937+21 pulsars. Table 1 gives the details of the expected signals.

The amplitudes shown here are too low to be detected by wideband gravitational wave detectors. However, resonant mass detectors, and narrow band laser interferometers can be tuned to look at a specific frequency over a very long integration time. For example, if the Crab Pulsar were to be observed over a one year period ( $3 \times 10^7$  s), then the detector would have to have a strain sensitivity of better than  $\sim 2.2 \times 10^{-23} / \sqrt{\text{Hz}}$  at 60 Hz, in order to give a signal to noise ratio above unity.

If the gravitational wave signature of a rotating neutron star is detected, then the amplitude and phases of the various components of the signal will give vital information on the structure and dynamics of the neutron star, and, if lucky, new information on the dynamics at work during a “star quake”.

## Binary Stars

Most stars in the galaxy are believed to be members of binary or multiple star systems. A simple binary system containing two main sequence stars is the best understood of all potential gravitational wave sources. However, the orbital period of this type of binary is likely to be longer than one hour, giving a corresponding gravitational wave frequency below  $10^{-3}$  Hz[11]. This is well below the observational

window of ground based detectors, but is within the detection band of space-borne interferometers. However with the multitude of sources, there will be a critical frequency limit (near 1 mHz) below which individual sources will not be resolvable due to a background confusion limit of signals.

Binary systems consisting of a white dwarf and neutron star (WD-NS), NS-NS or BH-BH, are the most likely candidates to be observed. The waveforms from such binaries have been calculated to high accuracy by *e.g.* Gal'tsov, Matiukhin and Petukov[10]. Due to the eccentricity of the orbit of binaries, the waves are emitted at not only twice the orbital frequency, but also at the harmonics of this fundamental frequency. For the case of low eccentricity ( $\varepsilon \leq 0.2$ ), the dominant gravitational wave frequency is at twice the orbital frequency, which leads to the expression for the amplitude of the waves of

$$h = 8.7 \times 10^{-21} \left( \frac{\mu}{M_{\odot}} \right) \left( \frac{M}{M_{\odot}} \right)^{\frac{2}{3}} \left( \frac{100 \text{ pc}}{r} \right) \left( \frac{f}{10^{-3} \text{ Hz}} \right)^{\frac{2}{3}} \quad (1.28)$$

where  $\mu$  is the reduced mass, and  $M$  is the total mass of the system.

The shortest known period of a binary is 11 minutes ( $\equiv 3 \times 10^{-3}$  Hz) for the WD-Helium star binary *AM CVn*. This places it at a frequency above the confusion limit, and thereby is a guaranteed gravitational wave source of known amplitude. The highest frequency expected for any type of WD binary is  $\sim 0.06$  Hz, as above this frequency the stars are so close that mass transfer begins from the more massive to the less massive star.

### 1.4.3 Stochastic Sources

#### Binary Sources

As stated in the previous section, the gravitational waves from binary star systems will superimpose at low frequencies ( $< 1$  mHz) to form a confusion limiting background noise. In order for a source to be observed below this frequency, it must have a gravitational wave amplitude of  $h > h_{background}$ . For periodic sources *e.g.* the binary *i Boo*, the signal will only be detectable if  $h_{periodic} > (f\tau)^{-\frac{1}{2}}$ , that is after an integration time of  $\sim 1$  year. However, planned space-borne laser interferometers

will observe with integration times of  $>1$  year, and so may be able to discern the signal from the background noise.

## Primordial Gravitational Waves

Like electromagnetic radiation, there is expected to be a cosmic background of gravitational radiation. However, unlike the electromagnetic case, gravitational waves do not interact with matter after a few Planck times ( $\sim 10^{-43}$  s) after the Big Bang. Therefore any background spectrum of gravitational waves seen at the present epoch is simply a redshifted version of the spectrum of the waves in the very early universe when they were formed. Thus if detected, primordial gravitational waves will be able to probe the very earliest universe.

Due to the amount of uncertainty in the understanding of the physics of the early universe, before and during inflation, it is impossible to put an estimate on the amplitude of the waves expected to be observed. If the waves have a wavelength comparable to the scale of the horizon when produced, Sazhin[13] has shown that the frequency of the radiation at the present epoch is given by

$$f \sim 1.5 \times 10^{-8} N_G^{\frac{1}{2}} \left( \frac{T_G}{1 \text{ GeV}} \right) \text{ Hz} \quad (1.29)$$

where  $N_G$  is the number of particle species at the plasma temperature,  $T_G$ , measured in GeV, at the time the waves are created. Ground based detectors working in the kHz regime will be able to investigate waves produced when the temperature of the universe was  $\sim 10^9 - 10^{12}$  GeV, and space-borne detectors observing gravitational waves emitted at temperatures of  $\sim 10^3 - 10^6$  GeV. The low frequency signals may have larger amplitudes than the higher frequency waves, as the amplitudes of waves will decrease as the Universe expands.

## 1.5 Conclusions

Over the past ten years, the theoretical understanding of the frequency and amplitude of gravitational radiation from astrophysical sources has been greatly improved. Astronomers and physicists from many different fields are now convinced of the ex-

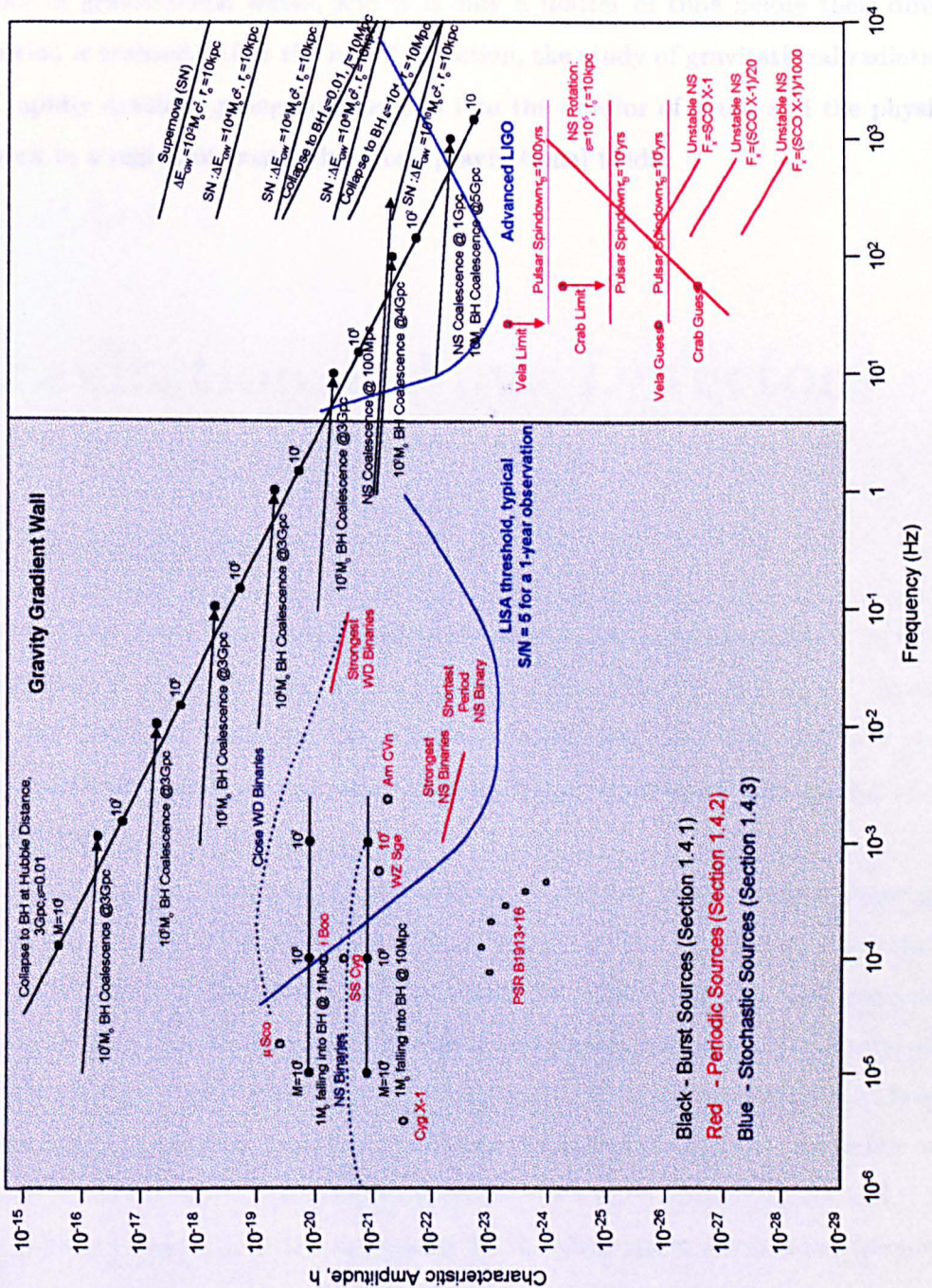


Figure 1.3: Spectra of expected gravitational wave sources. The “characteristic amplitude” is the amplitude expected for an optimised detector. To the left of the “Gravity Gradient Wall” (shaded area), background noise restricts the sensitivity of ground based detectors, and so any signals in this region are only accessible via space-borne detectors. (adapted from [10])

istence of gravitational waves, and it is only a matter of time before their direct detection is realised. After the initial detection, the study of gravitational radiation will rapidly develop, giving new insights into the interior of stars, and the physics at work in a region of extremely strong gravitational fields.

## Chapter 2

# Gravitational Wave Detectors

### 2.1 Introduction

For over thirty years, experimental physicists around the world have been developing instruments to search for the elusive signature from gravitational waves. In this time, the detection techniques has improved enormously, and it is only now that instruments with good enough sensitivity are being constructed that should allow direct detection of the waves.

In this chapter I will give a brief outline of the two most common detection techniques, namely *Resonant Mass Detectors* and *Ground Based Laser Interferometric Detectors*. Both these techniques search for radiation in the high frequency regime, above 10 Hz, as the sensitivity below this level is restricted by the unavoidable seismic and gravity gradient noise of the earth. To make observations at lower frequencies, it is essential to escape from earth induced noise sources - hence the use of space-borne detectors. Space-borne interferometers are discussed briefly, and then more fully in Chapter 3. Other techniques for the observation of ultra-low frequencies, based on the interaction of gravitational waves with electromagnetic radiation, are mentioned at the end of this chapter.

## 2.2 Resonant Mass Detectors

Resonant mass detectors were the first type of gravitational wave detector with good sensitivity.

The original detector was made in the early 1960s by Joseph Weber, and

consisted of a massive aluminum cylinder buried in a sand underground cavern.

The cylinder was suspended by thin wires. The bar, proper to the axis of the

cylinder, longitudinal vibrations are set up. It was this sound wave that generated

# Gravitational Wave Detectors

As shown in the previous chapter, a typical signal from a supernova or core galaxy

is likely to have strain sensitivity of  $h \sim 10^{-21}$ . Therefore, for a 1 m long bar, the

change in length is  $\sim 10^{-22}$  m - approximately  $10^{-17}$  of the diameter of an

atom. If the detector is operated at room temperature, then the typical thermal

For over thirty years, experimental physicists around the world have been developing instruments to search for the illusive signatures from gravitational waves. In this time, the detection technique has improved enormously, and it is only now that instruments with good enough sensitivity are being constructed that should allow direct detection of the waves.

In this chapter I will give a brief outline of the two most common detection techniques, namely *Resonant Mass Detectors* and *Ground Based Laser Interferometric Detectors*. Both these techniques search for radiation in the high frequency regime, above 10 Hz, as the sensitivity below this level is restricted by the unavoidable seismic and gravity gradient noise of the earth. To make observations at lower frequencies, it is essential to escape from earth induced noise sources - hence the use of space-borne detectors. Space-borne interferometers are discussed briefly, and then more fully in Chapter 3. Other techniques for the observation of ultra-low frequencies, based on the interaction of gravitational waves with electromagnetic radiation, are mentioned at the end of this chapter.

### 2.2.1 Sensitivity of Resonant Mass Detectors

The limit to the sensitivity of resonant mass detectors is affected by two main sources

of noise: thermal noise of the bar and seismic noise. The latter is reduced by using a

## 2.2 Resonant Mass Detectors

Resonant mass detectors were the first type of gravitational detector to be developed. The original detectors were made in the early 1960s by Joseph Weber [14], and consisted of a massive aluminium cylindrical bar ( $\sim 1.5$  tons), suspended in vacuum. When a gravitational wave passes through the bar, perpendicular to the axis of the cylinder, longitudinal vibrations are set up. It was this initial work that prompted experimentalists from around the world to build similar detectors, and in doing so started the new branch of experimental physics of gravitational wave detection.

As shown in the previous chapter, a typical signal from supernovæ in our galaxy is likely to have strain sensitivity of  $h \sim 10^{-18}$ . Therefore, for a 1 m long bar, the corresponding length change is  $10^{-18}$  m - approximately  $10^{-8}$  of the diameter of an atom! If the detector is operated at room temperature, then the internal thermal motion of the atoms (Brownian noise) give rise to an *rms* displacement fluctuation of  $x_{rms} \sim 3 \times 10^{-16}$  and even at cryogenic temperatures (a few degrees above absolute zero), the thermal motion of the end of the bar is still greater than the displacement caused by the gravitational wave.

Weber overcame this problem by using the natural resonance of the cylinder: if the bar is made to vibrate at its resonant frequency, then the amplitude of oscillation decays to  $1/e$  in a time  $\tau$ , the “relaxation time”. Therefore, for a bar with  $\tau = 1000$  s, the amplitude of vibration will fall by 0.1% in a time  $t = 1$  s. So if a burst of gravitational waves at the correct frequency (the resonant frequency of the bar, normally around 1 kHz), changes the amplitude by  $> 0.1\%$  in a time less than  $t$ , the signal will be detectable.

Table 2.1 gives an overview of current bar detectors around the world, The table shows the characteristics of the each bar (material, mass, and length) along with the resonant frequencies at which the detector is sensitive to gravitational waves.

### 2.2.1 Sensitivity of Resonant Mass Detectors

The limit to the sensitivity of resonant mass detectors is affected by two main sources of noise: thermal noise of the bar and sensor noise. The latter is reduced by using a

Experiment	Location	Material	Mass (kg)	Length of Bar (m)	Resonant Frequencies (Hz)
Allegro	U.S.A	Al5056	2 300	3	906 & 923
Explorer	CERN	Al5056	2 300	3	906 & 923
Nautilus	Frascati	Al5056	2 300	3	908 & 924
Altair	I.F.S.I	Al6061	389	1.5	1784 & 1827
Niobe	Australia	Niobium	1 500	1.5	700 & 710

Table 2.1: **Overview of resonant bar detectors around the world.**[15][16]

long integration time, and the former using a short integration time! The optimum integration time is when the thermal noise is equal to the sensor noise.

The strain sensitivity of a detector limited by thermal noise is related to the Quality Factor,  $Q$ ,<sup>1</sup> of the bar, and to the number of cycles of radiation detected,  $N$ , by [19]

$$h_{rms} = \frac{1}{L} \left[ \frac{k_B T}{\pi M f_o Q N} \right]^{\frac{1}{2}} \quad (2.1)$$

where,  $M$  is the mass,  $L$  the length, and  $T$  the temperature of the bar.

## 2.2.2 Resonant Spherical Mass Detectors

The next generation of resonant mass detectors may well differ in shape from present designs. Already under investigation is the idea of using a spherical detector, as opposed to the traditional bar design. Spherical gravitational wave detectors have the advantage of having five separate quadrupole modes, therefore allowing one detector to be sensitive to gravitational waves from all directions. By combining the signals from the five modes, the direction of the source and polarisation of the wave can be measured. The other major advantage of the spherical shape is in the mass

---

<sup>1</sup>The quality factor is defined

$$2\pi \frac{\text{energy stored in the system}}{\text{energy lost per cycle}}$$

of the detector. Spheres are likely to range in mass from  $\sim 3$ -100 ton, thereby having an energy cross-section of 3-100 times higher than the equivalent bar, but with the same resonant frequency. The actual geometry will not be a perfect sphere: the transducers used to measure the strain caused by the gravitational wave require a flat attachment surface. For this reason, present designs use a *truncated icosahedron*, *i.e.* football shape, giving the spheres their more common name of TIGAs<sup>2</sup>.

In order to cover a wide range of the high frequency spectrum, it is necessary to use an array of spheres. This array will consist of detectors of differing masses and diameters, creating a “xylophone” of resonant frequencies.

## 2.3 Laser Interferometric Detectors

Throughout the history of gravitational wave experiments, new and ingenious ways of improving the sensitivity have been invented. By considering Equation 2.1 it can be seen that the sensitivity of a bar is inversely proportional to the length, and therefore, by simply lengthening the bar, the sensitivity will improve. However, the resonant frequency decreases with length. With the most likely sources around 1 kHz, a bar longer than  $\sim 3$  m will have a peak sensitivity outwith the optimum frequency band. Fortunately, the idea of increasing  $L$  was not abandoned, but instead led to a new, and very different gravitational wave detection scheme - *Laser Interferometry*.

Laser interferometric detectors were first conceived in the early 1960s by Gertsenshtein and Pustovoit [21], and then independently by Joseph Weber (mid 1960s) and Rainer Weiss (1970). Weber did not pursue the idea, and did not publish this work, however, Weiss carried out a feasibility study [22], and his techniques for improving the sensitivity are still in use today. The concept was first tested in 1971 by Robert Forward and colleagues [23], who constructed the first interferometer and demonstrated that the idea could work. Table 2.2 lists prototype detectors currently in use, and Table 2.3 lists long baseline detectors under construction.

---

<sup>2</sup>Truncated Icosahedral Gravitational Wave Antenna

Location	Start	Interferometry Technique	Armlength (m)	Sensitivity ( $h$ [ $/\sqrt{\text{Hz}}$ ])
Glasgow	1976	FPM	10	$6 \times 10^{-20}$ (1992)
Garching	1975	MPM	30	$11 \times 10^{-20}$ (1986)
Caltech	1980	FPM	40	$1 \times 10^{-20}$ (1994)
Japan (ISAS)	1986	FPM	100	$20 \times 10^{-20}$ (1994)
Japan (NAO)	1991	FPM	20	$10^{-17}$ (1994)

Table 2.2: Overview of prototype interferometric detectors[12].

Name	Location	Collaborating Countries	Armlength	Completion Date
GEO 600	Ruthe, Germany	UK/Germany	600 m	2001
LIGO	Hanford, WA	USA	4 km & 2 km	2002
	Livingstone, LS	USA	4 km	2002
VIRGO	Cascina, Italy	Italy/France	3 km	2002
TAMA 300	Tokyo, Japan	Japan	300 m	1999

Table 2.3: Overview of long baseline interferometers.

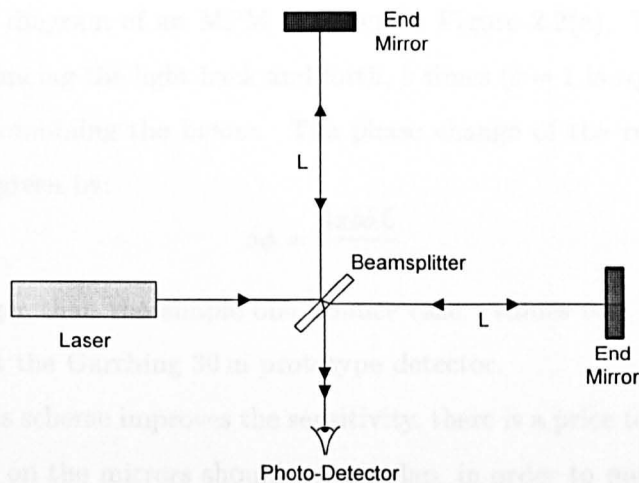


Figure 2.1: **Schematic diagram of a simple Michelson interferometer.**

The simplest interferometer is the *Michelson Interferometer* shown in Figure 2.1. This instrument is ideally suited to detecting gravitational waves, as the quadrupole nature of the wave will induce changes in the two arms of opposite sign. The normal mode of operation has zero path length difference, thereby creating a null in intensity (destructive interference) at the photodetector. If one, or both, armlengths are changed, the relative phase of the returning beam also changes according to

$$\delta\phi = \frac{4\pi\delta L}{\lambda} \quad (2.2)$$

where  $\delta L$  is the relative change in armlength, and  $\lambda$  is the laser wavelength. This phase change destroys the destructive interference condition and therefore by monitoring the intensity on the photodetector, a direct measure of the relative armlength difference can be made.

For all interferometers, there is an optimum armlength, corresponding to a length at which the storage time for the light in the arms is equal to half the gravitational wave period. As before, the most interesting sources are likely to be around a few hundred Hertz, corresponding to an optimum optical path length of  $L_{opt} = 750$  km, or armlength of 375 km. This armlength is not realistic (due mainly to financial constraints), and so other ways of synthetically increasing the armlength have been used. The two main ways of doing this are to use a *Multipass Michelson* (MPM)[22] or a *Fabry-Pérot Michelson* (FPM)[24].

A schematic diagram of an MPM is shown in Figure 2.2(a). The armlength is increased by bouncing the light back and forth,  $b$  times ( $b = 1$  is equal to one round trip), before recombining the beams. The phase change of the return beam from one arm is now given by:

$$\delta\phi = \frac{4\pi b\delta L}{\lambda} \quad (2.3)$$

*i.e.*  $b$  times larger than the simple one bounce case. Values of  $b \sim 50 - 100$  have been achieved at the Garching 30 m prototype detector.

Although this scheme improves the sensitivity, there is a price to pay. Ideally the individual spots on the mirrors should not overlap, in order to minimise scattering between adjacent beams. This puts a major constraint on the minimum mirror diameter. For a long baseline detector with  $L = 3$  km, and  $b=50$ , the minimum diameter of mirror has  $D = 1.27$  m [25]. Clearly the cost of such a mirror, and its vacuum system is impractical. By overlapping the spots the mirror diameter can be reduced, but at the expense of extra noise from scattered light.

The FPM was an idea conceived[24] after initial experiments with an MPM. The driving force behind the scheme was to design an interferometer with the same sensitivity as an MPM, but which did not require large diameter optics, or suffer from excess phase noise caused by scattered light. A schematic diagram of the interferometer is shown in Figure 2.2(b).

The light is again split at the beamsplitter and sent along both arms through a partially reflecting mirror (M1), normally with a power reflectivity,  $R_1 \sim 99\%$ . The far mirror is made to be as high reflecting as possible ( $R_2 > 99.9\%$ ). The system is analogous to the MPM case, with the number of bounces,  $b$ , now given by  $\frac{\mathcal{F}}{2\pi}$ , where  $\mathcal{F}$  is the cavity finesse,

$$\mathcal{F} = \frac{\pi(R_1 R_2)^{\frac{1}{4}}}{1 - \sqrt{R_1 R_2}} \quad (2.4)$$

One problem associated with the FPM design, is in the input laser frequency noise. In principal, laser frequency noise does not couple into the measurement, as the noise cancels in both arms. However, due to miss matching in the radii of curvature of the mirrors, *etc.* frequency noise can dominate the measurement. The resulting relationship between laser frequency noise and detector sensitivity for a

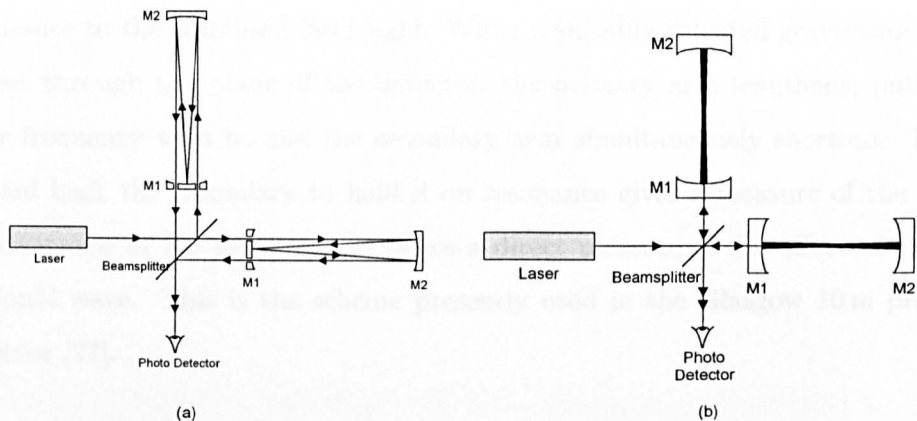


Figure 2.2: **Schematic diagrams of laser interferometers.** (a) A *Multipass Michelson*, (b) A *Fabry-Pérot Michelson*.

Fabry-Pérot is given by:

$$\frac{\delta\nu}{\nu} \sim h.D \quad (2.5)$$

where  $\nu$  is the frequency of the laser,  $\delta\nu$  is the laser frequency noise, and  $D$  is a measure of the common mode rejection of the whole system, which results from comparison of the light in the two arms. Substituting in typical values ( $\lambda = 1064 \text{ nm}$ ,  $D=100$ ), Equation 2.5 necessitates a laser frequency stability of  $\sim 3 \times 10^{-6} \text{ Hz}/\sqrt{\text{Hz}}$  over millisecond timescales, in order to reach the desired sensitivity of  $h \sim 10^{-22}$  at 1 kHz. A detailed description of the frequency stabilisation scheme is given in Chapter 4.

The FPM can be used with two different geometries. Firstly, the interferometer is arranged such that the light leaking back out of the cavities is recombined at the beamsplitter. This mode of operation is analogous to the single and multiple pass Michelson. However, due to mismatching of mirrors, and poor overlap of the beams at the photodetector, the visibility of fringes can be rather poor. The visibility can be improved by using a more complicated technique for keeping the interferometer optimally aligned[26]. However, there is another optical scheme for the FPM which does not require the beams from the two cavities to be recombined. In this scheme, one arm (the primary) is used as the frequency reference, with the laser frequency locked to the length of this cavity. The second arm (secondary) is then locked on

resonance to the stabilised laser light. When a suitably oriented gravitational wave passes through the plane of the detector, the primary arm lengthens, pulling the laser frequency with it, and the secondary arm simultaneously shortens. The signal fed back the secondary to hold it on resonance gives a measure of the relative displacement of the mirrors, and hence a direct measure of the effect of the gravitational wave. This is the scheme presently used in the Glasgow 10 m prototype detector [27].

### 2.3.1 Noise Sources in Laser Interferometers

All forms of laser interferometers are limited by various noise sources. The aim of every scientist and engineer building such detectors is to reduce each source to a minimum, and hence improve the overall sensitivity of the detector. Noise affects the instrument in many ways, and a few important sources will be discussed below. Figure 2.4 gives the noise spectrum for the GEO 600 interferometer, along with the expected sensitivity of the instrument.

#### Seismic and Gravity Gradient Noise

Seismic noise is simply the vibration of the earth at the location of the detector, and will limit all ground-based detectors at frequencies below 10 Hz. For an interferometer, it is primarily the horizontal ground motion that has the biggest effect, although, if the detector arms are not exactly level, or there is a coupling between vertical and horizontal modes, vertical motion may also become important.

If a calibrated seismometer is placed on a seismically quiet area of ground the spectrum of horizontal ground vibration is found to be approximately [28]

$$x(f) = \frac{10^{-7}}{f^2} \text{ m}/\sqrt{\text{Hz}} \quad (2.6)$$

where  $f$  is the frequency of the vibration, and  $x(f)$  is the ground displacement at frequency,  $f$ . To see how this affects current detectors, the example of GEO 600 [29] will be used. With an effective armlength of 1200 m, the unattenuated seismic noise would set a limit to the strain sensitivity of  $h = 1.7 \times 10^{-16}/\sqrt{\text{Hz}}$  at 1 kHz. Therefore, to reach the goal of  $h \sim 10^{-22}/\sqrt{\text{Hz}}$  from 50 Hz to 1 kHz, the seismic

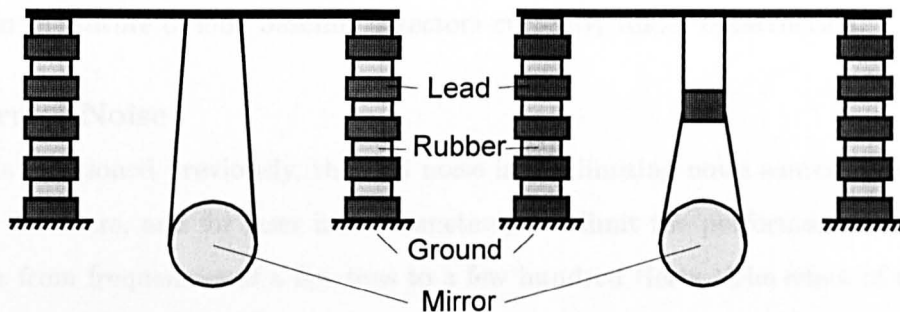


Figure 2.3: **Diagrams showing test mass suspension systems.** *The left hand diagram shows a single pendulum suspension, isolated from the ground through a 5-layer seismic isolation stack, the right hand diagram shows the same isolation stack, but with the test mass suspended using a double pendulum.*

noise must be reduced by  $\sim 10^6$  at 1 kHz, and by  $\sim 10^8$  at 100 Hz. This level of isolation is not as difficult as it may at first appear.

The first stage of isolation is performed by hanging the test masses as high  $Q$ -pendula, with a resonant frequency  $\sim 1$  Hz. This reduces the motion of the mass by a factor of  $(f_o/f)^2$ , where  $f_o$  is the resonant frequency of the pendulum. So at 1 kHz, the pendulum performs almost all the isolation required. This isolation can be improved further by using double, or multiple pendula (Figure 2.3).

However, as the frequency drops, the effect of the pendulum isolation also drops, but the seismic noise increases. This has led to the development of *acoustic isolation stacks*, consisting of alternating layers of a heavy metal (*e.g.* stainless steel) and a soft elastic material (*e.g.* rubber). These stacks are placed between the pendulum suspension point, and the ground (or to a point rigidly fixed to ground). Each layer of the stack acts like two masses attached by a spring: for horizontal motions, the shear force in the rubber provides the attenuation, and for vertical motions, the isolation is provided by the compressional force. In theory, a 5-layer stack with resonant frequency of 10 Hz, can provide up to a factor of  $10^5$  isolation at 100 Hz. In practice, the isolation may not reach this level, due to cross-coupling of modes, or from internal resonances of the masses. Even so, acoustic isolation stacks have been used in all gravitational detectors for many years, and will play an important

role in the future of long baseline detectors currently under construction.

## Thermal Noise

As mentioned previously, thermal noise is the limiting noise source in resonant mass detectors, and for laser interferometers, will limit the performance of the detector from frequencies of a few tens to a few hundred Hertz. The effect of thermal noise enters interferometers in two ways: (i) through the internal thermal motions of the test masses and, (ii) through the test mass suspension.

Referring back to Equation 2.1, the effect on the displacement sensitivity of a detector due to thermal noise is huge compared to the actual displacement caused by a gravitational wave. In the case of interferometers, which operate at room temperature, the effect is not as limiting as in bar detectors, as the laser spot is a few centimetres in diameter by the time it reaches the far mirror, and so the position of the plane of reflection (the surface of the mirror) is an average of all the atoms in the spot. For the case of GEO 600, the spot size on the far mirror will be  $\sim 5$  cm, therefore covering  $\sim 10^{17}$  atoms. Even so, the internal resonance of the mirrors in ground based detectors will still affect the sensitivity of the interferometer at the resonant frequency. Therefore, the size and mass of the mirrors are chosen such that the internal resonances lie outwith the observation band. Also, the mirrors are manufactured from a high Q material, forcing the energy in the resonance to be constrained to a very narrow frequency band.

A second thermal noise source in ground based interferometers enters through the test mass suspension. As stated above the pendula will have a resonant frequency of  $\sim 1$  Hz. This resonant mode will be excited not only by seismic noise, but also through thermal excitation. The resulting motion of the test mass will be[30]:

$$\delta x^2 = \frac{4k_B T \omega_o \delta f}{m Q \omega^4} \quad (2.7)$$

where  $\omega_o$  is the angular resonant frequency,  $\omega$  is the observation angular frequency,  $\delta f$  is the measurement bandwidth, and  $Q$  is the quality factor of the pendulum.

This leads to a corresponding limit to strain sensitivity of

$$h_{min} = 5 \times 10^{-24} \left[ \frac{f_g}{100 \text{ Hz}} \right]^{-2} \left[ \frac{mQ}{10^{10} \text{ kg}} \right]^{\frac{1}{2}} \left[ \frac{\omega_o}{2\pi \text{ s}^{-1}} \right]^{\frac{1}{2}} \left[ \frac{l}{3 \text{ km}} \right]^{-1} \sqrt{\delta f} \quad (2.8)$$

where  $f_g$  is the frequency of the gravitational wave. This suggests that the suspension system incorporated in ground based detectors will have to have very high  $Q$ -factors. Suspension systems consisting of a fused silica mass, suspended from fused silica fibres are being developed at the University of Glasgow[31], with measured  $Q$ -factors of the suspension greater than  $10^7$ .

## Photon Shot Noise

When considering the performance of an interferometer, the question, ‘‘How small a displacement can be measured?’’, should really be replaced with ‘‘How small a change in light power can be measured?’’. The sensitivity of all interferometers is limited, at the high frequency end, by photon shot noise. This noise source is caused by the fluctuations in arrival rates of photons at the photodetector, hence adding noise to the detected light power.

Since measuring the light power of a system is equivalent to counting the number of photons hitting the detector, the error in the measurement can be calculated using Poissonian statistics. If a measurement is made in a time  $\tau$ , with a photon flux denoted by  $\bar{n}$ , then the error in the average number of photons counted is given by[18]:

$$\frac{\sigma_{\bar{N}}}{\bar{N}} = \frac{\sqrt{\bar{n}\tau}}{\bar{n}\tau} = \frac{1}{\sqrt{\bar{n}\tau}} \quad (2.9)$$

where  $\bar{N}$  is the average number of photons counted.

To see how this limits the sensitivity of a simple Michelson interferometer, it is useful to write the photon flux in terms of the output power, *i.e.*

$$\bar{n} = \frac{\lambda}{2\pi\hbar c} P_{out} \text{ s}^{-1} \quad (2.10)$$

where  $\hbar$  is the reduced Planck constant<sup>3</sup>, and  $P_{out}$  is the measured output power, given by

$$P_{out} = \frac{P_{in}}{2} [1 + \cos(\phi)] \quad (2.11)$$

---

<sup>3</sup>The reduced Planck Constant ( $= 1.054 \times 10^{-34}$  J.s) will be used throughout, as the symbol,  $\hbar$ , is reserved for the strain sensitivity.

where  $\phi$  is the relative phase between the recombining beams.

Substituting Equation (2.11) into Equation (2.10), and using Equation (2.9), the output power of the interferometer is calculated to be:

$$\sigma_P = \sqrt{\frac{2\pi\hbar c P_{in} [1 + \cos(\phi)] \delta f}{\lambda}} \quad (2.12)$$

where  $\delta f$  is the measurement bandwidth. This fluctuation in the output power is indiscernible from changes caused by the motion of the test masses, and therefore puts a limit on the minimum relative armlength difference detectable.

The limit to the detectable signal occurs when  $P_{out}/\sigma_P = 1$ , *i.e.* a signal to noise ratio of unity. If the detector is locked onto a dark fringe, then using Equation (2.12) and Equation (2.1), the minimum gravitational wave amplitude detectable is:

$$h_{min} = \frac{1}{L} \sqrt{\frac{\lambda \hbar c \delta f}{\pi \varepsilon P_{in}}} \quad (2.13)$$

where  $P_{in}$  has been replaced by  $\varepsilon P_{in}$ , where  $\varepsilon$  is the quantum efficiency of the photodetector. As can be seen, shot noise limit is inversely proportional to the input power of the interferometer, and therefore can be lowered by increasing the input laser power. Current available lasers have output powers  $\sim 10$  W. However this can be increased somewhat by the use of advanced optical techniques, such as power recycling [19].

## Laser Noise

Noise associated with the laser used to illuminate the detector appears in three main forms: (i) laser frequency noise, (ii) laser intensity noise, and (iii) beam pointing fluctuations. Each of these noise sources will be dealt with separately.

### Laser Frequency Noise

As discussed earlier, laser frequency noise is, in principle, unimportant in interferometry. However, due to inevitable inequalities in the armlengths of long baseline detectors, frequency noise could dominate any measurement made. For a single or multiple pass detector of armlength  $L$ , laser frequency noise sets a limit to the strain sensitivity of [32]

$$h = \frac{\delta\nu}{\nu} \cdot \frac{\delta L}{L} \quad (2.14)$$

where  $\delta L$  is the relative armlength difference. For GEO 600, the error budget for frequency noise has been set at a corresponding strain of  $h = 10^{-24} / \sqrt{\text{Hz}}$  [29], and with an expected armlength difference of 1 m (needed for signal recycling schemes - see for example [30][19]), a laser frequency stability of  $3 \times 10^{-7} \text{ Hz}/\sqrt{\text{Hz}}$  at 100 Hz is needed.

### Laser Intensity Noise

Commercial lasers used in interferometers suffer from excess intensity noise below a certain frequency. Above this frequency (around several megaHertz) the output intensity shows shot noise corresponding to Poisson statistics. At lower frequencies, if the interferometer is not held on an intensity minimum (dark fringe), intensity noise will couple into the measurement. In this case the limit to sensitivity is given by:

$$h = \frac{\delta I}{I} \cdot \frac{\delta l}{l} \quad (2.15)$$

where  $I$  is the laser intensity,  $\delta I$  is the intensity noise, and  $\delta l$  is the offset of an arm of length  $l$  from its correct locking point. For present and future detectors, values of  $\frac{\delta I}{I} < 10^{-8}$  will be needed.

### Laser Beam Pointing Fluctuations

Fluctuations in the pointing of the laser beam can lead to the light traversing different distances in the two arms, and will also cause a decrease in the overlap of the two beams at the photodetector. Both of these cases will produce noise in the output, masking the gravitational wave signal.

The effect of beam pointing can be greatly reduced by the use of single-mode optical fibres, and by modecleaners [33], both of which will be used in all present, and future, long baseline interferometers.

## 2.4 Space-borne Laser Interferometers

In the previous section, it was shown that seismic and gravity gradient noise is likely to be the limiting factor to the sensitivity of ground based detectors at frequencies below  $\sim 10$  Hz. Referring back to Figure 1.3, a multitude of sources lie

**Sensitivity curve of GEO600**

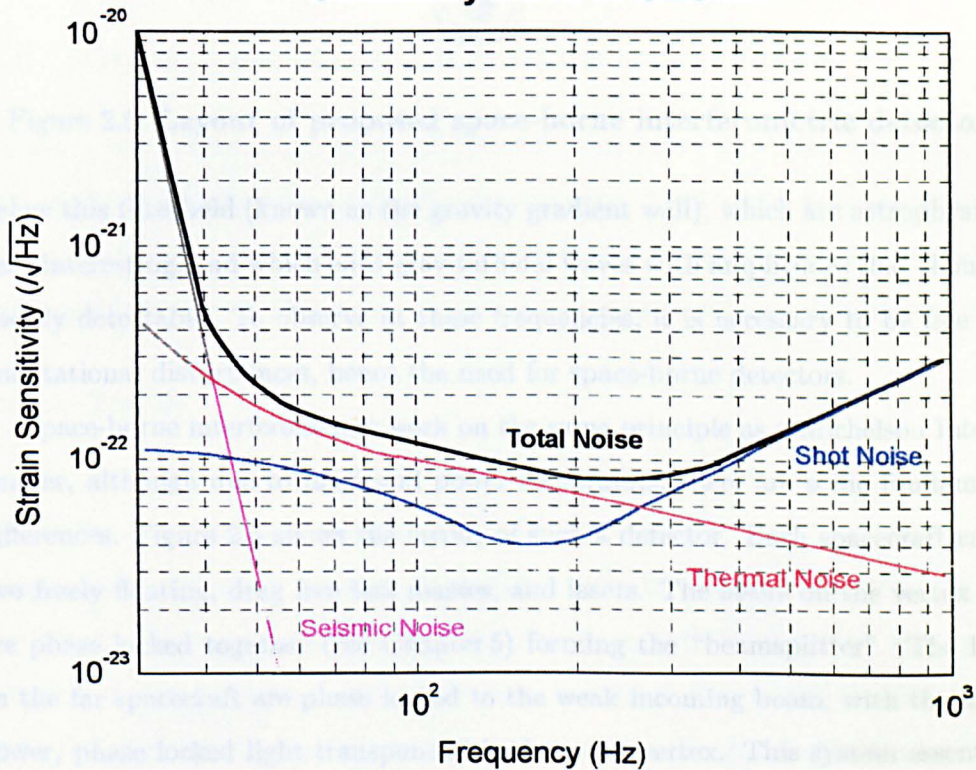


**Figure 2.4: Sensitivity limit for GEO 600 from individual noise sources.** The thermal noise calculation assumes a  $Q$ -factor for internal modes of  $5 \times 10^6$ , and a pendulum  $Q$ -factor of  $10^7$ . The shot-noise curve is calculated for a beamsplitter power of 7 kW (with power recycling).

Interferometers in space will be limited, like ground based detectors, by unavoidable noise sources. At the lower frequency band ( $\sim 10^{-2}$  Hz), spurious accelerations of the test masses will limit the sensitivity (See Table 2.4), and as with ground based interferometers, shot noise will be the limiting factor at higher frequencies (approaching 0.1 Hz). Beyond 0.1 Hz, the round-trip time of the light exceeds half

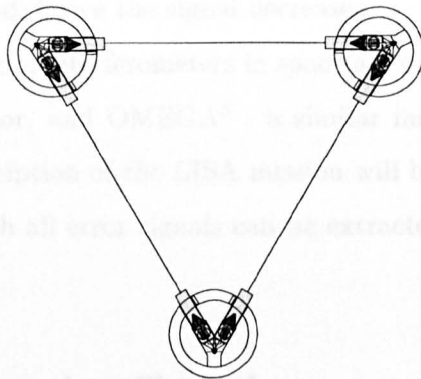


Figure 2.5: **Layout of proposed space-borne interferometric detectors.**

below this threshold (known as the gravity gradient wall), which are astrophysically very interesting, and which emit gravitational waves with amplitudes that should be readily detectable. To observe at these frequencies, it is necessary to be free from gravitational disturbances, hence the need for space-borne detectors.

Space-borne interferometers work on the same principle as a Michelson Interferometer, although due to mass and power constraints, there are some fundamental differences. Figure 2.5 shows the layout of such a detector. Each spacecraft carries two freely floating, drag free test masses, and lasers. The lasers on the vertex craft are phase locked together (see Chapter 5) forming the “beamsplitter”. The lasers on the far spacecraft are phase locked to the weak incoming beam, with the higher power, phase locked light transponded back to the vertex. This system essentially creates an *amplifying mirror* at the end of each interferometer arm. When a gravitational wave passes through the instrument, the armlength changes, and so the phase of the returning light, with respect to the transmitted, is changed. By comparing the differences in the phase of the two arms, the motion of the test masses can be measured.

Interferometers in space will be limited, like ground based detectors, by unavoidable noise sources. At the lower frequency bound ( $\sim 10^{-4}$  Hz), spurious accelerations of the test masses will limit the sensitivity (See Table 2.4), and as with ground based interferometers, shot noise will be the limiting factor at higher frequencies (approaching 0.1 Hz). Beyond 0.1 Hz, the round trip time of the light exceeds half

the gravitational period, hence the signal decreases.

Two missions to place interferometers in space are currently under study: LISA<sup>4</sup> - a heliocentric detector, and OMEGA<sup>5</sup> - a similar instrument, but in geocentric orbit. A detailed description of the LISA mission will be given in Chapter 3, along with a scheme in which all error signals can be extracted, to give the gravitational wave signal.

## 2.5 Other Detection Techniques

As the gravitational wave spectrum extends well below  $10^{-4}$  Hz, other detection techniques to observe at these frequencies are used. Most schemes are based on the timing of an electromagnetic signal, interacting with the gravitational wave, relative to a fixed clock signal. This makes the detector similar to a “one arm interferometer”.

### Pulsar Timing

Pulsar timing makes use of the the fact that a pulsar provides a very stable clock. By beating the pulsar signal with an equally stable clock (or another pulsar signal), irregularities in the beat note can be used to search for external influences affecting the signal. However, the arrival rate of pulses from individual pulsars can be very irregular, and so an average over many cycles is needed. Due to this long integration time, the technique is most sensitive when searching for gravitational waves with a period similar to the time in which the pulsar has been observed (normally > 10 years). Millisecond pulsars appear to be the most stable over long periods, and as such are being used for these observations. The frequency of waves detectable by this scheme are around  $10^{-9}$  Hz.

### Spacecraft Tracking

Spacecraft tracking[34] experiments work by transponding a microwave signal from interplanetary probes, such as ULYSSES, GALILEO, and CASSINI. The gravita-

---

<sup>4</sup>Laser Interferometer Space Antenna

<sup>5</sup>Orbiting Medium Explorer for Gravitational Astrophysics

<b>Error Source</b>	<b>Error Reduction Approach</b>
Thermal distortion of spacecraft	Carbon epoxy construction and limited power use variations
Thermal distortion of payload	Carbon epoxy construction with $\alpha = 4 \times 10^{-7}$ ,/K, plus two-stage thermal isolation of payload
Thermal noise due to dielectric losses	Very low electrostatic coupling
Gravity noise due to spacecraft displacement	1 nm/ $\sqrt{\text{Hz}}$ control of spacecraft displacements with FEOP thrusters
Temperature difference variation across cavity	Three stages of thermal isolation plus symmetrical heat leak paths
Electrical force on charged proof mass	Small spacecraft displacements, >1 mm position-sensor gaps, and discharging of proof mass
Lorentz force on charged proof mass from fluctuating interplanetary field	Intermittent discharging of proof mass, <i>e.g.</i> with U.V. light
Residual gas impacts on proof mass	Less than $3 \times 10^{-7}$ Pa pressure in proof mass cavity
Telescope thermal expansion	Low expansion secondary mounting plus two-stage thermal isolation
Magnetic force on proof mass from fluctuating interplanetary field	$10^{-6}$ proof mass susceptibility plus moderate spacecraft magnetic field gradient

Table 2.4: Sources of acceleration noise in LISA[12].

tional wave signal appears as an irregularity in the time-of-flight of the microwave communication signal after the orbit of the spacecraft has been fitted. This technique is limited by measurement noise, stability of frequency references, and errors caused by propagation through interplanetary plasmas. For these reasons, the sensitivity is unlikely to get below an *rms* strain sensitivity of  $10^{-17}$ [11], but nevertheless this scheme should still be pursued, as it sets limits to the amplitude of waves at this frequency.

### QUASAR Scintillation

Detection of gravitational waves by QUASAR<sup>6</sup> scintillation is still not technologically possible, but with improvements to VLBI<sup>7</sup>, and future satellite interferometry missions, may become possible. The method relies on a compact binary system being in the line of sight of a radio-loud quasar. The gravitational waves leaving the binary, cross the line of sight of the quasar, causing a slight scintillation effect due to gravitational lensing. The radio waves detected on earth will travel along multiple paths, and interfere at the detector.

## 2.6 Conclusions

The experimental search for gravitational waves has now been actively studied for almost forty years. Throughout this time, numerous detectors have been constructed, with each new generation being more advanced than the previous one, therefore leading to an ever increasing displacement sensitivity. With the advent of space-borne and long baseline ground based interferometers, as well as the next generation of resonant mass detectors, the use of gravitational radiation for the study of astrophysical bodies will soon become a reality.

---

<sup>6</sup>Quasi-Stellar Radio Source

<sup>7</sup>Very Long Baseline Interferometry

## Chapter 3

# LISA - The Laser

# Interferometer Space Antenna

## 3.1 Introduction

LISA - *The Laser Interferometer Space Antenna*[12] - is a proposed space-borne gravitational wave detector, aimed at detecting gravitational waves in the frequency range of  $10^{-4}$  to  $10^{-1}$  Hz. The idea of a space-borne detector was first made by a team of scientists from the Joint Institute for Laboratory Astrophysics (JILA) in 1985, and was named LAGOS<sup>1</sup>[35]. This mission concept has been the baseline for all further designs, and present missions still rely on many elements of the original study.

In the early 1990s, interest in space-borne detectors grew in Europe, and LISA was born[36]. The project was first proposed to the European Space Agency (ESA) in 1993, as the third “medium sized” (M3) mission in the *Horizon 2000* space science programme[36]. This proposal was for an interferometer consisting of four spacecraft (s/c) in heliocentric orbit, with armlength of  $5 \times 10^6$  km. At the same time, another mission, SAGITTARIUS<sup>2</sup>[37][38], was also proposed to ESA as an M3 candidate. SAGITTARIUS involved six s/c in geocentric orbit, with armlength of  $1 \times 10^6$  km.

---

<sup>1</sup>Laser Antenna for Gravitational-radiation Observation in Space

<sup>2</sup>Space-borne Astronomical Gravitational-wave Interferometer To Test Aspects of Relativity and Investigate Unknown Sources

As both missions were similar, ESA decided to merge the study of the two. However the cost of each project was outwith the budget for an M-class mission.

Later in 1993, a new design comprising six s/c in heliocentric orbit was put forward as a “cornerstone” mission in the new *Horizon 2000 +* programme. This time it was successful, and was recommended as the third of the cornerstone projects. Originally, the third cornerstone was scheduled to be launched around 2017, however, financial problems rapidly led to the timescale of the *Horizon 2000 +* program becoming extremely uncertain.

As the expected timescales appeared to be slipping further into the future, an effort was made to reduce the cost of LISA. The proposal, at the time of writing, is to fly three s/c, each carrying two optical benches, thereby keeping all three interferometric arms. The reduced cost of the mission, combined with possible funding from other space agencies (*e.g.* NASA), may allow LISA to fly as an ESA “flexible” (F-class) mission. The timescale for this funding scenario could yield a launch at the end of the first decade of the new millennium.

## 3.2 Overview of LISA Mission

As shown in Figure 3.1, there are a multitude of periodic gravitational wave sources in the LISA observation band, which can potentially be detected with extremely high signal-to-noise ratios. The signals from these sources will enable Einstein’s General Theory of Relativity[1] to be tested in the strong gravitational fields associated with astrophysical compact objects, and also to provide astrophysical information on the emitting bodies.

Putting a Michelson interferometer in space is conceptually easy. However the practicalities of such a scheme are far from trivial. The final design requires a mixture of spacecraft engineering, optical design and interferometry, attitude control, “drag free” control, and many other challenging techniques.

At the time of writing, LISA consists of three spacecraft, forming an equilateral triangle configuration of baseline  $5 \times 10^6$  km. The baseline is chosen to optimise the sensitivity of the detector at frequencies of known and expected sources of gravi-

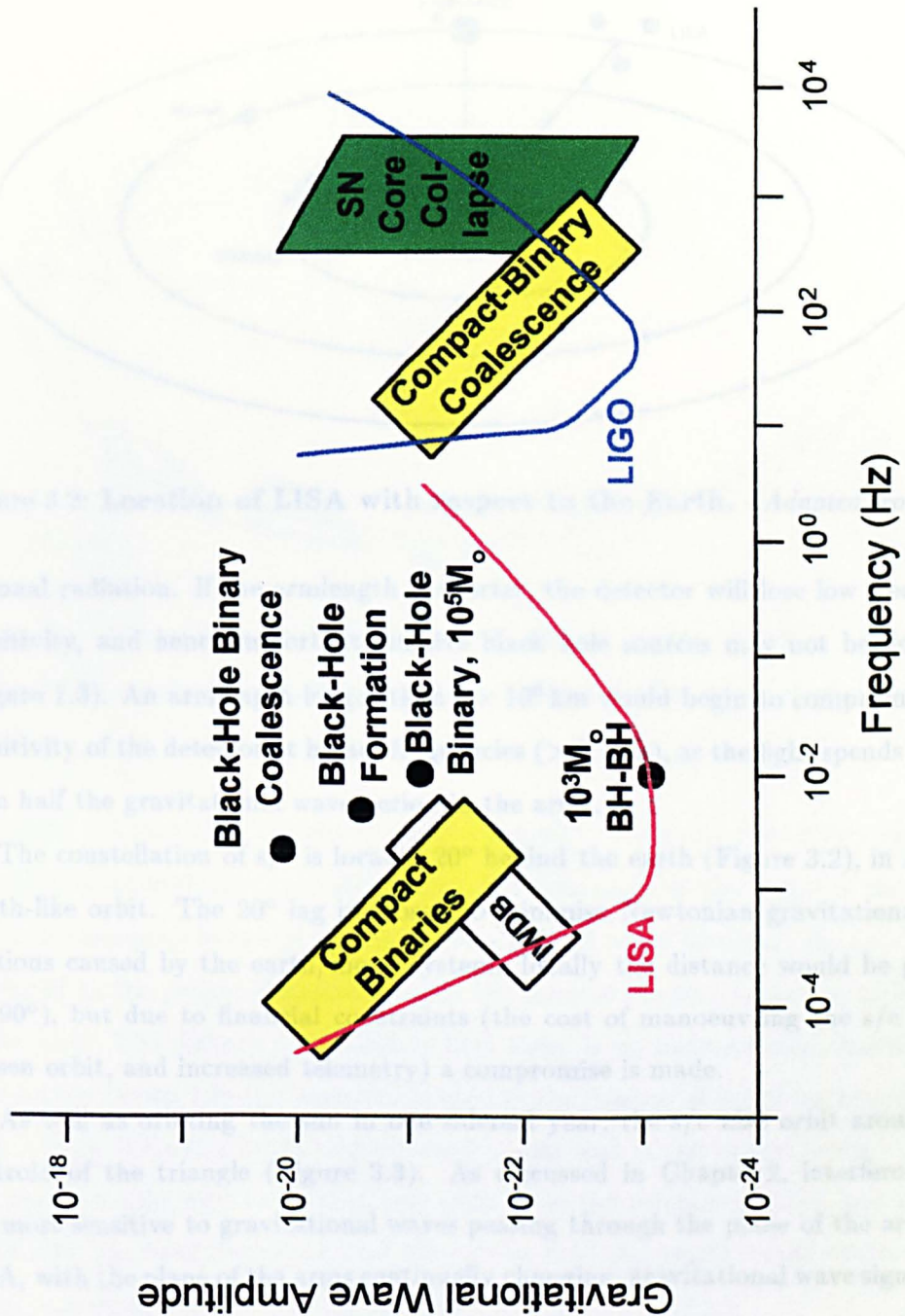


Figure 3.1: Comparison of the frequency range of sources for space-borne and ground based detectors. The line marked 'LISA' shows the expected noise floor for LISA. All signals above this line should be detectable. The sensitivity for an advanced ground based detector is shown for comparison. (IWB = Interacting White Dwarf Binary)[12]

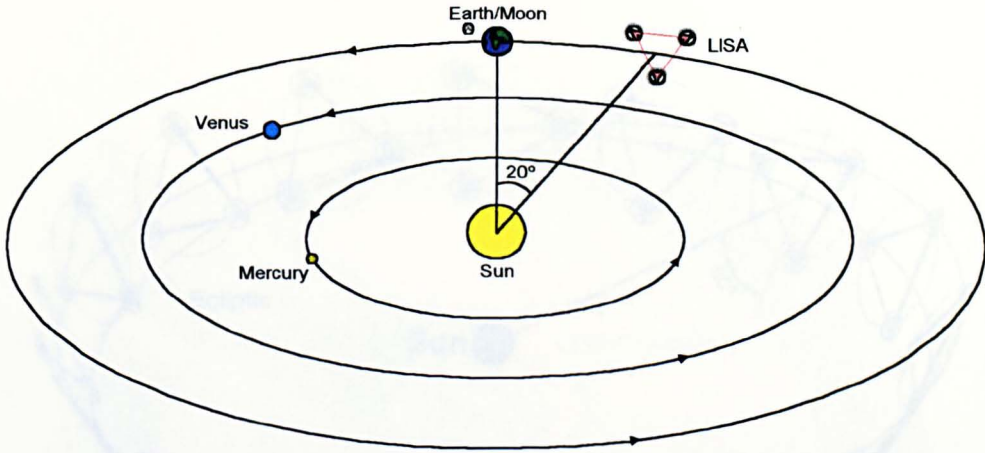


Figure 3.2: **Location of LISA with respect to the Earth.** *Adapted from [12]*

tational radiation. If the armlength is shorter, the detector will lose low frequency sensitivity, and hence important massive black hole sources may not be detected (Figure 1.3). An armlength longer than  $5 \times 10^6$  km would begin to compromise the sensitivity of the detector at higher frequencies ( $> 0.1$  Hz), as the light spends longer than half the gravitational wave period in the arms.

The constellation of s/c is located  $20^\circ$  behind the earth (Figure 3.2), in a 1 AU Earth-like orbit. The  $20^\circ$  lag is chosen to minimise Newtonian gravitational fluctuations caused by the earth/moon system. Ideally the distance would be greater ( $\sim 90^\circ$ ), but due to financial constraints (the cost of manoeuvring the s/c to the chosen orbit, and increased telemetry) a compromise is made.

As well as orbiting the sun in one sidereal year, the s/c also orbit around the centroid of the triangle (Figure 3.3). As discussed in Chapter 2, interferometers are most sensitive to gravitational waves passing through the plane of the arms. In LISA, with the plane of the arms continually changing, gravitational wave signals are amplitude modulated with a period of 1 year. Also, as the detector orbits the sun, its location in space with respect to the source changes, and hence the gravitational wave signal is Doppler shifted, again with a period of 1 year. The combined effect of the two modulations means that the location of the strongest sources (extragalactic super massive black holes) can be resolved to better than 1 arcminute, and weaker sources (galactic compact binaries) will be resolvable to  $\sim 1$  degree[39].

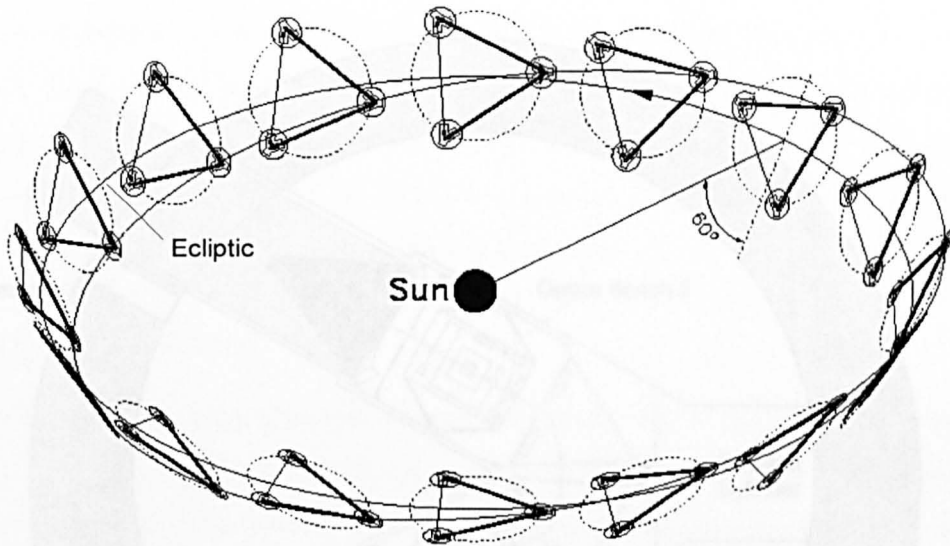


Figure 3.3: **Diagram of the LISA orbits, showing the rotation of the s/c around the centroid of the triangle.** *Diagram used with the permission of R. Schilling*

Figure 3.4 shows a diagram of a LISA satellite. Each s/c carries two identical optical benches and associated electronics. The test mass, at the centre of the optics bench, is analogous to one of the mirrors in a ground based detector: the arm length is defined as the proper distance between the faces of the test masses at either end of the arm. The difference in LISA is that there is no beamsplitter. Instead one laser (optics bench 1 in the diagram) is used as the master. A small fraction of light is split from the main beam and directed to the rear of the optics bench. Again, this beam is split into two paths; one path is to the reference cavity and is used to stabilise the laser frequency, and other path is to the neighbouring optics bench where it is used to phase lock an identical laser.

The main beam is sent out along the interferometer arm through a 30 cm aperture telescope, causing the diffraction limited beam diameter to increase to  $\sim 25$  km by the time the light reaches the far s/c. This leads to one of the major differences with LISA, compared to ground based interferometers. The detected power at the end of the arm is of the order of  $70 \times 10^{-12}$  W. If this was to be simply reflected back to

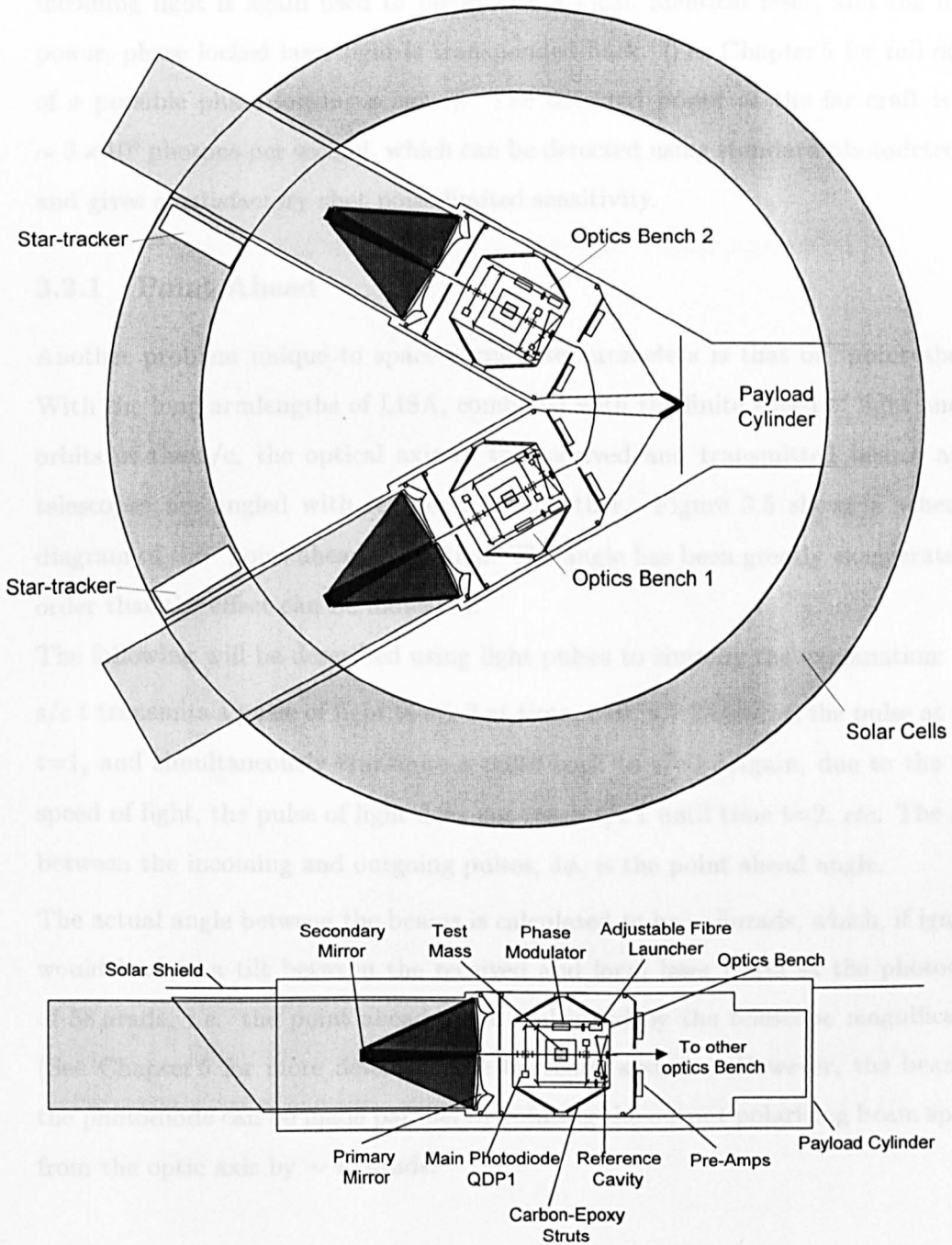


Figure 3.4: Diagram of a LISA spacecraft. Adapted from [12]

the master s/c, only  $\sim 190$  photons per hour would be detected! Instead, the weak incoming light is again used to phase lock a local, identical laser, and the higher power, phase locked laser light is transponded back. (See Chapter 5 for full details of a possible phase locking scheme). The detected power at the far craft is now  $\sim 3 \times 10^8$  photons per second, which can be detected using standard photodetectors, and gives a satisfactory shot noise limited sensitivity.

### 3.2.1 Point Ahead

Another problem unique to space-borne interferometers is that of “point ahead”. With the long armlengths of LISA, combined with the finite speed of light and the orbits of the s/c, the optical axis of the received and transmitted beams at the telescopes are angled with respect to each other. Figure 3.5 shows a schematic diagram of the “point ahead” situation. The angle has been greatly exaggerated, in order that the effect can be indicated.

The following will be described using light pulses to simplify the explanation:

s/c 1 transmits a pulse of light to s/c 2 at time,  $t=0$ . s/c 2 receives the pulse at time,  $t=1$ , and simultaneously transmits a pulse back to s/c 1. Again, due to the finite speed of light, the pulse of light does not reach s/c 1 until time  $t=2$ , *etc.* The angle between the incoming and outgoing pulses,  $\delta\phi$ , is the point ahead angle.

The actual angle between the beams is calculated to be  $\sim 5\mu\text{rads}$ , which, if ignored, would lead to a tilt between the received and local laser beam at the photodiode of  $58\mu\text{rads}$ , *i.e.* the point ahead angle multiplied by the telescope magnification. (See Chapter 6 for more details of the telescope system.) However, the beams at the photodiode can be made parallel by rotating the output polarising beam splitter from the optic axis by  $\sim 15\mu\text{rads}$ .

## 3.3 A LISA Satellite

Each LISA satellite can be split into two sections - the science payload and the spacecraft. The science payload is the part of the satellite that deals with the scientific instruments. The spacecraft is the part that deals with control of the

satellite, this includes attitude control, trajectory work to sort out the orbit

### 3.3.1 The Spacecraft

In this section "spacecraft" will be used to mean the part of the satellite that does not include the science payload. In other contexts, the "spacecraft" is used to mean the complete satellite. Referring to Figure 3.4, the spacecraft is the ring around the "Y" payload.

**Schematic diagram showing the "Point Ahead"**

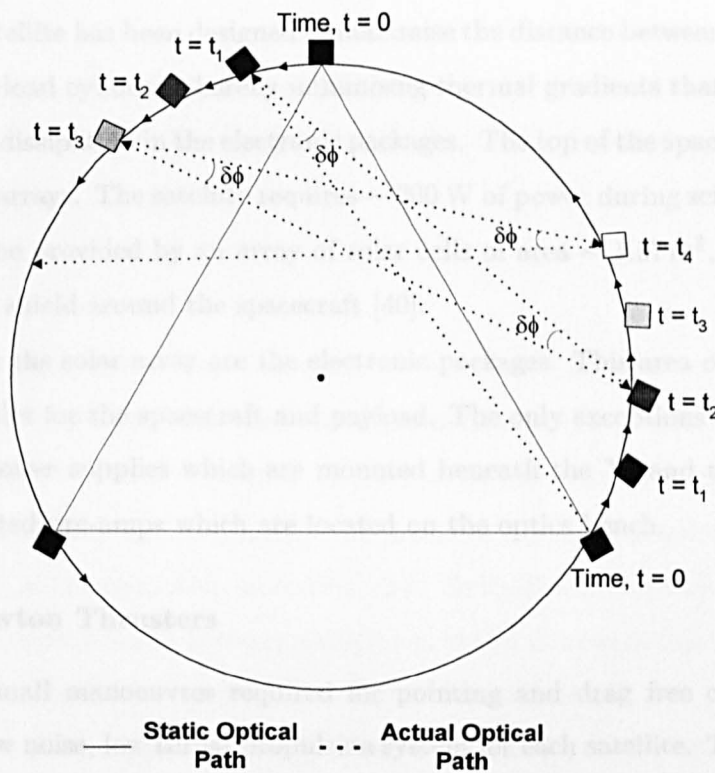


**Figure 3.5: Schematic diagram showing the need for "Point Ahead" in LISA.** *The point ahead angle in this diagram has been greatly exaggerated to allow the effect to be seen more clearly.*

As the LISA orbit is heliocentric, and far from the Earth, and far from the Sun, the spacecraft must be able to maintain its position and attitude. The ions are accelerated towards an anode where they are ejected (at 30 km/s) creating the required thrust[12]. In order to minimise the charging of the spacecraft, the ions are neutralised as they are ejected.

As the LISA orbit is heliocentric, the biggest disturbing force on the s/c will come from fluctuations in the solar wind and solar radiation pressure. This necessitates that the thruster used must be controllable in the range 0.1 - 100  $\mu$ N, with a

satellite, this includes attitude control, telemetry back to earth, and the solar cells.

### 3.3.1 The Spacecraft

In this section “spacecraft” will be used to mean the part of the satellite that does not include the science payload. In other sections, the “spacecraft” is used to mean the complete satellite. Referring to Figure 3.4, the spacecraft is the ring around the “Y” payload.

Each satellite has been designed to maximise the distance between the electronics and the payload cylinder, thereby minimising thermal gradients that may be set up due to heat dissipation in the electronic packages. The top of the spacecraft holds the solar panel arrays. The satellite requires  $\sim 200$  W of power during science operation, which will be provided by an array of solar cells of area  $\sim 1.57$  m<sup>2</sup>, located on top of the solar shield around the spacecraft [40].

Beneath the solar array are the electronic packages. This area contains most of the electronics for the spacecraft and payload. The only exceptions being the lasers and their power supplies which are mounted beneath the Y, and the photodiodes and associated pre-amps which are located on the optics bench.

#### Micro-Newton Thrusters

The very small manoeuvres required for pointing and drag free control of LISA require a low noise, low thrust propulsion system for each satellite. This is best provided by Field Emission Electric Propulsion (FEEP) thrusters[41][42], where liquid Caesium (or Indium) is exposed to vacuum via a very narrow slit ( $\sim 1$   $\mu$ m). An electric field is applied across the surface of the metal, forming cusps on the surface. The stronger the field is, the larger, and narrower the cusps, until eventually the tip of the cusp ionises. The ions are accelerated towards an emitter slit where they are ejected (at 60 kms<sup>-1</sup>) creating the required thrust[12]. In order to minimise the charging of the spacecraft, the ions are neutralised as they are emitted.

As the LISA orbit is heliocentric, the biggest disturbing force on the s/c will come from fluctuations in the solar wind and solar radiation pressure. This necessitates that the thruster used must be controllable in the range 0.1 – 100  $\mu$ N, with a

resolution better than  $0.1 \mu\text{N}$ [43]. FEEPS are the only system capable of meeting this requirement. Also, as the ions are ejected at such a high velocity, the mass per unit thrust is small compared to other systems, so reducing the total fuel load. For a two year operational lifetime, the amount of fuel needed per thruster is  $\sim 9 \text{ g}$ .

### 3.3.2 The Science Payload

The science payload consists of the Y-shaped cylinder in Figure 3.4. The primary function of the cylinder is to act as a thermal and radiation shield for the optics inside. The optical bench and telescope are attached to the outer cylinder by carbon-epoxy struts which provide both mechanical and thermal stability over the timescales of interest.

#### Optics

Each satellite carries two identical optical benches and associated equipment (Figure 3.4); the following description will describe one such optics bench.

The bench has two lasers optically coupled to it, one being the primary source of light and the other for redundancy. Both lasers are fibre coupled to the bench, terminating in an adjustable mounting unit. Initially the primary laser is aligned through the optical chain, however, should a problem arise with this laser, the second fibre can be moved into position. The adjustable mount can also be used to move the fibres longitudinally, enabling the laser mode to be matched into the telescope, allowing active focusing of the telescope. (See Chapter 6 for further details.) The optics bench consists of a solid ULE<sup>3</sup>[44] titanium silicate glass plate, with the components rigidly attached. Figure 3.6 shows an expanded view of a bench, along with the optical paths. The green line shows the received light, and the red line the local laser light.

After passing through an electro-optic phase modulator, that is used for the frequency and clock stabilisation schemes, a small fraction of the main beam is split off. This fraction of the light is sent to the rear of the optics bench, where it is

---

<sup>3</sup>Ultra-Low Expansion

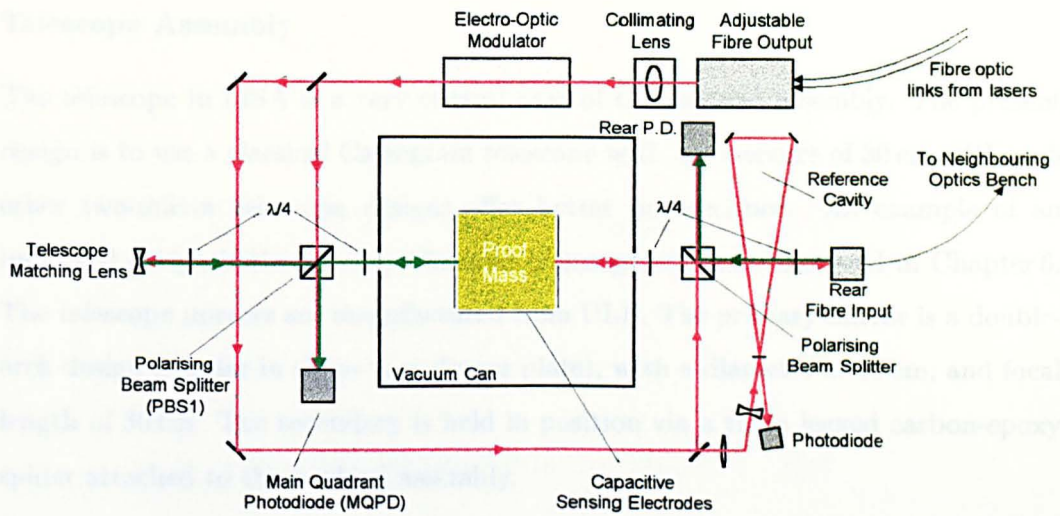


Figure 3.6: Detailed view of a LISA optics bench. The red line represents local laser light, and green lines represent light from the other optics benches. (P.D. = Photodiode)

again split, with  $\sim 10$  mW sent to the frequency reference cavity. Only one laser (the master) is frequency stabilised in LISA, with all other lasers offset phase locked to this master. (See Chapter 4 for details of the frequency stabilisation scheme used, and Chapter 5 for details of an offset phase locking scheme.) All s/c carry identical reference cavities, again giving redundancy. The remainder of the light at the back of the optics bench is reflected off the test mass and sent to the neighbouring bench. By reflecting the rear beam off the back of the test mass, and the received light from the far end of the arm off the front of the mass, motion of the spacecraft with respect to the test mass is removed to first order.

The main beam is reflected from the front polarising beam splitter (PBS1), and transmitted through the telescope. A small fraction of the beam ( $\sim 1$  mW) leaks through the beamsplitter, and is mixed with the received beam on the main quadrant photodiode (MQPD). This diode performs the heterodyne measurement of the phase of the returning beam from the far s/c.

## Telescope Assembly

The telescope in LISA is a very critical part of the payload assembly. The present design is to use a classical Cassegrain telescope with an aperture of 30 cm, although other two-mirror telescope designs offer better performance. An example of an improved design is the Ritchey-Chretien telescope which is discussed in Chapter 6. The telescope mirrors are manufactured from ULE. The primary mirror is a double-arch design (similar in shape to a dinner plate), with a diameter of 30 cm, and focal length of 30 cm. The secondary is held in position via a three legged carbon-epoxy spider attached to the payload assembly.

## The Test Mass

The test mass at the centre of the optics bench acts as the mirror at the end of the interferometer arm. The mass is made of an alloy of 10% gold and 90% platinum, chosen because of its high density ( $20,000 \text{ kg/m}^3$ ), and low magnetic susceptibility[11]. The test mass, combined with capacitive sensing electrodes, forms a sensor based on a three axis electrostatic suspension. Ideally, the mirrors in a gravitational wave detector should be floating freely in space. For ground based detectors this is not possible, and so the masses are hung as pendula. In LISA, the mirrors are effectively free floating masses (in the frequency detection bandwidth). The capacitive sensors, measuring the position of the mass, are used to servo the s/c around the mass, such that the mass is “drag-free”<sup>4</sup> [43]. As there are two masses per s/c, each cannot be truly free-floating, and hence the second mass has to be forced to follow the first. However the second mass drifts over timescales much longer than the gravitational wave periods of interest, and so can be considered as drag free in the detection bandwidth. As in ground based detectors, the dominant low frequency noise source is caused by spurious accelerations of the test mass, except in LISA, the accelerations of the mass are caused by the back action of the capacitive sensors, and through parasitic forces that may be applied directly to the proof mass (Table

---

<sup>4</sup>The term “drag-free” dates from the 1960s, when the concept was invented to shield geocentric satellites from the aerodynamic drag due to the Earth’s atmosphere.

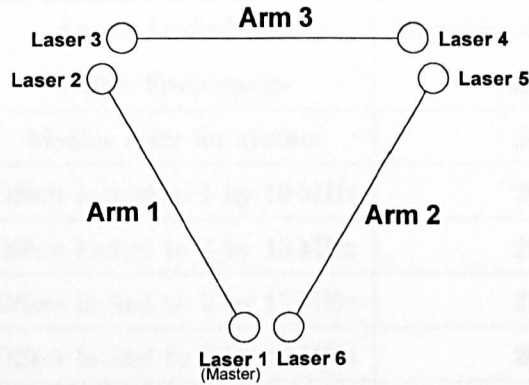


Figure 3.7: Nomenclature of lasers in LISA

2.4). In order to reach the desired displacement sensitivity limit for LISA, the test mass accelerations must be kept below  $10^{-14} \text{ ms}^{-2}/\sqrt{\text{Hz}}$  in the frequency range of  $10^{-4}$  to  $10^{-3} \text{ Hz}$ , corresponding to  $10^{-9} \text{ m}/\sqrt{\text{Hz}}$  at 1 mHz.

### 3.4 Interferometric Techniques

One satellite in the constellation is chosen to be the master satellite. For redundancy reasons, each satellite is identical, and therefore the choice of master is completely arbitrary, and can be changed during the lifetime of the mission. In the master s/c, one laser is frequency stabilised to its reference cavity. All other lasers (fibre linked to the other optics benches) are phase locked to the stabilised master. The light from each optical bench is sent out along the respective interferometer arm to a far s/c, where the local laser is phase locked to the received beam, and the higher power, phase locked light transponded back. At each stage, the lasers are frequency offset locked as shown in Table 3.1 (referring to Figure 3.7 for the nomenclature)[11]: the offset frequency is chosen to be at a spectral frequency where the amplitude noise of the laser is limited purely by photon shot noise.

The master laser is frequency stabilised to a triangular Fabry-Pérot reference cavity. The cavity will be manufactured from ULE (average linear expansion coefficient of  $2 \times 10^{-8} / \text{K}$ , but is temperature dependent), which sets a lower limit to the laser frequency fluctuations of

Laser	Lasers Locked and Offset Frequencies	Modulation Frequency (MHz)
1	Master laser for system	200
2	Offset locked to 1 by 10 MHz	202
3	Offset locked to 2 by 13 MHz	208
4	Offset locked to 5 by 17 MHz	210
5	Offset locked to 6 by 15 MHz	206
6	Offset locked to 1 by 12 MHz	204

Table 3.1: **Example of offset frequency and modulation scheme for LISA.**

$$\widetilde{\delta\nu} = \nu\alpha\widetilde{\Delta T} \quad (3.1)$$

where  $\nu$  and  $\widetilde{\delta\nu}$ <sup>5</sup> are the laser frequency and laser frequency fluctuations respectively,  $\alpha$  is the linear thermal expansion coefficient, and  $\widetilde{\Delta T}$  is the temperature fluctuation. In the case of LISA, where the expected thermal stability of the optics bench is  $\sim 10^{-6} \text{ K}/\sqrt{\text{Hz}}$ , the lower limit to the stabilised frequency noise is  $\sim 10 \text{ Hz}/\sqrt{\text{Hz}}$ , taking into account some uncertainty in the equilibrium temperature inside the payload cylinder. However, with the orbits chosen for LISA, adjacent armlengths are likely to vary by  $\Delta x = 10^5 \text{ km}$  in the timescales of interest, and with the laser stabilised as above, this frequency noise would set a limit to the relative armlength measurement attainable of

$$\widetilde{\delta x} \approx \Delta x \frac{\widetilde{\delta\nu}}{\nu} = 3.6 \times 10^{-6} \text{ m}/\sqrt{\text{Hz}} \quad (3.2)$$

corresponding to a gravitational wave amplitude of

$$h \approx 3.6 \times 10^{-16}/\sqrt{\text{Hz}} \quad (3.3)$$

where  $\widetilde{\delta x}$  is the smallest relative displacement that can be measured. This value is several orders of magnitude above the desired overall sensitivity of  $\widetilde{\delta x} = 2 \times 10^{-12} \text{ m}/\sqrt{\text{Hz}}$ [12]. In order to reach this requirement, a laser frequency noise below

---

<sup>5</sup>a “tilde” ( $\sim$ ) over a quantity represents the linear spectral density of that quantity.

$6 \times 10^{-6} \text{ Hz}/\sqrt{\text{Hz}}$  is needed. Although it is not possible to stabilise the laser frequency to this level, the frequency noise can be estimated by applying a frequency correction algorithm. The following gives a brief description of the frequency correction algorithm. (See [45] [46] for more details of this scheme.)

For an armlength  $L$ , the phase difference between the outgoing and returning beams is given by

$$\phi = \frac{4\pi\nu L}{c} \quad (3.4)$$

For slow variations in  $L$  and  $\nu$ ,

$$\delta\phi = \left[ \frac{4\pi}{c} \right] (L\delta\nu + \nu\delta L) \quad (3.5)$$

By comparing the mean phase of the light returning in two adjacent arms, with the transmitted light, the phase difference (measured over the time of flight of the two arms) allows an estimate of the laser frequency noise to be made:

$$\delta\phi = \left[ \frac{4\pi}{c} \right] L\delta\nu \quad (3.6)$$

(since  $\nu\delta L \ll L\delta\nu$ ). Thus if the phase difference is measured, the laser frequency noise can be estimated at frequencies away from multiples of the inverse round trip travel time.

### 3.5 Interferometer Readout

The following will describe the beat signals obtained from the interferometer in which the master laser is located at the vertex (arms one and two in Figure 3.7).

Before considering the interferometric signals, the electric fields of the individual laser sources are first considered. Optics bench 1 is taken as the master; the electric field of its laser can be represented by:

$$E_1 = E_o e^{i(\omega_1 t + \beta e^{i\omega_{m_1} t} + \phi_1)} \quad (3.7)$$

The expression for the field of laser 6 has a similar form to that for the master, except that the frequency is offset (as given in Table 3.1):

$$E_6 = E_o e^{i(\omega_6 t + \beta e^{i\omega_{m_6} t} + \phi_6)} \quad (3.8)$$

The electric fields of the transmitted beams from spacecraft 2 and 5 are more complicated, since the lasers are phase locked to light which has traversed the full interferometer arm. If the s/c are moving with respect to each other, the received (and therefore the phase locked transponded) light is Doppler shifted. Furthermore the beams travelling along the arm also contains the phase shift produced by a gravitational wave. The electric fields can be written as:

$$E_2 = E_o e^{i((\omega_2 + 2\omega_{d_1})t + \beta e^{i\omega_{m_2} t} + \phi_2 + \phi_{gw})} \quad (3.9)$$

and

$$E_5 = E_o e^{i((\omega_5 + 2\omega_{d_2})t + \beta e^{i\omega_{m_5} t} + \phi_5 + \phi_{gw})} \quad (3.10)$$

where  $\omega_x$  (for  $x=1..6$ ) are the carrier frequencies of the transmitted laser light,  $\omega_{m_x}$  (for  $x=1..6$ ) are the modulation frequencies,  $\omega_{d_{1/2}}$  is the Doppler frequency shift associated with each arm (assumed constant over one return trip),  $\phi_{gw}$  is the phase change produced by the gravitational wave,  $\phi_x$  (for  $x=1..6$ ) are the static offsets for each laser (equals 0 when the lasers are phase locked), and  $\beta$  is the modulation index.

### 3.5.1 Vertex Interference Signal

Firstly, the simplest case will be considered: the interference signal between the vertex lasers (1 and 6). This signal is detected on the rear photodiode of bench two, and is used primarily to phase lock laser 6 to laser 1, and also to stabilise the clock used for optics bench 2.

Assuming that the phase modulation sidebands are small compared to the carrier, the modulation term can be approximated by:

$$e^{i\beta e^{i\omega_m t}} \approx 1 + i\beta e^{i\omega_m t}. \quad (3.11)$$

Therefore, taking laser 1 as an example, the electric field becomes:

$$E_1 = E_o e^{i(\omega_1 t + \phi_1)} (1 + i\beta e^{i\omega_{m_1} t}) \quad (3.12)$$

The two laser beams are added together on the polarising beam splitter at the rear of the optics bench. The combined electric field is:

$$\begin{aligned} E_{1/6} &= E_1 + E_6 \\ &= E_o [e^{i(\omega_1 t + \phi_1)} + i\beta e^{i(\omega_1 - \omega_{m_1})t} + i\beta e^{i(\omega_1 + \omega_{m_1})t} + \\ &\quad e^{i(\omega_6 t + \phi_6)} + i\beta e^{i(\omega_6 - \omega_{m_6})t} + i\beta e^{i(\omega_6 + \omega_{m_6})t}] \end{aligned} \quad (3.13)$$

Assuming that the lasers are phase locked, then there is no static phase offset, and hence  $\phi_{1/6}$  is set equal to zero. The combined beam is detected on the rear photodiode. The resulting interference signal is given by:

$$\begin{aligned} I_{1/6} &\propto E_{1/6} \cdot E_{1/6}^* \\ &\propto I_o \{ \sin(\Delta\omega)t \\ &\quad + \beta \sin(\Delta\omega + \omega_{m_1})t + \beta \cos(\Delta\omega - \omega_{m_1})t \\ &\quad + \beta \sin(\Delta\omega + \omega_{m_6})t + \beta \cos(\Delta\omega - \omega_{m_6})t \\ &\quad + \text{terms at optical frequencies} \\ &\quad + \text{terms at twice the modulation frequency} \\ &\quad + \text{terms at the difference of the modulation frequencies} \} \end{aligned} \quad (3.14)$$

where  $\Delta\omega = \omega_6 - \omega_1$ . Table 3.2 summarises the photodiode output, using the offset and modulation frequencies listed in Table 3.1.

The important signals (bold font) from the photodiode are the signal at the offset frequency ( $\Delta\omega$ ), and the signal containing the phase modulation sideband of the master laser. Figure 3.8 shows a possible scheme to extract the relevant information from the multitude of signals present. The photodiode output is heavily filtered to remove high frequency signals (at and above twice the modulation frequency), and is then split into two paths; one to phase lock the slave laser, and the other to stabilise the clock.

Beat Signals	Carrier/Sideband	Beat Frequency	Normalised Powers
$\Delta\omega$	<b>c1_c6</b>	<b>12 MHz</b>	<b>100%</b>
$\Delta\omega + \omega_{m1-}$	<b>c6_c1_sb1-</b>	<b>(200-12) MHz</b>	<b>10%</b>
$\Delta\omega - \omega_{m1+}$	<b>c6_c1_sb1+</b>	<b>(200+12) MHz</b>	<b>10%</b>
$\Delta\omega - \omega_{m6-}$	c6_c1_sb6-	12 MHz - 204 MHz	10%
$\Delta\omega - \omega_{m6+}$	c6_c1_sb6+	12 MHz + 204 MHz	10%
$\Delta\omega + \omega_{m1-} - \omega_{m6-}$	c6_c1_sb1-_sb6-	12 MHz - 4 MHz	5%
$\Delta\omega + \omega_{m1-} - \omega_{m6+}$	c6_c1_sb1-_sb6+	12 MHz + 404 MHz	5%
$\Delta\omega - \omega_{m1+} - \omega_{m6-}$	c6_c1_sb1+_sb6-	12 MHz - 404 MHz	5%
$\Delta\omega - \omega_{m1+} + \omega_{m6+}$	c6_c1_sb1+_sb6+	12 MHz + 4 MHz	5%
$\omega_{m1-} + \omega_{m1+}$	sb1-_sb1+	400 MHz	5%
$\omega_{m6-} + \omega_{m6+}$	sb6-_sb6+	408 MHz	5%

Table 3.2: **Beat signals and strengths at the output of the rear photodiode of optics bench 6.** *The bold entries are the signals that can be used to phase lock the lasers and clocks.*

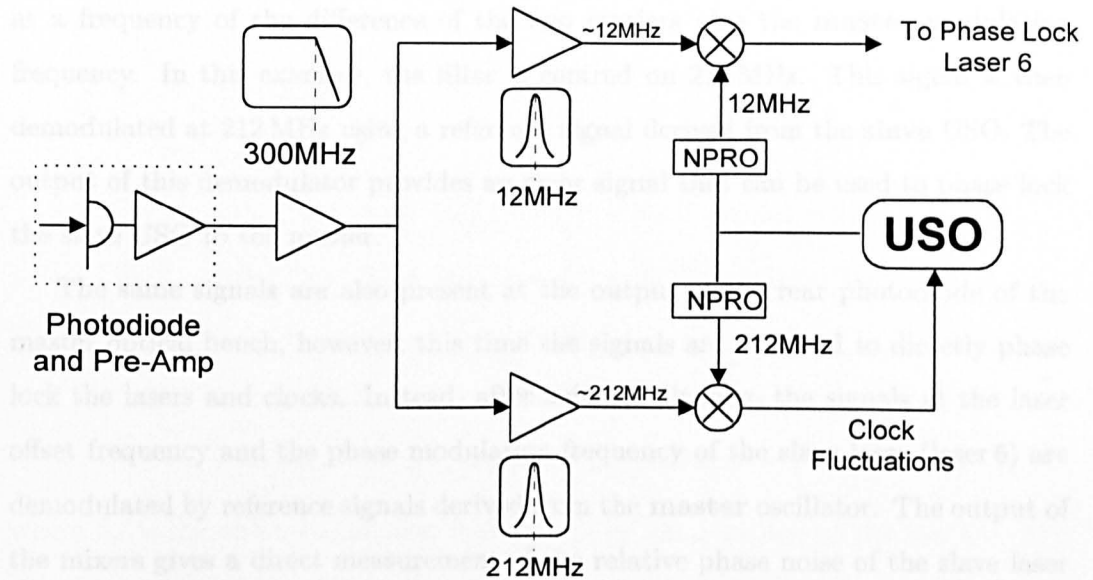


Figure 3.8: **Scheme to extract error signal for phase locking and clock stabilisation.** Where *NPRO* = Numerical Programmed Oscillator, and *USO* = Ultra Stable Oscillator

Firstly the phase locking of the slave is considered. The signal is passed through a narrow band resonant filter centred on the offset frequency. The output is demodulated at the offset frequency reference, derived using the clock associated with optics bench 6, leaving the error signal used to phase lock the local laser to the stabilised master. (This is the scheme demonstrated experimentally in Chapter 5.)

Each optics bench has an Ultra Stable Oscillator (USO) associated with it, which is used to drive all Numerical Programmed Oscillators (NPRO), which in turn are used to derive the offset frequency, phase modulation frequency, and to compensate for the Doppler signal superimposed on the light returning along the interferometer arm. Any fluctuations in this clock frequency will look like relative phase noise of the slave laser. In order to minimise clock noise, one USO is treated as the master oscillator (in the same sense as the master laser) and all other USOs are locked to this master. Using a scheme similar to the laser phase locking, the USO of the second optics bench is locked to the master clock. The signal from the photodiode is passed through a narrow band resonant filter. The filter is designed to pass only signals

at a frequency of the difference of the two carriers plus the **master** modulation frequency. In this example, the filter is centred on 212 MHz. This signal is then demodulated at 212 MHz using a reference signal derived from the **slave** USO. The output of this demodulator provides an error signal that can be used to phase lock the slave USO to the master.

The same signals are also present at the output of the rear photodiode of the master optical bench, however, this time the signals are not used to directly phase lock the lasers and clocks. Instead, after suitable filtering, the signals at the laser offset frequency and the phase modulation frequency of the slave laser (laser 6) are demodulated by reference signals derived from the **master** oscillator. The output of the mixers gives a direct measurement of the relative phase noise of the slave laser and USO, and can be used to mathematically subtract the excess noise imposed on the measurement using the frequency correction algorithm described briefly in Section 3.4.

With the two lasers and clocks phase locked in the vertex s/c, the interferometry signals in the long arm can be investigated.

### 3.5.2 Long Arm Interference Signal

The long arm of the interferometer is similar to the vertex case, except now there is the added complication of the Doppler signal, and more importantly, the gravitational wave signal, being superimposed on the received light. The main difference in the laser phase locking and clock stabilisation is in the power of the received beam. The biggest single noise source in LISA, not including the spurious accelerations that limit the detector at very low frequencies, is due to the noise imposed on the transponded laser light due to shot noise in the detected signal. The shot noise limit to the phase stability corresponds to a displacement error of  $10 \text{ pm}/\sqrt{\text{Hz}}$ .

Considering Arm 1 (s/c 1 and 2), and using the same notation as before, the detected intensity **back** at the master s/c is given by:

$$\begin{aligned}
I_{1/6} &\propto E_{1/2} \cdot E_{1/2}^* \\
&\propto \{ \sin(\Delta\omega + 2\omega_{d_1})t \\
&\quad + \beta e^{igw} \sin(\Delta\omega + 2\omega_{d_1} + \omega_{m_1})t + \beta e^{igw} \cos(\Delta\omega + 2\omega_{d_1} - \omega_{m_1})t \\
&\quad + \beta e^{igw} \sin(\Delta\omega + 2\omega_{d_1} + \omega_{m_2})t + \beta e^{igw} \cos(\Delta\omega + 2\omega_{d_1} - \omega_{m_2})t \\
&\quad + \text{terms at optical frequencies} \\
&\quad + \text{terms at twice the modulation frequency} \\
&\quad + \text{terms at the difference of the modulation frequencies} \} \quad (3.15)
\end{aligned}$$

where  $\omega_d$  is the one way Doppler shift caused by axial motion of the two s/c,  $e^{igw}$  is the phase change caused by the passage of a gravitational wave, and  $\Delta\omega$  is now taken to mean the beat frequency between the carriers of laser 1 and 2. As expected, the signals are identical to the vertex case, apart from the added Doppler shift and gravitational wave signal.

The detected intensity at the main photodiodes of optics benches 2 and 4, are similar to the above, the only differences being the offset and modulation frequencies, and the increased Doppler shift of arm 3.

Before the interferometry signals are telemetered back to earth, the effect of the Doppler shift is removed by mixing the detected signal with an estimate of the Doppler frequency. The Doppler shift between the s/c can be estimated by two means: i) by telemetering signals between the s/c, and calculating the Doppler shift from the time delay and, ii) the orbits of the s/c are known to very high accuracy, and so the expected Doppler shift can be estimated mathematically. For arms 1 and 2, the Doppler rate can be kept below 1 MHz using orbital correction manoeuvres once per year, or below 20 kHz with corrections taking place monthly. The Doppler shift of arm 3 cannot be corrected without compromising the sensitivity in arms 1 and 2, and so may be as high as 15 MHz.

Taking the Doppler signal to be of the form

$$Dopp = E_{dop} \cos(\omega_{d_1} t) \quad (3.16)$$

the down-converted signal is:

$$\begin{aligned}
I_{dopp} &\propto Dopp.I_{1/2} \\
&\propto e^{igw} \{ \sin(\Delta\omega)t + \sin(\Delta\omega + 4\omega_{d_1})t \\
&\quad + \beta\sin(\Delta\omega + \omega_{m_1})t + \beta\cos(\Delta\omega - \omega_{m_1})t \\
&\quad + \beta\sin(\Delta\omega + \omega_{m_2})t + \beta\cos(\Delta\omega - \omega_{m_2})t \\
&\quad + \beta\sin(\Delta\omega + 4\omega_{d_1} + \omega_{m_1})t + \beta\cos(\Delta\omega + 4\omega_{d_1} - \omega_{m_1})t \\
&\quad + \beta\sin(\Delta\omega + 4\omega_{d_1} + \omega_{m_2})t + \beta\cos(\Delta\omega + 4\omega_{d_1} - \omega_{m_2})t \\
&\quad + \text{terms at optical frequencies} \\
&\quad + \text{terms at twice the modulation frequency} \\
&\quad + \text{terms at the difference of the modulation frequencies} \} \quad (3.17)
\end{aligned}$$

As can be seen, the signal contains the same terms as in the simpler vertex case, although now there is an extra set of components shifted in frequency by four times the one way Doppler frequency shift. The most important signals out of the above spectrum are the components at the beat frequency between the carriers, and the phase modulation frequency of laser 2. These signals are used in the frequency correction algorithms to reduce the excess laser frequency noise and clock noise, and also contain the gravitational wave signature (as do all components, although with much lower signal-to-noise ratio). In order to separate the carrier beat note from the other signals, the above signal is again down converted, using a comb of frequencies, separated by 50 kHz. The comb is centred on the expected beat note frequency (in the case of arm 1, 10 MHz), with the output band-pass filtered between 75 kHz and 125 kHz. A tracking filter is used to anti-alias the data, removing all signals above  $\sim 100$  Hz[12].

The resulting signal is sent to a phase comparison unit, similar in design to a Global Positioning System receiver, where the data is reduced and resampled. As LISA is a low frequency detector, the sampling frequency need not be faster than 2Hz. In practice, the data may be sampled faster. However, as there is no useful gravitational wave data above 1 Hz, due to the length of the arms, the telemetered data will be anti-alias filtered, and resampled at  $\sim 2$  Hz.

The same process occurs at both optics bench 2 and 4, before being telemetered to earth, where the three semi-independent measurements can be correlated for the gravitational wave signal.

### 3.6 Conclusions

The idea of placing a gravitational wave detector in space is not a new one. However it is only within the last few years that the mission has gained backing from national and international space agencies. LISA is not a simple mission. The final design requires expertise in all fields of space science and engineering, as well as expertise in the detection of gravitational waves.

The displacement sensitivity of LISA will be on a par with all long baseline ground based interferometers, although the peak sensitivity will be at very different frequencies. For LISA, sources have already been identified, with signal-to-noise ratios approaching  $10^5$  (for a one year observation time), thereby guaranteeing the detection of gravitational waves, and more importantly, allowing astrophysical models of massive, and supermassive compact objects to be directly tested.

LISA, combined with the growing family of ground based detectors, should allow gravitational waves to be observed over 7 decades in frequency.

In long baseline ground based antennae, e.g. GEO600[28], the laser must be stabilised to a level of  $\sim 10^{-7}$  Hz/ $\sqrt{\text{Hz}}$  at 100 Hz in order that the displacement sensitivity is not limited by laser noise.

In space-borne interferometers, where a relative wavelength change of 2% is expected, the laser frequency must be stabilised to a level of  $\sim 10^{-6}$  Hz/ $\sqrt{\text{Hz}}$  at a Fourier frequency of 1 mHz[12]. This will be achieved using a two stage noise reduction scheme. Initially the laser will be frequency stabilised to an onboard frequency reference cavity, reducing the noise to  $\sim 10$  Hz/ $\sqrt{\text{Hz}}$ . Then, following the scheme described in Chapter 3, Section 4, the excess frequency noise will be removed, giving an apparent stability of  $\sim 10^{-6}$  Hz/ $\sqrt{\text{Hz}}$ .

This chapter will describe experiments concerned with the frequency stabilisation of a solid state Nd:YAG laser at the Fourier frequencies of interest to space-borne

## Chapter 4

# Laser Frequency Stabilisation for LISA

### 4.1 Introduction

As shown in Chapter 2, laser frequency noise can seriously hinder the operation of all interferometric gravitational wave detectors. Fluctuations of the laser frequency at the gravitational wave frequencies of interest will couple into the measurement, and be indistinguishable from signals caused by the passage of a gravitational wave. In long baseline ground based antennae, *e.g.* Geo 600[29], the laser must be stabilised to a level of  $\sim 10^{-7}$  Hz/ $\sqrt{\text{Hz}}$  at 100 Hz in order that the displacement sensitivity is not limited by laser noise.

In space-borne interferometers, where a relative armlength change of 2% is expected, the laser frequency must be stabilised to a level of  $\sim 10^{-6}$  Hz/ $\sqrt{\text{Hz}}$  at a Fourier frequency of 1 mHz[12]. This will be achieved using a two stage noise reduction scheme. Initially the laser will be frequency stabilised to an onboard frequency reference cavity, reducing the noise to  $\sim 10$  Hz/ $\sqrt{\text{Hz}}$ . Then, following the scheme described in Chapter 3, Section 4, the excess frequency noise will be removed, giving an apparent stability of  $\sim 10^{-6}$  Hz/ $\sqrt{\text{Hz}}$ .

This chapter will describe experiments concerned with the frequency stabilisation of a solid state Nd:YAG laser at the Fourier frequencies of interest to space-borne

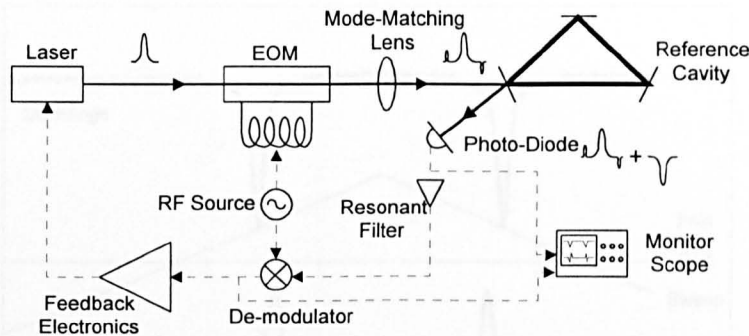


Figure 4.1: **Schematic layout of *rf* reflection locking scheme.**

interferometers. Firstly the reflection locking technique is described, followed by the experimental arrangement, and results obtained.

## 4.2 Radio Frequency Reflection Locking

The radio frequency (*rf*) reflection locking scheme was developed in 1983 by Drever *et al* [48], in the context of producing low noise laser sources for use in Fabry-Pérot gravitational wave detectors (see Chapter 2). Figure 4.1 shows a schematic diagram of a frequency stabilisation, *rf* reflection locking system. The laser light passes through an electro-optic modulator (EOM), producing phase modulation sidebands on the light, and is then mode-matched into the frequency reference cavity. The laser frequency,  $\omega$ , is tuned until it is resonant in the cavity, so causing a build up of intra-cavity power. The phase modulation frequency,  $\omega_m$ , is chosen such that, when the carrier is resonant in the cavity, the sidebands (at frequency  $\omega \pm \omega_m$ ) are not at an integer number of cavity Free Spectral Ranges (FSR) from the carrier frequency, and hence will not be resonant. The sidebands, and most of the carrier, are reflected from the input mirror, and mixed with the light leaking back out of the cavity.

Using the analogy with the “Pound Stabiliser” [49]<sup>1</sup>, the leakage field is in anti-phase with the reflected field, so creating a null in the detected intensity (Figure 4.2). The output of the photo-detector is filtered using a passband resonant filter,

<sup>1</sup>Due to the similarity of the two techniques, the locking scheme is commonly referred to as the *Pound-Drever* scheme.

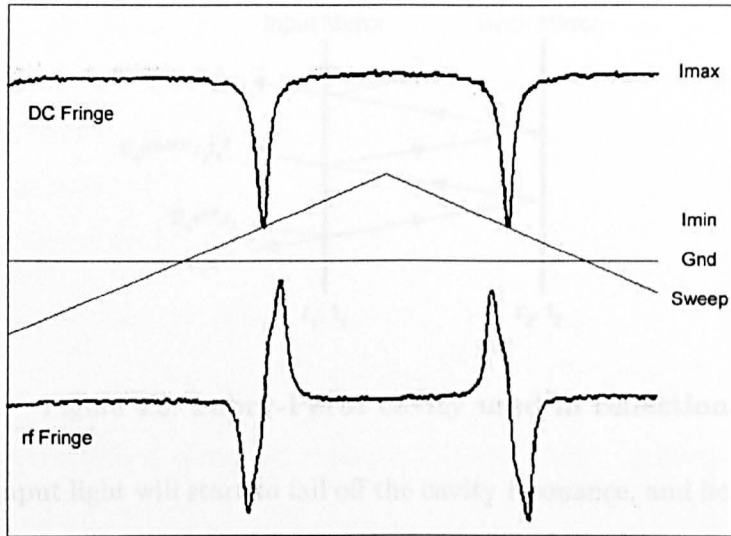


Figure 4.2: **Experimental DC and de-modulated fringes.** *The reflected fringes are obtained by scanning the frequency of the laser through the resonant frequency of the cavity.*

centred on the modulation frequency, before being de-modulated by the *rf* source, used to drive the EOM, producing the characteristic bi-polar “S” fringe (error) signal (Figure 4.2).

The frequency noise of the laser can be considered to consist of two terms: one slow (almost static), and the other fast<sup>2</sup>. Firstly, fast variations will be considered. The intracavity resonant field acts as a “phase memory” *i.e.* an average of the phase of the input light, whereas the reflected field gives a measure of the instantaneous laser phase. If the laser is noiseless (a perfect optical sine wave), then the de-modulated signal is zero. However, if the laser carries some phase noise, then the de-modulated signal will not be zero, but will be directly proportional to the instantaneous phase. This signal (known as the “error signal”) is electronically filtered and fed back to the laser to correct the phase fluctuations.

For laser frequency noise on timescales longer than the cavity response time, the system performs as a frequency, rather than phase, detector. As the laser frequency

<sup>2</sup>“Fast” meaning that the cavity field cannot react quick enough to reach equilibrium with the input field.

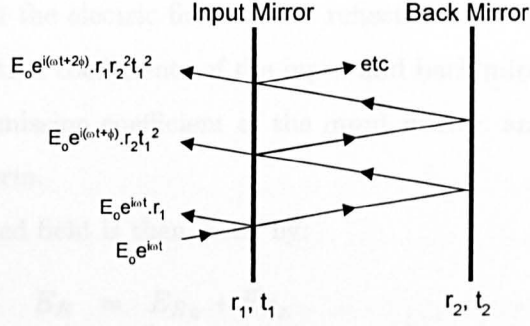


Figure 4.3: Fabry-Pérot cavity used in reflection.

drifts, the input light will start to fall off the cavity resonance, and hence the leakage field amplitude will decrease, changing the intensity of the detected signal.

The transition from phase to frequency detection is smooth, and, allowing for the  $\frac{\pi}{2}$  phase change between frequency and phase (which is performed by the cavity roll off), can be handled by the feedback electronics.

### 4.3 *rf* Reflection Locking Theory

The theory behind *rf* reflection locking is based on the principles of a simple Fabry-Pérot (FP) interferometer[50]. It is therefore best to introduce the concept of the FP before considering the effects of phase modulation on the input light.

In its simplest form, the FP consists of two parallel surfaces, with light bouncing back and forth between them. Figure 4.3 shows the simplest case. As mentioned previously, the electric field back along the optic axis consists of two components: the reflected field off the input mirror, and the leakage field, consisting of an infinite number of beams emerging from the cavity. For an incident beam of the form:

$$E = E_0 e^{i\omega t} \quad (4.1)$$

the two components of the detected field will be (assuming  $N$  bounces within the cavity)[19]

$$E_{RR} = E_0 e^{i\omega t} \cdot r_1 \quad (4.2)$$

$$\begin{aligned} E_{RL} &= -E_{N-1} e^{i\phi} r_1 r_2 \\ &= -E_0 e^{i(\omega t + N\phi)} t_1^2 r_2 (r_1 r_2)^{N-1} \end{aligned} \quad (4.3)$$

where  $E_{R_{R/L}}$  are the electric fields of the reflected and leakage beams,  $r_{1/2}$  are the amplitude reflection coefficients of the input and back mirrors respectively,  $t_1$  is the amplitude transmission coefficient of the input mirror, and  $N\phi$  is the static phase of the leakage term.

The total reflected field is then given by:

$$\begin{aligned} E_R &= E_{R_R} + E_{R_L} \\ &= E_o e^{i\omega t} \left[ r_1 - t_1^2 r_2 \sum_{N=1}^{\infty} (r_1 r_2)^{N-1} e^{iN\phi} \right] \end{aligned} \quad (4.4)$$

This can be simplified, using the expansion of the sum to infinity of a geometric series,

$$\sum_{N=1}^{\infty} (r_1 r_2)^{N-1} e^{iN\phi} = \frac{e^{i\phi}}{1 - r_1 r_2 e^{i\phi}} \quad (4.5)$$

to give

$$E_R = E_o e^{i\omega t} \left[ r_1 - \frac{t_1^2 r_2 e^{i\phi}}{1 - r_1 r_2 e^{i\phi}} \right] \quad (4.6)$$

Multiplying by the complex conjugate gives an expression proportional to the detected intensity of the reflected field (*i.e.* the signal that would be detected on a photodiode):

$$I_R \propto E_R \cdot E_R^* = E_o^2 \left[ \frac{r_1^2 + r_2(r_1^2 + t_1^2) [r_2 - 2r_1 \cos\phi]}{(1 - r_1 r_2)^2 [1 + F' \sin^2 \frac{\phi}{2}]} \right] \quad (4.7)$$

where  $F'$  is the coefficient of Finesse, defined as

$$F' = \frac{4r_1 r_2}{(1 - r_1 r_2)^2} = \frac{4\mathcal{F}^2}{\pi^2} \quad (4.8)$$

and  $\mathcal{F}$  is the Finesse of the cavity.

Re-writing in terms of power reflection and transmission coefficients ( $R_i = r_i^2$ ), and assuming the ideal case of lossless mirrors ( $R_i + T_i = 1$ ), Equation 4.7 becomes:

$$I_R \propto E_o^2 \left[ \frac{R_1 + \sqrt{R_2} (\sqrt{R_2} - 2\sqrt{R_1} \cos\phi)}{(1 - \sqrt{R_1 R_2})^2 [1 + F' \sin^2 \frac{\phi}{2}]} \right] \quad (4.9)$$

When the light is resonant in the cavity, the phase term,  $\phi$ , is zero, and the detected intensity simplifies further to

$$I_R \propto E_o^2 \left[ \frac{\sqrt{R_1} - \sqrt{R_2}}{(1 - \sqrt{R_1 R_2})} \right]^2 \quad (4.10)$$

This equation leads to a convenient expression for the visibility of the DC fringes:

$$V = \frac{I_{max} - I_{min}}{I_{max}} = 1 - \left[ \frac{\sqrt{R_1} - \sqrt{R_2}}{R_1 (1 - \sqrt{R_1 R_2})} \right]^2 \quad (4.11)$$

where  $I_{max}$  is the intensity of the off-resonance detected light ( $= E_o^2 \cdot \sqrt{R_1}$ ), and  $I_{min}$  is the intensity of the detected signal when the light is resonant in the cavity.

Having derived the general expression for a Fabry-Pérot cavity used in reflection, phase modulation on the input light will now be considered. The phase modulation frequency is chosen such that when the carrier frequency is resonant in the cavity, the modulation sidebands will not be resonant, and thereby will have negligible effect on the intracavity standing wave. In this case the input field can be written as:

$$E = E_o e^{i(\omega t + \beta e^{i\omega_m t})} \quad (4.12)$$

Where  $\beta e^{i\omega_m t}$  is the phase modulation on the input field. This produces sidebands on the light of the form[51]:

$$\begin{aligned} E = E_o \{ & J_0(\delta) \cos(\omega t) \\ & + J_1(\delta) \cos(\omega + \omega_m)t + J_1(\delta) \cos(\omega - \omega_m)t \\ & + J_2(\delta) \cos(\omega + 2\omega_m)t + J_2(\delta) \cos(\omega - 2\omega_m)t \\ & + J_3(\delta) \cos(\omega + 3\omega_m)t + \dots \dots \dots \} \end{aligned} \quad (4.13)$$

where  $J_N(\delta)$  are the Bessel functions of the first order<sup>3</sup>, and  $\delta$  is the phase modulation index.

The reflected field is calculated as before, except that the field directly reflected off the input mirror is now composed of the carrier and sidebands. The leakage field, to a good approximation, is the same as the case with no modulation (there is an extremely small sideband component, but this is negligible compared to the carrier leakage field).

<sup>3</sup>First order Bessel functions are defined as

$$J_N(x) = \sum_{m=0}^{\infty} \frac{(-1)^m \left(\frac{x}{2}\right)^{N+2m}}{m! (N+m)!} \quad (4.14)$$

Assuming that  $\beta$  is small, the input field can be approximated by

$$E = E_o e^{i\omega t} (1 + i\beta e^{i\omega_m t}) \quad (4.15)$$

giving a total reflected field of

$$\begin{aligned} E_R &= E_{R_R} + E_{R_L} \\ &= \frac{E_o e^{i\omega t}}{(1 - r_1 r_2 e^{i\phi})} \left\{ r_1 - r_2 (r_1^2 + t_1^2) e^{i\phi} \right. \\ &\quad \left. + i r_1 \beta e^{i\omega_m t} (1 - r_1 r_2 e^{i\phi}) \right\} \end{aligned} \quad (4.16)$$

As before, multiplying by the complex conjugate gives an expression proportional to the detected intensity. Assuming zero loss at the input mirror, the detected intensity as a function of the phase of the input light is given by:

$$\begin{aligned} I_R \propto E_o^2 \left[ Const - 2\sqrt{R_1}\beta \sin(\omega_m t) \right. \\ \left. \left\{ \frac{\sqrt{R_2}(2R_1 + T_1)\cos\phi - \sqrt{R_1}(1 + R_2)}{(1 - \sqrt{R_1 R_2})^2} \right. \right. \\ \left. \left. - \frac{2\sqrt{R_1 R_2} T_1 \beta \cos(\omega_m t) \sin\phi}{(1 - \sqrt{R_1 R_2})^2} \right\} \right] \end{aligned} \quad (4.17)$$

where the constant is composed of the reflectance and transmittance coefficients of the mirrors, and in the size of the phase modulation sidebands:

$$Const = \frac{R_1 + R_2 + R_1\beta(1 + R_2) - 2\sqrt{R_1 R_2}(1 + \beta^2 R_1)\cos\phi}{(1 - \sqrt{R_1 R_2})^2} \quad (4.18)$$

When the light is resonant in the cavity, the phase term,  $\phi$  goes to zero, and the expression for the detected light becomes:

$$I_R \propto E_o^2 \left[ Const - \frac{2\sqrt{R_1}\beta(\sqrt{R_1} - \sqrt{R_2})\sin(\omega_m t)}{(1 - \sqrt{R_1 R_2})} \right] \quad (4.19)$$

In the limit of no modulation,  $\beta \rightarrow 0$ , Equation 4.19 simplifies to

$$I_R \propto E_o^2 \left[ \frac{\sqrt{R_1} - \sqrt{R_2}}{(1 - \sqrt{R_1 R_2})} \right]^2 \quad (4.20)$$

*i.e.* Equation 4.10, as expected.

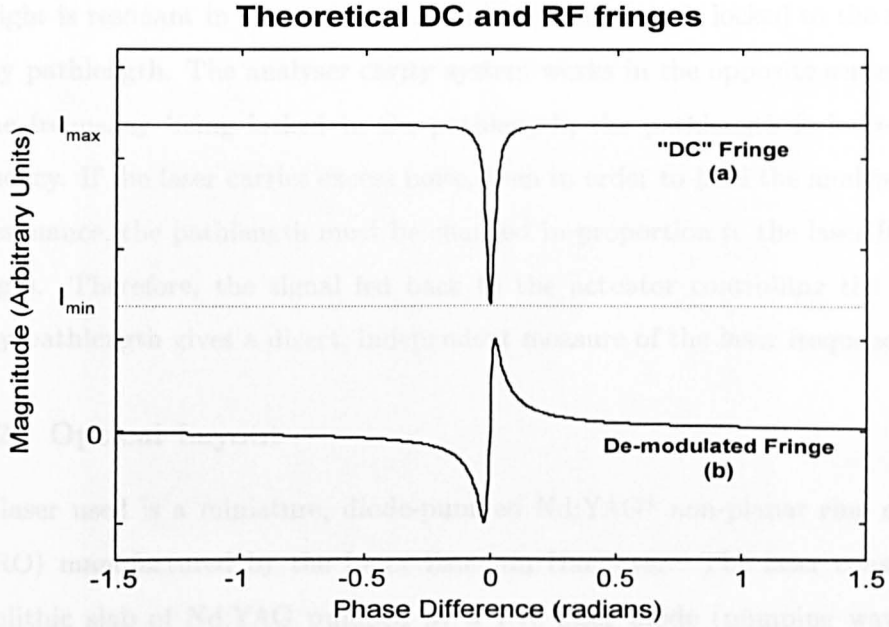


Figure 4.4: DC and de-modulated fringes obtained using Equations 4.18 and 4.21.

The detected signal is de-modulated at the modulation frequency by a phase-sensitive detector (mixer), the output of which, as a function of phase,  $\phi$ , is:

$$I_{mix} \propto \frac{\sin\phi}{1 + F' \sin^2 \frac{\phi}{2}} \quad (4.21)$$

This signal is used as the error signal for the feedback electronics. Figure 4.4(b) shows a plot of this function as the phase is swept through the resonance condition. Figure 4.4(a) shows the DC component of the detected intensity, again as the phase is swept through the resonance.

## 4.4 Experimental Arrangement

### 4.4.1 Introduction

These experiments simulate the frequency stabilisation on the master optics bench of LISA. The experimental arrangement consists of two identical cavities: one as the frequency discriminator, and the other to analyse the residual noise carried on the laser. The frequency of the laser light is adjusted and held at a point when

the light is resonant in the cavity, *i.e.* the laser frequency is locked to the reference cavity pathlength. The analyser cavity system works in the opposite sense; instead of the frequency being locked to the pathlength, the pathlength is locked to the frequency. If the laser carries excess noise, then in order to hold the analyser cavity on resonance, the pathlength must be changed in proportion to the laser frequency changes. Therefore, the signal fed back to the actuator controlling the analyser cavity pathlength gives a direct, independent measure of the laser frequency noise.

#### 4.4.2 Optical Layout

The laser used is a miniature, diode-pumped Nd:YAG<sup>4</sup> non-planar ring oscillator (NPRO) manufactured by the Laser Zentrum Hannover. The laser consists of a monolithic slab of Nd:YAG pumped by a 1 W laser diode (pumping wavelength,  $\lambda = 808$  nm). The slab forms the lasing cavity via internal reflections from its faces, giving a maximum output power of  $\sim 400$  mW at 1064 nm. Figure 4.5 shows a photograph of the laser head, with a schematic diagram shown in Figure 4.6. This laser is based on the MISER<sup>5</sup> design of Kane and Byer[52], and is often referred to by this name.

Figure 4.7 shows the experimental layout. The optical path can be summarised as follows. As the polarisation of the output of the laser is not perfect, the light is made to pass through a correctly oriented combination of quarter and half waveplates, giving approximately linear polarisation in the s-plane. The light then passes through an electro-optic modulator (EOM), with the electric field parallel to the optic axis, so producing phase modulation on the light. The EOM used is a Gsänger PM 25 (non-linear crystal of ADP<sup>6</sup>), modulated at 13.2 MHz, with modulation index of 0.6. The laser beam is then split into two paths: one to the reference cavity, and the other to the analyser.

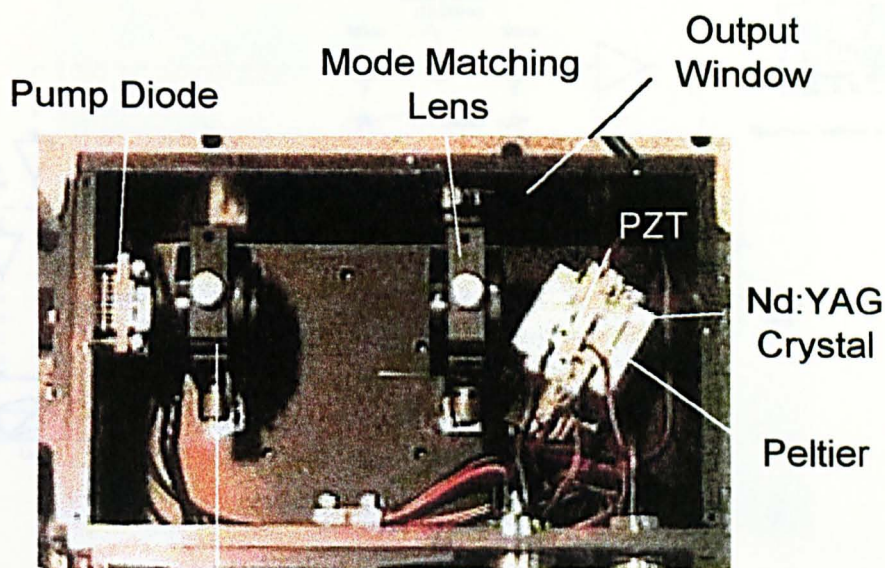
---

The cavities used are manufactured from monolithic blocks of Zerodur ceramic

<sup>4</sup>Neodymium doped Yttrium Aluminium Garnet

<sup>5</sup>Monolithic Isolated Single-mode End-pumped Ring

<sup>6</sup>Ammonium Di-Hydrogen Phosphate



Cylindrical Lens

Figure 4.5: Photograph of miniature diode-pumped Nd:YAG non-planar ring oscillator. Laser manufactured by the Laser Zentrum Hannover.

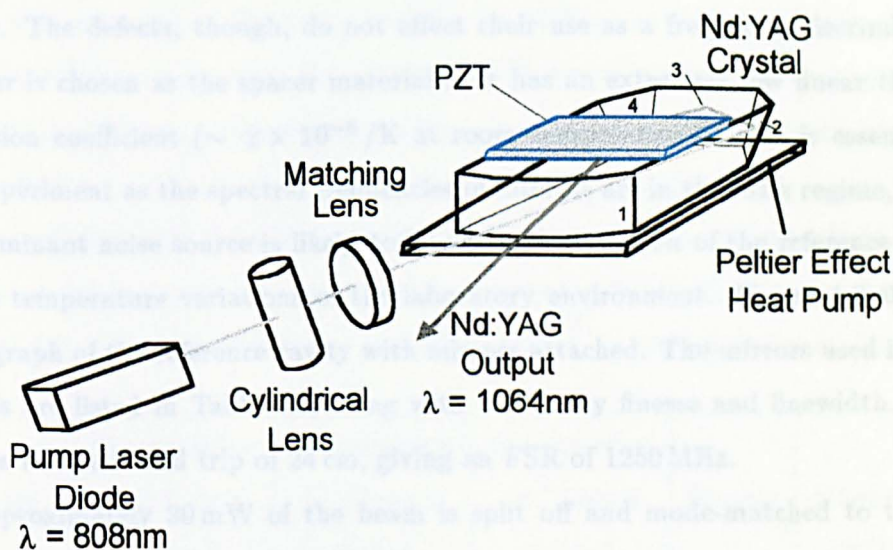


Figure 4.6: Diagram of miniature diode-pumped Nd:YAG non-planar ring oscillator. The lasing cavity is formed from internal reflections from faces 1-4. The reflection at face 2 reflects the light up to the top of the crystal, creating the non-planar ring cavity.

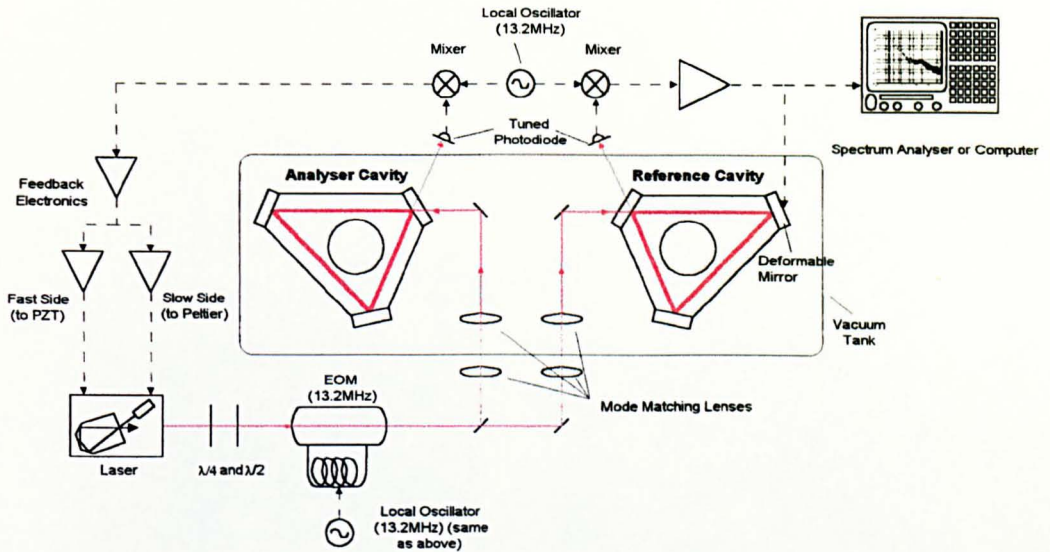


Figure 4.7: **Experimental arrangement to frequency stabilise and measure the frequency noise of the laser.**

glass[53] by GEC Marconi Avionics[54]. They are designed to be used in laser gyroscope guidance systems, however, due to minor defects, are unable to function as this. The defects, though, do not affect their use as a frequency discriminator. Zerodur is chosen as the spacer material as it has an extremely low linear thermal expansion coefficient ( $\sim 2 \times 10^{-8} / \text{K}$  at room temperature). This is essential to this experiment as the spectral frequencies of interest are in the mHz regime, where the dominant noise source is likely to be thermal expansion of the reference cavity due to temperature variations of the laboratory environment. Figure 4.8 shows a photograph of the reference cavity with mirrors attached. The mirrors used in both cavities are listed in Table 4.1, along with the cavity finesse and linewidth. Both cavities have a round trip of 24 cm, giving an FSR of 1250 MHz.

Approximately 30 mW of the beam is split off and mode-matched to the frequency reference cavity. The remainder of the beam is also split into two paths, with most of the light used for a separate experiment to phase lock a second laser to the stabilised master (See Chapter 5), and the small amount left ( $\sim 50 \text{ mW}$ ) being mode-matched to the analyser cavity. As the path length of the analyser is locked to the laser frequency, the length of the cavity must be adjustable. This is achieved

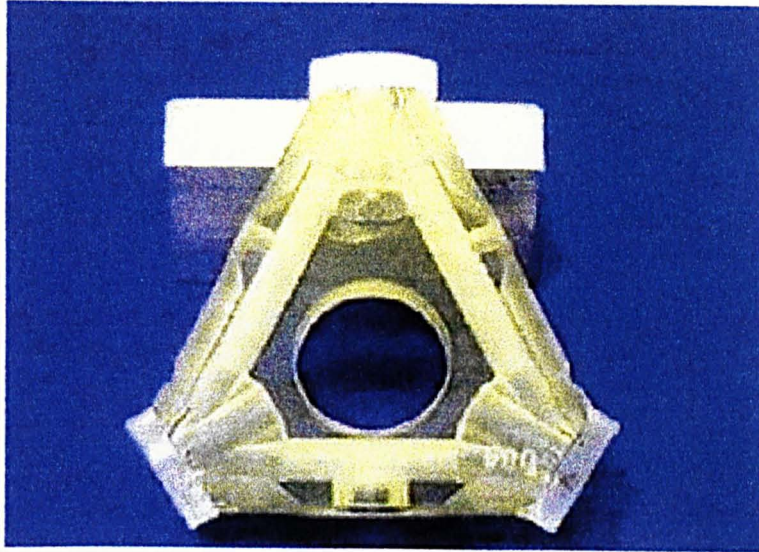


Figure 4.8: **Photograph of reference cavity.** *The reference and analyser cavity are both manufactured from monolithic blocks of Zerodur, giving the cavity better structural stability, and low thermal expansion.*

by using a deformable mirror[54], consisting of a substrate with a thin front face, with a post attached to the back. Pushing (or pulling) on the post moves the face of the mirror, hence changing the pathlength. Figure 4.9 shows a photograph of the substrate, and Figure 4.10, a schematic diagram of the complete structure, including PZT actuator.

The reflected light from both cavities is directed onto photodiodes. Both diodes and associated pre-amps are identical and consist of an EG&G YAG 200 series diode, followed by a resonant bandpass amplifier centred on the modulation frequency.

Cavity	Transmission and Loss 1 (ppm)	Transmission and Loss 2 (ppm)	Transmission and Loss 3 (ppm)	Finesse	Linewidth (kHz)
Reference	1000 & 100	30 & 600	30 & 600	2778	450
Analyser	1000 & 100	1000 & 100	30 & 600	2300	543

Table 4.1: **Properties of Reference and Analyser Cavities.** *1,2,3 refer to the cavity mirrors, with 1 being the input coupler.*



Figure 4.9: **Photograph of “Actuator Mirror”**. *This mirror is used as the actuator to control the pathlength of the analyser cavity, thereby allowing the cavity length to be locked to the laser frequency.*

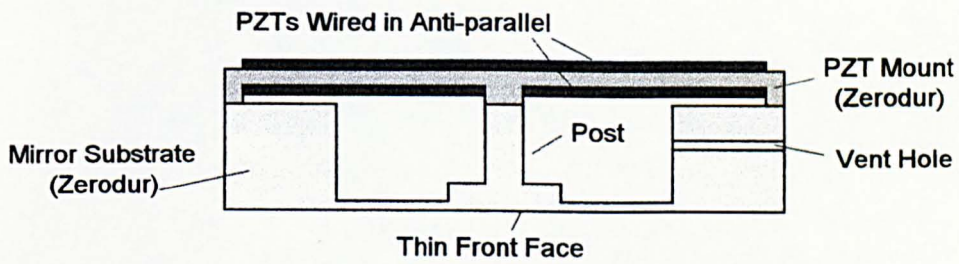


Figure 4.10: **Schematic diagram of “Actuator Mirror”**.

Figure 4.11 shows the circuit diagram of the photodiode and pre-amp.

The output of the locking photodiode is demodulated by the local oscillator (which is also used to drive the EOM), producing the error signal for the frequency stabilisation electronics. The output of the analyser photodiode is similarly demodulated, producing the error signal used to lock the analyser cavity pathlength to the laser frequency.

### 4.4.3 Feedback Control Electronics

#### Digital Auto-locking Circuit

Before the frequency stabilisation servo can actively stabilise the laser frequency, the light must first be resonant in the cavity. Initially this was achieved by manually tuning the laser frequency by adjusting the temperature of the Nd:YAG crystal. However, this is not ideal, as the speed of response of the temperature drive is limited

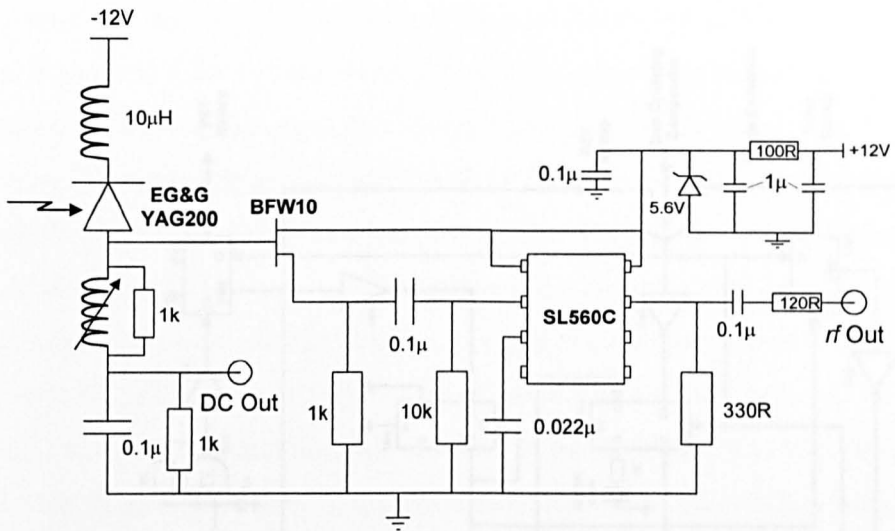


Figure 4.11: **Circuit diagram of photodiode and resonant passband amplifier.**

by the thermal time constant of the crystal, leading to the problem of “overshoot”: when the light is resonant in the cavity, the drive to the temperature is switched off, however the crystal temperature continues to change over the timescale it takes to reach equilibrium, hence pushing the frequency through the resonance. An initial solution was to use a high voltage amplifier at the output of the fast feedback path of the servo, thereby increasing the dynamic range of the fast side. This allows the fast side to pull the laser frequency over a much wider frequency range, and hence counteract the slow overshoot.

This solution was superseded by a digital circuit that carries out the same operation as above, but with no overshoot, thereby removing the need for the high voltage amplifier. Figure 4.12 show the circuit diagram of the digital “auto-locking” circuit. The circuit works as follows:

Once the switch is pressed to start the locking procedure, all memories are immediately cleared, and the PZT and temperature drives are returned to their initial states. After a short delay to allow the temperature of the crystal to reach equilibrium, the circuit sends a ramp voltage to the PZT, sweeping the frequency over a small range (30 MHz). If a fringe is detected during this sweep (see below for

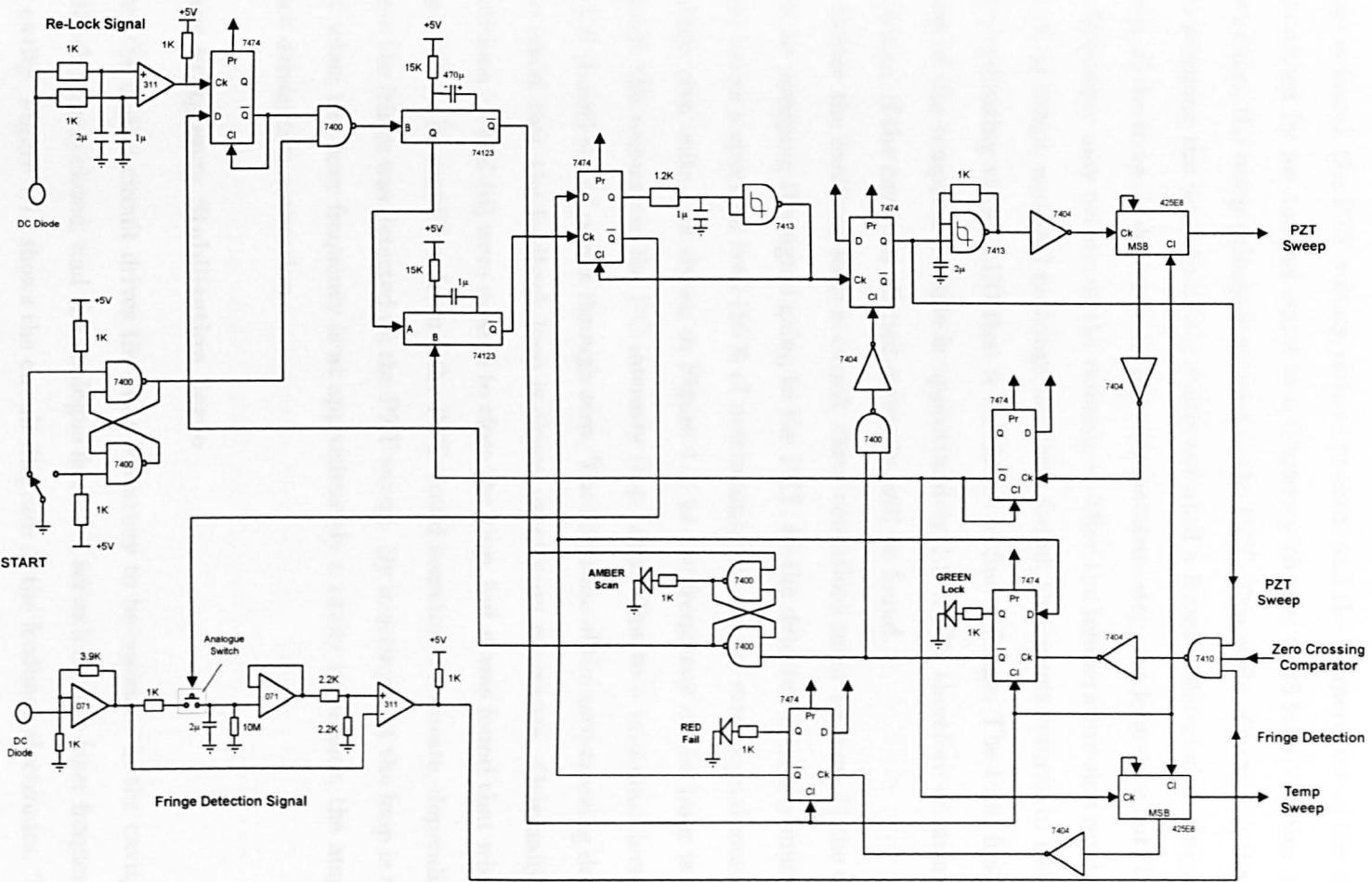


Figure 4.12: Digital auto-locking circuit to find resonance condition, and close feedback loop.

fringe detection), the ramp immediately stops, and the feedback loop is closed. If no fringe is found, the PZT voltage returns to zero, and the temperature of the crystal is increased by an amount equal to a frequency change of 28 MHz. Again, after a short delay, the ramp voltage is applied to the PZT. This cycle of sweeping the PZT, then stepping the temperature is continued until a fringe is detected during a PZT sweep. If the fringe is detected during a temperature step, the loop does not close, as the frequency may overshoot the resonance. After the temperature side reaches the end of its range, and still no fringe has been found, the circuit returns to its initial state, indicating via an LED that it has failed to find a fringe. The total frequency sweep of the temperature side is approximately  $1.5 \times \text{FSR}$ , therefore ensuring that the fringe, if the cavity is aligned correctly, will be found.

Before the feedback loop is closed, three conditions must be met: i) the circuit must be sweeping the signal going to the PZT, ii) the detected intensity must have fallen below a specified level (50% of maximum), and iii) the error signal must cross through zero volts. As shown in Figure 4.2, as the frequency of the laser is swept through the resonance, the DC intensity (top trace) dips to a minimum level, and the RF (error) signal passes through zero. The inclusion of the zero-crossing detector is to insist that the feedback loop is closed exactly on resonance. Originally, only conditions (i) and (ii) were needed to close the loop, but it was found that when the loop closed, the amplifier driving the PZT would sometimes saturate, depending on where the fringe was detected on the PZT sweep. By insisting that the loop is closed only when the laser frequency is at approximately a cavity resonance, the amplifier is not driven into saturation.

### **Laser Frequency Stabilisation Servo**

After the digital circuit drives the laser frequency to be resonant in the cavity, the feedback loop is closed, and the analogue feedback servo locks the laser frequency to the cavity. Figure 4.13 shows the circuit diagram of the feedback electronics. The  $rf$  output of the photodiode is demodulated at the mixer, before being heavily filtered (4 poles at 500 kHz) to remove the signal at twice the modulation frequency. The signal at the difference frequency is used as the feedback error signal. This signal

is electronically amplified and filtered, with the transfer function of the entire loop having unity gain frequency of 20 kHz. After some initial filtering (two transitional integrators, acting over 100 Hz to 10 kHz, and 40 Hz to 400 Hz, respectively), the feedback is split into two paths: one (slow side) to the crystal temperature controller, and the other (fast) to the PZT mounted on top of the crystal (see Figures 4.5 and 4.6).

The fast side has one more passive low-pass filter, to take the loop through unity gain with a slope of -6 dB/octave, incorporating the capacitance of the PZT actuator. The slow side is filtered at low frequencies by two passive low-pass transitional filters, operating from 7 mHz to 48 mHz and 220 mHz respectively. These filters are needed to remove the extra relative gain of the slow side frequency actuator (response of temperature drive = 3125 MHz/V, compared to the PZT drive of 1.9 MHz/V). This along with the integration due to the thermal time constant of the Nd:YAG crystal sets the loop cross-over to be at  $\sim 0.1$  Hz.

During the acquisition phase (when the digital circuit is searching for a fringe), the servo is fixed in a low gain state, therefore reducing the chance of the amplifier chain saturating. Once the frequency is locked to the cavity, the magnitude of the error signal is greatly reduced, allowing the gain of the servo to be increased, without the danger of saturation.

The overall (DC) gain is changed in the following ways:

- The potentiometer after the first amplifier allows the overall gain to be smoothly adjusted
- The input and feedback (in series with capacitor) resistors of the second amplifier can be switched to increase the gain at low frequency, while still preserving the same high frequency gain
- The  $1\text{ M}\Omega$  feedback resistor (in parallel with the capacitor path) of the second amplifier, can be switched out, thereby increasing the DC gain to the open loop amplifier gain, again without changing the high frequency transfer function

The gain and phase response for the highest gain state is shown in Figure 4.14. This is the transfer function of the servo when the laser frequency is locked to the cavity.

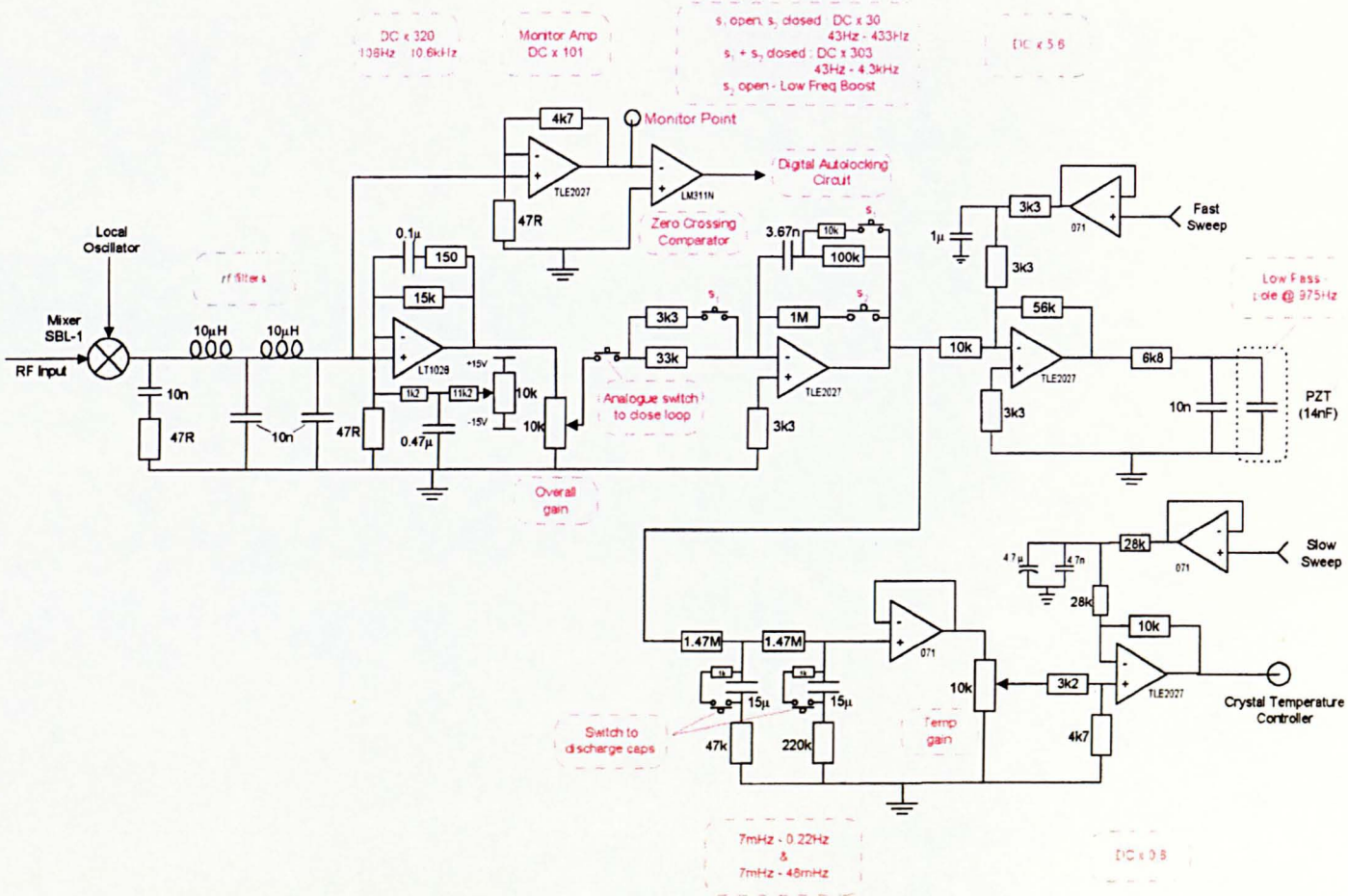


Figure 4.13: Feedback circuit to lock laser frequency to reference cavity.

The solid lines show the gain response of the two paths, and the dotted lines show the phase. The phase of the temperature side is positive ( $> 0^\circ$ ), as the feedback path has a net inversion. Figure 4.15 shows the actual response of the laser frequency. The transfer function is measured from the output of the mixer through to, and including, the frequency actuators. As expected, the loop cross-over is at  $\sim 0.1$  Hz, with unity gain frequency at 20 kHz.

### **Analyser Length Control Servo**

As mentioned earlier, the excess frequency noise of the stabilised laser is measured using a second “analyser” cavity locked to the laser light. The feedback circuit (Figure 4.16) is similar to the frequency stabilisation servo above, except that the signal is fed back to only one actuator. Figure 4.17 shows the electronic gain and phase response of the feedback circuit. As before the DC gain can be increased by adjusting the overall gain of the circuit, via the potentiometer, or once the cavity is locked, by opening the resistive feedback path on one of the amplifiers, or finally by changing the value of the feedback resistor on the second amplifier via the variable resistor. Again, the last two means of changing the gain are designed not to affect the high frequency gain for the same reasons as above. However, as shown in Figure 4.16, the high frequency gain does change. This is due to the variable resistor on the second amplifier. When the resistor is set to minimum resistance ( $\equiv 1$  k), the combined parallel impedance at high frequency is  $\sim 280 \Omega$ , giving a DC gain of 11. When the variable resistor is set to maximum resistance ( $\equiv 51$  k), the combined impedance at high frequency becomes  $387 \Omega$ , thereby changing the overall gain by a factor of approximately 3 dB.

One difference between this circuit and the laser frequency stabilisation servo, is that instead of connecting one side of the PZT to ground, it is now connected to a variable voltage supply. This allows the cavity pathlength to be manually adjusted until the laser light is resonant in the cavity.

The signal measured at the monitor output is a direct measure of the voltage fed back to the cavity PZT. This is then subtracted from the DC level (cavity length adjustment) applied to the other side of the PZT. If the feedback signal was directly

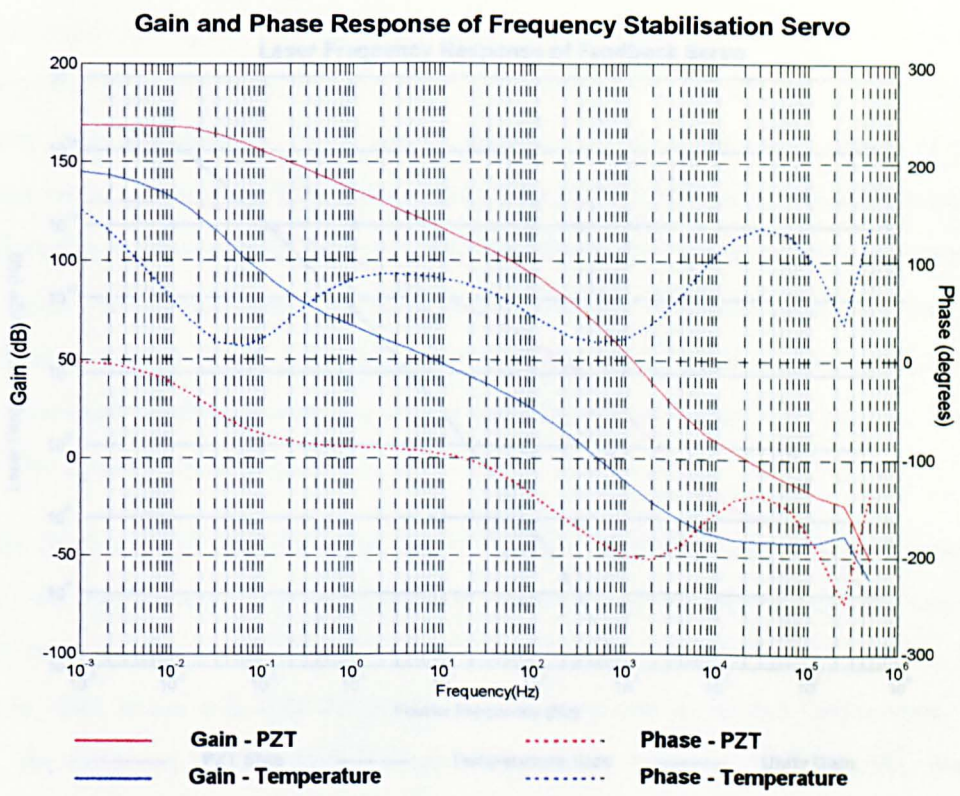
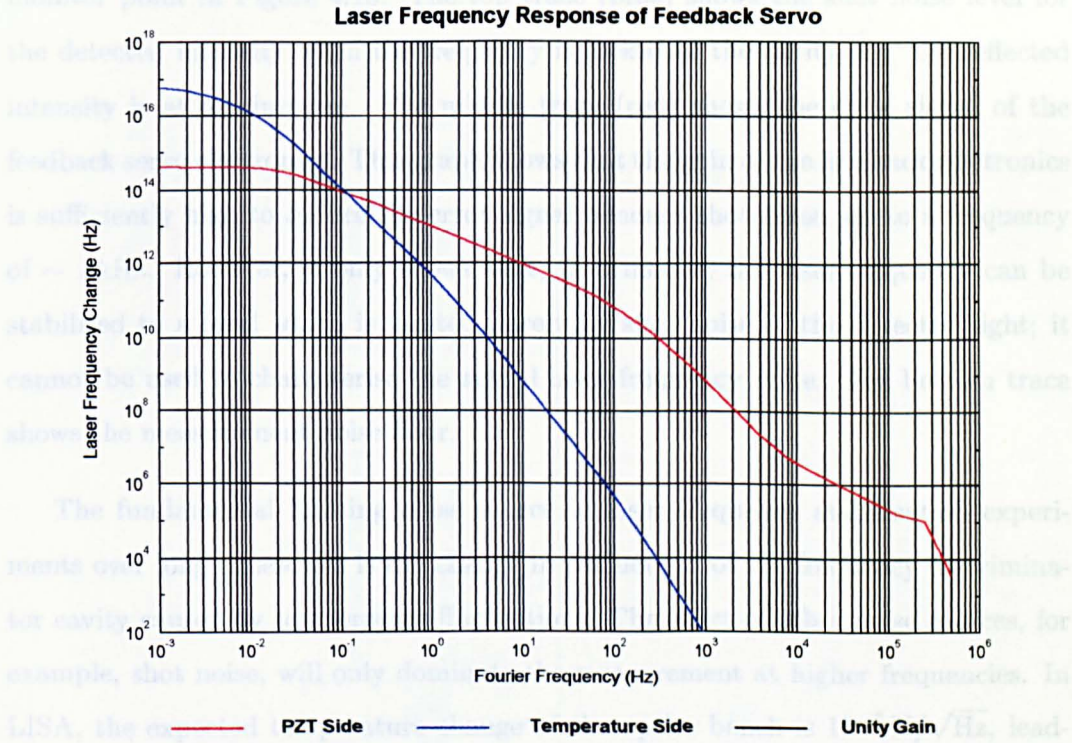


Figure 4.14: Gain and phase response of the laser frequency stabilisation servo - HIGH gain state

measured on a spectrum analyzer, then any drift in the DC level would appear as frequency noise in the data. By taking a differential measurement, the data recorded is insensitive to drifts at the DC adjustment level.

## 4.5 Results

Figure 4.15 shows a graph of the uncalibrated, in-loop error signal, measured at the monitor point in Figure 4.14. The graph shows the error level for the data



**Figure 4.15: Transfer function of feedback electronics including laser frequency actuators.**

...ing to a limit to the laser frequency stabilization by the onboard reference cavity of ... but requires a great deal of care in the design of the cavity environment, involving both active and passive thermal isolation. In this experiment, the cavities are not temperature stabilized. Thermal isolation is provided by passive thermal shielding around both the reference and analyzer cavities, which are then placed inside an evacuated chamber to reduce thermal conduction, and acoustic noise. Figure 4.19 shows the temperature spectrum of the reference cavities.

The left hand axis shows the temperature change, and on the right hand axis, the scale has been calibrated in terms of the limit imposed by the temperature fluctua-

measured on a spectrum analyser, then any drift in the DC level would appear as frequency noise on the laser. By taking a differential measurement, the data recorded is insensitive to drifts in the DC adjustment level.

## 4.5 Results

Figure 4.18 shows a graph of the uncalibrated, in-loop error signal, measured at the monitor point in Figure 4.13. The top trace (blue) shows the shot noise level for the detected intensity when the frequency is locked to the cavity, *i.e.* the reflected intensity is at a minimum. The middle trace (red) shows the error signal of the feedback servo electronics. This graph shows that the gain of the feedback electronics is sufficiently high to reduce the error signal beneath shot noise, up to a frequency of  $\sim 1$  kHz. However, it only shows that, in principle, the laser frequency can be stabilised to a level which is limited purely by shot noise of the detected light; it cannot be used to characterise the actual laser frequency noise. The bottom trace shows the measurement noise floor.

The fundamental limiting noise source in laser frequency stabilisation experiments over long timescales is the change in pathlength of the frequency discriminator cavity caused by temperature fluctuations. The effect of other noise sources, for example, shot noise, will only dominate the measurement at higher frequencies. In LISA, the expected temperature change of the optics bench is  $10^{-6}$  K/ $\sqrt{\text{Hz}}$ , leading to a limit to the laser frequency stabilisation by the onboard reference cavity of  $10$  Hz/ $\sqrt{\text{Hz}}$ . This level of temperature stability may be possible to reach in an Earth based laboratory[39], but requires a great deal of care in the design of the cavity environment, involving both active and passive thermal isolation. In this experiment, the cavities are not temperature stabilised. Thermal isolation is provided by passive thermal shielding around both the reference and analyser cavities, which are then placed inside an evacuated chamber to reduce thermal conduction, and acoustic noise. Figure 4.19 shows the temperature spectrum of the reference cavities.

The left hand axis shows the temperature change, and on the right hand axis, the scale has been calibrated in terms of the limit imposed by the temperature fluctua-

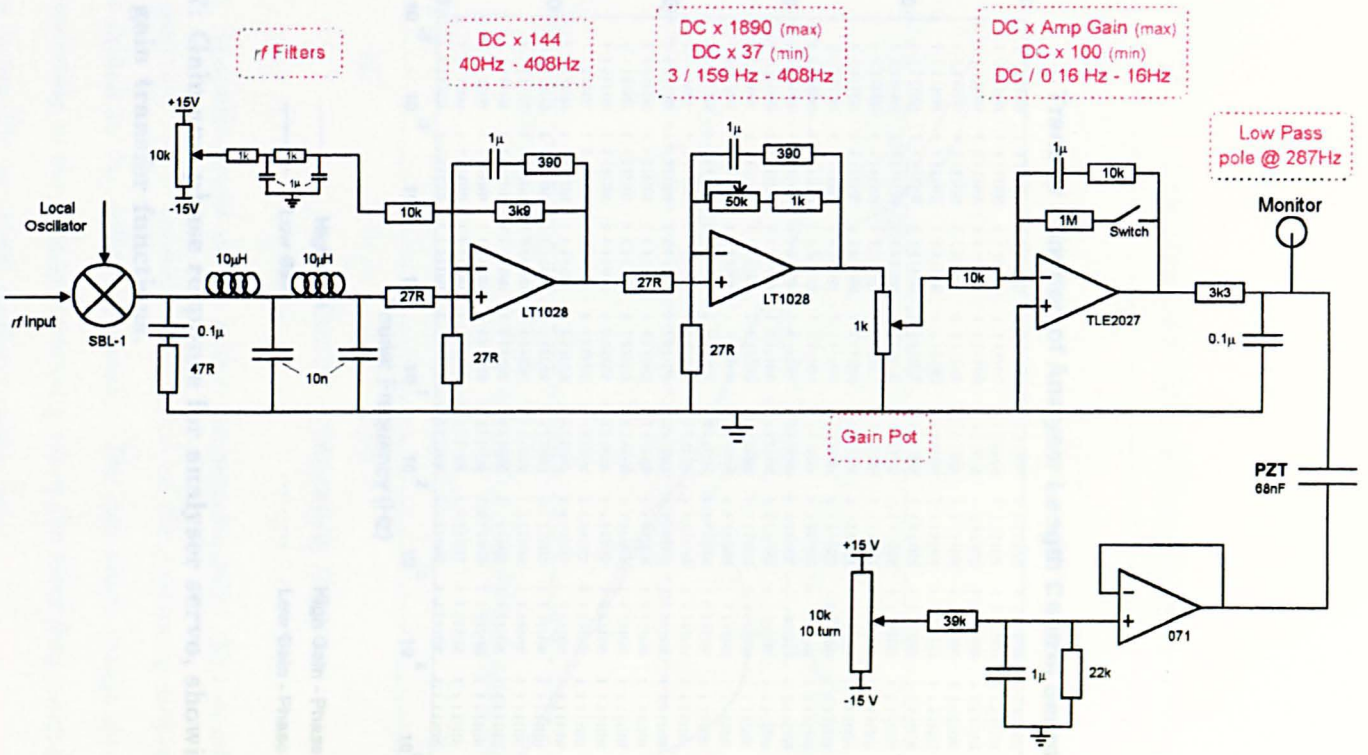


Figure 4.16: Feedback circuit to lock analyser cavity length to laser frequency.

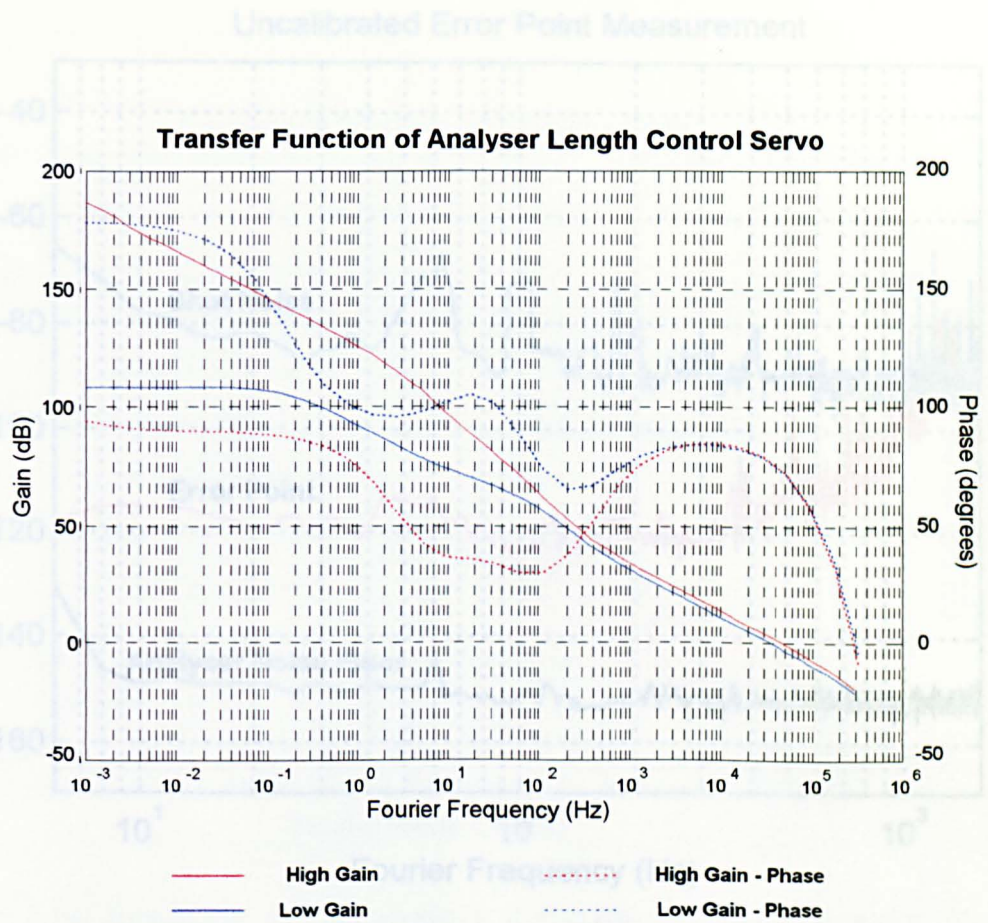


Figure 4.17: Gain and phase response for analyser servo, showing both low and high gain transfer functions.

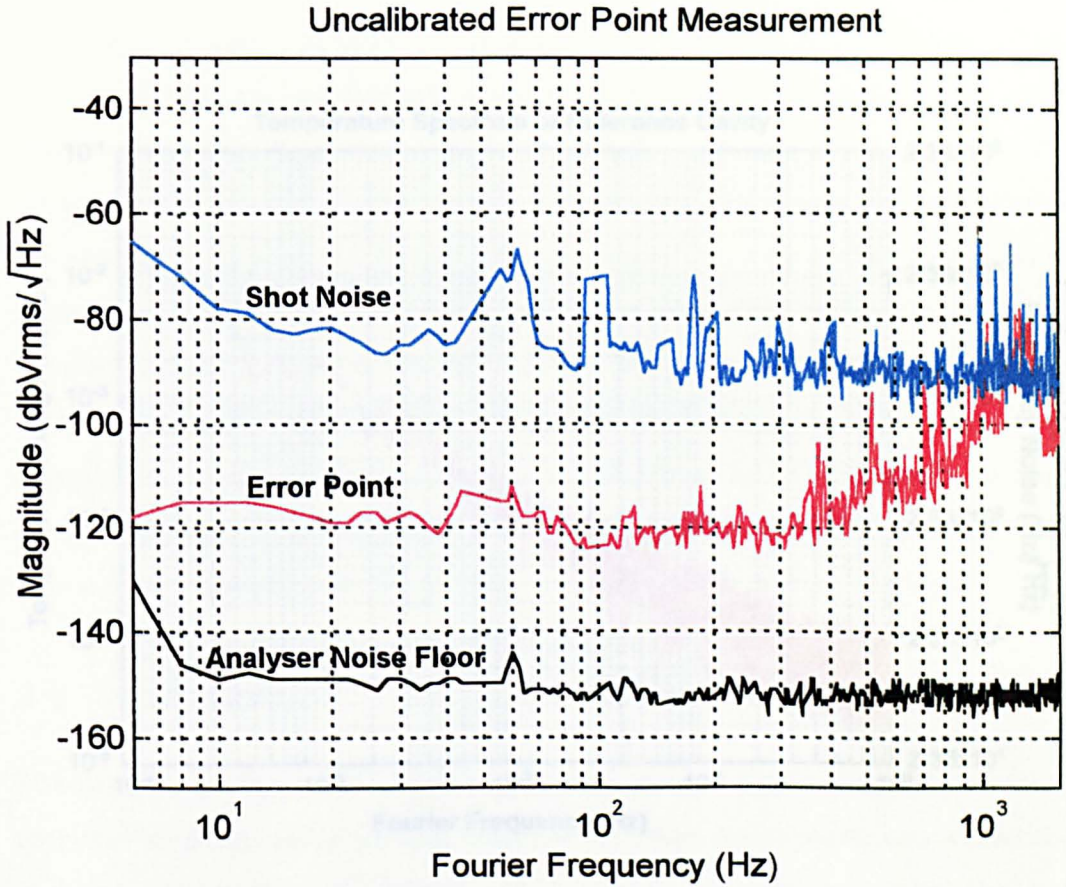


Figure 4.18: Spectrum of in-loop error signal measured inside the

Figure 4.18: **Uncalibrated error point measurement.** The middle trace (red) shows the spectrum of the in-loop error signal of the frequency locking servo when the laser is locked to the reference cavity. The top trace shows the level of shot noise corresponding to the detected intensity when the laser frequency is locked. The bottom trace shows the spectrum analyser noise floor.

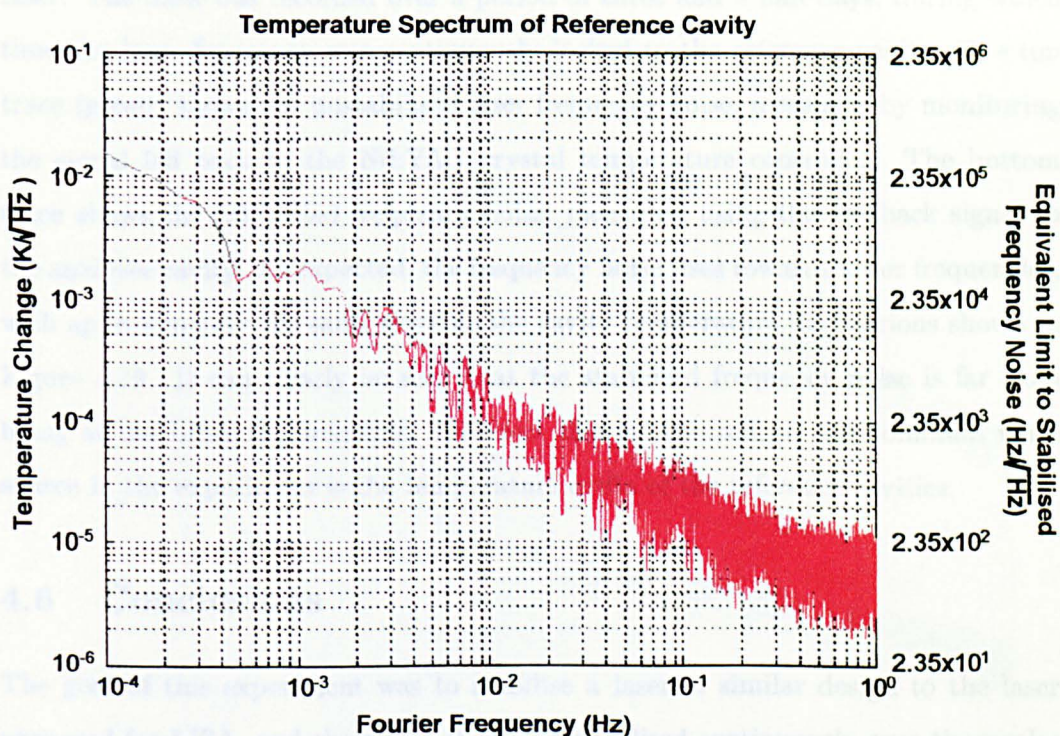


Figure 4.19: **Spectrum of temperature fluctuations measured inside the reference cavity vacuum tank.** The right hand axis shows the equivalent limit to laser frequency noise due to these temperature fluctuations, assuming a thermal expansion coefficient for Zerodur of  $\alpha = 2 \times 10^{-8} / K$ .

tions on the laser frequency stability. As can be seen, it is impossible to stabilise the laser to the LISA requirement in a laboratory with such high temperature variation.

As LISA can only detect gravitational waves in the sub-Hertz regime, the main aim of this experiment is to minimise the laser frequency noise at these spectral frequencies. Figure 4.20 shows the independently measured frequency noise of the laser. The data was recorded over a period of three and a half days, during which time the laser frequency was continuously locked to the reference cavity. The top trace (green) shows the unstabilised laser frequency noise, measured by monitoring the signal fed back to the Nd:YAG crystal temperature controller. The bottom trace shows the calibrated frequency noise, measured using the feedback signal to the analyser cavity. As expected, the frequency noise rises towards lower frequencies, with approximately the same slope as the cavity temperature fluctuations shown in Figure 4.19. It can clearly be seen that the stabilised frequency noise is far from being at the LISA requirements. However, this is expected, as the dominant noise source in the experiment is the temperature drifts of the reference cavities.

## 4.6 Conclusions

The goal of this experiment was to stabilise a laser of similar design to the laser proposed for LISA, and show that it can be stabilised continuously over timescales of days, at the levels required for the LISA mission. As mentioned above, the laser can be locked to the reference cavity indefinitely. The only reason for breaking the lock, is to allow the data to be analysed.

The second of the goals has not been achieved. The temperature variations inside the vacuum tank are too large to allow the laser to reach the performance needed for LISA. However, the slope of the laser frequency noise matches that of the temperature fluctuations, indicating that the dominant noise source is indeed caused by the pathlength change of the reference cavity. By extrapolation to the LISA case, where the optics bench is in an extremely stable temperature environment, it should be possible to actively stabilise the laser frequency to the required level.

### Independent Measure of Frequency Noise of Master Laser

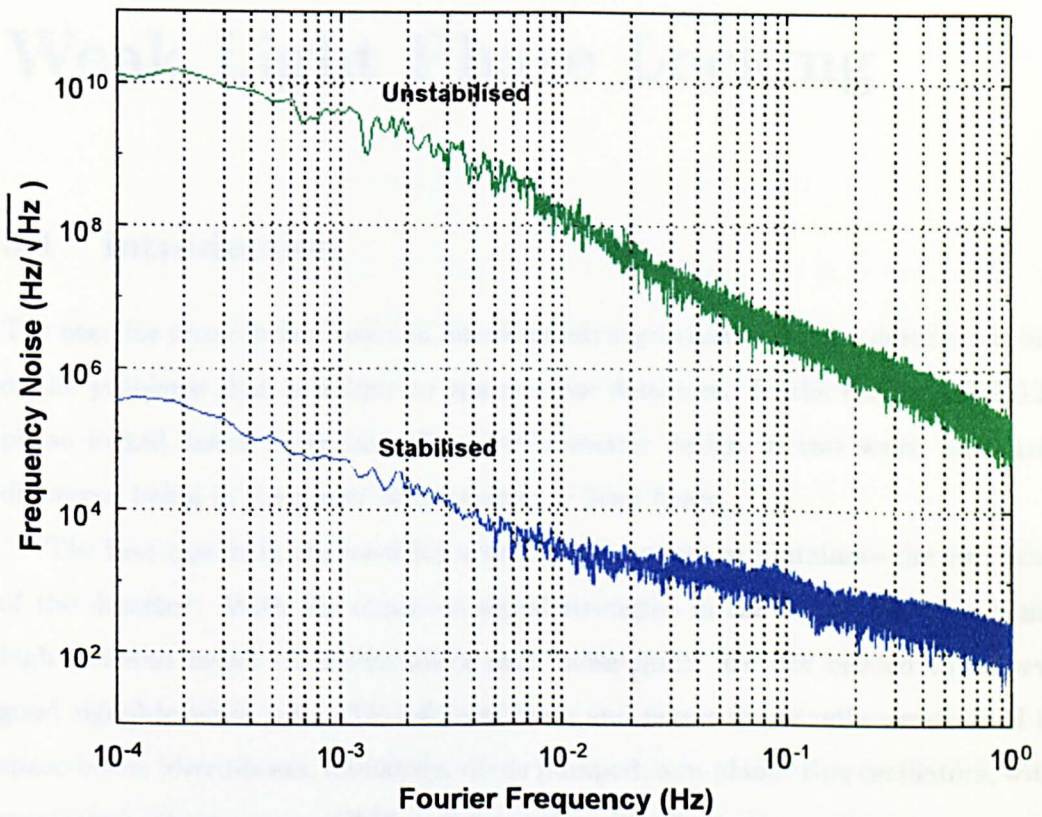


Figure 4.20: **Frequency Noise of Master Laser.** The top trace shows the noise spectrum of the free running laser, and the bottom trace shows the apparent frequency noise of the stabilised laser measured by the analyser cavity.

## Chapter 5

# Weak Light Phase Locking

### 5.1 Introduction

The need for phase locked lasers in interferometric gravitational wave detectors is one of the problems that is unique to space-borne detectors. In the case of LISA[12], phase locked lasers enter into the interferometric design in two ways; the main difference being in the power of the reference laser beam.

The first case is in the need for a single light source to illuminate the two arms of the detector. With the expected signal strengths in the LISA detection band, high powered lasers (therefore lower shot noise limit) are not needed to achieve good signal-to-noise ratio. Therefore as mass and power are heavily constrained in space-borne instruments, miniature, diode pumped, non-planar ring oscillators, with maximum output power of 2 W, will be used to illuminate the arms.

At the master optics bench, the laser will be frequency stabilised to a rigid reference cavity, with a small amount of the stabilised light being fibre coupled to the neighbouring optics bench. This light is used to offset phase lock the laser of arm two (Figure 3.6). The two output beams from this spacecraft (s/c) now appear to have originated from one light source, with the frequency of one beam shifted with respect to the other.

The second case for phase locking is more important, as it is essential for any interferometer design involving such long armlengths. This involves phase locking a

local laser to the weak incoming light received from the opposite end of the  $5 \times 10^9$  m interferometer arm. In ground based Michelson interferometers, the light at the far end of an arm is simply reflected back; in the case of LISA, the extremely long armlength would make simple reflection grossly inefficient.

Each laser in the system will be run with an output power of  $\sim 1$  W. After passing through the optics chain (where the total optical loss in the transmitted light is  $\sim 50\%$ ) each spacecraft (s/c) transmits  $\sim 500$  mW of light ( $\lambda = 1064$  nm) through a 30 cm aperture telescope. The beam then traverses the  $5 \times 10^9$  m arm, with a half angle divergence of

$$\theta = \frac{\lambda}{\pi \omega_o} = 2.53 \times 10^{-6} \text{ rads} \quad (5.1)$$

Even with this extremely well collimated beam, by the time the light reaches the far s/c, the beam diameter has increased from 30 cm to  $\sim 25$  km! The telescope at the far s/c only intercepts  $1.4 \times 10^{-10}$  of the emitted beam, or an intensity of  $\sim 70$  pW. If this light was to be simply reflected off a highly reflecting mirror, the detected signal back at the original spacecraft would be completely swamped by photon counting noise. For this reason, the received light at the end of the arm must be amplified **before** being transponded back to the originating s/c. This is achieved by phase locking the local laser at the far s/c to the received beam, and transponding the phase locked, higher power light back along the arm. This scheme can be thought of as acting as an “**amplifying mirror**” at the end of the interferometer arm.

This chapter will discuss the development of experimental techniques to simulate the “amplifying mirror” at a receiving s/c in LISA. The experimental arrangement is also applicable to the vertex s/c - the only major difference being in the intensity of the light being used as the phase locking reference.

## 5.2 Calculation of the Shot Noise Limit

The phase locking of two lasers works using the same principle as a second order phase-locked-loop [55]. Figure 5.1 shows a block diagram of a simple loop. The phase detector senses the phase difference between two signals: the beat frequency

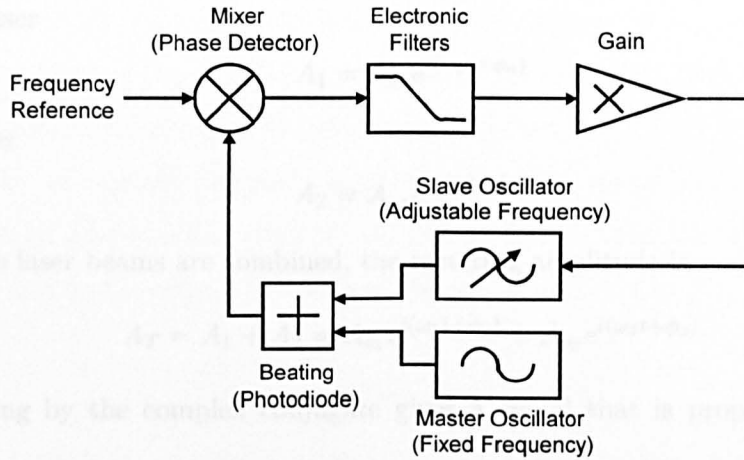


Figure 5.1: **Block diagram of a second order phase-locked-loop to offset phase lock two independent oscillators.**

between the lasers, and an offset frequency reference. The servo electronics then drive the phase difference between the signals to be  $90^\circ$ .

The goal of all experiments of this type is to reach a level of relative phase noise that is limited purely by the shot noise in the detected signal. This noise source can be thought of as entering the system in one of two ways; arising from the quantum mechanical fluctuations in the arrival rates of photons at the photodetector, or arising from the random generation and flow of mobile charge carriers in the photocurrent.

As the shot noise depends on the arrival rates of photons, it is easy to see that if the power is decreased, then the number of photons is also decreased, and hence the statistical fluctuations in the arrival rates increases. This leads to an increase in the shot noise limit of the measurement. In these experiments, the power of the master laser at the locking diode is many orders of magnitude lower than the slave laser, hence the shot noise limit imposed by the master light dominates the measurement. For simplicity, the following derivation will be given for the case of no phase modulation on either laser. Consider two laser sources of the form:

Master laser

$$A_1 = A_{o1} e^{i(\omega_1 t + \phi_o)} \quad (5.2)$$

Slave laser

$$A_2 = A_{o2} e^{i(\omega_2 t + \phi_2)} \quad (5.3)$$

When the laser beams are combined, the resulting amplitude is

$$A_T = A_1 + A_2 = A_{o1} e^{i(\omega_1 t + \phi_1)} + A_{o2} e^{i(\omega_2 t + \phi_2)} \quad (5.4)$$

Multiplying by the complex conjugate gives a signal that is proportional to the intensity:

$$I_{int} \propto A_T \cdot A_T^* = A_{o1}^2 + A_{o2}^2 + 2A_{o1} A_{o2} \cos[(\omega_1 - \omega_2)t + (\phi_1 - \phi_2)] \quad (5.5)$$

Offset phase locking the lasers leads to a simpler expression for the intensity, as the phase difference between the lasers is fixed at  $90^\circ$ , and the frequency difference is fixed at the offset frequency. The detected intensity becomes:

$$I_{lock} \propto A_{o1}^2 + A_{o2}^2 + 2A_{o1} A_{o2} \sin(\omega_{off} t) \quad (5.6)$$

where  $\omega_{off}$  is the offset frequency.

The intensity signal is composed of two components, one at DC, and the other at the offset frequency. The DC term may be written as

$$I_{DC} \propto I_{o1} + I_{o2} \quad (5.7)$$

which in terms of photocurrent becomes

$$i_{DC} \propto i_{o1} + i_{o2} \quad (5.8)$$

where  $I$  is the laser intensity, and  $i$  denotes the photocurrent. In terms of photocurrent, the peak value of the  $rf$  term of Equation 5.6 may be written

$$i_{off} \propto 2\sqrt{i_1 i_2} \quad (5.9)$$

The shot noise limit can now be estimated. The shot noise is dominated by the DC term (Equation 5.8) and can be written (using the standard shot noise formula) as

$$\delta i = \sqrt{2ei \delta f} = \sqrt{2e(i_1 + i_2) \delta f} \cdot \sqrt{2} \quad (5.10)$$

where  $i_{1/2}$  are the photocurrents associated with intensities  $I_{1/2}$  respectively, and the  $\sqrt{2}$  has been added as there are two sidebands of white (shot) noise at a given spectral frequency away from the reference frequency.

In order to convert this limit to phase noise as opposed to current noise, the calibration of Amps/radian must be calculated. This is contained in the  $rf$  term of Equation 5.6, and is simply the slope of the sine function, *i.e.*

$$\left. \frac{\delta i}{\delta \phi} \right|_0 = \left. \frac{\delta}{\delta \phi} [2\sqrt{i_1 i_2} \sin \phi] \right|_0 = 2\sqrt{i_1 i_2} \quad (5.11)$$

Therefore, the shot noise limit to the relative phase stability of the slave laser is given as

$$\frac{\delta \phi}{\delta i} \cdot \delta i = \sqrt{\frac{4e(i_1 + i_2)\delta f}{4i_1 i_2}} \quad (5.12)$$

*i.e.*

$$\widetilde{\delta \phi} = \sqrt{e \left[ \frac{1}{i_2} + \frac{1}{i_1} \right]} \approx \sqrt{\frac{e}{i_1}} \quad \text{rads}/\sqrt{\text{Hz}} \quad (5.13)$$

for  $i_1 \ll i_2$

where  $\delta \phi$  has been divided by  $\sqrt{\delta f}$  to give the linear spectral density,  $\widetilde{\delta \phi}$ . As expected, the shot noise limit to the relative phase stability of the slave laser is dominated by the photocurrent due to the master laser. For LISA, where the detected power is  $\sim 70$  pW, the relative phase noise of the slave laser will be shot noise limited at  $6.5 \times 10^{-5}$  rads/ $\sqrt{\text{Hz}}$ [12].

### 5.3 Capture and Lock of a Phase-Locked-Loop

The output of the detection photodiode and pre-amp is capacitively coupled to a mixer for down-conversion with the frequency reference, producing the error signal for the feedback electronics.

When the frequency difference between the lasers is equal to the reference, the output of the mixer provides a DC level, which goes to zero when the phase of the beat note leads or lags the reference by  $90^\circ$  (in quadrature). Figure 5.2 shows a typical calibration curve of a mixer, with the frequency of the two inputs held constant, but the phase difference swept through  $180^\circ$ . As can be seen, the transfer

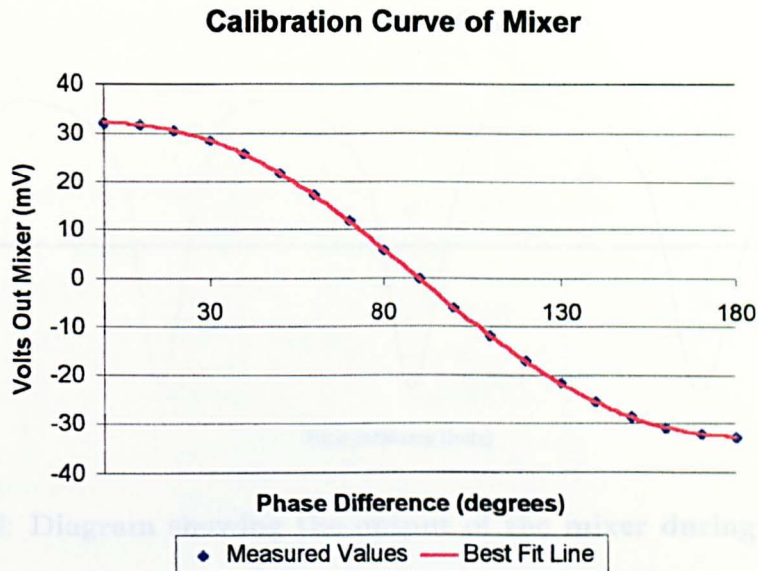


Figure 5.2: **Calibration curve for mixer.** *This graph shows a typical mixer response for the two input frequencies being equal, with the phase difference between them swept through 180°.*

function is bi-polar, and hence provides a good error signal for the feedback electronic servo system.

However, the above transfer function only occurs when the two inputs are at the same frequency. In practice, before lock is acquired, the frequency of the lasers will not differ by exactly the reference frequency. So, how does the feedback servo pull the beat note and reference frequencies together, *i.e.* how does the system acquire lock?

When the beat frequency is not equal to the reference frequency, the output of the mixer comprises two components: the difference and sum frequencies between the beat and offset. The latter signal is not needed, and indeed may hinder the functionality of the feedback electronics. For this reason, the output signal is heavily filtered to remove the higher frequency component. When the difference frequency is within the capture range of the phase-locked-loop, determined by the bandwidth of the servo, the capture transient goes as follows (assuming the feedback loop is closed)[55]:

The filtered mixer output is a periodic signal with non-zero average, which is fed

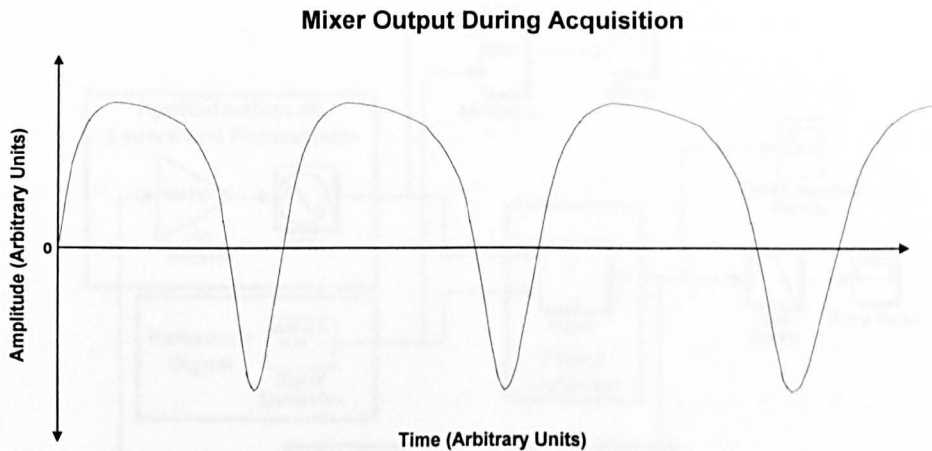


Figure 5.3: **Diagram showing the output of the mixer during acquisition.** *The non-symmetric nature of the output produces a non-zero average level, which pulls the beat note between the lasers towards the offset frequency.*

back to the slave laser. This has the effect of either pulling the beat note towards the reference, thereby lowering the frequency of the output of the mixer, or pushing the beat note frequency away from the reference, increasing the output frequency of the mixer.

As the input to the mixer is changed, the output becomes asymmetrical (Figure 5.3). During the first half cycle of Figure 5.3, the laser is pulling the beat note towards the reference, and hence the output shifts to a lower frequency. The feedback therefore spends longer than half the original period pulling the slave laser frequency in the correct direction. In the second half of the cycle, the sign of feedback is wrong, and the beat note is pushed away from the reference. This time the feedback spends shorter than half the original period pushing the inputs apart. Therefore, over one period of oscillation of the mixer output, the net shift in frequency is towards lower frequencies, *i.e.* pulling the beat note towards the offset frequency. This continues until the mixer can directly measure the phase difference between the inputs, and the error signal becomes a true bi-polar signal.

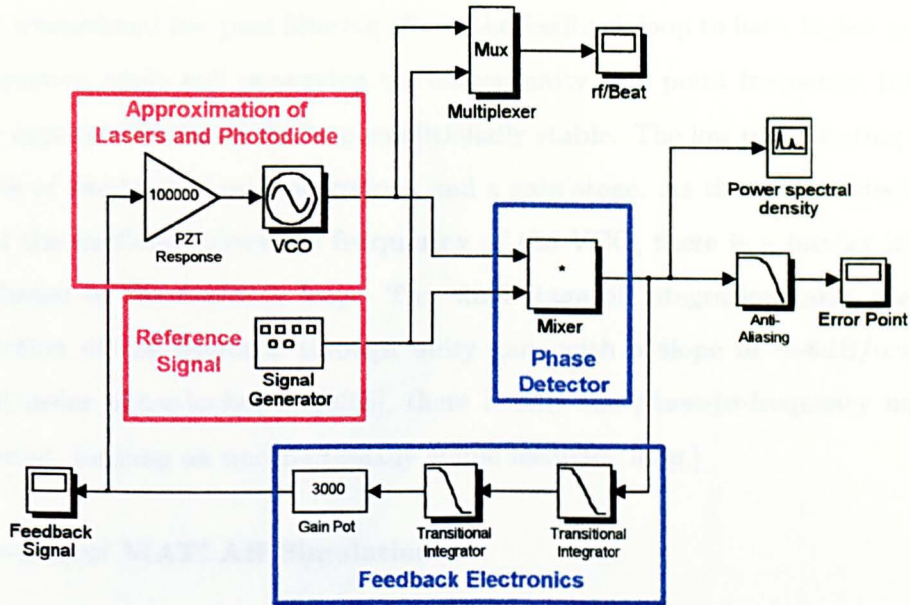


Figure 5.4: **Simulink Model of Phase-Locked-Loop.** *This simulation approximates the two lasers and photodiode as a single voltage controlled oscillator, producing the beat note at the input of the phase detector.*

### 5.3.1 MATLAB Simulation of a Phase-Locked-Loop

In order to check the validity of the above method for acquiring lock, a simulation was carried out using MATLAB Simulink [56]. This allows all relevant signals to be monitored as the beat note frequency approaches that of the reference. Figure 5.4 shows the block diagram of the model used for the simulation.

To simplify the model, the two lasers along with the detection photodiode have been combined into one unit. This unit contains a gain stage along with a Voltage Controlled Oscillator (VCO). In the real case, the feedback signal is used to drive the frequency of the slave laser, which in turn changes the beat frequency at the input of the mixer. In the simulation, the feedback drives the VCO, thereby changing the frequency at the input of the mixer. The rest of the model is similar to that of an actual experimental system. The output of the VCO is down-converted by the reference frequency at the mixer, the output of which is low pass filtered (as is the case in a second order phase-locked-loop[55]), and fed back to the VCO. The effect of

the transitional low-pass filtering allows the feedback loop to have higher gain at low frequency, while still preserving the chosen unity gain point frequency, however, at the expense of making the loop conditionally stable. The low pass filtering takes the form of two transitional integrators, and a gain stage. As the mixer detects **phase**, and the feedback drives the **frequency** of the VCO, there is a further integration included in the feedback loop. This final stage of integration takes the transfer function of the feedback through unity gain with a slope of  $\sim -6\text{dB/octave}$ . [In first order phase-locked-loops[55], there is only the phase-to-frequency integration present, forming an unconditionally stable feedback loop.]

### Results of MATLAB Simulation

Figure 5.5 shows the evolution of the error signal (output of mixer) and feedback signal against time as the phase-locked-loop acquires lock. When the loop is closed, the error signal sits symmetrically about zero volts, with a short period of oscillation. As time progresses, the period of oscillation slowly decreases, and the average “DC” level rises. Once the beat frequency between the lasers is equal to the reference frequency, the “AC” component of the error signal becomes much smaller, as the only signals present are the signal at twice the reference frequency superimposed on a pure DC term. The shape of the transfer function of the mixer is now as shown in Figure 5.2. The phase difference between the inputs is driven to  $90^\circ$ , *i.e.* when the error signal is symmetrically about zero volts.

The lower trace in Figure 5.5 shows the feedback signal to the VCO. The rate of change of the DC level of this trace gives an indication of how quickly the VCO is being pulled towards the reference. As expected, as the two inputs approach the same frequency, the VCO is driven faster, since the feedback loop has higher gain at the lower frequencies. Once the two inputs to the mixer are at a common frequency, the feedback signal becomes almost flat.

**TIME EVOLUTION OF ERROR AND FEEDBACK SIGNAL DURING ACQUISITION**

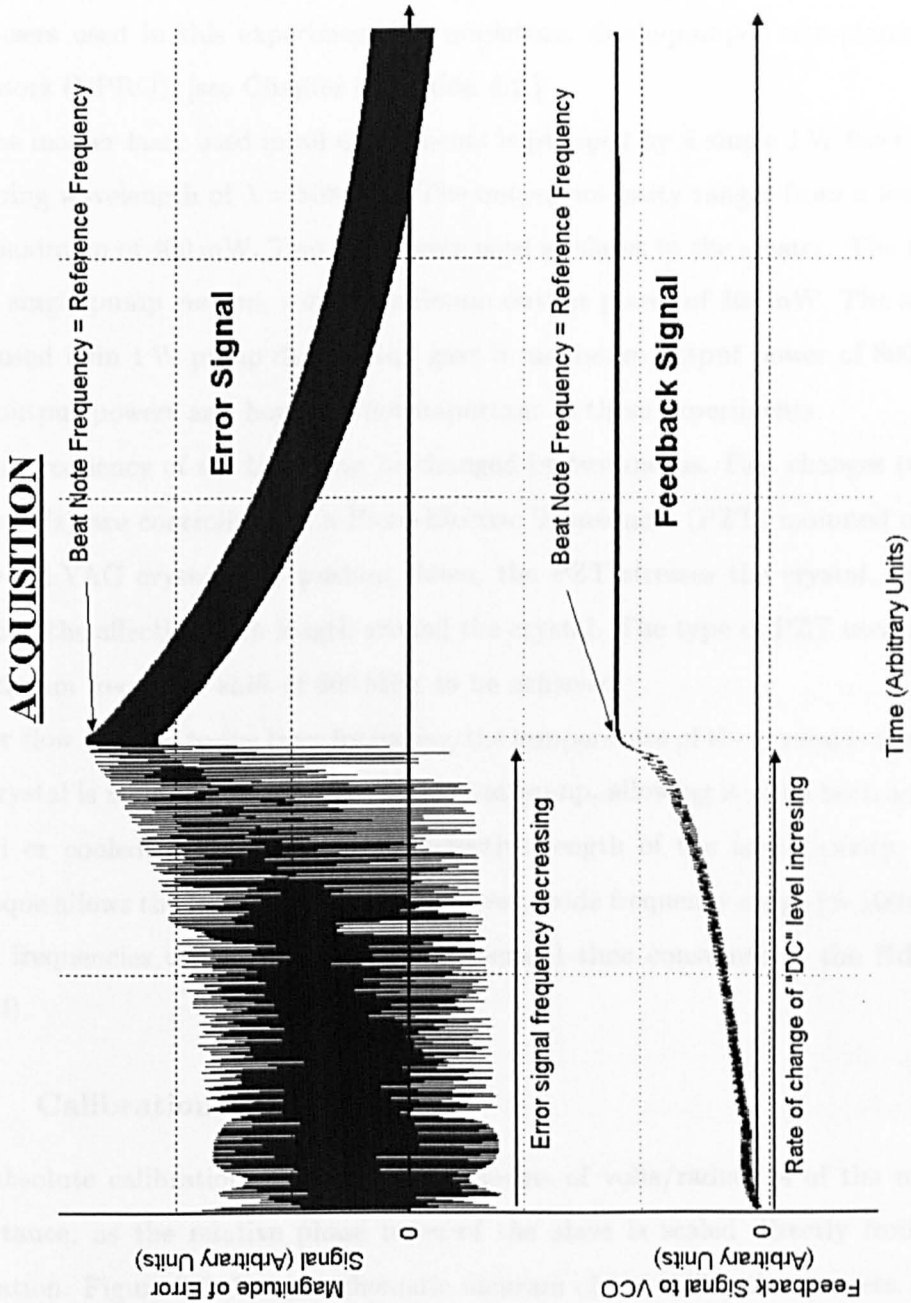


Figure 5.5: **Time Evolution of Error and Feedback Signal.** *The top graph shows the time evolution of the error signal as the system acquires lock. The bottom trace shows the evolution of the feedback signal. Once the signals are at a common frequency, the feedback becomes almost constant, as the phase of the VCO is pulled to 90° away from the reference.*

## 5.4 Experimental Arrangement

The lasers used in this experiment are miniature, diode-pumped non-planar ring oscillators (NPRO). [see Chapter 4, Section 4.2.]

The master laser used in all experiments is pumped by a single 1 W laser diode (pumping wavelength of  $\lambda = 808$  nm). The output intensity ranges from a few mW to a maximum of 400 mW. Two lasers were used as slaves to the master. The first is also a single pump version, with a maximum output power of 300 mW. The second slave used twin 1 W pump diodes, and gave a maximum output power of 800 mW. High output powers are, however, not important in these experiments.

The frequency of the lasers can be changed by two means. Fast changes (0.1 Hz to few kHz) are controlled via a Piezo-Electric Transducer (PZT) mounted on top of the Nd:YAG crystal. By pushing down, the PZT stresses the crystal, thereby changing the effective path length around the crystal. The type of PZT used allows a maximum frequency shift of 600 MHz to be achieved.

For slow changes to the laser frequency, the temperature of the crystal is changed. The crystal is mounted on a Peltier Effect heat pump, allowing it to be both actively heated or cooled, again changing the effective length of the lasing cavity. This technique allows the laser to be tuned over a very wide frequency range ( $> 100$  GHz), up to frequencies of  $\sim 1$  Hz (limited by thermal time constants in the Nd:YAG crystal).

### 5.4.1 Calibration of Mixer

The absolute calibration of the mixers in terms of volts/radian is of the utmost importance, as the relative phase noise of the slave is scaled directly from this calibration. Figure 5.6 shows a schematic diagram of the calibration process.

Once the lasers are locked, the size of the signal, directly at the input of the mixer, is measured. The photodiode input is then disconnected, and replaced by a simulated signal of the same amplitude from a signal generator. The signal generator is identical to the one supplying the reference frequency (Hewlett Packard 33120A) and can be phase locked to the reference frequency via an external connection. The

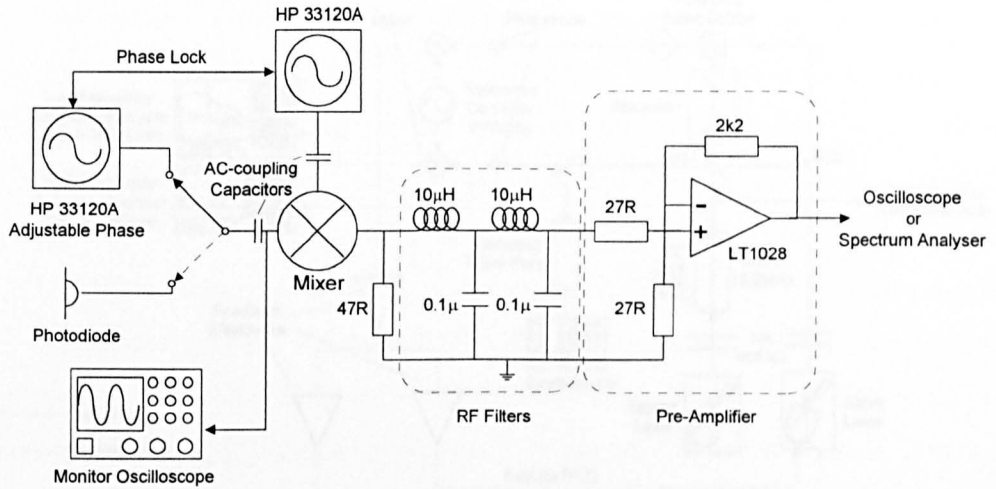


Figure 5.6: Schematic diagram to show the calibration scheme of the locking side mixer

relative phase of the slave generator is adjusted such that the output of the mixer and following amplifier is at zero volts (*i.e.* the inputs are in quadrature). The slave is then offset by  $-90^\circ$  from this point, and swept through  $180^\circ$  giving the full transfer function of the mixer at the fixed signal amplitudes. An example of a transfer function is shown in Figure 5.2.

## 5.5 Initial Optical Layout

Figure 5.7 shows an initial experimental layout to simulate the case of phase locking at a far s/c in LISA. As the polarisation of the laser outputs is not perfect (approximately 4:1, vertical (s-plane) to horizontal (p-plane)), the light from both lasers was made to pass through quarter and half waveplates to maximise the polarisation in the s-plane. The light from the master then passed through an electro-optic modulator (EOM), applying phase modulation sidebands to the carrier (needed for the frequency stabilisation scheme). The light was then split into two paths: one used as the locking path, where the intensity of the master was greatly attenuated, and the other, where the intensity of the master is similar to that of the slave, was used to measure the relative phase noise of the slave with respect to the master. The slave

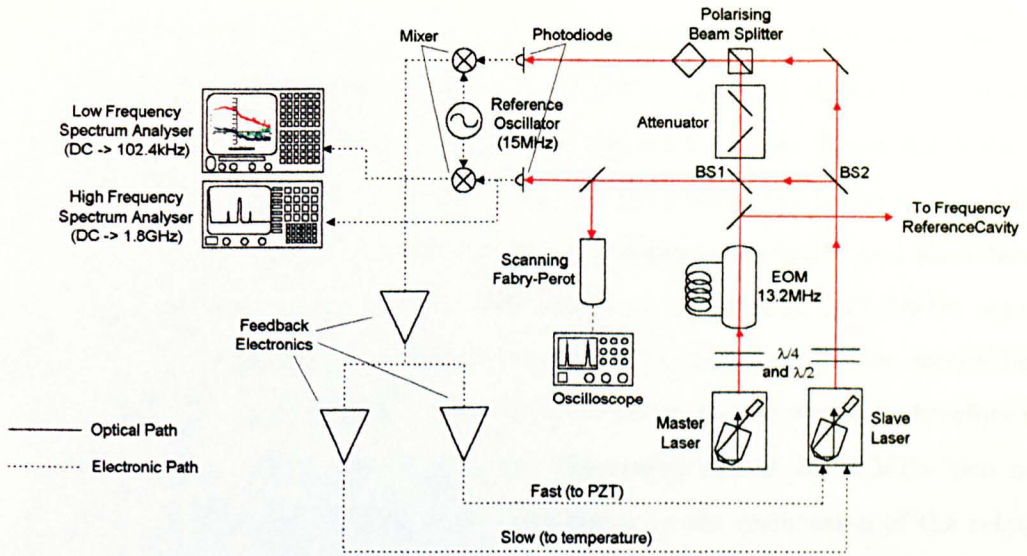


Figure 5.7: Schematic diagram of an initial optical layout to simulate phase locking in a far  $s/c$  of LISA.

laser light was also split into two paths, and combined with the master light, with the splitting approximately 50-50 to each path. The output of the phase detector in the locking path is used to derive the error signal for the feedback electronics, and the signal from the phase detector in the measurement side is sent directly to a spectrum analyser.

Both lasers were mode matched to the photodiodes, to ensure the maximum amount of overlap between the beams. A small fraction of the light in the measurement path was split off and mode matched into a scanning Fabry-Pérot interferometer (Burleigh SA-200-x), the output of which gives an optical spectral analysis of the two laser beams. This was used to aid in the alignment of the beams in the measurement path, and was also used in the initial crude adjustment of the laser frequencies, so that the mixer output frequency was within the capture range of the phase-locked-loop. The output of the measurement photodiode (BPX 65) was split into two paths: one to the phase detector, and was used to measure the relative phase noise of the slave laser, and the other to a high frequency  $rf$  spectrum analyser (Hewlett Packard 8591E). The  $rf$  analyser gave an output similar to the scanning Fabry-Pérot, although the signal measured was the beat note between the lasers, not

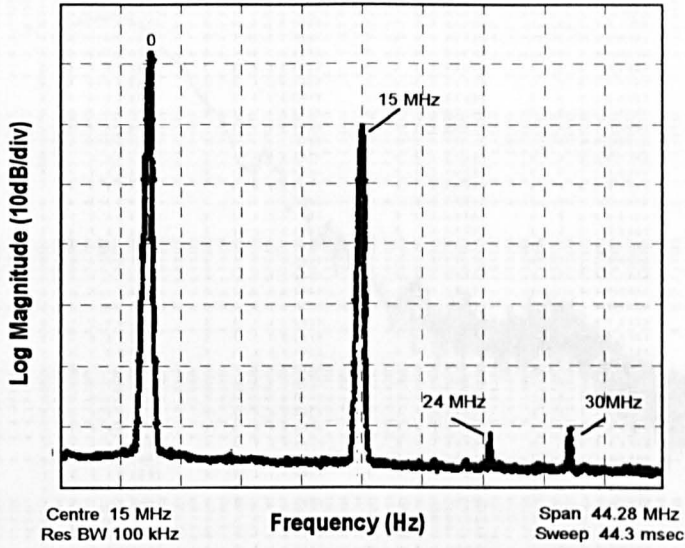
the actual optical frequencies. Figure 5.8 shows traces taken from the *rf* analyser when the lasers are offset phase locked by 15 MHz. Trace (a) shows the case when there is NO phase modulation sidebands on the master laser. Trace (b) is for the case when the master laser is phase modulated (13.2 MHz), as is the case in LISA. The centre peak at 15 MHz is the beat signal between the master and slave lasers, with its first harmonic at 30 MHz. The signals at 1.8 MHz and 28.2 MHz are the beat frequencies between the modulation sidebands, and the 15 MHz carrier beat. The peaks at 13.2 and 24 MHz are due to *rf* electrical interference and therefore not related to the optical frequencies present. The magnitude of the 15 MHz beat note is used in the calibration of the mixer, and hence in the calibration of the relative phase noise measurement (see next section for more details).

The master laser light was attenuated before being combined with the slave. The attenuation was achieved by reflecting the beam off superpolished, high reflecting mirrors, and used the tiny fraction of transmitted light for the phase locking. Each mirror attenuates the beam by  $\sim 3$  orders of magnitude. Before striking the photodiode, the light must first pass through a PBS, at an angle of  $45^\circ$  to the vertical. This was necessary as the electric fields of the two laser beams are orthogonal to each other, and hence the fields will not interfere. The signal from the locking photodiode was sent directly to the locking mixer, the output of the which was used as the error signal for the feedback electronics. The circuit diagram for the locking photodiode and pre-amp is shown in Figure 5.12(a).

### 5.5.1 Results

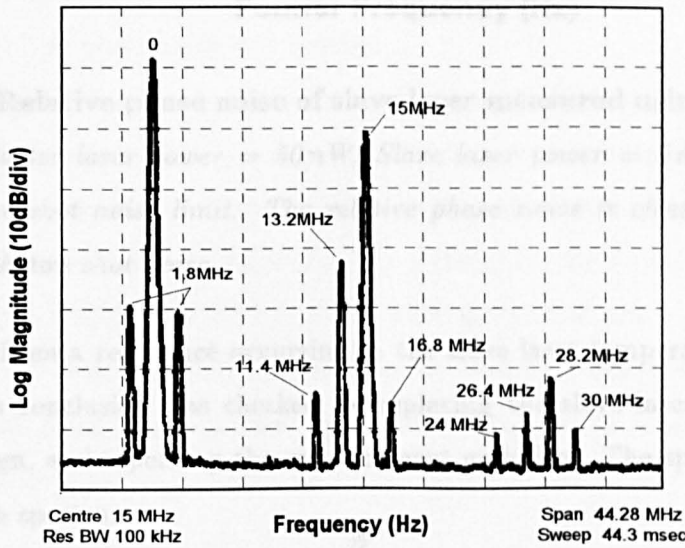
Figure 5.9 shows a graph of the relative phase noise of the slave laser with respect to the master at Fourier frequencies below 1 Hz. This data was taken over a period of 56 hours, during which time the lasers remained locked continuously. The laser powers at the locking photodiode are calculated to be 50 nW (master) and 5 mW (slave), giving a shot noise limit to the measurement of  $2 \times 10^{-6}$  rads/ $\sqrt{\text{Hz}}$  (red line on graph). Clearly the relative phase noise of the slave laser is not stabilised to the shot noise limiting performance. At a frequency of  $\sim 0.78$  Hz, there is a very large, narrow spike of noise. The cause of the spike was investigated, and was found to be

**RF Spectral Analysis of Measurement Side Beat Note -  
Note - NO Phase Modulation on Master Laser**



(a)

**RF Spectral Analysis of Measurement Side Beat Note -  
WITH Phase Modulation on the Master Laser**



(b)

Figure 5.8: RF spectral analysis of measurement photodiode output. Trace (a) shows the case with no phase modulation on the master laser, trace (b) is with phase modulation (13.2 MHz).

**Initial experimental layout:  
relative phase noise of slave laser**

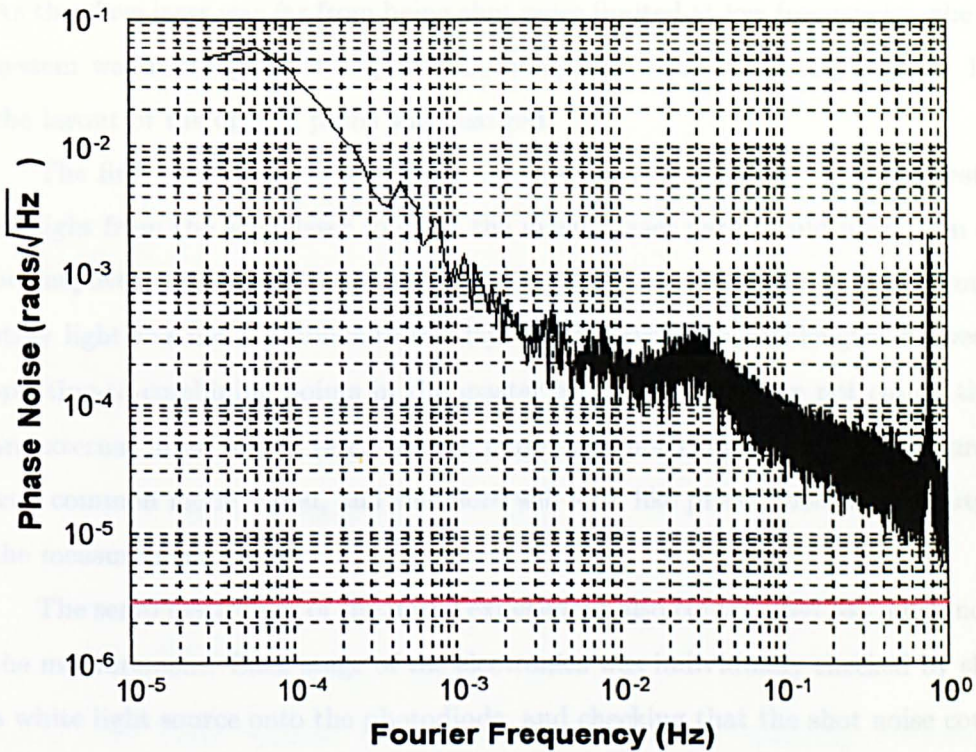


Figure 5.9: **Relative phase noise of slave laser measured using initial optical layout.** Master laser power = 50 nW, Slave laser power = 5 mW. The red line indicates the shot noise limit. The relative phase noise is clearly far from being limited by photon shot noise.

The spike in the spectrum is clearly not limited by photon shot noise, but is originating from a resonance occurring in the slave laser temperature stabilisation servo. This conclusion was checked by replacing the slave laser with another of similar design, and repeating the measurement as before. The spike was no longer found in the spectrum.

The next section deals with improvements made to the system in order reduce the excess noise down to a level at, or close to, the shot noise limit.

## 5.6 Improvements to Optical Layout and Electronics

As the slave laser was far from being shot noise limited at low frequencies, the entire system was re-designed to improve the noise performance in every aspect. Firstly the layout of the optical paths was changed.

The first consideration was stray light in the locking path. The simplest path for light from the slave laser to enter the master laser path would have been at the beamsplitter (labelled BS1 in Figure 5.7). After investigation, it was found that stray light was not a problem in this layout. However, the pathlengths between the splitting-to-combining points in the master and slave paths are not equal, thereby an external noise source (*e.g.* seismic noise) will not couple into the measurement as a common mode signal, and therefore will look like phase noise on the output of the measurement diode.

The servo electronics of the initial experiment also contributed too much noise to the measurement. Each stage of the electronics was individually checked by shining a white light source onto the photodiode, and checking that the shot noise could be seen. Firstly, the photodiode was checked.

White light was shone onto the photodiode, and adjusted until the DC output was the same as when the lasers are unlocked. The intensity of the light was increased by an order of magnitude. If the photodiode is shot noise limited, the capacitively coupled output level should have risen by a factor of the square root of the ratio of the two powers, *i.e.* by  $\sqrt{10} = 3.16$ . This was indeed the case. Therefore the photodiode is taken to be shot noise limited. The feedback electronics were also checked, and found to be limited by excess noise, and so would not be able to stabilise the slave to the desired shot noise limiting level.

The first change to be made was in the optical layout, ensuring that stray light is kept to a minimum, and that coupling of seismic noise is reduced. The final optical design relies on using polarisation techniques to split the lasers into the two paths, and also to attenuate the intensity of the master laser in the locking path. Figure 5.10 shows the new optical layout, and Figure 5.11 shows a more detailed picture of

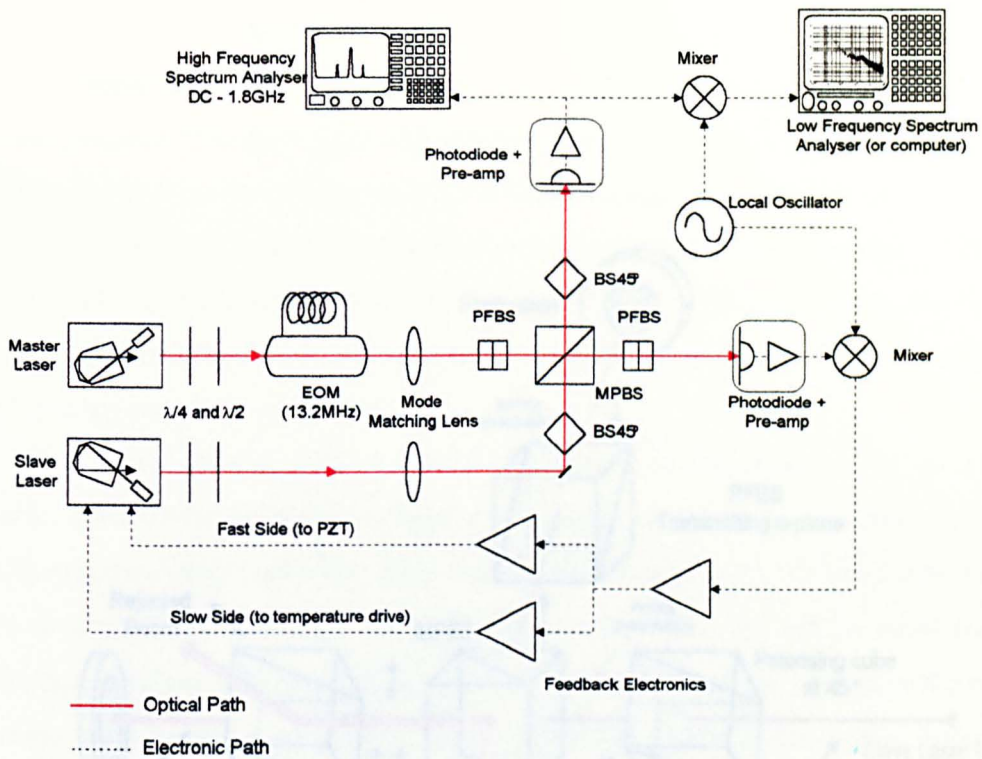


Figure 5.10: **New optical layout using polarisation splitting techniques.** *PFBS - Polarisation Fixing Beam Splitter, MPBS - Main Polarising Beam Splitter, BS45° - Beam Splitter oriented at 45° to the master laser polarisation*

the combining polarising beam splitter with polarisation components shown.

The light from the master is again made to pass through quarter and half waveplates before the electro-optic modulator. The polarisation of the phase modulated light is fixed using a polarising beam splitter (PFBS), giving linear polarisation in the s-plane, before hitting the main polarising beam splitting cube (MPBS).

The polarisation of light from the slave laser is also corrected using waveplates, before being set at 45° using a PBS, oriented at 45° to the s-plane. The slave light then hits the MPBS, at an orthogonal port to the master. The light is now split into the two paths.

The light along the locking path is composed of two components: i) approximately half of the slave laser light, and ii) a tiny fraction of the master light. The master laser light is composed of two orthogonal polarisation components - a small

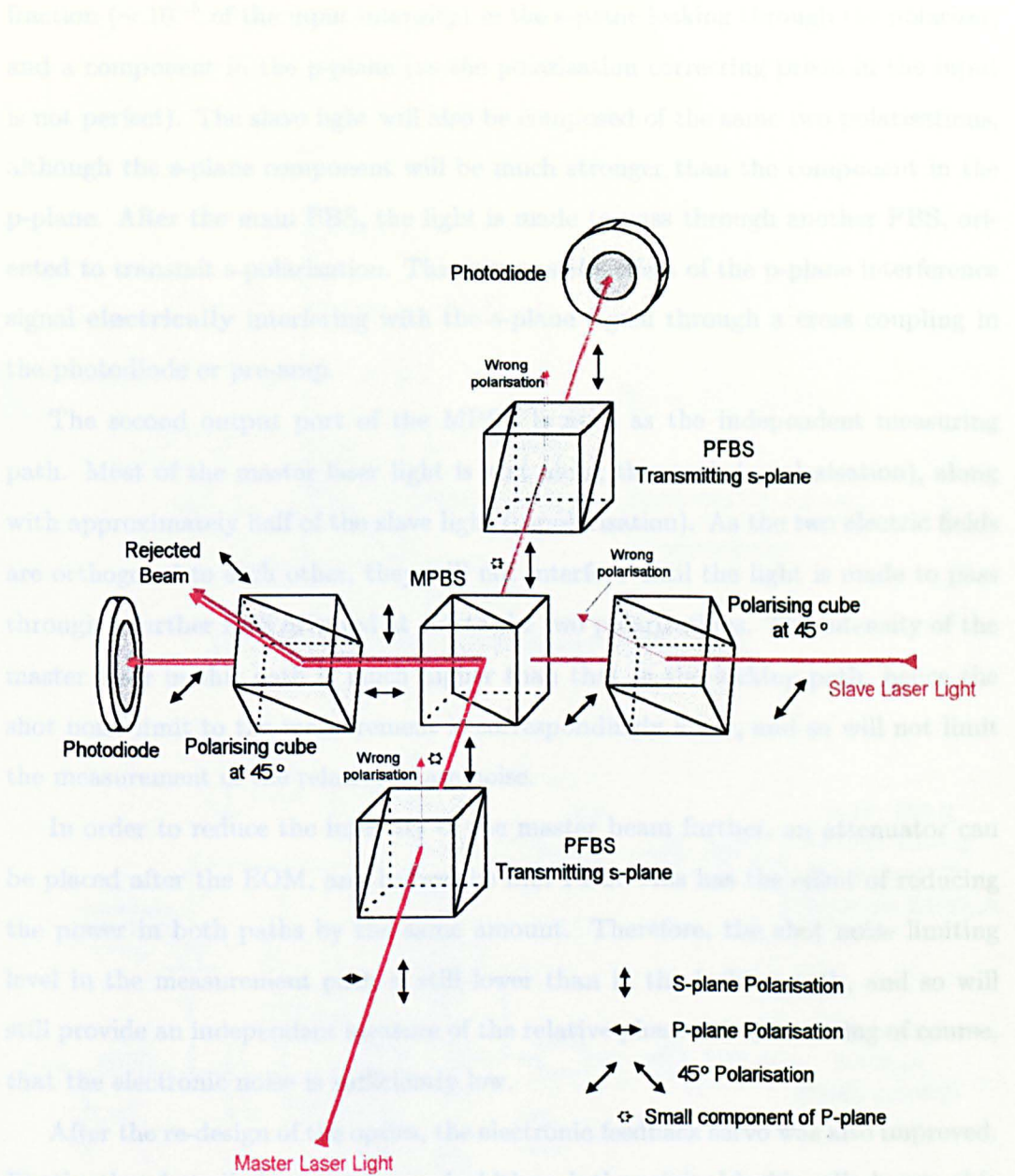


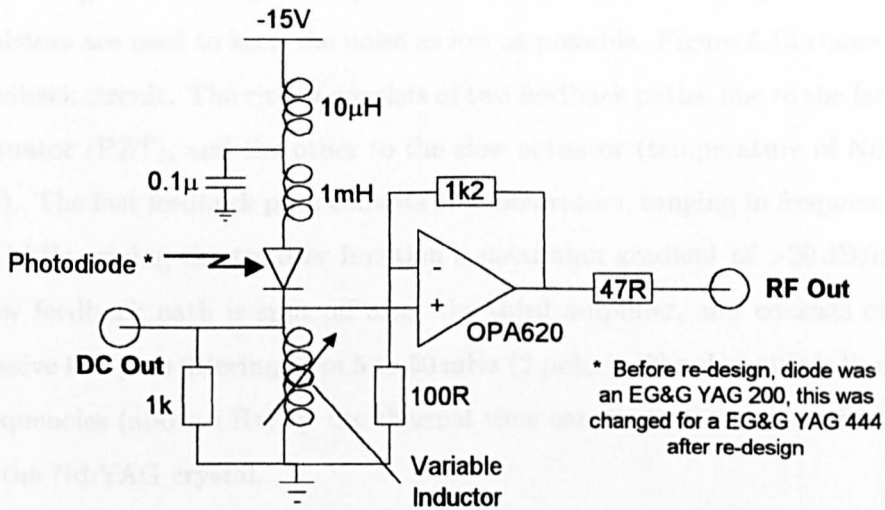
Figure 5.11: Detailed view of Main Polarising Beam Splitter (MPBS), showing polarisation of beams.

fraction ( $\sim 10^{-5}$  of the input intensity) in the s-plane leaking through the polariser, and a component in the p-plane (as the polarisation correcting prism in the input is not perfect). The slave light will also be composed of the same two polarisations, although the s-plane component will be much stronger than the component in the p-plane. After the main PBS, the light is made to pass through another PBS, oriented to transmit s-polarisation. This removes the effect of the p-plane interference signal **electrically** interfering with the s-plane signal through a cross coupling in the photodiode or pre-amp.

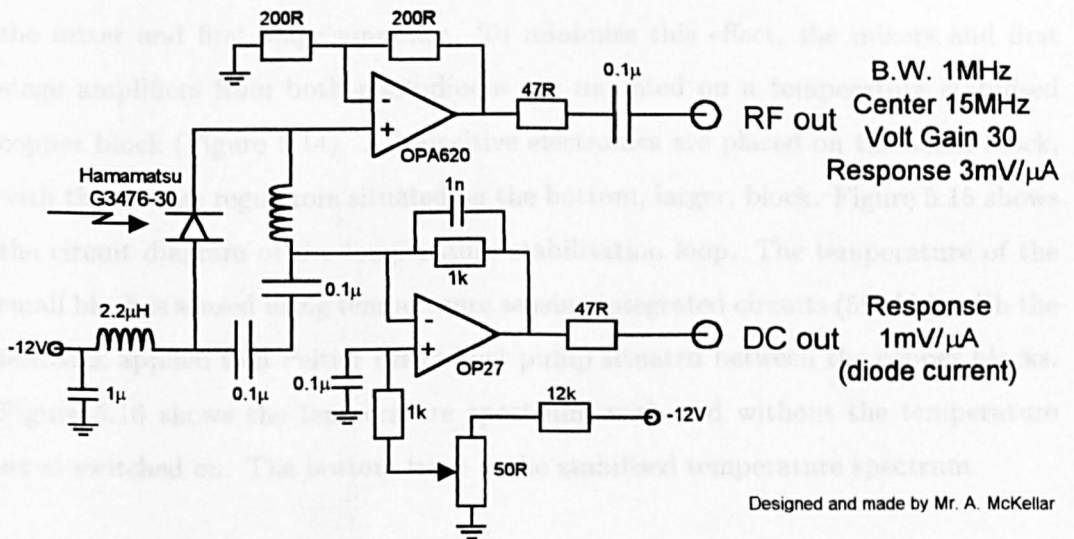
The second output port of the MPBS is used as the independent measuring path. Most of the master laser light is sent along this path (s-polarisation), along with approximately half of the slave light (p-polarisation). As the two electric fields are orthogonal to each other, they will not interfere until the light is made to pass through a further PBS oriented at  $45^\circ$  to the two polarisations. The intensity of the master laser in this path is much higher than that in the locking path, hence the shot noise limit to the measurement is correspondingly lower, and so will not limit the measurement of the relative phase noise.

In order to reduce the intensity of the master beam further, an attenuator can be placed after the EOM, and before the first PBS. This has the effect of reducing the power in both paths by the same amount. Therefore, the shot noise limiting level in the measurement path is still lower than in the locking path, and so will still provide an independent measure of the relative phase noise, assuming of course, that the electronic noise is sufficiently low.

After the re-design of the optics, the electronic feedback servo was also improved. Firstly, the photodiodes were changed. Although the original locking diode was able to see the shot noise in the detected light, it was replaced by a higher quantum efficiency InGaAs photodiode (Hamamatsu G3476-30) and pre-amp with even better noise performance. The original locking diode pre-amp is now used in the measurement path, with the higher power version of the same photodiode series (EG&G YAG 444) now used as the photo-detector. Figure 5.12 shows the circuit diagram for (a) the measurement photodiode and pre-amp, and (b) the locking photodiode and pre-amp.



(a) Measurement photodiode and pre-amp



(b) Locking photodiode and pre-amp

Figure 5.12: Circuit diagrams of photodiodes and associated pre-amplifiers.

(a) Measurement photodiode, and (b) Locking photodiode.

The electronic feedback circuit was redesigned, again with low noise operation as the main driving force. Wideband, low-noise amplifiers (LT1028) are now used in all stages of filtering, with special care taken in the first stages, where low valued resistors are used to keep the noise as low as possible. Figure 5.13 shows the revised feedback circuit. The circuit consists of two feedback paths, one to the fast frequency actuator (PZT), and the other to the slow actuator (temperature of Nd:YAG crystal). The fast feedback path consists of 4 integrators, ranging in frequency from 8 Hz to 1 kHz, giving the transfer function a maximum gradient of  $>20$  dB/octave. The slow feedback path is split off after the third amplifier, and consists of additional passive low-pass filtering from 5 to 50 mHz (2 poles). The slow side is limited at high frequencies (above 1 Hz) by the thermal time constants associated with the heating of the Nd:YAG crystal.

Referring back to Figure 4.19, the temperature of the laboratory environment changes dramatically over the period of one day. In this experiment, the temperature fluctuations are most likely to enter into the measurement noise through drifts in the mixer and first stage amplifier. To minimise this effect, the mixers and first stage amplifiers from both photodiodes are mounted on a temperature stabilised copper block (Figure 5.14). All sensitive electronics are placed on the small block, with the voltage regulators situated on the bottom, larger, block. Figure 5.15 shows the circuit diagram of the temperature stabilisation loop. The temperature of the small block is sensed using temperature sensing integrated circuits (590 kh), with the feedback applied to a Peltier Effect heat pump situated between the copper blocks. Figure 5.16 shows the temperature spectrum, with and without the temperature servo switched on. The bottom trace is the stabilised temperature spectrum.

### 5.6.1 Results

Figure 5.17 shows a graph of the uncalibrated error point, measured at the output of the locking mixer. The top trace shows the level of shot noise associated with the laser powers incident on the photodiode. This measurement is made by unlocking the lasers, thereby maintaining the same DC light level, but removing the beat signal at 15 MHz. The middle trace is the measured output of the mixer when the lasers

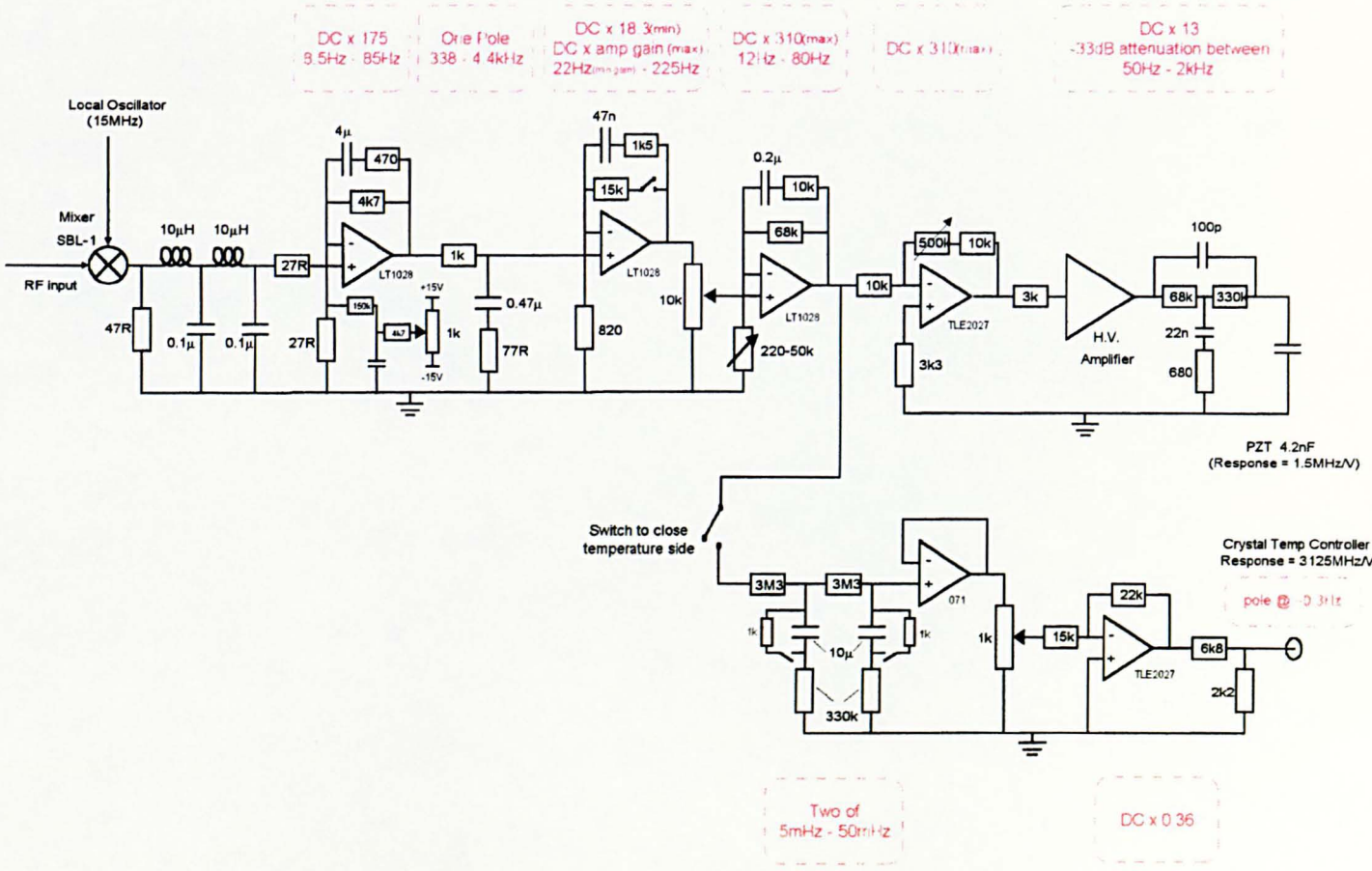


Figure 5.13: Circuit diagram of new feedback circuit to phase lock lasers.

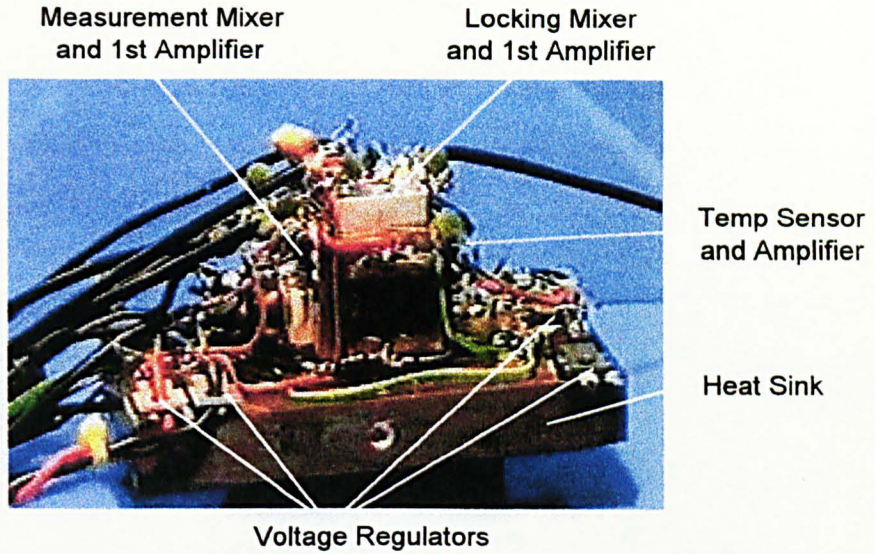


Figure 5.14: Photograph of temperature stabilised copper block, with mixers and 1st stage amplifiers attached.

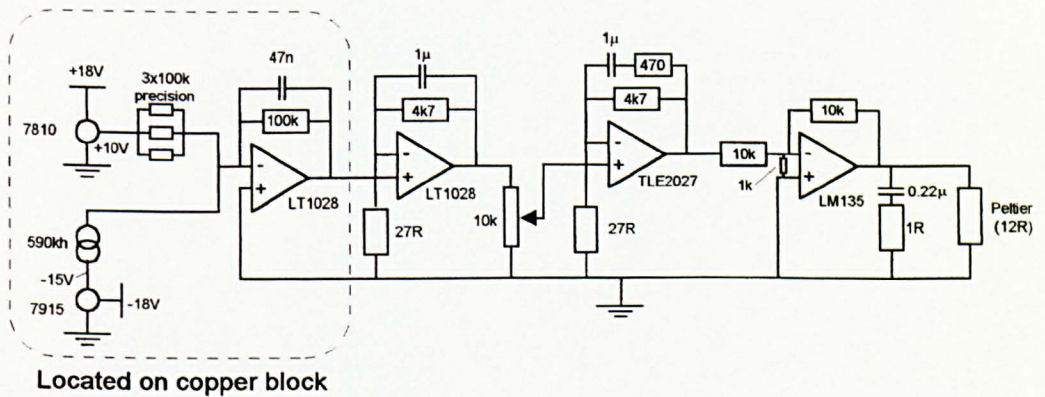


Figure 5.15: Circuit diagram for temperature stabilisation of mixers and first stage amplifiers. 590 kh - IC temperature sensor (current output), 78/9xx - voltage regulators, and LM135 - high current op-amp.

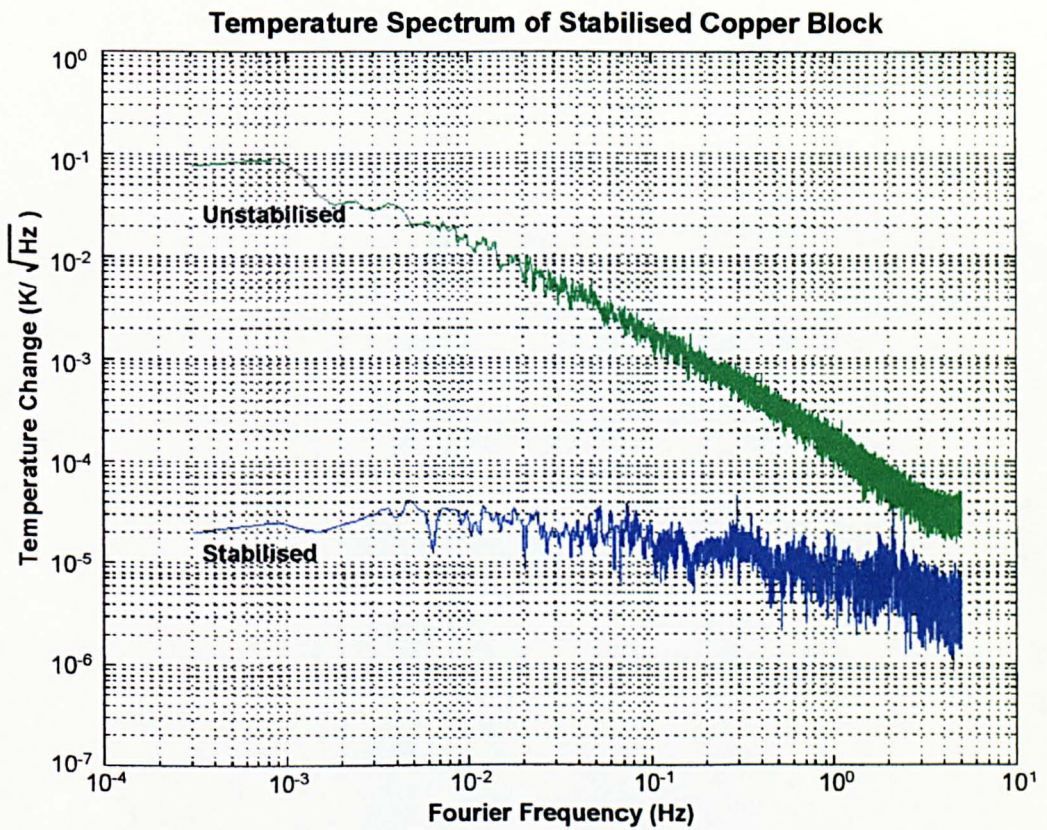


Figure 5.16: **Temperature spectrum of stabilised copper block.** *The top trace (green) shows the temperature spectrum of the lab environment. The bottom trace (blue) shows the temperature spectrum of the stabilised copper block (both passive and active stabilisation used).*

are locked, and the bottom trace is the spectrum analyser noise floor. This graph shows that the error point is reduced well below shot noise, thereby in principle, allowing the lasers to be phase locked to the shot noise limit. However, this does not say anything about the absolute stability of the lasers; instead it gives an idea of the gain, and transfer function of the electronic servo system - the higher the gain, the smaller the error point signal.

Figure 5.18 shows a graph of the independent measure of the relative phase noise of the slave laser. The data is recorded at the output of the measurement side mixer, which has already been calibrated as mentioned previously. The top trace (red) shows the calibrated feedback signal to the slave laser PZT, and gives a direct measure of the unstabilised phase noise of the laser. The bottom trace (blue) shows the independent measure of the relative phase noise of the slave. The straight line (green) shows the value of the shot noise limit for this measurement, calculated using the signals from the locking photodiode (see Section 5.3 for details of the calculation).

The laser powers interfering at the locking diode are: master - 50 pW, and slave - 1 mW, giving a shot noise limiting level of  $6.64 \times 10^{-5}$  rads/ $\sqrt{\text{Hz}}$ . At the measurement side, the power of the master laser is not attenuated and strikes the diode with an intensity of  $\sim 2$  mW, with a slave power of  $\sim 5$  mW, giving a shot noise limit of  $1.3 \times 10^{-11}$  rads/ $\sqrt{\text{Hz}}$  - well below the noise level in the locking side. This ensures that, if the photodiode and pre-amp are quiet enough (as is the case), then the inherent noise in the measurement path is lower than the phase stability being measured.

Apart from some resonant structure, the relative phase of the slave laser is close to the shot noise limit from a few Hz up to  $\sim 1$  kHz. The data was recorded over short timescales (approximately 100 seconds), and so is well outside the LISA measurement band. However, it does show that it is possible to stabilise two independent lasers down to levels that are limited purely by the shot noise of the weaker beam. To check that this is the case, the shot noise on the photodiode was increased by shining a white light source onto the diode while the lasers are locked. If the relative phase noise of the slave is indeed limited by photon shot noise, then the effect of increasing

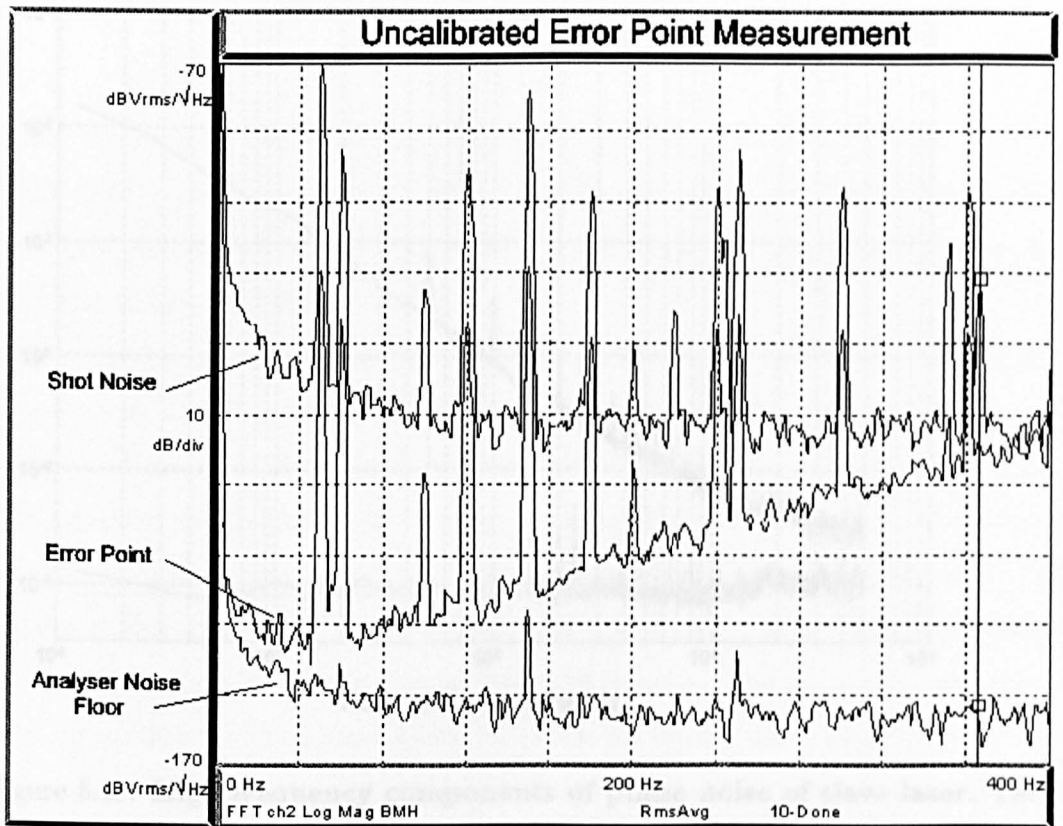


Figure 5.17: Uncalibrated error point measurement.

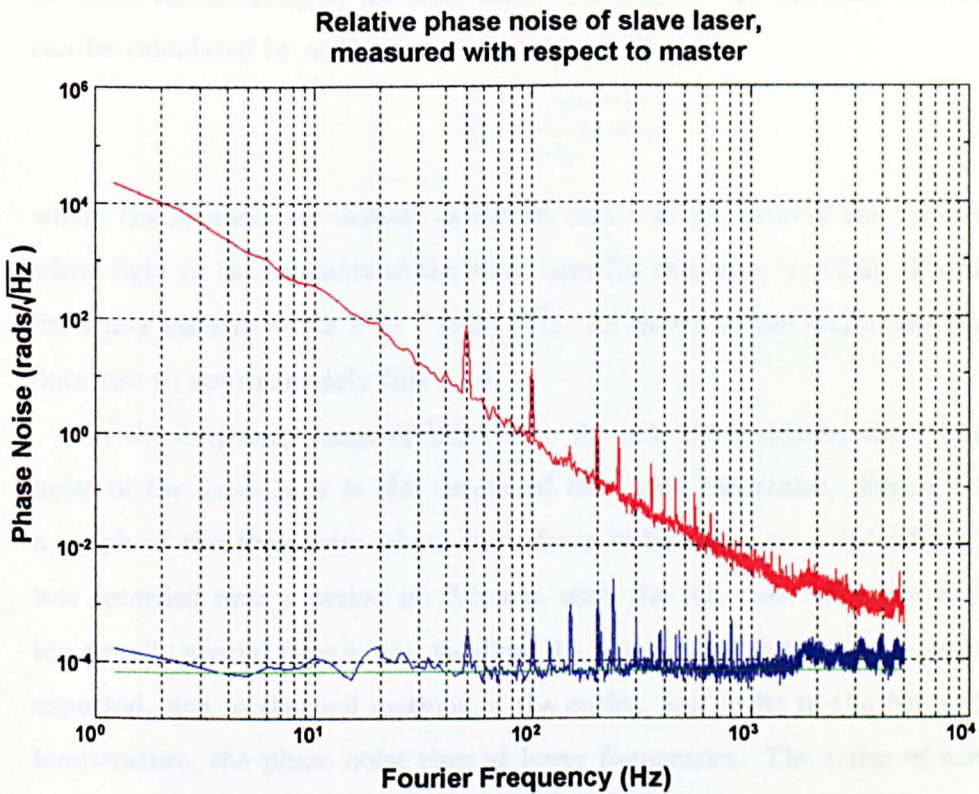


Figure 5.18: **High frequency components of phase noise of slave laser.** *The red curve shows the unstabilised phase noise of the slave laser, the blue curve shows the stabilised laser performance. The green (straight) line shows the calculated level of the photon shot noise limit.*

the shot noise should increase the relative phase noise accordingly. Figure 5.19 shows a graph of the relative phase noise with and without the extra white noise. The bottom trace shows the phase noise of the slave under normal locking conditions (no excess noise), the top trace shows the phase noise with the additional shot noise. The intensity of the white light was set such that the detected DC intensity was 3.5 times the intensity of the slave laser. The level of the increased shot noise limit can be calculated by analogy with Equation 5.13 to be,

$$\widetilde{\delta\phi} = \sqrt{\frac{e}{i_1}(1 + \gamma)} \quad (5.14)$$

where the symbols are defined as before, and  $\gamma$  is the ratio of the intensity of the white light to the intensity of the slave laser (in this case,  $\gamma = 2.5$ ). The shot noise limit now rises to  $\sim 1.2 \times 10^{-4}$  rads/ $\sqrt{\text{Hz}}$ . As shown in the graph, the phase noise does rise to approximately this level.

As the frequency range of LISA is in the sub-Hertz regime, the relative phase noise of the slave laser is also measured over long timescales. Figure 5.20 shows a graph of the slave laser phase noise from 10 Hz down to  $\sim 0.5$  mHz. The data was recorded over a period of 15 hours, with the full data set being divided into ten equally spaced time series, to allow the phase noise spectra to be averaged. As expected, due to thermal motions of the optics, and drifts in the Nd:YAG crystal temperature, the phase noise rises at lower frequencies. The bulge of excess noise centred around 0.1 Hz is most likely to be due to seismic noise coupling into the apparatus. As the lasers are mounted outside the vacuum chamber, any relative motion between the vacuum chamber and laser optics bench will couple into the measurement through beam pointing jitter. If the pointing of one laser beam changes relative to the other laser, the overlap of the beams at the photodiodes changes, therefore changing the magnitude of the detected beat notes. Excess noise on the locking side error signal is directly fed back onto the slave laser, thereby increasing the phase noise of the slave. Any noise on the measurement mixer output is directly recorded as relative phase noise between the lasers. Even so, the relative phase noise between the lasers is only one order of magnitude above the shot noise limit.

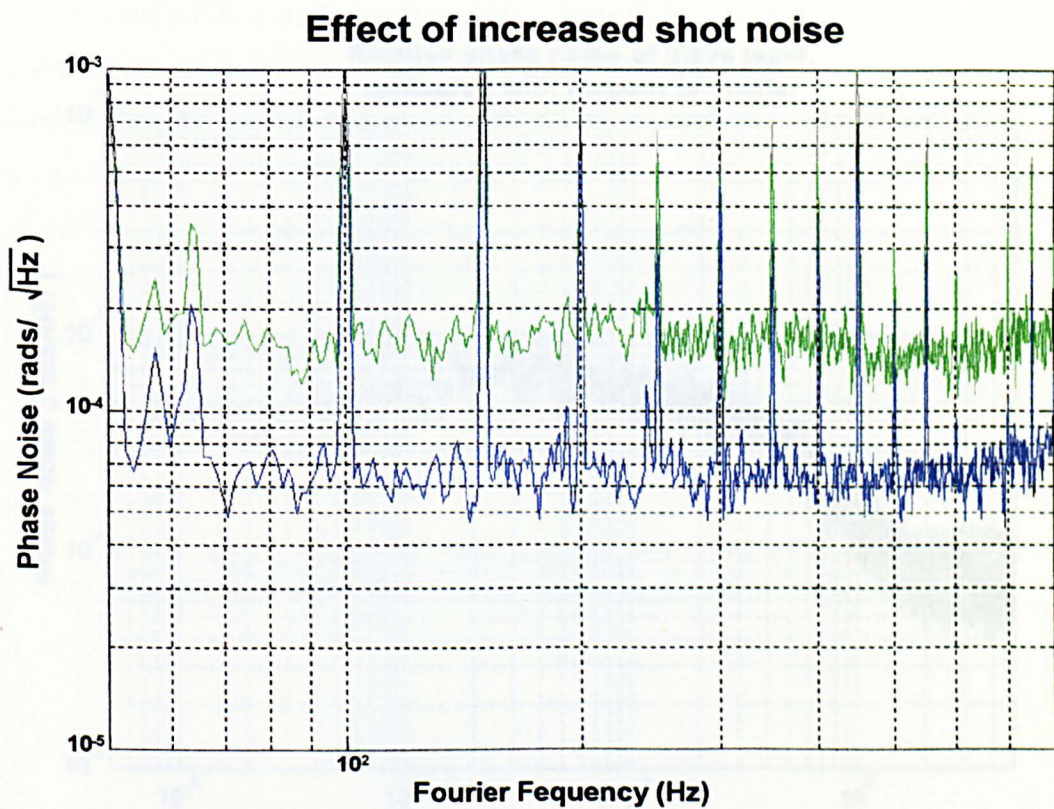


Figure 5.19: **Effect of increasing shot noise on locking photodiode.** *The blue trace (bottom) shows the relative phase noise of the slave laser under normal locking conditions. The green trace shows the relative phase noise when the shot noise level on the locking photodiode is increased.*

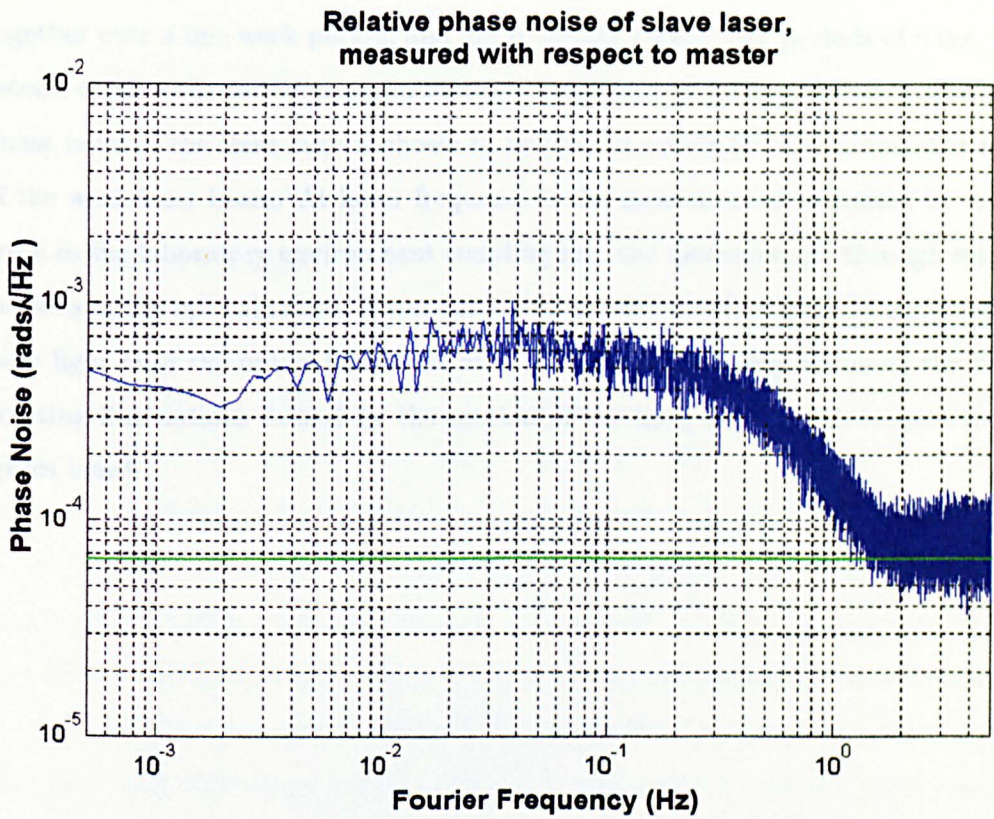


Figure 5.17: **Low frequency components of relative phase noise of slave laser.** *The green line shows the shot noise limiting level for this measurement.*

## 5.7 Conclusions

The aims of this study were to show firstly that two independent lasers could be phase locked together over extremely long timescales, and then to attenuate the intensity of one of the lasers and show that the relative phase noise of the slave laser is at or close to the shot noise limiting performance needed for LISA.

The first of these aims has been met. The lasers have been continuously locked together over a one week period, and are routinely locked over periods of days. The second of the aims has been shown to be achievable. At high frequencies, the relative phase noise of the slave laser is shown to be limited purely by the photon shot noise of the weak laser beam. At lower frequencies, the measurement is limited by excess noise in the laboratory environment coupling into the measurement through seismic motions of the optical tables. Future experiments will involve optically coupling the laser light onto the optics bench via fibre optic cables, thereby reducing the beam pointing fluctuations caused by the motion of the laser bench with respect to the optics bench.

## Chapter 6

# Telescope Design for LISA

### 6.1 Introduction

As discussed in Chapter 3, the shot noise limited phase error between the received and transmitted beams at a far s/c is the biggest single noise source in the displacement sensitivity of LISA[12]. The magnitude of this noise is limited fundamentally by the intensity of the detected laser light, which is directly dependent on the length of the interferometer arm, the beam width at the output of the telescope, and on how well the beam is mode matched into the transmitting telescope (or, put another way, how well the telescope is focused). Also, as the light entering the telescope will not be along the optic axis (because of the “point ahead” - Chapter 3, Section 2.1), the image may suffer from coma<sup>1</sup> *i.e.* a point source object appears “lobe” shaped, as opposed to circular, in the telescope focal plane.

The original design in LISA was to use a classical two mirror Cassegrain[57][58] telescope, of 30 cm aperture. However, there are other telescope designs which offer better performance than the classical Cassegrain in both field of view, and image quality. This chapter will describe one such variation of the Cassegrain telescope, the Ritchey-Chretien[60], followed by a brief error budget analysis of some of the major causes of displacement noise caused by the transmitting telescope.

---

<sup>1</sup>This aberration is so named because a star observed off-axis through a telescope looks similar in shape to the tail of a comet, *i.e.* the *coma*.

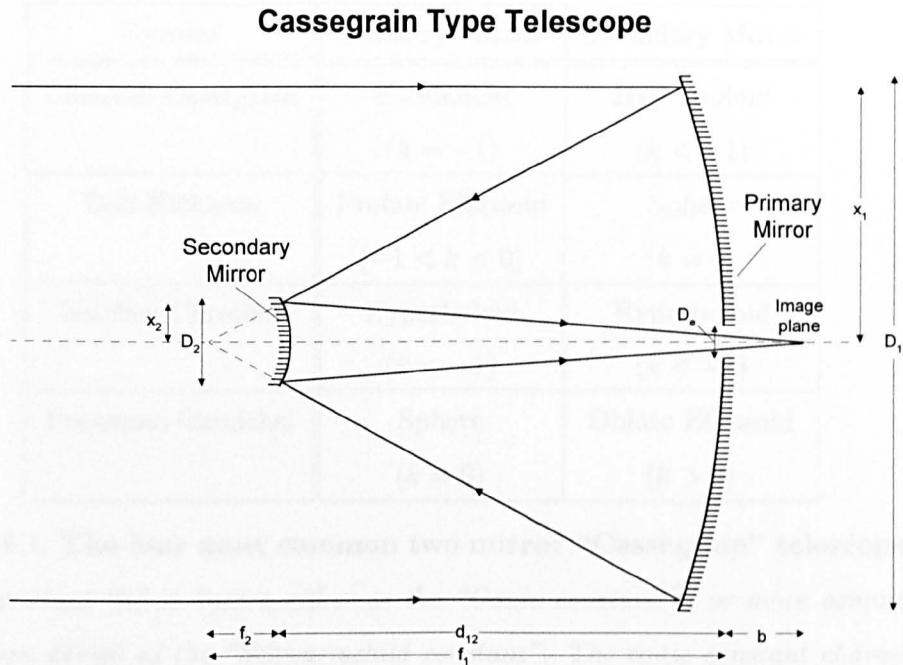


Figure 6.1: **Diagram of a Cassegrain type telescope.** *The subscripts 1/2 refer to the primary and secondary mirrors respectively. “d” is the separation of the mirrors, and  $(d+b)$  is known as the back focal length.*

## 6.2 Two Mirror Reflecting Telescopes

The choice of telescope design for LISA is restricted to reflecting telescopes only, as the overall length of each optical bench plus telescope is constrained by the size of the s/c (in general, reflectors are physically shorter than the corresponding refractor of the same aperture). Of all the reflecting telescopes available, the two mirror Cassegrain type is best favoured, due to its long focal length, but short physical length. Figure 6.1 shows the basic layout for a Cassegrain type telescope.

The Cassegrain design has been used as the baseline for a wide range of other telescopes, with each using the same basic optical layout, but with different mirror shapes. Provided that the correct combination of optical surfaces is chosen, all designs can be free of spherical aberration, permitting a sharp on-axis image. However if the object is observed off-axis (as is the case in LISA), the sharpness of the image is strongly dependent on the form of the mirrors. The four most common

System	Primary Mirror	Secondary Mirror
Classical Cassegrain	Paraboloid ( $k = -1$ )	Hyperboloid ( $k < -1$ )
Dall-Kirkham	Prolate Ellipsoid ( $-1 < k < 0$ )	Sphere ( $k = 0$ )
Ritchey-Chretien	Hyperboloid ( $k < -1$ )	Hyperboloid ( $k < -1$ )
Pressman-Camichel	Sphere ( $k = 0$ )	Oblate Ellipsoid ( $k > 0$ )

Table 6.1: **The four most common two mirror “Cassegrain” telescopes**[60]. The constant “ $k$ ” is known either as the “Conic constant”<sup>2</sup>, or more commonly in telescope design as the “Schwarzschild constant”. The conic constant characterises the deformation of a surface from a perfect sphere.

combinations are shown in Table 6.1.

The original design (classical Cassegrain) was first constructed in 1627[59], but did not come into common use until almost two centuries later, mostly due to the difficulty in forming the correct hyperboloid for the secondary mirror. The design is still the most common of all Cassegrain type telescopes, although it has now been superseded in all modern, large aperture telescopes, by the Ritchey-Chretien. The Dall-Kirkham and Pressman-Camichel are not used in modern large aperture telescopes, as the aberrations associated with such designs far outweigh the ease with which the mirrors can be formed.

Figure 6.2 shows spot diagrams for an off-axis object imaged through the four types of telescope listed above. The spot diagrams shown are for a much more exaggerated off-axis angle than is likely in LISA, but do, however, show the coma aberration associated with each optical design. In LISA, where the received beam is mixed with the local laser, the amount of overlap between the beams is important. If the overlap changes, for example, due to relative non-axial motion of the s/c, the

---

<sup>2</sup>The conic constant is defined as negative of the square of the eccentricity,  $k = -(e^2)$

amplitude of the beam with distance. The large size diameter of the beam causes the phase-fronts with maximum phase error, then change in the wavefront, surface etc will not propagate the transmission. However, since this can be the case (due to short focal length of the focused light) fluctuations in the beam wave amplitude will couple directly into the measurement, appearing as phase noise on the transmitted beam. The spot diagrams for the classical Cassegrain originally proposed for LISA[11]

### Spot diagrams for an off-axis object

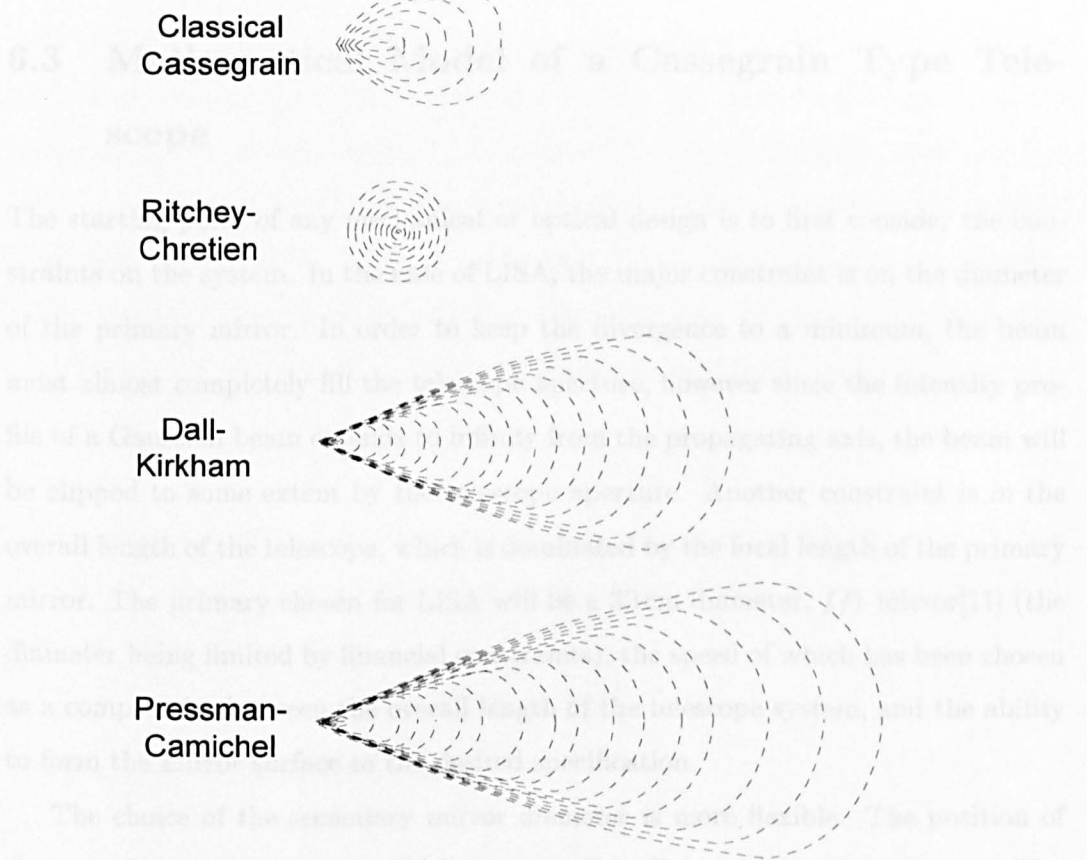


Figure 6.2: Spot diagrams showing the intensity patterns for an off-axis object imaged through a Cassegrain type telescope[60].

amplitude of the beat note between the lasers also changes. If the lasers could be phase locked with no relative phase noise, then changes in the amplitude in the beat note will not couple into the measurement. However, since this can never be the case (due to shot noise in the detected light) fluctuations in the beat note amplitude will couple directly into the measurement, appearing as phase noise on the transponded beam. For this reason, the Ritchey-Chretien telescope was studied as a replacement for the classical Cassegrain originally proposed for LISA[11].

### 6.3 Mathematical Model of a Cassegrain Type Telescope

The starting point of any mechanical or optical design is to first consider the constraints on the system. In the case of LISA, the major constraint is on the diameter of the primary mirror. In order to keep the divergence to a minimum, the beam must almost completely fill the telescope aperture, however since the intensity profile of a Gaussian beam extends to infinity from the propagating axis, the beam will be clipped to some extent by the telescope aperture. Another constraint is in the overall length of the telescope, which is dominated by the focal length of the primary mirror. The primary chosen for LISA will be a 30 cm diameter,  $f/1$  mirror[11] (the diameter being limited by financial constraints), the speed of which has been chosen as a compromise between the overall length of the telescope system, and the ability to form the mirror surface to the desired specification.

The choice of the secondary mirror diameter is more flexible. The position of the secondary means that it will block some of the light entering the telescope. The fraction of detected to incident power is given by:

$$\frac{P_{det}}{P_{in}} = 1 - \left[ \frac{D_2}{D_1} \right]^2 \quad (6.1)$$

As the ratio is proportional to the square of the diameters, the reduction in detected power caused by the secondary obscuration is not a major concern. A more serious problem is the way the secondary obscuration affects the wavefront in the far field (see later in this chapter for a discussion of the secondary obscuration). For this

investigation, a diameter of  $\sim 0.027$  m for the secondary mirror has been chosen.

With the constraints in place, the complete telescope can be defined. The following notation is as given in Figure 6.1, with the assumption that a beam waist (plane wavefront) is formed on, or close to, the primary mirror.

Using the method of similar triangles, the separation of the mirrors is calculated to be

$$d_{12} = \frac{f_1 (x_1 - x_2)}{x_1} \quad (6.2)$$

The back focal length of the system can now be calculated. For most astronomical telescopes, the focus behind the primary mirror, one back focal length from the secondary, is where instruments (*e.g.* cameras) are placed. In LISA, there is a lens placed in the plane of the primary mirror, which is used to collimate the received laser light and to mode-match the transmitted light into the telescope, therefore removing the image plane behind the primary mirror. However, the back focal length is useful in calculating other parameters of the system, and is given by

$$B = b + d_{12} = d_{12} \left( 1 + \frac{x_2}{x_2 - x_e} \right) \quad (6.3)$$

The focal length of the full telescope and of the secondary mirror can now be characterised in terms of the parameters already known. Firstly the “secondary magnification” is calculated as [60]

$$M_s = \frac{b + d_{12}}{f_1 - d_{12}} \quad (6.4)$$

which gives the system focal length

$$f_s = f_1 M_s \quad (6.5)$$

Finally the focal length of the secondary is calculated. In the case of all Cassegrain telescopes, the secondary mirror is convex, and located such that the real focus of the primary, and imaginary focus of the secondary are almost coincident. The secondary focal length is defined as

$$f_2 = \frac{f_1 M_s \left( 1 - \frac{d_{12}}{f_1} \right)}{M_s - 1} \quad (6.6)$$

The above equations describing the relative positions and focal lengths of the optics are general for all Cassegrains. The final details are dependent on the type of telescope under study, *i.e.* on the shape of the mirrors. All telescope configurations shown in Table 6.1 are constructed from mirrors formed from conic sections, chosen to minimise the aberrations associated with the telescope. The six main aberrations for reflectors are known as the *Third Order Seidel Aberrations* and are[61]:

- A) Spherical Aberration
- B) Coma Aberration
- C) Astigmatism
- D) Field Curvature
- E) Distortion
- F) Defocus

If the telescope is aligned correctly, the last two aberrations are zero, and therefore do not enter into the telescope design.

Again, referring back to Table 6.1, the classical Cassegrain, Dall-Kirkham, and Pressman-Camichel all have one degree of freedom in the shape of one of the mirrors. Taking the example of the classical Cassegrain, the primary shape is fixed (paraboloid  $\Rightarrow k = -1$ ), but the secondary form is free (hyperboloid  $\Rightarrow k < -1$ ). With this degree of freedom, the mirrors can be chosen such that the first of the Seidel aberrations is zero.

The advantage of the Ritchey-Chretien lies with the fact that it has two degrees of freedom (both mirrors are hyperboloids). Therefore, with the correct choice of mirrors, the telescope can have zero spherical and coma aberration<sup>3</sup> (Figure 6.2).

The first three Seidel aberrations are given by the following equations[60]:

$$A = 1 + k_1 - \left[ k_2 + \left( \frac{M_s + 1}{M_s - 1} \right)^2 \right] \frac{(M_s - 1)^3 (1 - N)}{M_s^3} \quad (6.7)$$

$$B = \frac{2}{M_s^3} + \left[ k_2 + \left( \frac{M_s + 1}{M_s - 1} \right)^2 \right] \frac{(M_s - 1)^3 N}{M_s^3} \quad (6.8)$$

---

<sup>3</sup>A telescope without spherical and coma aberration is known as an *Aplanatic Telescope*

$$C = \frac{4(M_s - N)}{M_s^2(1 - N)} - \left[ k_2 + \left( \frac{M_s + 1}{M_s - 1} \right)^2 \right] \frac{(M_s - 1)^3 N^2}{M_s^3(1 - N)} \quad (6.9)$$

where  $N$  is defined as  $\frac{d_1^2}{f_1}$

Since the Ritchey-Chretien can be constructed to be aplanatic, Equations 6.6 and 6.7 are solved with  $A$  and  $B$  both set to zero, giving the conic constants of the two mirrors to be

$$k_1 = - \left( 1 + \frac{2(1 - N)}{M_s^2 N} \right) \quad (6.10)$$

and

$$k_2 = - \left( \frac{2M_s}{(M_s - 1)^3 N} + \left( \frac{M_s + 1}{M_s - 1} \right)^2 \right) \quad (6.11)$$

With the focal lengths and shapes of the mirrors, and the separation of the two surfaces known, the complete telescope system is defined. The system is verified by performing a raytrace through the optical chain, looking at the beam size and shape at each of the optical surfaces. The following section describes the numerical raytrace model used.

## 6.4 Numerical Model of the LISA Telescope

The model was set up in the optical design package, CODEV[64], as follows:

As above, the constraints are used to calculate the focal lengths, conic constants and separation of the mirrors. The program then calculates the radii of curvature of the collimating lens in the plane of the primary, and the focusing lens at the output of the fibre, using the thick lens approximation[62]. All transmissive optics are assumed to be manufactured from silica (refractive index: 1.450), however this can be changed to any other transmissive material (*e.g.* Zerodur) if need be. Using the parameters calculated for the telescope, the actual physical surfaces are created. Each surface must be defined individually, *i.e.* each face of a lens is contained in a

## CODEV Plot of Off-Axis Ray Through Telescope

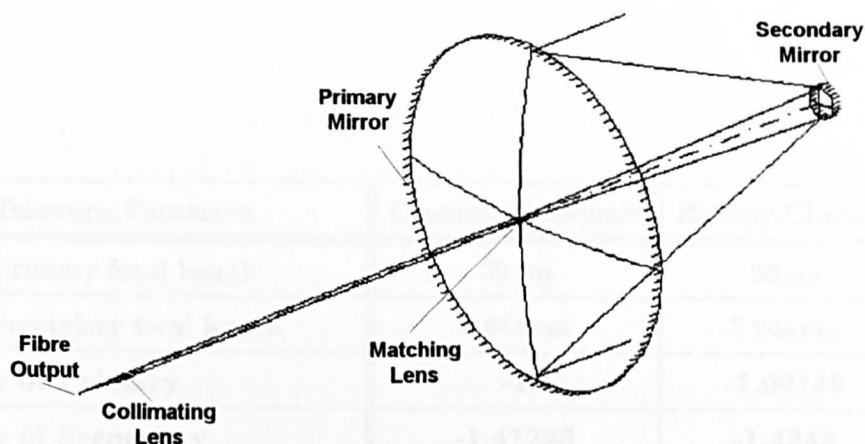


Figure 6.3: CODEV plot of the LISA telescope. The model has been set up to trace an off-axis ray from the fibre output through the telescope, stopping just after the primary mirror.

separate line of code. A surface is defined by its radius of curvature (ROC), distance to next surface, whether it is reflective or transmissive, and its conic constant. If the surface is transmissive, then the medium **after** the surface is specified (*e.g.* silica or air).

The program then either traces a ray, parallel to the optic axis, through the system, or numerically propagates a Gaussian beam through the optics chain. Both of the analysis modes take an initial condition (in this case the size of the waist at the fibre output) and mathematically calculates the beam parameters at each optical surface in turn. If the original model is correct, then the beam sizes at the primary and secondary should be the same as the original constraints put on the system.

Figure 6.3 shows the telescope with the off-axis ray traced from the fibre output through to the primary mirror. As each surface mathematically extends to infinity, the raytrace alone does not give enough information on the real telescope, as each ray **must** hit the next surface, even if the beam diameter is bigger than the actual mirror diameter. However, it does show if the beam can be propagated through the system along approximately the correct optical path. The Gaussian analysis gives

Telescope Parameter	Classical Cassegrain	Ritchey-Chretien
Primary focal length	30 cm	30 cm
Secondary focal length	2.944 cm	2.944 cm
<b><math>k</math> of Primary</b>	<b>-1</b>	<b>-1.00146</b>
<b><math>k</math> of Secondary</b>	<b>-1.41296</b>	<b>-1.4343</b>
Separation of Mirrors	27.3094 cm	27.3094 cm
Collimating Lens Power	-25.6 D	-25.6 D
Focusing Lens Power	32.2046 D	32.2046 D
Beam Width on Focus Lens	0.14515 cm	0.14515 cm
Beam Width on Coll. Lens	0.15036 cm	0.15036 cm
Beam Width on Secondary	1.2 cm	1.2 cm
Beam Width on Primary	13.382 cm	13.385 cm
Wavefront ROC on Primary	$-2.75 \times 10^4$ m	$-2.74 \times 10^4$ m
Distance to Waist	$2.16 \times 10^4$ m	$2.16 \times 10^4$ m
<b>Seidel A : Spherical</b>	<b><math>1.13 \times 10^{-7}</math></b>	<b><math>-3 \times 10^{-9}</math></b>
<b>Seidel B : Coma</b>	<b>0.0178</b>	<b><math>3 \times 10^{-8}</math></b>
Seidel C : Astigmatism	3.694	3.694

Table 6.2: **Comparison of a classical Cassegrain and a Ritchey-Chretien telescopes.** *The two telescopes have been set-up to have the same size of mirrors, and approximately the same beam sizes on the two mirrors. The beam sizes on the lenses are for the beam striking the surface nearer the fibre.*

much more detailed information on the performance of the telescope, by listing the beam parameters (width, radius of curvature) at each optical surface. The output (shown in Appendix B, Table B.1) allows the telescope design to be optimised for a laser beam propagated through the system, as opposed to a simple geometrical ray.

Table 6.2 shows the telescope parameters calculated for both a revised classical Cassegrain and the improved Ritchey-Chretien. As expected, the focal lengths and separation of the mirrors are the same for both designs; it is only the shapes of the mirror surfaces that differ. The major difference in the beam quality of the two telescopes is in the amount of Coma aberration of the classical Cassegrain.

## 6.5 ASAP Analysis of the LISA Telescope

With the telescope design fully verified, the model was transferred to the optical raytrace and analysis program, ASAP<sup>4</sup>[65]. The ASAP model of the telescope was first used to check a full Gaussian raytrace through the system, and then was adapted to include telescope error sources which are likely to contribute to the overall displacement noise of the LISA mission.

ASAP models the optical chain in a similar way to CODEV, except that all surfaces must be bounded: if the beam width is wider than the mirror diameter, some of the rays will miss the mirror, indicating an error in the model. As ASAP carries out a full Gaussian raytrace, the light source is set up differently. Initially a single Gaussian beam is created with the desired width at the fibre output. The single beam is then decomposed into a number of individual rays (in this case, 10000). The rays are further subdivided into either 4 or 8 rays, which when propagated, produce an intensity profile identical to that which would have been produced by the original, single Gaussian beam[66]. In this way, the number of rays to be traced can be set: the higher the number of rays, the better the approximation to the real case, but the slower the computation time. As in CODEV, the simulated laser beam was made to pass through the telescope to check that the model is set up correctly. Figure 6.4 shows the raytrace of the decomposed Gaussian field transmitted through the optical

---

<sup>4</sup>Advanced Systems Analysis Program

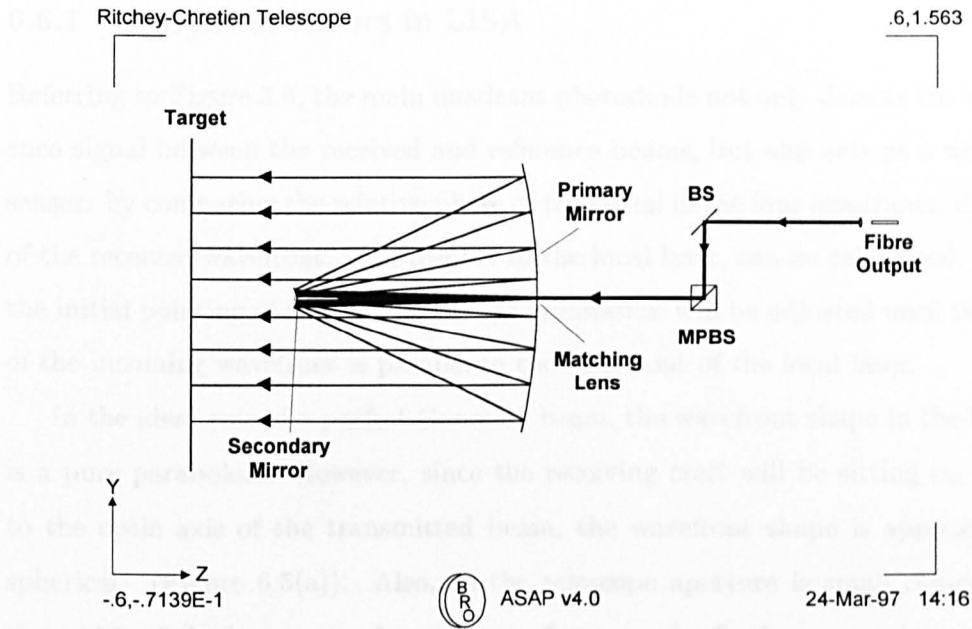


Figure 6.4: ASAP ray trace of the LISA telescope. The target has been placed a short distance from the primary to reduce the computation time of the raytrace.

The only criterion that can be used to decrease weight the weight of the beam chain. The program traces the full 10000 beams, although, for clarity, only a small number are plotted. The target is set a short distance from the primary in order to minimise the computation time required. The model simulates the LISA case as closely as possible, in that the free space from the fibre to collimating lens takes into account the optical path length change through the electro-optic modulator and beamsplitters.

## 6.6 Wavefront Aberration Analysis in the Far-Field

The ASAP model can now be used to analyse the telescope in more detail, by introducing wavefront aberrations into the transmitting telescope system, and seeing the effect in the far field. Before considering the wavefront errors in detail, it is useful to introduce why such errors affect the displacement sensitivity of LISA.

### 6.6.1 Wavefront Errors in LISA

Referring to Figure 3.6, the main quadrant photodiode not only detects the interference signal between the received and reference beams, but also acts as a wavefront sensor: by comparing the relative phase of the signal in the four quadrants, the angle of the received wavefront, with respect to the local laser, can be calculated. During the initial pointing of the beams, the s/c orientation will be adjusted until the angle of the incoming wavefront is parallel to the wavefront of the local laser.

In the ideal case of a perfect Gaussian beam, the wavefront shape in the far field is a pure paraboloid. However, since the receiving craft will be sitting on or near to the optic axis of the transmitted beam, the wavefront shape is approximately spherical. (Figure 6.5(a)). Also, as the telescope aperture is small compared to the width of the beam, the detected wavefront can be further approximated to be considered as flat. Therefore, the receiving craft can be located anywhere on the far-field wavefront, and will still be pointing back towards the transmitting craft. The only criterion that can be used to determine where the receive craft is located with respect to the optic axis, is the detected intensity of the weak beam.

However, the beam in LISA is not “ideal”, due to the outgoing beam being clipped by the secondary mirror, “spider”<sup>5</sup> and telescope aperture[63]. There are also likely to be other aberrations in the wavefront, caused, for example, by mis-alignment of the telescope mirrors or ripples on the surface of the optics. Figure 6.5(b) shows a schematic diagram of an exaggerated aberrated wavefront in the far field. As well as the problems in initial alignment, a much more serious problem arises if the wavefront is not spherical. If the pointing of the transmitting craft changes (a pointing “jitter” of  $6 \text{ nrad}/\sqrt{\text{Hz}}$  is expected[11]), the phase of the detected light will also change, coupling into the measurement as increased phase noise in the transponded beam.

---

<sup>5</sup>The “spider” is taken to mean the struts holding the secondary mirror in position.

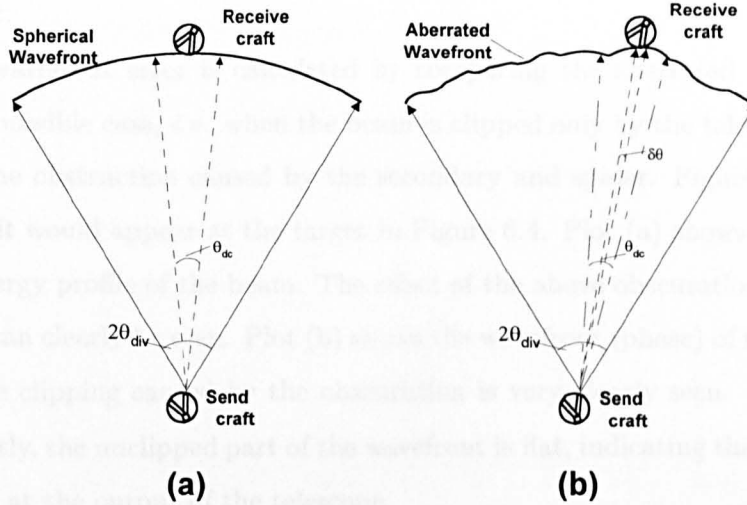


Figure 6.5: **Schematic diagrams of (a) ideal wavefront, and (b) aberrated wavefront.** Figure (a) shows the case of an ideal spherical wave, centred on the transmitting craft. (b) shows a diagram of the real case where the wavefront is likely to deviate from being ideal.

## 6.6.2 Wavefront Error Budget

The following analysis deals with the telescope error sources individually. The most pessimistic contribution to the overall instrument noise is given by the arithmetic sum of the individual noise sources.

Due to computational limitations, it is not possible to numerically propagate the beam the full LISA armlength ( $5 \times 10^9$  m). Instead, the beam is propagated a distance equal to ten times the Rayleigh length<sup>6</sup> ( $\sim 5 \times 10^5$  m). The Rayleigh length,  $z_r$  is given by[67]

$$z_r = \frac{\pi \omega_o^2}{\lambda} \quad (6.12)$$

where  $\omega_o$  is the radius of the beam waist, and  $\lambda$  is the laser wavelength. Beyond this distance, the divergence of the beam becomes linear, therefore, by extrapolation, the wavefront at the receiving telescope can be determined from the ASAP calculated

<sup>6</sup>The Rayleigh length is defined to be the distance from the beam waist at which the beam diameter has increased by a factor of  $\sqrt{2}$ , and is approximately the dividing line between the near-field (Fresnel) region and the far-field (Fraunhofer) region.

wavefront.

The wavefront error is calculated by comparing the aberrated wavefront with the best possible case, *i.e.* when the beam is clipped only by the telescope aperture, and by the obstruction caused by the secondary and spider. Figure 6.6 shows the beam as it would appear at the target in Figure 6.4. Plot (a) shows a cross section of the energy profile of the beam. The effect of the above obscurations and primary clipping can clearly be seen. Plot (b) shows the wavefront (phase) of the same beam. Again the clipping caused by the obscuration is very clearly seen. However, more importantly, the unclipped part of the wavefront is flat, indicating that a beam waist is formed at the output of the telescope.

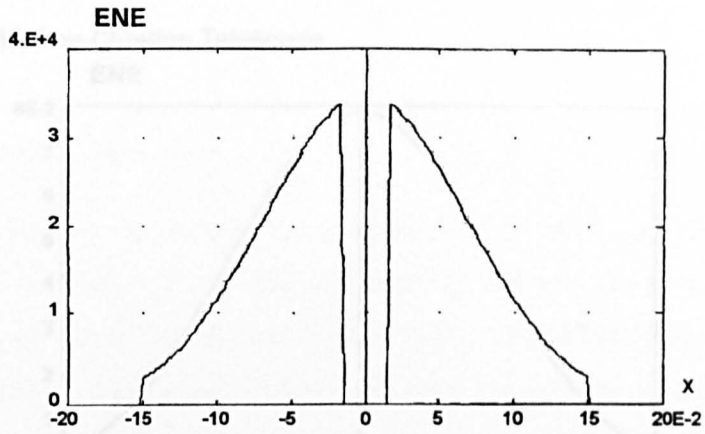
Propagation of the beam to  $10 \times z_r$  shows the divergence as expected due to diffraction. Also, as shown in Figure 6.7(a,b), the effect of the obscurations and aperture clipping are removed, again through diffraction. Figure 6.7(a) shows a cross section of the energy profile, and Figure 6.7(b) an isometric plot of the wavefront in the far field. As expected, the wavefront is no longer flat, but instead is a paraboloid in shape. The x,y-axes of the graphs in the far field are calibrated both in position (m) and also in angular deviation from the optic-axis (rads). As the transmitting s/c can be positioned with an initial offset pointing angle of  $\theta_{dc} = \pm 15$  nrad towards the approximate location of receiving craft (set by the resolution of the proposed star-trackers), only aberrations within this angle will be of concern in LISA.

The error budget for the aberrations in the far field has only been compiled for the larger aberrations caused by the telescope. All of the following are also applicable to the smaller optical components on the optics bench, however, their effect is not included here. For more details, see Caldwell, *et al*[70].

The transmitting telescope can distort the far-field wavefront by a combination of two means:

- 1) Errors caused by defects in the telescope system, *e.g.*
  - mis-alignment of one of the mirrors (tilt), or a change in the mirror separation (de-focus)
- 2) Errors in the pointing of the transmitting telescope

### Ritchey-Chretien Telescope

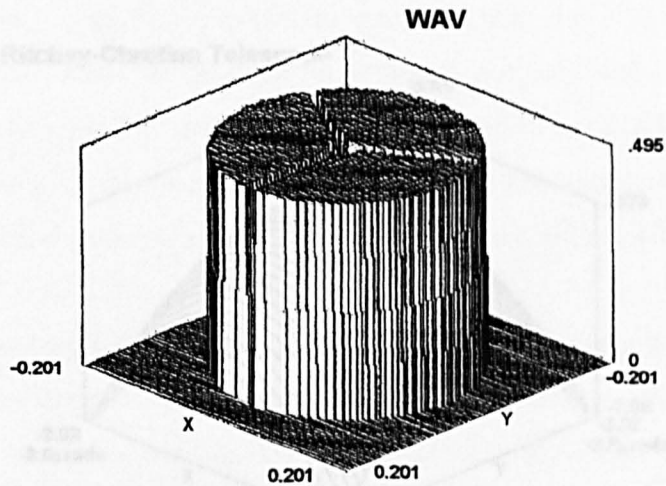


ASAP v4.0

7-APR-97 14:00

(a)

### Ritchey-Chretien Telescope



ASAP v4.0

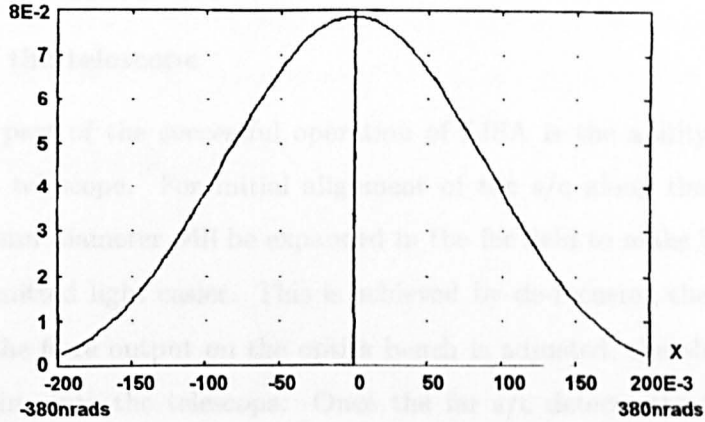
7-APR-97 14:00

(b)

Figure 6.6: ASAP plots of the reference beam in the near field. (a) shows a cross section of the energy of the beam located at the target of Figure 6.4, (b) shows an isometric plot of the wavefront at the target plane. Both (a) and (b) clearly show the clipping of the telescope aperture, and the obscuration caused by the secondary and spider.

### Ritchey-Chretien Telescope

ENE



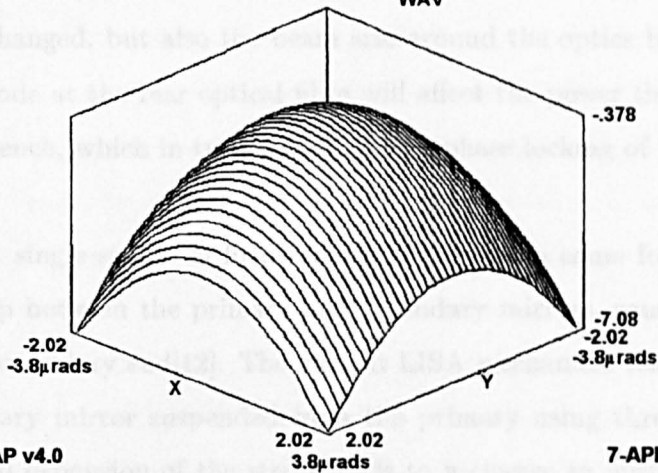
ASAP v4.0

7-APR-97 14:01

(a)

### Ritchey-Chretien Telescope

WAV



ASAP v4.0

7-APR-97 14:01

(b)

Figure 6.7: ASAP plots of the reference beam in the far field. Plot (a) shows the cross section of the energy profile, and (b) an isometric plot of the wavefront at a distance equal to ten times the Rayleigh length.

The following sections give details on the individual sources considered and Table 6.3 shows the calculated values of the errors associated with each of the above aberrations.

### **Defocus of the telescope**

An integral part of the successful operation of LISA is the ability to change the focus of the telescope. For initial alignment of the s/c along the interferometer arms, the beam diameter will be expanded in the far field to make initial detection of the transmitted light easier. This is achieved by de-focusing the telescope: the position of the fibre output on the optics bench is adjusted, thereby changing the mode-matching into the telescope. Once the far s/c detects the beam from the transmitting craft, the fibre will be moved back to its original position, optimising the mode-matching into the telescope. Moving the fibre can also be used to keep the telescope in focus throughout the operational lifetime of LISA. Motion of the fibre should, however, be kept to a minimum when the instrument is making scientific measurements, as, when the fibre output is moved, not only is the beam mode into the telescope changed, but also the beam size around the optics bench. A change in the beam mode at the rear optical fibre will affect the power throughput to the neighbouring bench, which in turn will affect the phase locking of the other vertex laser.

The biggest single source of focusing error is likely to come from temperature gradients set up between the primary and secondary mirrors, caused by radiative cooling at the secondary end[12]. The current LISA mechanical telescope assembly has the secondary mirror suspended from the primary using three carbon-epoxy struts. Thermal expansion of the struts leads to a change in mirror separation of  $5\ \mu\text{m}$  from ground testing, to in-orbit conditions. However, this can be reduced by making the complete telescope structure (mirrors and struts) from a low linear thermal expansion coefficient material such as Zerodur or ULE[44]. Such a telescope has been constructed and space qualified[68][69], with a change in mirror separation from ground to orbit of  $< 2\ \mu\text{m}$ . With a similar telescope system in LISA, the corresponding fibre movement would be reduced.

Figure 6.8 shows the deviation of the wavefront from the best possible case of Figure 6.7(b). This aberration has been calculated for a change in the mirror separation of  $5\ \mu\text{m}$  from the optimum position. The left hand axis is calibrated in terms of the wavelength of the laser light. The bottom axis is again calibrated in terms of displacement from the optic axis, as well as angular deviation.

### **Tilt of the received wavefront**

The tilt of the wavefront in the far field enters the system in more than one way. The most obvious tilt of the outgoing wavefront is from a mis-alignment of the telescope mirrors. This can enter in two ways. The first is in the manufacture of the telescope. Each telescope will be optically aligned before final assembly into the spacecraft, and then re-checked once fully integrated. However, the best specification that can be guaranteed through ground checking is of the order of 1 arcsec ( $\equiv 5\ \mu\text{rads}$ ).

The second way for the mirrors to become tilted with respect to each other, is again caused by the temperature gradient in the telescope when in orbit. If the telescope is constructed to be identically symmetric along the optic axis, then this error can be small. However, an error of  $3\ \mu\text{rads}$  is expected.

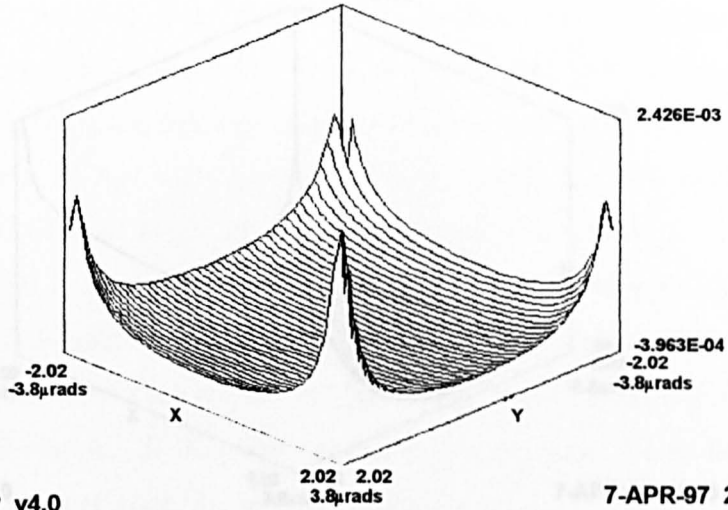
Finally a large source of tilt of the wavefront enters the system through the “point ahead” of the beam. As the receiving s/c aligns itself using a plane wavefront in the detected beam, the re-transmitted beam must be offset in order to intercept the original emitting s/c (see Figure 3.4). The point ahead angle is calculated to be approximately  $5\ \mu\text{rads}$ .

Figure 6.9 shows an isometric plot and cross section of the aberrated wavefront error. This plot is for the case of the primary mirror being tilted with respect to the secondary, and is calculated by subtracting the aberrated wavefront from the reference wavefront (Figure 6.7(b)). The error associated with each tilt source is quoted in Table 6.3.

#### **6.6.3 Calculation of the Wavefront Error**

The displacement noise caused by wavefront error due to the above aberrations is calculated using a cross section of the wavefront data in the far field. As the ASAP

Ritchey - Chretien Telescope : Defocus  
WAV



Ritchey-Chretien Telescope : Defocus  
WAV

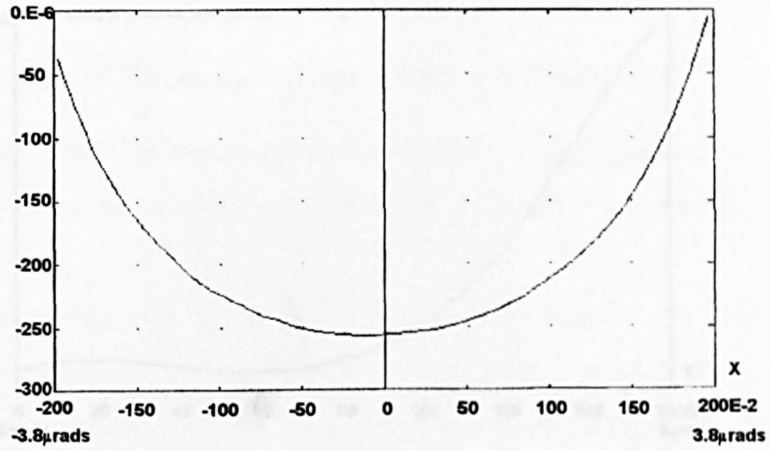
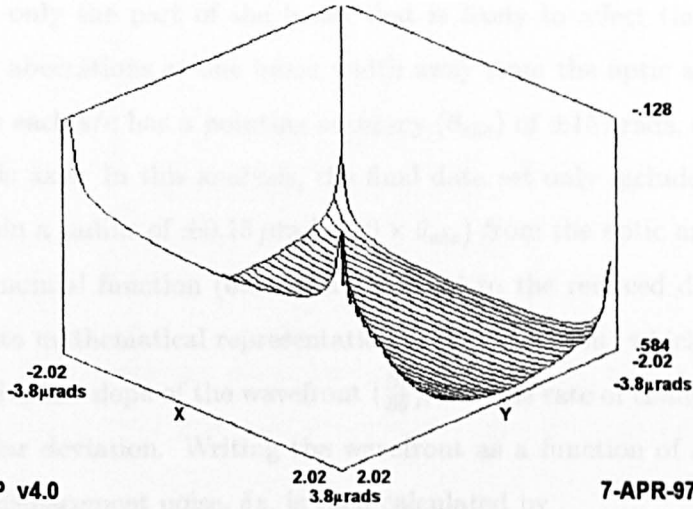


Figure 6.8: ASAP plots of wavefront aberration due to defocus of the telescope. The wavefront aberrations at the extremities of the beam are due to numerical rounding errors in ASAP.

Ritchey - Chretien Telescope : Tilt  
WAV



Ritchey-Chretien Telescope : Tilt  
WAV

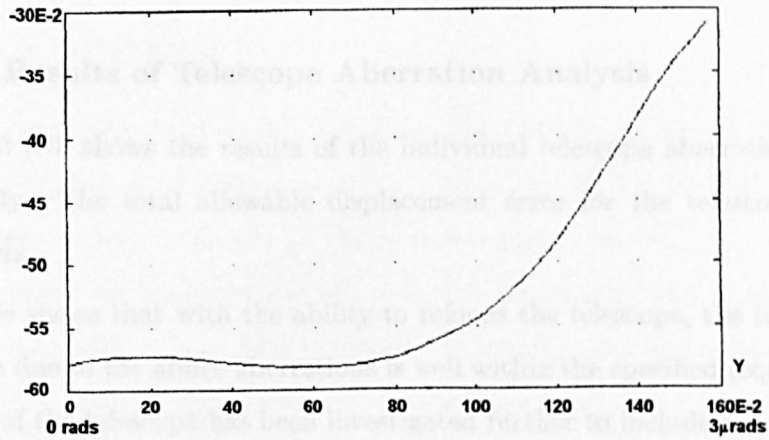


Figure 6.9: ASAP plots of wavefront aberration due tilt of the primary mirror. The wavefront aberrations at the extremities of the beam are due to numerical rounding errors in ASAP.

calculated wavefront (Figures 6.8 and 6.9) is limited at its extremities by numerical rounding errors, the data set is initially reduced to include only the centre of the beam (out to a radius equal to the beam width<sup>7</sup>). The data set is further reduced to include only the part of the beam that is likely to affect the LISA sensitivity. Wavefront aberrations at one beam width away from the optic axis are unlikely to be seen, as each s/c has a pointing accuracy ( $\theta_{abs}$ ) of  $\pm 15$  nrad, centred on or near to the optic axis. In this analysis, the final data set only includes that part of the beam within a radius of  $\pm 0.15 \mu\text{rads}$  ( $10 \times \theta_{abs}$ ) from the optic axis.

A polynomial function (6th order) is fitted to the reduced data set to give an approximate mathematical representation of the wavefront, which is easily differentiated to give the slope of the wavefront ( $\frac{\partial z}{\partial \theta}$ ), *i.e.* the rate of change of displacement with angular deviation. Writing the wavefront as a function of angular deviation, the axial displacement noise,  $\delta z$ , is then calculated by

$$\delta z = \frac{\partial z}{\partial \theta} \cdot \delta \theta \quad (6.13)$$

where  $\delta \theta$  is the pointing “jitter”.

#### 6.6.4 Results of Telescope Aberration Analysis

Table 6.3 [70] shows the results of the individual telescope aberrations mentioned previously. The total allowable displacement error for the telescope is fixed at  $1 \text{ pm}/\sqrt{\text{Hz}}$ .

The table shows that with the ability to refocus the telescope, the total noise contribution due to the above aberrations is well within the specified requirement. The analysis of the telescope has been investigated further to include the effects of form error<sup>8</sup> on the mirrors, and also the above aberrations applied to the components on the optics bench, by Caldwell *et. al.* [70] using the same ASAP telescope model developed in this analysis. Again the analysis shows that the telescope system will

<sup>7</sup>The beam width is defined as the point at which the intensity of the beam falls to  $\frac{1}{e^2}$  of its peak value.

<sup>8</sup>Mirror form error occurs when the shape of the mirror surface differs from the specified shape, defined by the conic constants in Table 6.2

Error Source	Condition	Percentage of Total Telescope Budget
Defocus	$\Delta l = 1.2 \mu\text{m}$ NO-refocus	40%
Defocus	$\Delta l = 2 \mu\text{m}$ With Refocus	< 1%
Tilt	Manufacture Error ( $5 \mu\text{rad}$ )	0.4%
Tilt	Orbit Temp Gradient ( $3 \mu\text{rad}$ )	0.2%
Point Ahead	$5 \mu\text{rad}$	0.4%

Table 6.3: **The telescope error budget for defocus, tilt, and point ahead.** *The percentage of total error budget assumes a total error in displacement noise of  $1 \text{ pm}/\sqrt{\text{Hz}}$ .*

not contribute any significant excess noise to the total displacement sensitivity of the LISA mission.

## 6.7 Conclusions

The optical model of the LISA telescope was initially set up as a starting point for the telescope error budget analysis. However, the original telescope did not produce the correct beam size or shape at the output mirror, and therefore had to be re-designed. In the process of the re-design, the opportunity of using a Ritchey-Chretien two mirror Cassegrain telescope was investigated, and found to give better performance than the corresponding classical Cassegrain.

With the new design of telescope giving the correct beam size and shape at the output, the effects of wavefront aberrations due to the telescope system were investigated. The conclusion drawn from the analysis is that the telescope can be constructed such that the errors associated with it are well within the allowable margin.

## Chapter 7

# Conclusions

The LISA mission presents many technical challenges, particularly in the field of laser interferometry. This thesis has addressed aspects of the necessary laser frequency stabilisation, the weak-light phase-locking and the telescope design.

Laser frequency stability is vital for LISA since unavoidable arm length differences can result in frequency fluctuations causing an apparent gravitational wave signal. In LISA the goal is to stabilise the on-board laser to a reference cavity, resulting in a frequency stability of  $10 \text{ Hz}/\sqrt{\text{Hz}}$  at 1 mHz, limited by the temperature stability of the reference cavity of  $10^{-6} \text{ K}/\sqrt{\text{Hz}}$ . Chapter 4 described an experiment to frequency stabilise a LISA-style laser, and measure the excess frequency noise. Frequency stabilisation by a factor of  $\sim 10^5$  was demonstrated at milliHertz frequencies, consistent with a limit due to the measured thermal fluctuations of the reference cavity used. The achieved stability was still significantly above the LISA goal, but it could be expected that improved thermal stability of the reference cavity would yield the LISA stability goal.

Phase-locked transponding of the very weak light received by a spacecraft is an integral part of the design of LISA. Chapter 5 described the experimental tests of such a phase locking scheme. The intensity of the master laser was attenuated by 9 orders of magnitude (to 50 pW) before being used to offset phase lock an identical slave laser. The relative phase noise of the slave laser was measured using a second optical path, where the powers of the two interfering beams were approximately

equal. Using weak light power levels that were similar to those in LISA, the relative phase noise of the slave laser was limited by the photon shot noise in the weak beam over the frequency band from a few tens of Hz to  $\sim 1$  kHz. At the lower frequencies of relevance to LISA the relative phase noise was seen to rise to approximately one order of magnitude above the shot noise limit. The use of single mode optical fibres to transport the laser light to the optical table will reduce the coupling of seismic noise to beam pointing fluctuations, hence improving the long term stability of the optical chain. This, along with improved thermal isolation of the optics bench, suggests that the slave laser can be stabilised to the level required for LISA.

The original LISA telescope design suffered from a number of shortcomings. Chapter 6 deals with the design of a telescope which offers significantly improved performance. The new design takes the same diameter of primary mirror, but now uses the improved Ritchey-Chretien design. Gaussian raytracing was used to check how near field wavefront aberrations affect the wavefront phase in the far field. Using in-orbit focusing of the beam mode into the telescope, the analysis showed that the residual wavefront errors due to the telescope system will satisfy the LISA requirements.

While each of the areas addressed merits further study, the results obtained in these first investigations are encouraging. The optical challenges of the LISA design seem manageable and the target interferometric sensitivity should be ultimately achievable.

With the growing interest in space-borne laser interferometers, combined with the increasing family of ground based detectors, the future of gravitational wave research has never been more promising, and may soon offer new insights into the astrophysics associated with strong gravitational fields.

## Appendix A

# MATLAB Code To Calculate Voltage Spectral Density

The following MATLAB[71] program has been written to calculate the Voltage Spectral Density (PSD) of a time series, and display the results in graphical format. The data from all the low frequency measurements made were recorded on a computer running LabVIEW[72] virtual instrument language, via the 12-bit, National Instruments data acquisition card, AT-MIO-16D. The data is read in as a voltage time series, and saved in a multi-column data file, with the number of columns (N) being determined by the number of channels of data being acquired. The MATLAB program then reads in the data and sorts it into N separate column vectors. The data is divided into equal length segments. The Power Spectral Density of each time series is then calculated, and the results averaged. The header to the source code listed below gives more details about the use of the MATLAB PSD command.

Before being acquired by the computer, the data is first anti-aliased to remove out of band noise. The effect of the filters is mathematically removed in the MATLAB program, leaving the true Power Spectrum of the data. Finally, before plotting, the power spectrum is converted to the voltage spectrum, and calibrated accordingly (*e.g.* in units of  $\text{Hz}/\sqrt{\text{Hz}}$  or  $\text{rads}/\sqrt{\text{Hz}}$ )

```

%%%%%%%%%%%%%%%%%%%%%%%%%%%%%%%%%%%%%%%%%%%%%%%%%%%%%%%%%%%%%%%%%%%%%%%%
%%%
%%%                                     Power Spectral Density      %%%
%%%
%%% This program reads in a file containing one column of data. If the %%%
%%% data is contained in more than one row, (e.g. raw data and time), %%%
%%% then split into single columns using program FILE.M. The first few %%%
%%% lines of set up the variables for use later on. The important ones %%%
%%% to change are "samp-freq", "num-av", "k" (length of FFT). The other %%%
%%% variables (rf_resp" to "mix-resp" are use to calculate the shot %%%
%%% noise limit of the measurement. Variables "fc" to "c" are the chara- %%%
%%% cteristics of the pre-whitening and anti-aliasing filters. "fc" is %%%
%%% the corner frequency of the anti-aliasing filters, "n" is the %%%
%%% number of poles, "r1", "r2", and "c" define the high pass transit- %%%
%%% ional pre-whitening filter. The "window constants" are used to %%%
%%% correct magnitude of the output of the windowing function. Change %%%
%%% the later lines of code depending on the window function being used. %%%
%%%
%%% The "for" loops calculate the power spectral density (PSD) of the %%%
%%% data and take the average (depending on "num_av"). The full data set %%%
%%% is split into "num_av" sections of data, each of length "k". This %%%
%%% way PSD only sees a set of data of length NFFT. If data length is %%%
%%% less than NFFT, then PSD automatically averages the output (in some %%%
%%% way). After the "for" the data is averaged and corrected for the %%%
%%% window function, then effects of the anti-aliasing filters and pre- %%%
%%% whitening filters are removed. If data contains peaks (and the %%%
%%% magnitude of the peaks is important) then set "W" equal to %%%
%%% "norm(w)^2/sum(w)^2", as in Signal Processing manual. If the data %%%
%%% is noisy (i.e. peak heights are not important) then set W=1. The %%%
%%% conversion to "dBVrms/rtHz" is very strange. It appears that the %%%
%%% output of psd only makes sense when it is divided by twice the %%%
%%% sampling frequency. This is described briefly in the Matlab %%%
%%% Technical Support note #7250. %%%
%%%
%%% The rest of the file calculates the shot noise limit to the measur- %%%
%%% ement, by using the size of the beat notes, and the response of the %%%
%%% photodiodes (see lab book for more details of the calculation). %%%
%%% Finally a graph is drawn of the data, and title and labels added. %%%
%%%
%%%%%%%%%%%%%%%%%%%%%%%%%%%%%%%%%%%%%%%%%%%%%%%%%%%%%%%%%%%%%%%%%%%%%%%%
clear all % Reset all values to zero
format long e % Use double precision numbers

load time_s.txt % Load measurement data set
data = time_s(:,1)/30; % Let Data = measure "error point" data set
data2 = time_s(:,3)/50; % Let Data2 = PZT feedback data set
data3 = time_s(:,2)/1e4;% Let Data3 = Locking side error point

pi=3.14159265359; % pi to too many decimal places
ec = 1.6021892e-19; % Electric charge (also to too many places)

%%%%%%%%%%%%%%%%%%%%%%%%%%%%%%%%%%%%%%%%%%%%%%%%%%%%%%%%%%%%%%%%%%%%%%%%
%%%
%%%                                     Definition of calibration variables and %%%

```

```

%%%                               anti-aliasing filter variables                               %%%
%%%                               %%%
%%%%%%%%%%%%%%%%%%%%%%%%%%%%%%%%%%%%%%%%%%%%%%%%%%%%%%%%%%%%%%%%%%%%%%%%%%%%%%

rf_resp = 3; % Response of the lock diode to rf signals (3mV/uA)
DC_resp = 1; % Locking diode response to DC (1mV/uA)
lock_beat = 55; % RF beat note at the locking mixer (mV)
lock_DC = 1531; % Locking diode DC output (mV) - Response : 1mV/uA
meas_beat = 560; % Measurement side beat note at mixer (mV)
volt = 0.1; % Calibration of mixer : volt(V) = mix_resp(degrees)
mix_resp = 0.6; % Measure mixer response :volt(V)=mix_resp (degrees)
pzt_resp = 0.3e6; % Response of PZT in slave laser : 1V=pzt_resp (Hz)
temp_resp = 3125e6; % Response of temperature controller of miser
lock_mix_resp = 2.9; % Lock mixer resp : volt(V)=lock_mix_resp (degrees)

fc = 3000; % -3dB point of antialiasing filters
epfc = 300; % -3db point of antialiasing of lock side error point
fc_l = 300; % -3db point of L.P. antialiasing of PZT feedback
fc_h = 300; % -3db point of high pass filter in PZT feedback
n = 16; % Number of poles of antialiasing (measurement side)
ml = 1; % Number of poles of L.P. filters (feedback side)
mh = 1; % Number of poles of H.P. filters (feedback side)
nep = 2; % Number of poles of locking side error point

r1 = 1.5e6; % Size of parallel R in H.P. transitional filter
r2 = 1500; % Size of grounded R in H.P. transitional filter
c = 10.02e-6; % Size of capacitor in H.P. transitional filter
rlpt1 = 4700; % Size of parallel R in L.P. trans filter }
rlpt2 = 470; % Size of series R in L.P. trans filter } Locking
clpt = 4e-6; % Size of cap in L.P. trans filter } Side

k = 65536; % k = Length of each data set
num_av=1; % num_av = Number of averages to be taken
samp_freq=2; % Sampling Frequency used in LabVIEW

w=hanning(k); % Window function and length to be used
%w=0.5*(1-cos(2*pi*(0:k-1)/k)); % Non-symmetric, periodic Hanning
%w=1-cos(2*pi/k) % Hanning window used in Stanford Analyser

High_pass_roll_on = 1/(2*pi*r1*c) % Echo to screen pre-whitening filter,
High_pass_roll_off = 1/(2*pi*r2*c) % antialiasing filters, number of samples
Anti_aliasing = fc % per spectra, number of averages, and
No_samps_per_spectra = k % sampling frequency.
Sampling_freq = samp_freq %

hann_wind_const = 1.5; % Window constants for different window functions
hamm_wind_const = 1.36;
black_harris_wind_const = 1.708538;
black_wind_const = 1.726757;
flat_wind_const = 2.965606;
no_window = 1;

%%%%%%%%%%%%%%%%%%%%%%%%%%%%%%%%%%%%%%%%%%%%%%%%%%%%%%%%%%%%%%%%%%%%%%%%%%%%%%
%%%                               %%%
%%% Calculation of the relative phase noise of the slave laser, %%%
%%% measured using independant path %%%
%%%%%%%%%%%%%%%%%%%%%%%%%%%%%%%%%%%%%%%%%%%%%%%%%%%%%%%%%%%%%%%%%%%%%%%%%%%%%%

```

```

%%%                                                                 %%%
%%%%%%%%%%%%%%%%%%%%%%%%%%%%%%%%%%%%%%%%%%%%%%%%%%%%%%%%%%%%%%%%%%%%%%%%

for p=1:((k/2)+1), % Set array values to be zero
    pnew(p,1)=0;
    pold(p,1)=0;
end % End of loop to set values to zero

for i=1:num_av, % Averaging Loop
    pold=pnew; % Let old array values equal new values

    for j=1:k, % Work out which part of data array to be used
        o=((i-1)*k)+j; % Splits up array to sections of length k
        elem(j,1)=data(o,1); % Set elem to equal part of array to be analysed
    end % End of loop to calculate elements

    [pxx,fs] = psd(elem,k,samp_freq,w,0); % Take PSD of data

    % plpxx=10*log10(pxx); %
    % plot(fs,plpxx)      % Plot individual FFTs before averaging
    % axis([0 800 -80 20]);grid;title 'this one!' %
    % figure              %

    for p=1:((k/2)+1), % Sum up psd array components to calculate average
        pnew(p,1)=pold(p,1)+(pxx(p,1));
    end % End of loop to sum individual elements

end % End of averaging loop

df = length(fs)/k      % Calculate frequency spacing of points
window_const = df*hann_wind_const

pav = pnew/(num_av*window_const); % Take average of FFTs
                                     % and scale psd to correct /rtHz

%low1 = (sqrt(1 + ((fs/fc).^(2)))).^(-1); % Transfer function of
                                     % single pole RC low pass filter
%low_pass = low1.^(n); % Transfer function of "n" poles of filtering

butter = (sqrt(1+(fs/fc).^(2*n))).^(-1); % Transfer Function of
low_pass = butter; % Butterworth Filter

alias_pav = pav.*(low_pass.^(1)); % Remove effects of anti-aliasing filters

% Calculating effect of High Pass filter on the output, used to suppress
% DC drifts and hence allow more of the dynamic range of the DAQ to be used
high1 = (r2^2)*(1+(2*pi*c*r1.*fs(:,1)).^2);
high2 = (r2*2*pi*c*r1.*fs(:,1)).^2;
high3 = (r1^2)+(2*r1*r2)+(r2^2);
high_pass = sqrt(high1.*((high2 + high3).^(1)));

true_pav = alias_pav.*(high_pass.^(1)); % Remove effects of the H.P. filter

%loglog(fs,pav,'y',fs,true_pav,'g'); % Show difference between
%title 'This One!!!' % corrected and uncorrected data

```

```

%figure % New figure

W = 1; % Used to get correct noise level
%W=norm(w)^2/sum(w)^2; % Normalisation of the spectrum to fix peak heights
pavdb = 10*log10(2*W*(true_pav/(2*samp_freq))); % Convert to dBVrms/rHz
pavrad = (10.^(pavdb/20))*(mix_resp/volt)/(180/pi); % Convert to rads/rHz

loglog(fs,pavrad,'b'); % Plot Data on a log-log plot
hold

%%%%%%%%%%%%%%%%%%%%%%%%%%%%%%%%%%%%%%%%%%%%%%%%%%%%%%%%%%%%%%%%%%%%%%%%
%%%
%%%      Calculation of the unstabilised slave laser phase noise      %%%
%%%
%%%%%%%%%%%%%%%%%%%%%%%%%%%%%%%%%%%%%%%%%%%%%%%%%%%%%%%%%%%%%%%%%%%%%%%%

for p=1:(k/2)+1, % Set array values to be zero
    unstab_new(p,1)=0;
    unstab_old(p,1)=0;
end % End of loop to set values to zero

for x=1:num_av, % Averaging Loop
    unstab_old=unstab_new;% Let old array values equal new values

    for y=1:k, % Work out which part of data array to be used
        z=((x-1)*k)+y; % Splits up array to sections of length k
        uelem(y,1)=data2(z,1); % Set elem to equal part of array to be analysed
    end % End of loop to calculate element

    [uxx,fs] = psd(uelem,k,samp_freq,w,0); % Take PSD of data

    % plpxx=10*log10(pxx); %
    % plot(fs,plpxx) % Plot individual FFTs before averaging
    % axis([0 800 -80 20]);grid;title 'this one!' %
    % figure %

    for q=1:(k/2)+1, % Sum up psd array in order to calculate average
        unstab_new(q,1)=unstab_old(q,1)+(uxx(q,1));
    end % End of loop to sum individual elements

end % End of averaging loop

unstab = unstab_new/(num_av>window_const); % Take average of FFTs
        % and scale psd to correct /rHz

%polyf = polyfit(hvfreq,hvdata,30); % Fit polyn to transfer fnct to data

%t_function = 10.^((polyval(polyf,fs))/20); % Transfer function of
        % HV amp and last filter

%correct_unstab = unstab.*t_function; % Remove effects of high
        % voltage amp, and following filter

low1 = (sqrt(1 + ((fs/fc_1).^2))).^(-1); % Transfer function of single
        % pole RC L.P. filter

```

```

low_pass = low1.^(ml); % Transfer function of "m" poles of filtering

alias_unstab = unstab.*(low_pass.^(-1));

high1 = fs/fc_h;
high2 = sqrt(1 + ((fs/fc_h).^2));
high_pass = (high1.*(high2.^(-1))).^(mh);

true_unstab = alias_unstab.*(high_pass.^(-1));

W = 1; % Used to get correct noise level
%W=norm(w)^2/sum(w)^2; % Normalisation of the spectrum to fix peak heights
unstab_db = 10*log10(2*W*(true_unstab/(2*samp_freq)));
% Convert to dBVrms/rHz
unstab_rad = (10.^(unstab_db/20))*pzt_resp.*(fs.^(-1));
% Convert to frequency and then rads/rHz

loglog(fs,unstab_rad,'r'); % Plot Data on a log-log plot

%%%%%%%%%%%%%%%%%%%%%%%%%%%%%%%%%%%%%%%%%%%%%%%%%%%%%%%%%%%%%%%%%%%%%%%%%%%%%%
%%%
%%% Calibration of locking side error point
%%%
%%%%%%%%%%%%%%%%%%%%%%%%%%%%%%%%%%%%%%%%%%%%%%%%%%%%%%%%%%%%%%%%%%%%%%%%%%%%%%

for p=1:(k/2)+1, % Set array values to be zero
    epnew(p,1)=0;
    epold(p,1)=0;
end % End of loop to set values to zero

for i3=1:num_av, % Averaging Loop
    epold=epnew; % Let old array values equal new values

    for j3=1:k, % Work out which part of data array to be used
        o3=((i3-1)*k)+j3; % Splits up array to sections of length k
        elem(j3,1)=data3(o3,1); % Set elem to equal part of array to be analysed
    end % End of loop to calculate elements

    [epxx,fs] = psd(elem,k,samp_freq,w,0); % Take PSD of data

    % plpxx=10*log10(pxx); %
    % plot(fs,plpxx) % Plot individual FFTs before averaging
    % axis([0 800 -80 20]);grid;title 'this one!' %
    % figure %

    for p3=1:(k/2)+1, % Sum up psd array in order to calculate average
        epnew(p3,1)=epold(p3,1)+(epxx(p3,1));
    end % End of loop to sum individual elements

end % End of averaging loop

df = length(fs)/k % Calculate frequency spacing of points
window_const = df*hann_wind_const

epav = epnew/(num_av*window_const); % Take average of FFTs

```

```

% and scale psd to correct /rtHz

lp_trans1 = 1 + ((2*pi.*fs*rlpt2*clpt).^2);
lp_trans2 = 1 + ((2*pi.*fs*clpt*(rlpt1 + rlpt2)).^2);
lp_trans = sqrt(lp_trans1.*(lp_trans2.^(-1)));

correct_epav = epav.*(lp_trans.^(-1));

low1 = (sqrt(1 + ((fs/epfc).^2))).^(-1);
% Transfer function of single pole RC L.P. filter
low_pass = low1.^(nep); % Transfer function of "n" poles of filtering

alias_epav = correct_epav.*(low_pass.^(-1));
% Remove effects of anti-aliasing filters

W = 1; % Used to get correct noise level
%W=norm(w)^2/sum(w)^2; % Normalisation of the spectrum to fix peak heights
epavdb = 10*log10(2*W*(alias_epav/(2*samp_freq))); % Convert to dBVrms/rtHz
epavrad = (10.^(epavdb/20))*(lock_mix_resp/volt)/(180/pi);
% Convert to rads/rtHz

loglog(fs,epavrad,'m'); % Plot Data on a log-log plot

%%%%%%%%%%%%%%%%%%%%%%%%%%%%%%%%%%%%%%%%%%%%%%%%%%%%%%%%%%%%%%%%%%%%%%%%%%%%%%
%%%
%%% Calculation the shot noise limit for the photocurrents staed above %%%
%%%
%%%%%%%%%%%%%%%%%%%%%%%%%%%%%%%%%%%%%%%%%%%%%%%%%%%%%%%%%%%%%%%%%%%%%%%%%%%%%%

weak_curr = ((0.5*lock_beat/(2*rf_resp))^2)/(lock_DC*DC_resp);
% Calculate the amount of weak photoc at lock diode
sht_nois = sqrt(ec*(1/(weak_curr*1e-6))); % Estimation of shot noise level
% (dominated by weak light)
Shot_noise = (sht_nois).*fs.*(fs.^(-1)); % Make an array of length fs
loglog(fs,Shot_noise,'g'); % Plot a log-log plot of the shot noise level

%%%%%%%%%%%%%%%%%%%%%%%%%%%%%%%%%%%%%%%%%%%%%%%%%%%%%%%%%%%%%%%%%%%%%%%%%%%%%%
%%%
%%% Calculate limits to axes and print title and axes labels %%%
%%%
%%%%%%%%%%%%%%%%%%%%%%%%%%%%%%%%%%%%%%%%%%%%%%%%%%%%%%%%%%%%%%%%%%%%%%%%%%%%%%

low_y = min(epavrad)/10; % Automatically scale the axes -
% 10 times lower than Shot Noise
high_y = max(unstab_rad)*10; % Ten times higher than highest data point
low_x = 0; % Set lowest x-value to be 0
high_x = samp_freq/2; % Set highest x-value to be at Nyquist Freq

axis([low_x high_x low_y high_y]) % Set axis to desired values
grid % Put grid on graph
title 'Relative phase noise of slave laser, measured using independant path'
xlabel 'Fourier Frequency (Hz)' % Put label on x-axis
ylabel 'Relative Phase Noise (rads/rtHz)' % Put label on y-axis
hold

```

```
save samp_freq.txt fs -ascii %
save pav.txt pav -ascii      % Save data to file to be plotted later
save true_pav.txt true_pav -ascii
save pavdb.txt pavdb -ascii  %
```

## Appendix B

# Telescope Model: Source Code

### B.1 CODEV Model of LISA Telescope System

The following telescope model is written in the optical design package, CODEV[54]. The telescope model includes the optical chain starting at the lens at the output of the fibre, through to the primary mirror of the telescope. All surfaces are assumed to stretch to infinity, thereby ensuring that the beam must hit the next surface. This allows the optical path to be visually checked, to ensure that a beam waist is not formed at the wrong position. The program can then be changed to perform a Gaussian beam analysis through the system. In this mode, the program does not perform a graphical raytrace, but instead outputs the beam parameters (width, radii of curvature etc.) in tabular format, an example of which is shown after the source code listing.

## Appendix B

# Telescope Model: Source Code

### B.1 CODEV Model of LISA Telescope System

The following telescope model is written in the optical design package, CODEV[64]. The telescope model includes the optical chain starting at the lens at the output of the fibre, through to the primary mirror of the telescope. All surfaces are assumed to stretch to infinity, thereby ensuring that the beam must hit the next surface. This allows the optical path to be visually checked, to ensure that a beam waist is not formed at the wrong position. The program can then be changed to perform a Gaussian beam analysis through the system. In this mode, the program does not perform a graphical raytrace, but instead outputs the beam parameters (width, radii of curvature *etc.*) in tabular format, an example of which is shown after the source code listing.



```

!!!!!!!!!!!!!!!!!!!!!!!!!!!!!!!!!!!!!!!!!!!!!!!!!!!!!!!!!!!!!!!!!!!!!!!!!!!!!!

!!!!!!!!!!!!!!!!!!!!!!!!!!!!!!!!!!!!!!!!!!!!!!!!!!!!!!!!!!!!!!!!!!!!!!!!!!!!!!
!!!   Defining Variables   !!!
!!!!!!!!!!!!!!!!!!!!!!!!!!!!!!!!!!!!!!!!!!!!!!!!!!!!!!!!!!!!!!!!!!!!!!!!!!!!!!

!^range==1e8           ! 100 km required for raytrace (must be large)
^range==1e-5           ! Required for Gaussian beam (small ^0)
^diam==300             ! Primary mirror diameter
^n==1.449629           ! Refractive index (Silica in this case)
^t==3.0                ! Thickness of lenses (mm)
^wfoc==0.007           ! Beam size at fibre (mm)
^ofs==0+^t/2           ! Distance of collimating lens surface
                       ! to primary

EPD  ^diam             ! Exit pupil diameter
DIM  M                 ! Dimensions
WL   1064              ! Wavelength of light (WL assumes nm)
REF  1
WTW  1
INI  'ORA'
XOB  0.0
YOB  0.0
VUY  0.0
VLY  0.0

!!!!!!!!!!!!!!!!!!!!!!!!!!!!!!!!!!!!!!!!!!!!!!!!!!!!!!!!!!!!!!!!!!!!!!!!!!!!!!
!!!                               Telescope Parameters                               !!!
!!!!!!!!!!!!!!!!!!!!!!!!!!!!!!!!!!!!!!!!!!!!!!!!!!!!!!!!!!!!!!!!!!!!!!!!!!!!!!

!!!!!!!!!!!!!!!!!!!!!!!!!!!!!!!!!!!!!!!!!!!!!!!!!!!!!!!!!!!!!!!!!!!!!!!!!!!!!!
!!!   For telescope   !!!
!!!!!!!!!!!!!!!!!!!!!!!!!!!!!!!!!!!!!!!!!!!!!!!!!!!!!!!!!!!!!!!!!!!!!!!!!!!!!!

^d12==^fo1*(^x1-^x2)/^x1 ! Mirror separation
^b==( ^xe*^d12)/(^x2-^xe) ! Back focal length
^p==^d12/^fo1            ! 1/(Fnumber)
^et==^b/^fo1            ! Back focal length/primary focal length
^m==( ^et+^p)/(1-^p)     ! Magnification of secondary
^fos==^m*^fo1           ! Focal length of system
^fo2==^fo1*^m*(1-^p)/(^m-1) !focal length of secondary
^sc1=-1*(1+(2*(1-^p)/(^m*^m*^p))) !Schwarzschild Constant of primary
^sc2=-1*(2*^m/(((^m-1)**3)*^p)+(((^m+1)/(^m-1))**2))
                       ! Schwarzschild (conic) constant of secondary

!!!!!!!!!!!!!!!!!!!!!!!!!!!!!!!!!!!!!!!!!!!!!!!!!!!!!!!!!!!!!!!!!!!!!!!!!!!!!!
!!!   For thin lens approximation   !!!
!!!!!!!!!!!!!!!!!!!!!!!!!!!!!!!!!!!!!!!!!!!!!!!!!!!!!!!!!!!!!!!!!!!!!!!!!!!!!!

!^diop==-26.55          ! Power of collimating lens (at telescope)
!^diop2==32.76         ! Power of focusing lens (at fibre)

!!!!!!!!!!!!!!!!!!!!!!!!!!!!!!!!!!!!!!!!!!!!!!!!!!!!!!!!!!!!!!!!!!!!!!!!!!!!!!
!!!   For thick lens approximation   !!!
!!!!!!!!!!!!!!!!!!!!!!!!!!!!!!!!!!!!!!!!!!!!!!!!!!!!!!!!!!!!!!!!!!!!!!!!!!!!!!

^diop==-25.6           ! Power of collimating lens (at telescope)
^diop2==32.2046       ! Power of focusing lens (at fibre)

```



```

S    -r2 0  air          ! Focusing lens (second side)

!!!!!!!!!!!!!!!!!!!!!!
!!!   Image   !!!
!!!!!!!!!!!!!!!!!!!!!!
SI    0.0 0.0           ! Image plane

!!!!!!!!!!!!!!!!!!!!!!
!!!                               Raytrace and Gaussian Analysis          !!!
!!!!!!!!!!!!!!!!!!!!!!

!!!!!!!!!!!!!!!!!!!!!!
!!!   Option to analyse telescope only - Raytrace   !!!
!!!!!!!!!!!!!!!!!!!!!!
!del s3..6             ! Delete objects 3 to 6
!draw                  ! Remember to change range above
!GOT endl              ! End program

!!!!!!!!!!!!!!!!!!!!!!
!!!   Optical Chain Analysis   !!!
!!!!!!!!!!!!!!!!!!!!!!
FLY S1..i-1           ! Flip order of optical components
nao 0.0483831         ! Numerical aperture (beam dispersion)
thi so 30             ! Distance from fibre to lens
thi s6 1000           ! Image distance (as a check)
sto s1                ! Source is at object 1
GO                    ! Analyse optics chain
out t dum             ! Direct output to terminal and file dum.lis

!!!!!!!!!!!!!!!!!!!!!!
!!!   Gaussian Beam Analysis   !!!
!!!!!!!!!!!!!!!!!!!!!!
BEA                   ! Gaussian beam propagation (need short range)
wrx ~wfoc             ! Set waist size on object (at fibre)
go                    ! Do Gaussian analysis
out t                 ! Direct output to screen

LBL end              ! Label - End of program

```

Table B.1: Results from CODEV Gaussian beam analysis

Table B.1: Results from CODEV Gaussian beam analysis

GAUSSIAN BEAM PROPAGATION											
POSITION 1					Ritchey						
FIELD POSITION = ( 0.00, 0.00)					DIMENSIONS = MILLIMETERS			WAVELENGTH = 1064.0 NM			
DISTANCE FROM WAIST TO SURFACE		WAIST RADIUS BEFORE REFRACTION		PHASE ORIENTATION ( DEGREES )	WAVEFRONT RADIUS OF CURVATURE BEFORE REFRACTION		BEAM ORIENTATION ( DEGREES )	BEAM RADIUS ON SURFACE		PROPAGATION DISTANCE TO NEXT SURFACE	SUR
X	Y	X	Y		X	Y		X	Y		
0.0000	0.0000	0.0070	0.0070	0.0	INF	INF	0.0	0.0070	0.0070	30.0000	OBJ
-30.0000	-30.0000	0.0070	0.0070	0.0	-30.0007	-30.0007	0.0	1.4515	1.4515	3.0000	1
88.5028	88.5028	0.138	0.138	0.0	-88.5102	-88.5102	0.0	1.5024	1.5024	360.0000	2
279.3325	279.3325	1.5023	1.5023	0.0	-159261.84	-159261.84	0.0	1.536	1.536	3.0000	3
117.6599	117.6599	0.0178	0.0178	0.0	-117.6756	-117.6756	0.0	1.5430	1.5430	271.600	4
311.6730	311.6730	0.0088	0.0088	0.0	-311.6731	-311.6731	0.0	12.005	12.005	-273.100	5
-299.9967	-299.9967	0.0008	0.0008	0.0	299.9967	299.9967	0.0	138.499	138.499	100.0000	6
21616971.22	21616971.22	61.6131	61.6131	0.0	-0.27429E8	-0.27429E8	0.0	138.504	138.504		IMG

## B.2 ASAP Model of LISA Telescope System

The ASAP model again initially calculates the telescope parameters, before performing a full Gaussian raytrace through the system. The program then propagates the beam out to a distance of ten times the Rayleigh length, before re-analysing the energy profile, and wavefront aberrations. The near-field wavefront can be aberrated in the following ways:

0) Nominal	Beam clipped purely by telescope aperture
1) Defocus	Mirror separation changed from optimum
2) Tilt	Primary tilted with respect to secondary
3) Spider	Spider and secondary obscuration included
4) Ripple	Form Error included on primary mirror
5) Nothing	Simple Gaussian propagated (no aberration)

chosen by setting the ABCHOIC variable at the start of the program.

All results (near and far field) are stored in the files with extension .DIN and .DIS. DIN files save the data in **ascii** format, which can be read into a mathematical analysis program, MATLAB. The .DIS files are **display** files and are used to generate plots of the wavefront, energy, *etc.*

```

!!!!!!!!!!!!!!!!!!!!!!!!!!!!!!!!!!!!!!!!!!!!!!!!!!!!!!!!!!!!!!!!!!!!!!!!!!!!!!!!!!!!!!!!!!!!!!!!!!!!!!!!!!!!!!!!!!!!!!!!
*****
!* ASAP program to look at aberrations with of the 30cm Ritchey-Chretien  *!
!* type telescope.                                                         *!
!*                                                                           *!
!* Paul McNamara                                                            *!
!* April 1997                                                                *!
!*                                                                           *!
*****
!!!!!!!!!!!!!!!!!!!!!!!!!!!!!!!!!!!!!!!!!!!!!!!!!!!!!!!!!!!!!!!!!!!!!!!!!!!!!!!!!!!!!!!!!!!!!!!!!!!!!!!!!!!!!!!!!!!!!!!!

```

```

!!!!!!!!!!!!!!!!!!!!!!!!!!!!!!!!!!!!!!!!!!!!!!!!!!!!!!!!!!!!!!!!!!!!!!!!!!!!!!!!!!!!!!!!!!!!!!!!!!!!!!!!!!!!!!!!!!!!!!!!
*****
!* Adapted from RUN2D2.INR (pmn)                                           *!
!*                                                                           *!
!* ASAP program to model the effects of the telescope system on the output*!
!* wavefront of the LISA system.                                           *!
!*                                                                           *!
!* The program is taken from the CODEV code - Ritchey.seq. This sets up  *!
!* a Ritchey-Chretien model of a 30cm aperture telescope, with beam sizes *!
!* applicable to the LISA design of March 1997. See pmn for details of    *!
!* the telescope design.                                                  *!
!*                                                                           *!
!* This program takes the known parameters of the telescope. In this case *!
!* the focal length of the primary, and the beam sizes on the primary,    *!
!* secondary, and output plane of the primary. It makes the simplification*!
!* of assuming plane wavefronts in the telescope, therefore using         *!
!* geometrical optic techniques to work out the various parameters,       *!
!* although final analysis is conducted with a full Gaussian raytrace.    *!
!*                                                                           *!
!* The program offers five choices:                                        *!
!* 0) Nominal - This sets up a beam clipped by the telescope aperture. So *!
!*           there are no wings to the Gaussian beam.                    *!
!* 1) Defocus - Changes the separation of the primary and secondary        *!
!*           mirrors, causing the telescope to become defocused.         *!
!* 2) Tilt    - Puts a tilt angle in between the primary and secondary    *!
!*           mirror. Can either tilt primary or secondary.               *!
!* 3) Spider  - This cuts out the spider and secondary from the main     *!
!*           transmitted and received beams.                              *!
!* 4) Ripple  - Puts a ripple on the primary mirror. Can change order and *!
!*           amplitude of ripple.                                         *!
!* 5) Nowt    - Transmits a perfect Gaussian, with no clipping of the    *!
!*           the wings.                                                   *!
!*                                                                           *!
*****
!!!!!!!!!!!!!!!!!!!!!!!!!!!!!!!!!!!!!!!!!!!!!!!!!!!!!!!!!!!!!!!!!!!!!!!!!!!!!!!!!!!!!!!!!!!!!!!!!!!!!!!!!!!!!!!!!!!!!!!!

```

ABCHOIC=0 ! 0=nominal 1=defoc (astig) 2=tilt 3=spid 4=ripple 5=nowt

!The files are numbered by their symmetry and ripple order. So the  
!second order symmetric ripple is called "RIPXS.DIS", and the third order  
!antisymmetric ripple is called "RIPXA.DIS".

```

***** Initialise Variables *****
RIPDON=0 ! Is the ripple file done (1) or does it need re-calcn (0)?
DELT=0   ! For defocus. Change mirror separation by delta

```

```

TANG_P=0 ! For tilting of primary
TANG_S=0 ! For tilting secondary

RAYS 0 ! Create new set of rays
SYS NEW ! Wipe out all old objects

UNITS M ! Metres
PI=3.14159265359 ! Pi to too many decimal places

DIAM=0.3 ! Primary mirror diameter
LAM=1.064E-6 ! Wavelength in meters

RAYS 0 ! Create new ray set
BEAMS COHERENT DIFFRACT ! Using monochromatic, coherent, Gaussian beam
WAVELENGTH LAM. M ! Set wavelength as LAM.
PARA 8; WIDTH 1.414 ! Number of paraboloidal rays, and widths (if
! PARA = 4 or 8, beam is Gaussian)

WX=0.446*DIAM./2 ! Beam waist size on primary mirror
WY=WX. ! Makes it a circular beam
T=3E-3 ! Thickness of lenses
N=1.449629 ! Refractive index of silica
SDET=1.5 ! Distance to detector for rippled surface

MEDIA ! Set up media
1.0 *VAC ! Assume system in vacuum

$IF ABCCHOIC. EQ 1 THEN set the extra mirror separation
DELTA=10E-6 metres ! Delta is amount of prim/sec separation error
$ENDIF

$IF ABCCHOIC. EQ 2 THEN ! Set the tilt angles - input radians
TANG_P=(180/PI.)*0.0 ! Tilt angle for the primary (in degrees)
TANG_S=(180/PI.)*5E-6 ! Tilt angle for the secondary
$ENDIF

*****
*** ! Telescope Parameters ! ***
*****

*****! Known Parameters !*****
***
F1=0.300 ! Focal length of primary ***
XE=1.5E-3 ! Beam radius at output through primary ***
X1=0.1338 ! Beam radius on primary ***
X2=0.012 ! Beam radius on secondary ***
***
*****

*****! Parameters to be calculated !*****
***
D12=F1.*(X1.-X2.)/X1. ! Separation of mirrors ***
B=(XE.*D12.)/(X2.-XE.) ! Back focal length ***
P=D12./F1. ! 1 / F number ***
ET=B./F1. ! Back FL / Primary FL ***
M=(ET.+P.)/(1.-P.) ! Magnification of secondary ***

```

```

FS=F1.*M.                ! System focal length          ***
F2=F1.*M.*(1-P.)/(M.-1) ! Secondary focal length          ***
SC1=-1*(1+(2*(1-P.)/(M.*M.*P.)))          ***
SC2=-1*(2*M./(((M.-1)^3)*P.))+(((M.+1)/(M.-1))^2))          ***
***                ! Schwarzschild (conic) constants ***
***                ! for primary and secondary          ***
***
*****
*****! Collimating lens !*****
***                ! Using Thick lens approximation !          ***
***
DIOP1=-25.6              ! Power of collimating lens          ***
DIOP2=32.2046           ! Power of focusing lens          ***
FLENS=1/DIOP1.          ! Focal length of coll lens          ***
*****
***! Collimating lens radii of curvature for given thickness ***
***! refractive index, and power          ***
***
RN=2+SQRT(4-(4*DIOP1.*T./N.))! Thick lens formula          ***
RD=2*DIOP1./(N.-1)      ***
R=RN./RD.              ***
***
*****
*****                ! End of Telescope Parameters !          ***
*****
!$GO notel              ! Option to bypass creating telescope
PMFAC=1.5               ! Make mirror surface bigger than beam

**** Primary Mirror ****
SURFACE
  OPTICAL Z 0 -2*F1. SC1.
  LOCAL -4@(PMFAC.*0.15) -2@(PMFAC*0.0285)
  OBJECT; .1 *PRIMARY_MIRROR
  INTERFACE 1 0 VAC VAC ! 1=100% reflecting | 0=100% trans
  ROTATE X TANG_P.      ! Rotate primary by TANG_P degrees
  SHIFT Z 1.000         ! Move mirror to correct location

**** Secondary Mirror ****
SURFACE
  OPTICAL Z 0 -2*F2. SC2.
  LOCAL -4@(2*0.015) -2@0.0285 Z
  OBJECT; .1 *SECONDARY_MIRROR
  INTERFACE 1 0 VAC VAC ! 1=100% reflecting | 0=100% transmitting
  ROTATE X TANG_S.      ! Rotate mirror by TANG_S degrees
  SHIFT Z (1.00-D12-DELT.) ! Move mirror to correct location

**** Detector ****
SURFACE
  PLANE Z 0              ! Set up plane in which detector is located
  LOCAL -2@0.3 -2@0.3 -2@0.001 Z ! Size of detector
  OBJECT; .1 *DETECTOR
  INTERFACE 0 1 VAC VAC

```

```

SHIFT Z -0.0          ! Allows position of det to be changed

RET                  ! Return to main program
notel                ! Label for notel GOTO command

*****

*****
***                  Setting up Source                    ***
*****

*****! Define one ray with gaussian beam shape !*****
WXO=8.8E-6           ! Virtual waist size for telescope system
WYO=WXO.             ! Circular beam
THLIM=1.65*57.3*LAM./(PI.*WXO.) !Divergence angle (deg). 1.65 fudge factor
RAYS Z 0             ! Create rayset at Z=0
x 0 y 0 f 1000 xp (0.88695*WXO.) yp (0.88695*WYO.)
                    ! Centred on origin (x=0, y=0)
                    ! flux=1000, beam size=WXO
                    !(0.88695=scaling factor)
SHAPE -2            ! Gaussian Shape
SOURCE DIRECTION 0 0 -1 ! Source radiates in -z direction
RET

!$GO nodecom        ! Option to trace single beam
CONSIDER ONLY 0     ! Only look at source

*****! Analyse single-ray field for decompose !*****
WSEGO=2*WXO.       ! Dimensions of window
NPTSO=25           ! Number of pixels in Window
WIN Y -2@(WSEGO.) X -2@(WSEGO.) !Output window size
PIXEL NPTSO. 1     ! Number of pixels in one side of window
FIELD ENE 0        ! Calculate Field at windowz=0
                    ! (N.B. doesn't matter if ENE, PHA asked for
                    ! - calculates full complex field
*****! End analysis !*****

*****! Prepare for decomposition !*****
RAYS 0             ! New set of rays
HALT 1 badnes -Z relcut 1E-9 ! Only hit same object once, no rays
                    ! in -Z dir, cutoff when ray flux falls to
                    ! 1e-9 of centre max
CUTOFF abs 1E-22 totobj 5 ! Absolute cutoff at flux=1e-22,
                    ! same object 5 times

***! Decompose Field into many Gaussian Rays !***
DECOMPOSE DIR m 10000 a THLIM. THLIM. deg ! Used for point sources
*****! End of decompose section !*****

**** Reconstruction of beam to test fidelity ****
$GO norecons       ! Option to avoid beam reconstruction
CONSIDER ALL       ! Consider all optical components
NPT=100            ! Number of pixels in window
WIN X -2@WSEGO. Y -2@WSEGO. ! Setting up window
PIXEL NPT. 1       ! Number of pixels

```

```

FIELD ENERGY 0          ! Calculate the full complex Field at z=0
!SPOTS POSITION ATTRIBUTE 1 ! Spot diagram
!DISPLAY 29 ENE         ! Display complex data
!$SYS COPY FOR029.DAT RECON.DAT ! Option to copy reconstructed beam data
!GRA *Graph of reconstructed beam ! Draw graph of reconstructed beam
$IO                     ! Pause
RETURN                 ! Return to main program
norecons               ! Label for no reconstruction
nodecom               ! Label for single beam trace

CONSIDER ALL objects
SHIFT Z 1+B.          ! Shift rays to focus of telescope
WIN Y Z
TITLE *Ritchey Chretien Telescope
PROFILE OVE 'Ritchey-Chretien Telescope' ! Draw surfaces defined above
CONS ONLY 0 SECONDARY_MIRROR ! Consider only source and secondary
TRACE STEP 1 PLOT 50 OVE      ! Trace rays to next surface
                                ! (plot every 100th)
CONS ONLY SECONDARY_MIRROR PRIMARY_MIRROR ! Cons only sec and prim
TRACE STEP 1 PLOT 50 OVE      ! Trace rays to next surface
                                ! (plot every 100th)
CONS ONLY 1             ! Consider only primary
RETURN

CONSIDER ALL
*****! Number of points for rest of program !*****
NPTS1=250      !20 ! SHORT      !200 ! MEDIUM      !250 ! LONG
NPTS3=150      !20 ! ~FEW       !150 ! ~20MINS     !250 ! ~13HRS
NPTS4=100      !20 ! MINS       !40  !              !250 !

OBSC_Z=D12.    ! Position of Obscuration
W=1/SQRT(2)    ! Weighting factor for Bezier Curves

!!!Aperture of telescope!!!
EDGES          ! Set up surface as edges
ELLIPSE Z OBSC_Z. x DIAM./2 y DIAM./2 ! Circular, at obsc_z, radius D/2

*****
***           Start of Spider Creation           ***
*****

$IF ABCHOIC. EQ 3 THEN make spider obscuration
EDGES          ! Set up surface as edges
POINTS,       ! Points define the edges
*one*         0.0050      0.15      Z0. 1, ! x,y,z,q (q=link to next point)
*two*         0.0050      0.015     Z0. 2, ! 2=next point is vertex for curve
*curve*       0.02        0.012     Z0. W., ! For curve q>1.
*three*       0.01469     -0.003   Z0. 1, ! q=1 staight line to next point
*four*        0.1323      -0.071   Z0. 1, ! q=0 means no link to next point
*five*        0.1273      -0.07928 Z0. 1,
*six*         0.00995     -0.01122 Z0. 2,
*curve*       0.0         -0.017   Z0. W.,
*seven*       -0.00995    -0.01122 Z0. 1,
*eight*       -0.1273     -0.07928 Z0. 1,
*nine*        -0.1323     -0.071   Z0. 1,
*ten*         -0.01469    -0.003   Z0. 2,

```

```

*curve*   -0.022      0.0075   ZO. W.,
*eleven*  -0.0050     0.015    ZO. 1,
*twelve*  -0.0050     0.15     ZO. 1

SURFACE;
  PLANE Z OBSC_Z.          ! Surface from which obscuration will be cut
  OBJECT; .1 *SPIDER; BOUNDS -4 5 !Object from last surface,
                                ! bounds from objects 4 and 5
                                ! (+ve means obscuration opaque, -ve means
                                ! obscuration transparent, rest opaque

$ENDIF                      ! Back to main program

$IF ABCHOIC. NE 3 THEN      ! Beam clipped by telescope aperture
  SURFACE;
  PLANE Z OBSC_Z.          ! Surface form which Obsc will be cut
  OBJECT; .1 *APERTURE(no spider); BOUNDS -4
                                ! From last surface, bounded by object 4
$ENDIF

***! Option to plot clipping apertures !***
$GO noplot                  ! Option to plot obscuration
WIN Y X                     ! Auto set window to see obsc (WIN Y X)
WIN 1.2                     ! Make window slightly bigger
PLOT EDGES OVER             ! Draw obscuration
RETURN                      ! Return to main program
WIN Y Z                     ! Auto set window to see obsc (WIN Y X)
WIN 1.2;OBLIQUE             ! Make window wee bit bigger, oblique view
PLOT EDGES OVER             ! Draw obscuration
RETURN                      ! Return to main program
OBLI OFF                    ! Turn Oblique drawing off
noplot                      ! Label for noplot above

*****! End of Spider creation !*****

*****
***                          Start of Surface Ripple                      ***
*****

$IF ABCHOIC. EQ 4 THEN      rippled surface
  ***** !Create Rippled Surface ! *****
  ETA=1                     ! Scale factor to bring within budget eta<< 1
  M=2                       ! Order of surface ripple
  FRAC=ETA./M.
  PHAS=PI./2                ! Phase term to create non-symmetric ripples
  !PHAS=0                   ! Phase=0 for symmetric, pi/2 non-symmetric
  RAMPL=(FRAC.)*LAM./30     ! Peak to trough amplitude
  PERIOD=DIAM./M.          ! Period of ripple
  OSIZ=1.0                 ! For sampling rate (Greater than unity)
  NSPT=(30*DIAM.)/PERIOD.  ! Number of sampling points
  $REG NSPT OSIZ DIAM      ! Echo values to screen
  KRIP=2*PI./PERIOD.
  KRIP2=2*PI.*M./DIAM.
  XIT=OSIZ.*DIAM./2        ! Boundary of rippled surface

&$MAKEDIS EOM

```

```

$ITER X -1*XIT. XIT. -NSPT. Y -1*XIT. XIT. -NSPT. Z ! Iteration command
Z=(RAMPL./4)*(COS(PHAS.+(KRIP.*X))+COS(PHAS.+(KRIP.*Y)))
EOM ! Set up ripple as a 2D cosine function

$IF RIPDON. EQ 0 THEN make new surface
MAKEDIS ! Create rippled surface file makedis.dis
$ENDIF

SURFACE
SAMPLED MAKEDIS ! Make ripple surface into an object
LOCAL -4@OSIZ.*DIAM./2 -2@1E-3 Z ! Size of surface (bigger than primary)
OBJECT; .1 *SAMPLE_SURFACE !Give it a name
INTERFACE 1 ! 100% reflecting
DEFORM 0.1
SHIFT Z -0.1 ! Move it away from telescope

SURFACE ! Set up a detector for the ripple
PLANE Z 0 ! Made from a plane
LOCAL -2@0.3 -2@0.3 -2@0.001 Z ! Size of detector (-2@X means +/-X)
OBJECT; .1 *SURFACE_DETECTOR ! Give it a name
INTERFACE 0 1 VAC VAC
SHIFT Z SDET. ! Move it to behind primary
RET

CONS ALL ! Consider all surfaces
WIN Y -2@0.5 Z -0.3 1.6 ! Set window size (for analysis)
PROFILE OVE 'Ritchey Chretien telescope with surface ripple'
CONS ONLY PRIMARY_MIRROR SAMPLE_SURFACE ! Only want to cons pri and ripp
PRO OVE ! Option to plot surfaces
TRACE STEP 1 PLO 50 OVE ! Trace rays to next surface (plot every 100th)
CONS ONLY SAMPLE_SURFACE SURFACE_DETECTOR
PRO OVE
TRACE STEP 1 PLO OVE ! Trace rays to detector and plot

$ENDIF ! Back to main program
*****! End of Surface Ripple !*****

*****! Analyse clipped field for second decompose !*****
WSEG=3*WX. ! Set up window size
WIN X -2@WSEG. Y -2@WSEG. ! Output window size
PIX NPTS3. 1 ! Number of pixels in 1 side of window

!findme - Label to search for

$IF ABCHOIC. EQ 0 THEN beam clipped by aperture !(NOMINAL)
MOVE TO Z 0.0 ! Move rays to z=0
FIELD ENE 0.0 CLIP 4 ! Calculate field at z=0, clipping round ob 4
$$SYS COPY FORO29.DAT RCON.DAT ! Copy complex field data to RCON.DAT
$ENDIF

$IF ABCHOIC. EQ 1 THEN beam clipped by aperture !(DEFOCUS)
MOVE TO Z 0.0 ! Move rays to z=0
FIELD ENE 0.0 CLIP 4 ! Calculate field at z=0, clipping round ob 4
$$SYS COPY FORO29.DAT RCDN.DAT ! Copy complex field data to RCDN.DAT
$ENDIF

```

```

$IF ABCHOIC. EQ 2 THEN beam clipped by aperture !(TILT)
  MOVE TO Z 0.0          ! Move rays to z=0
  FIELD ENE 0.0 CLIP 4   ! Calculate field at z=0, clipping round ob 4
  $SYS COPY FORO29.DAT RCTN.DAT ! Copy complex field data to RCTN.DAT
$ENDIF

$IF ABCHOIC. EQ 3 THEN move to obscuration and calculate field !(SPIDER)
  MOVE TO Z OBSC_Z.      ! Move rays to z=obsc_z
  FIELD ENE OBSC_Z. CLIP 4 ! Calculate field at obsc_z, clip round ob 4
  $SYS COPY FORO29.DAT RCSN.DAT ! Copy complex field data to RCSN.DAT
$ENDIF

$IF ABCHOIC. EQ 4 THEN calculate field at ripple surface detector !(RIPPLE)
  MOVE TO Z SDET.       ! Move to z=sdet
  FIELD ENE SDET. CLIP 4 ! Calculate field at z=sdet, clip round ob 4
  $SYS COPY FORO29.DAT RCRN.DAT ! Copy complex field data to RCRN.DAT
$ENDIF

$IF ABCHOIC. EQ 5 THEN there is no clipping !(NO CLIPPING)
  MOVE TO Z 0.0          ! Move rays to z=0
  FIELD ENE 0.0          ! Calculate field at z=0
  $SYS COPY FORO29.DAT RCOON.DAT ! Copy complex field to RCOON.DAT
$ENDIF

RET      ! Return to main program
$IO
*****
***      End of first section of program      ***
***      Now trace rays to the far field      ***
*****
!$GO nored          ! Option not to remove edge aberrations
*****! Reduce the big aberrations at the edge of beam !*****
!Want to reduce data set to only include the points that lie in the !
!telescope diameter. Up to now, have clipped beam, and all the rest !
!(which is approx zero) but is different for different data sets !
!(rounding errors) !
*****

DISPLAY 29 WAV      ! Display current field data
REDUCE 15 135 1 15 135 1 ! Reduce data set to size of telescope
!ISO STEP 3        ! Option to plot isometric view of data
RET                ! Return to main program
*****! End of Reduce !*****
nored
!$GO noredef       ! Re-define field for onward propagation?

*****! Decompose field using decompose position !*****
RAYS 0             ! New set of rays
HALT 1 +Z 1E-9    ! Only one intersection per object, no beams
                  ! in -Z direction relative cutoff at 1e-9
CUTOFF 1E-22 5    ! Absolute cutoff at E/Eo of 1e-22,
                  ! max 5 intersections/object
WAVELENGTH LAM. ! M; ! Keep same wavelength (in metres)
DECOMPOSE POSITION  ! Decompose Beam into many Gaussian beams

```

```

! This dec pos is used for extended objects
*****! End decomposing field !*****

noredef          ! Label for no second decompose

*****! Trace to final surface !*****
*****! source geometry !*****
WX=X1.           ! Waist size at telescope of aperture=DIAM
WY=WX.           ! Circular beam
XDIV=LAM./(PI.*WX.) ! Beam divergence angles (Gaussian optics)
YDIV=LAM./(PI.*WY.)
ZSOU=0           ! Source at z=0
ZX=PI.*WX.*WX./LAM. ! Confocal distance (distance >> ZX,
! can extrapolate linearly
ZRAN=10*ZX       ! Distance to far off spacecraft (<5e9m due to
! computational problems)
RRAY=ZRAN.*(1+(ZX./ZRAN.)^2) ! Beam Radius at Z=ZRAN
WRAY=SQRT(WX.*WX.*(1+(ZRAN./ZX.)^2)) ! Waist size at Z=ZRAN
$REG WX          !
$REG ZRAN        ! Echo parameters to screen as a check
$REG WRAY        !

CONS ALL         ! Consider all objects
RAYS             ! Pick up ray data from file
  SHIFT Z -ZRAN. ! Shift data in z back to origin
  RET            ! Return to main program

*****! Final field analysis !*****
APE=1.5*WRAY.    ! Set aperture for analysis
WIN X -2@APE. Y -2@APE. ! Set window dimensions
PIX NPTS4. 1     ! Set pixel number on one side of window
FIE ENE 0        ! Calculate complex field

*****
***             Copy complex far-field data to appropriate file name             ***
*****
$IF ABCHOIC. EQ 0 THEN ! NOMINAL - Clipped by aperture
  $SYS COPY FOR029.DAT RCOF.DAT ! Copy field data
  DIS RCOF.DAT WAV          ! Display wavefront data
  WRITE REFCLIP             ! Create a .DIS and .DIN file
                           ! (needed for combine)
$ENDIF                    ! .DIS is a binary file, .DIN is an ASCII file

$IF ABCHOIC. EQ 1 THEN ! DEFOCUS - Separation of mirrors changed
  $SYS COPY FOR029.DAT RCDF.DAT ! Copy field data
  DIS RCDF.DAT WAV            ! Display wavefront data
  WRITE RCDF                  ! Create a .DIS and .DIN file
  DIS REFCLIP                ! Display Reference data
  COMBINE RCDF -1             ! Subtract DEFOCUS data from reference
  WRITE RCDF                  ! Write Defocus error .DIS and .DIN file
$ENDIF

$IF ABCHOIC. EQ 2 THEN ! TILT - Primary or secondary tilted
                           ! from optic axis
  $SYS COPY FOR029.DAT RCTF.DAT ! Copy field data
  DIS RCTF.DAT WAV           ! Display wavefront data

```

```

WRITE RCTF                ! Create a .DIS and .DIN file
DIS REFCLIP               ! Display reference data
COMBINE RCTF -1          ! Subtract TILT data from reference
WRITE RCTF                ! Write Tilt error .DIS and .DIN file
$ENDIF

$IF ABCHOIC. EQ 3 THEN    ! SPIDER - Obscuration in beam
$SYS COPY FOR029.DAT RCSF.DAT ! Copy field data
DIS RCSF.DAT WAV         ! Display wavefront data
WRITE RCSF               ! Create a .DIS and .DIN file
DIS REFCLIP             ! Display reference data
COMBINE RCSF -1         ! Subtract SPIDER data from reference
WRITE RCSF              ! Write Spider error .DIS and .DIN file
$ENDIF

$IF ABCHOIC. EQ 4 THEN    ! RIPPLE - Primary has form error
$SYS COPY FOR029.DAT RCRF.DAT ! Copy field data
DIS RCRF.DAT WAV        ! Display wavefront data
WRITE RCRF              ! Create a .DIS and .DIN file
DIS REFCLIP            ! Display reference data
COMBINE RCRF -1        ! Subtract RIPPLE data from reference
WRITE RCRF             ! Write Ripple error .DIS and .DIN file
$ENDIF

$IF ABCHOIC. EQ 5 THEN    ! NOTHING - Full Gaussian beam - no clipping
$SYS COPY FOR029.DAT RCOOF.DAT ! Copy field data
DIS RCOOF.DAT WAV       ! Display wavefront data
WRITE REFUNCL           ! Create Unclipped reference .DIS and .DIN file
WRITE RCOOF             ! Create .DIS and .DIN file for combining
DIS REFCLIP            ! Display clipped reference
COMBINE RCOOF -1       ! Subtract NOTHING data from reference
WRITE RCOOF            ! Write Nothing error .DIS and .DIN file
$ENDIF

*****! End final analysis !*****
$IO                      ! Pause, to allow the data to be analysed
endl

*****
***                      END OF PROGRAM                      ***
*****

```

# Bibliography

- [1] Einstein, A., (1918). *Preuss. Akad. Wiss. Berlin, Sitzungsberichte der Physikalisch-mathematischen Klasse*, p154.
- [2] Einstein, A., (1916). *Preuss. Akad. Wiss. Berlin, Sitzungsberichte der Physikalisch-mathematischen Klasse*, p688.
- [3] Schutz, B., (1985). In *A First Course In General Relativity*, Cambridge University Press
- [4] Pran, T., and Stark, R.F., In *Dynamical Spacetimes and Numerical Relativity*, ed Centrella, J.M., p 40, Cambridge University Press.
- [5] Backer,C., Kulkarni, S.R., (1990) *Physics Today, American Institute of Physics*, p26-35
- [6] Hulse, R.A., Taylor, J.H. (1975), *Astrophysical Journal*, **195**, L51-3
- [7] Taylor, J.H., (1992) In *Proceedings of General Relativity and Gravitation*, ed Glessier, R.J., Kozameh, C.N., Moreschi, O.M., p 287-294
- [8] Schutz, B., (1996), Albert-Einstein-Institut, Max-Planck-Institut fuer Gravitationsphysik, **AEI-003**
- [9] Wilson, J.R., and Mathews, G.J., (1995) *Physics Review Letters*, **75**, 23, p4161-4164
- [10] Thorne, K.S., In *300 Years of Gravitation*, ed. Hawking, S.W. and Israel, W., Cambridge University Press.
- [11] Danzmann, K., et al (1995), In *LISA - Pre Phase A Report*, **MPQ 208**

- [12] Danzmann, K., *et al* (1998), *LISA - Pre Phase A Report, 2nd Edition*, MPQ **233**
- [13] Sazhin, M.V., (1998) In *Experimental Gravitational Physics*, ed Michelson, P.F., World Scientific, Singapore
- [14] Weber, J., (1960) *Physical Review*, **117**, p306
- [15] Pizzella, G., (1997) *Classical and Quantum Gravity*, **14**, p1481-1485
- [16] *World Wide Web* pages relating to resonant mass detectors
- [17] Blair, D.G., *et al* (1991) In *The Detection of Gravitational Waves*, ed Blair, D.G., Cambridge University Press
- [18] Saulson, P.R., (1994) In *Interferometric Gravitational Wave Detectors*, World Scientific, Singapore
- [19] Meers, B.J., (1983) *Ph.D. Thesis*, University of Glasgow
- [20] Thorne, K.S., (1995) In *Proceedings of the Snowmass 95 Summer School on Particle and Nuclear Astrophysics and Cosmology*, eds. Kolb, E.W., and Peccei, R., World Scientific, Singapore.
- [21] Gertsenshtein, M.E., and Pustovoit, V.I. (1962) *Soviet Physics - JETP*, **16**, p433
- [22] Weiss, R., (1972) *Quarterly Progress Report of the Research Laboratory of Electronics of the Massachusetts Institute of Technology*, **105**, p54
- [23] Forward, R.L. and Moss, G.E., (1972) *Bulletin of the American Physical Society*, **17**, 1183(A)
- [24] Drever, R.W.P., *et al* (1983) In *Proceedings of the Ninth International Conference on General Relativity and Gravitation*, ed. Schmutzer, E., p265, Cambridge University Press
- [25] Maischberger, K., *et al*, (1987) In *International Symposium on Experimental Gravitational Physics*, ed. Michelson, P.F., p316, World Scientific, Singapore.

- [26] Morrison, E., *et al*, (1994), *Applied Optics*, **33**, 22, p5041-5049
- [27] Robertson, D.I., *et al*, (1995) *Review of Scientific Instruments*, **66** p4447-4451
- [28] Robertson, N.A., (1991) In *The Detection of Gravitational Waves*, ed. Blair, D.G., p353, Cambridge University Press
- [29] Danzmann, K., *et al*, (1994) *GEO 600 - Proposal for a laser-interferometric gravitational-wave antenna*, Max Planck Institut für Quantenoptik, **MPQ**
- [30] Strain, K., (1990) *Ph.D. Thesis*, University of Glasgow
- [31] Rowan, S., *et al*, (1997) *Physics Letters A*, **233**, p303
- [32] Hough, em et al (1991) In *The Detection of Gravitational Waves*, ed. Blair, D.G., p,330 Cambridge University Press
- [33] Skeldon, K.S., (1995) *Ph.D. Thesis*, University of Glasgow
- [34] Hellings, R., (1978) *Physical Review D* **17**, 12, p3158-3163
- [35] Faller, J.E., *et al* (1985) In *Proceedings of the Colloquium on Kilometric Optical Arrays in Space*, Cargese, **ESA report SP-226**
- [36] Danzmann, K., (1993) *LISA-Proposal for a Laser-Interferometric Gravitational Wave Detector in Space*, **MPQ 177**
- [37] Hellings, R.W., (1993) *SAGITTARIUS - Mission Concept Study*, JPL Engineering Memorandum 314-569
- [38] Hellings, R.W., (1993) *SAGITTARIUS - Space-borne Astronomical Gravity-wave Interferometer To Test Aspects of Relativity and Investigate Unknown Sources*, **ESA M3 Proposal**
- [39] Peterseim, M., *et al* (1996) *Classical and Quantum Gravity*, **13**, A279-A284
- [40] *LISA - Advanced projects Design Team: Final Report*, (1997) Jet Propulsion Laboratory, **JPL D-14350**
- [41] Bartoli, C., *et al* (1984) *Journal of Physics D: Applied Physics*, **17** p1473-2483

- [42] Gonzalez, J., *et al*, *Field Emission Electric Propulsion: Experimental Investigations on Microthrust FEEP Thrusters*, **IEPC-91-104**
- [43] Touboul, P., *et al* (1996) *Classical and Quantum Gravity*, **13**, A259-A270
- [44] ULE - Ultra-Low Expansion Glass, Corning Incorporated, New York
- [45] Giampieri, G., *et al*, (1996) *Optics Communications* **123**, p 669
- [46] Hellings, R., *et al* (1996) *Optics Communications*, **124** p 313-320
- [47] Peterseim, M., (1998) In *Proceedings of the Second International LISA Symposium*, In Press
- [48] Drever, R. W. P., *et al*, (1983) *Applied Physics B* **31**, 97
- [49] Pound, R.V., (1946) *Review of Scientific Instruments* **17** p 490-505
- [50] Vaughan, J.M., (1989) In *The Fabry-Pérot Interferometer*, Adam Hilger
- [51] Yariv, A., (1989) In *Quantum Electronics*, Third Edition, Wiley
- [52] Kane, T.J., and Byer, R.L., (1985) *Optics Letters* Vol **10** No 2 65-67
- [53] Zerodur, Low Thermal Expansion Ceramic Glass, Schott Glaswerke, Mainz, Germany
- [54] GEC Marconi Avionics, Silverknowes, Edinburgh, Scotland
- [55] Horowitz and Hill, (1995), In *The Art of Electronics*, Cambridge University Press
- [56] *MATLAB Simulink*, The MathWorks Inc., Massachusetts, USA
- [57] Kitchin, C.R., (1991), In *Astrophysical Techniques, 2nd Edition*, Adam Hilger
- [58] Schroeder, D.J., (1987) In *Astronomical Optics*, Academic Press
- [59] Amateur Telescope Making, <http://atmpage.com/design/cass.html>
- [60] Rutten and Van Venrooij, In *Telescope Optics-Evaluation and Design*, Willmann-Bell

- [61] Born, M., and Wolf, E., (1975) *Principles of Optics, Fifth Edition*, Pergamon Press
- [62] Hecht and Zajac, (1979), In *Optics, Fourth Edition*, Addison-Wesley
- [63] Winkler, W., (1997) *Classical and Quantum Gravity*, **12** pp1578-1585
- [64] *CODEV*, Optical Research Associates, Tucson, Arizona
- [65] *ASAP - Advanced Systems Analysis Program*, Breault Research Organisation, Inc., Tucson, Arizona
- [66] Greynolds, A.W., (1985) *Diffraction Phenomena in Optical Engineering Applications*, SPIE, **560**, p33-50
- [67] Seigman, (1986), In *Lasers*, Oxford University Press
- [68] Henneberg, P., Schubert, H., (1990), *Free-Space Laser Communication Technologies II*, SPIE, **1218**, p153-159
- [69] Juranek, H.J., *et al* (1994), SPIE, **2210** p407-418
- [70] Caldwell, M., McNamara, P.W., and Glenmar, A., *Proceedings of the Second International LISA Symposium, In Press*
- [71] *MATLAB for Windows*, The MathWorks Inc., Massachusetts, USA
- [72] *LabVIEW -Graphical Programming for Instrumentation, Ver. 4*, National Instruments

